Diffusion processes in white dwarf stellar atmospheres

Dissertation
zur Erlangung des Grades eines
Doktors der Naturwissenschaften
der Fakultät für Mathematik und Physik
der Eberhard-Karls-Universität Tübingen

vorgelegt von

Sonja Landenberger-Schuh

aus Stuttgart
2005

Tag der mündlichen Prüfung:	22. 02. 2005
Dekan:	Prof. Dr. P. Schmid
1. Berichterstatter:	Prof. Dr. K. Werner
2. Berichterstatter:	Prof. Dr. M. A. Barstow

Deutsche Zusammenfassung

Landenberger-Schuh, Sonja

Diffusionsprozesse in Sternatmosphären

Die Atmosphären Weißer Zwerge zeigen eine praktisch mono-elementare Zusammensetzung. Aufgrund hoher Oberflächenschwerebeschleunigungen spielt die Elementtrennung durch gravitatives Absinken eine große Rolle, so dass in diesen Sternen der überwiegende Anteil aller schwereren Elemente aus den äußeren Schichten verschwunden ist. Diese gravitationsbedingte Sedimentation geschieht auf sehr viel kürzeren Zeitskalen als die Entwicklung Weißer Zwerge entlang der Abkühlsequenz.

Beobachtungen junger Weißer Zwerge im Röntgen- und extrem ultravioletten Spektralbereich haben gezeigt, dass das Absinken dort nicht ungestört vor sich gehen kann, da zusätzliche Opazität beobachtet wird, die in den Atmosphären übriggebliebenen Metallen zugeschrieben werden muss. Es war ein interessantes Ergebnis der von ROSAT durchgeführten Himmelsdurchmusterung, dass praktisch keine Weißen Zwerge oberhalb einer Effektivtemperatur von etwa 65 000 K gefunden wurden. Das wird durch den Strahlungsauftrieb in heißen Weißen Zwergen erklärt, der der nach unten gerichteten Diffusion schwerer Elemente effizient entgegenwirken kann. Das Zusammenspiel dieser Kräfte bestimmt die chemische Zusammensetzung der Atmosphäre. Spuren von Metallen können dann durch radiativen Auftrieb gehalten werden, wenn das Strahlungsfeld intensiv genug ist, um der nach unten gerichteten Schwerkraft ausreichenden Impulsübertrag entgegenzusetzen. Dies ist in den meisten Objekten, die heißer als $T_{\rm eff} \approx 40\,000\,\mathrm{K}$ sind, der Fall.

Eine Umsetzung dieser konkurrierenden Prozesse in Sternatmosphären-Modellrechnungen liefert Vorhersagen für die vertikale Schichtung und absolute Häufigkeit von Metallen. Da die Strahlungsbeschleunigung durch ein NLTE-Strahlungsfeld auf in Spuren vorhandene Elemente über deren lokale Opazität übertragen wird, kann sie stark mit der Tiefe variieren und somit zu einer chemisch geschichteten Atmosphärenstruktur führen. Es wird insbesondere im Hinblick auf Weiße Zwerge ein Überblick über Modellierungsarbeiten auf dem Gebiet solcher Diffusionsrechnungen gegeben, mit den einschlägigen Referenzen sowohl zu ersten Erwähnungen dieser Ideen als auch solchen zu neuen Arbeiten, die die aktuellen Implementierungen und deren Anwendungen beschreiben. Innerhalb dieser neueren Ansätze spielt die Gleichgewichtsformulierung eine besondere Rolle, da sie eine relativ einfache Beschreibung der Balance zwischen gravitativem Absinken und Strahlungsauftrieb erlaubt.

Solche Modelle werden in dieser Arbeit vorgestellt. Sie berücksichtigen das Zusammenspiel zwischen Schwere- und Strahlungsbeschleunigung, um die chemische Schichtung aus einer Gleichgewichtsbedingung für die beiden Kräfte herzuleiten, und

lösen selbstkonsistent gleichzeitig die zugehörige Atmosphärenstruktur. Im Gegensatz zu Atmosphärenmodellen mit der Annahme chemischer Homogenität wird die Anzahl der freien Parameter auf allein die Effektivtemperatur und die Oberflächenschwerebeschleunigung reduziert. Ihre Stärke im Vergleich zu anderen Diffusionsmodellen liegt in der Selbstkonsistenz, die zudem unter NLTE-Bedingungen errechnet wird. Die Modelle berücksichtigen außerdem voll die Effekte des Line-Blanketing und verwenden detaillierte Atomdaten bis hin zu den Eisengruppenelementen.

Es werden die Ergebnisse verschiedener theoretischer Diffusionsrechnungen miteinander verglichen. Ein Gitter früherer, nicht-selbstkonsistenter Modelle sowie Varianten der neuen Modelle, die sich in der nummerischen Behandlung des Strahlungstransports und des Temperaturkorrekturschemas sowie in der Komplexität der verwendeten Atomdaten unterscheiden, werden untersucht und liefern bei näherer Betrachtung unterschiedliche Ergebnisse.

Mit einem großen Diffusions-Modellgitter aus Atmosphärenmodellen diesen neuen Typs wird ein EUV-selektiertes Sample heißer Weißer Zwerge analysiert. Die insgesamt gute Übereinstimmung mit beobachteten EUVE-Spektren macht deutlich, dass diese Modelle die physikalischen Bedingungen in den Atmosphären heißer Weißer Zwerge im Großen und Ganzen gut beschreiben.

Die EUVE-Spektren werden durch die Eisenopazität dominiert, so dass die tatsächlichen Eisenhäufigkeiten offensichtlich durch die Vorhersagen der Theorie gut getroffen werden. In einem Vergleich von Häufigkeitsmessungen an einzelnen Linien in einem umfassenden Datensatz von IUE- und HST-STIS-Beobachtungen mit Vorhersagen für Gleichgewichtshäufigkeiten gelangt man zu einer ähnlichen Schlussfolgerung für Eisen, und zu einem gewissen Grad auch für Sauerstoff und Silizium, während die Häufigkeitsniveaus für die Elemente Kohlenstoff, Stickstoff und Nickel nicht im gesamten Parameterbereich genauso gut wiedergegeben werden. Um den Einfluss eventuell bekannter Variabilitätserscheinungen oder Akkretionsprozesse mit zu berücksichtigen, werden alle Objekte des Samples einzeln diskutiert. Der Fall des Objekts RE J1032+535 wird besonders hervorgehoben, um die möglichen Schwierigkeiten, die sich bei der Analyse geschichteter Häufigkeitsprofile ergeben können, exemplarisch aufzuzeigen.

Eine wesentliche Grenze der Modelle scheint zu sein, dass der unbegrenzte Vorrat für alle beliebigen Elemente, den der Gleichgewichtsansatz voraussetzt, in Wirklichkeit nicht zur Verfügung steht. Das sollte dann kein Problem darstellen, wenn die Metallhäufigkeiten, die aus diesem Vorrat bezogen werden, tatsächlich sehr geringen Verunreinigungen entsprechen, aber diese Annahme ist nicht mehr gültig, wenn die Gleichgewichtshäufigkeiten eines Elements nahe der seiner kosmischen Häufigkeit liegen. Da diese Einschränkung auf versteckte Art und Weise auch andere Elemente betreffen könnte, wären als eine zukünftige Entwicklung zeitabhängige Diffusionsrechnungen ohne die Einschränkung auf den Gleichgewichtsfall wünschenswert.

Abstract

The atmospheres of white dwarfs exhibit a quasi-mono-elemental composition. Due to high surface gravities, element segregation by gravitational settling is of great importance so that a large fraction of all heavy elements in these stars has disappeared from the outer layers. This gravitational sedimentation happens on much smaller time scales than the evolution along the white dwarf cooling sequence.

Observations of young white dwarfs in the X-ray and extreme ultra-violet spectral ranges have revealed that the settling cannot act undisturbed there because additional opacity is observed which must be attributed to metals remaining in their atmospheres: It was one interesting result of the all-sky survey performed by ROSAT that essentially no hydrogen-rich white dwarfs above effective temperatures of about 65 000 K were found. This is being explained by radiative levitation in hot white dwarfs that can efficiently counteract the downward diffusion of heavy elements. The interplay between these forces governs the atmospheric chemical composition. Traces of metals may be sustained by radiative levitation provided the radiation field is intense enough to supply substantial momentum transfer against gravity's downward pull. This is the case in most objects hotter than $T_{\rm eff} \approx 40\,000$ K.

Incorporating the competition of these processes into stellar atmosphere model calculations provides predictions for the vertical stratification and absolute abundances of metals. The radiative acceleration is exerted on trace elements by a NLTE radiation field through the element's local opacity and therefore can vary strongly with depth, which results in a chemically stratified atmospheric structure. An overview of the modelling work done in the field of such diffusion calculations, with a focus on white dwarfs, is given, with the relevant references where these ideas were first mentioned as well as recent papers which describe current implementations and their applications. Within these latest approaches, the equilibrium formulation is of special interest since it permits a relatively simple description of the balance between gravitational settling and radiative levitation.

Such models are presented in this work. They take into account the interplay between gravitational settling and radiative acceleration to predict the chemical stratification from an equilibrium between the two forces while self-consistently solving for the atmospheric structure. In contrast to atmospheric models with the assumption of chemical homogeneity, the number of free parameters in the new models is reduced to the effective temperature and surface gravity alone. Their superiority over other diffusion calculations is the full self-consistency, calculated under NLTE conditions. The models are also fully line-blanketed and incorporate detailed atomic data up to the iron group elements.

The results from various theoretical diffusion calculations are compared. A grid of earlier, not self-consistent models as well as variations of the new models that differ

in the numerical treatment of the radiative transfer and the temperature correction scheme as well as in the complexity of atomic input data are considered and found to yield different solutions when examined in detail.

Based on a large diffusion model grid, a EUV selected sample of hot DA white dwarfs is analysed using this new type of atmospheric models. The overall good agreement with observed EUVE spectra reveals that these models are on the whole able to describe the physical conditions in hot DA white dwarf atmospheres.

The EUVE spectra are dominated by the opacity due to iron, so the real iron abundances appear to be relatively well matched by the predictions of radiative levitation theory. In a comparison of abundance measurements from individual lines in a comprehensive set of IUE and HST-STIS UV spectra with equilibrium abundance predictions, a similar conclusion is reached for iron, and to some extent also for oxygen and silicon, while the abundance levels for the elements carbon, nitrogen and nickel are not equally well reproduced over the full photospheric parameter range. To take into account effects such as known variability or accretion, all sample objects are discussed individually. The case of RE J1032+535 is given special consideration to demonstrate the potential difficulties in the analysis of stratified abundance profiles in an exemplary way.

One of the main constraints for the models seems to be that the theoretically unlimited reservoir of any element implied by the equilibrium approach is not available in reality. This should not be a problem when the metal abundances drawn from that reservoir correspond to almost negligible pollutants, but the assumption breaks down in those cases where the equilibrium abundance of an element starts to be of the same order of magnitude as its cosmic abundance. Since this restriction may, in a more subtle way, also affect the other element species, time-dependent non-equilibrium diffusion calculations would be a desirable future development.

Contents

1 Introduction **1**
- 1.1 Stellar evolution and white dwarfs . . . 1
- 1.2 White dwarf atmospheres and diffusion . . . 5
- 1.3 Line formation and spectral analysis . . . 9

2 Computational method **15**
- 2.1 Radiative transfer . . . 15
  - 2.1.1 Basic equations . . . 15
  - 2.1.2 Line formation in the case of inhomogeneous abundances . 18
  - 2.1.3 Radiative transfer under realistic conditions . . . 21
- 2.2 Atmospheric structure . . . 21
- 2.3 Diffusion . . . 24
- 2.4 Peculiarities of subsequent numerical implementations used . . . 29
- 2.5 Model atoms . . . 30

3 Model grids and high resolution spectra **33**
- 3.1 Overview . . . 33
- 3.2 The model grid used for the EUV analysis . . . 33
  - 3.2.1 Parameter range, atomic data and computational details . . 33
  - 3.2.2 Spectra . . . 34
- 3.3 Extended model grid . . . 35
  - 3.3.1 Parameter range and computational details . . . 35
  - 3.3.2 Example results: spectral features . . . 36
  - 3.3.3 Spectra from SYNSPEC . . . 37
- 3.4 New models: Test calculations . . . 38

4 Abundance tables **39**
- 4.1 Characteristics of the models . . . 39
- 4.2 Comparison to earlier models . . . 46
- 4.3 Discussion of test calculations with more opacities . . . 48

5 Analysis of spectroscopic EUVE data **53**
5.1 Introduction . . . 53
5.2 EUVE observations of hot DA white dwarfs . . . 54
5.2.1 The EUV selected DA sample . . . 54
5.2.2 Treatment of the ISM . . . 55
5.3 Equilibrium abundances from stratified model atmospheres . . . 55
5.3.1 Diffusion models . . . 55
5.3.2 Scope of application . . . 56
5.4 Testing the diffusion models and re-analysing the DA sample . . . 57
5.4.1 Comparison of theoretical and observed spectra . . . 57
5.4.2 Revised atmospheric parameters . . . 58
5.4.3 Metal index . . . 58
5.5 Discussion . . . 63
5.5.1 Summary . . . 63
5.5.2 Remarks on g and $g_{\rm rad}$ . . . 63
5.5.3 Outlook . . . 67

6 Abundance analysis in the UV **69**
6.1 Graphical representation of the results . . . 69
6.2 Object-by-object discussion . . . 83
6.2.1 Objects contained in the EUVE sample . . . 83
6.2.2 Other objects without EUVE spectra . . . 94
6.2.3 A closer look at the nitrogen lines in RE J1032+535 . . . 97
6.3 Element species in the full grid . . . 103

7 Conclusions **119**
7.1 Status of modelling . . . 119
7.2 Recapitulation of results from EUV and UV observations . . . 120
7.3 Perspective . . . 124

Bibliography **127**

A Equilibrium abundances **135**

Acknowledgements **157**

Lebenslauf **159**

List of Tables

2.1	Summary of ”old” model atoms	30
2.2	Summary of ”new” model atoms	31
5.1	Results of the EUV analysis	60
6.1	The N V doublet in RE J1032+535 from HST-STIS spectra . . .	101
6.2	The N V doublet in RE J1032+535 - comparison of two models .	103
6.3	Location of $\tau_{\rm ross} = \frac{2}{3}$ on the mass scale for Chayer et al. models	118

List of Figures

1.1	Line profiles for a stratified absorber	13
2.1	Radiative transfer quantities for a stratified absorber	18
3.1	The extended model grid	35
3.2	Emergent fluxes for selected parameters	36
3.3	EUV spectra from PRO2 and SYNSPEC	37
4.1	Iron abundances for different effective temperatures	40
4.2	Iron abundances for different surface gravities	41
4.3	Silicon abundances for different effective temperatures	42
4.4	Silicon abundances for different surface gravities	43
4.5	Nitrogen abundances for different effective temperatures	44
4.6	Nitrogen abundances for different surface gravities	45
4.7	$\tau_{\rm ross} = \frac{2}{3}$ on the mass scale as a function of $T_{\rm eff}$ and $\log g$	46
4.8	Comparison to Chayer's elemental abundances	47
4.9	Temperature stratifications with the "old" and "new" codes	49
4.10	Abundance stratifications with the "old" and "new" codes	50
5.1	EUVE spectrum of MCT 2331−4731	57
5.2	Revised parameters of the program stars	59
5.3	EUVE spectra of the program stars with theoretical spectra	62
5.4	Comparison of old and new $\rm T_{eff}$ and $\log g$	64
5.5	Comparison of different measures of the metal content	65
5.6	Parameters for G 191–B2B from different studies	66
6.1	UV elemental abundances of PG 0948+534	71
6.2	UV elemental abundances of Ton 21	71
6.3	UV elemental abundances of RE J1738+665	72
6.4	UV elemental abundances of PG 1342+444	72
6.5	UV elemental abundances of RE J2214−492	73
6.6	UV elemental abundances of Feige 24	73
6.7	UV elemental abundances of RE J0558−373	74
6.8	UV elemental abundances of WD 2218+706	74
6.9	UV elemental abundances of RE J0623−371	75
6.10	UV elemental abundances of PG 1123+189	75

6.11 UV elemental abundances of RE J2334−471 76
6.12 UV elemental abundances of G 191-B2B 76
6.13 UV elemental abundances of HS 1234+482 77
6.14 UV elemental abundances of GD 246 77
6.15 UV elemental abundances of RE J0457−281 78
6.16 UV elemental abundances of HZ 43 78
6.17 UV elemental abundances of RE J2156−546 79
6.18 UV elemental abundances of RE J1032+532 79
6.19 UV elemental abundances of PG 1057+719 80
6.20 UV elemental abundances of GD 394 80
6.21 UV elemental abundances of GD 153 81
6.22 UV elemental abundances of RE J1614−085 81
6.23 UV elemental abundances of GD 659 82
6.24 UV elemental abundances of EG 102 82
6.25 Complete spectral energy distribution of GD 394 93
6.26 Nitrogen stratification profiles for RE J1032+535 99
6.27 The N V doublet in RE J1032+535 from HST-STIS spectra . . . 100
6.28 The N V doublet in RE J1032+535 - comparison of two models . 102
6.29 UV C III abundances as a function of $T_{\rm eff}$ and $\log g$ 104
6.30 UV C III abundances as a function of mi 105
6.31 UV C IV abundances as a function of $T_{\rm eff}$ and $\log g$ 106
6.32 UV C IV abundances as a function of mi 107
6.33 UV N abundances as a function of $T_{\rm eff}$ and $\log g$ 108
6.34 UV N abundances as a function of mi 109
6.35 UV O abundances as a function of $T_{\rm eff}$ and $\log g$ 110
6.36 UV O abundances as a function of mi 111
6.37 UV Si abundances as a function of $T_{\rm eff}$ and $\log g$ 112
6.38 UV Si abundances as a function of mi 113
6.39 UV Fe abundances as a function of $T_{\rm eff}$ and $\log g$ 114
6.40 UV Fe abundances as a function of mi 115
6.41 UV Ni abundances as a function of $T_{\rm eff}$ and $\log g$ 116
6.42 UV Ni abundances as a function of mi 117
6.43 Location of $\tau_{\rm ross} = \frac{2}{3}$ on the mass scale for different models . . . 118
7.1 Summary of predicted and measured UV abundances 122
7.2 Summary of abundance deviations 123
A.1 Helium abundances as a function of $T_{\rm eff}$ 136
A.2 Helium abundances as a function of $\log g$ 137
A.3 Carbon abundances as a function of $T_{\rm eff}$ 138
A.4 Carbon abundances as a function of $\log g$ 139
A.5 Nitrogen abundances as a function of $T_{\rm eff}$ 140

A.6 Nitrogen abundances as a function of $\log g$ 141
A.7 Oxygen abundances as a function of $\mathrm{T_{eff}}$ 142
A.8 Oxygen abundances as a function of $\log g$ 143
A.9 Silicon abundances as a function of $\mathrm{T_{eff}}$ 144
A.10 Silicon abundances as a function of $\log g$ 145
A.11 Iron abundances as a function of $\mathrm{T_{eff}}$ 146
A.12 Iron abundances as a function of $\log g$ 147
A.13 Nickel abundances as a function of $\mathrm{T_{eff}}$ 148
A.14 Nickel abundances as a function of $\log g$ 149
A.15 Helium abundances as a function of mi 150
A.16 Carbon abundances as a function of mi 151
A.17 Nitrogen abundances as a function of mi 152
A.18 Oxygen abundances as a function of mi 153
A.19 Silicon abundances as a function of mi 154
A.20 Iron abundances as a function of mi 155
A.21 Nickel abundances as a function of mi 156

”The fault, dear Brutus, is not in our stars,
But in ourselves, that we are underlings.”

Cassius to Brutus in act I, scene II of ”Julius Caesar” (1598 – 1600) by W. Shakespeare.

CHAPTER 1

Introduction

1.1 Stellar evolution and white dwarfs

The visible matter in the universe is organised in galaxies, the building blocks of larger structures, where – under the influence of their own gravity – gas and dust clouds contract to form clumps that can give rise to star birth. Stars are self-gravitating gas balls which are hot and dense enough to maintain stable thermonuclear fusion in their cores. As such, they are essentially factories that reprocess the material they are made of, and return most of it to interstellar space during the last stages of their lives, leaving only a compact remnant of stellar ashes behind (or in some cases nothing at all). For an overwhelming majority of stars, this stellar remnant will simply be the left-over, burnt-out core of the former star and is commonly known as a white dwarf (WD). The following introduction aims at retracing only the most important steps leading to this common variant of stellar remnant.

Tracks in the Hertzsprung-Russell diagram (HRD[1]) are a very suitable way to describe the evolutionary paths of stellar objects. Stars spend most of their lifetime on the so-called main sequence, where they produce helium from hydrogen via nuclear fusion processes in their cores. If, at this main sequence stage, the mass of an isolated star exceeds about 8-10 $M_\odot$[2], it can subsequently evolve into an object as enigmatic as a neutron star or black hole. Most stars however are not massive enough to evolve into either of these objects, but will eventually turn into white dwarf stars instead.

A typical white dwarf has a radius of $\sim 10\,000$ km (i.e. roughly the same size as the earth). The mass distribution of white dwarfs peaks near 0.6 $M_\odot$. This implies a high mean density for these objects, as well as a large surface gravity of $\sim 10^8$ cm s^{-2} (or 10^5 times the earth's gravitational acceleration), which is equivalent to a steep pressure gradient in the stellar remnant envelope. Since – by definition – at this stage all

[1] Spectral type or colour plotted against the absolute magnitude or luminosity, allowing a graphical representation of correlations for stellar parameters (developed by Hertzsprung 1911 and Russell 1913).

[2] 1 $M_\odot$, i.e. one solar mass, corresponds to $1.989 \cdot 10^{33}$ g.

nuclear fusion processes inside the former star have ceased, the immense hydrostatic pressure built up by the weight of matter in above layers needs to be balanced by Fermi degeneracy of the electron gas. The equilibrium allowed for by this equation of state prevents the degenerate, nearly isothermal white dwarf core from collapsing. The gravitational energy released through slow contraction provides some additional luminosity, but essentially the overall luminosity, which is high at first – about 10^3 $L_\odot$[3] – rapidly decreases as the dead star cools. Likewise, from roughly 100 000 K at the exhaustion of the last fusion processes, the effective temperature ($T_{\rm eff}$) subsequently drops to 50 000 K in only 0.003 Gyr (Koester & Chanmugam 1990), while the lowest observed temperatures are not reached until roughly 10 Gyrs have passed (Koester 2002). Despite the high uncertainties for this last number (of the order of 20%), the determination of cooling times is quite relevant to questions beyond stellar physics issues, as outlined for example in a nice review by Fontaine et al. (2001).

Since the majority of all stars end their lives as a white dwarf, studying them helps to understand the evolution processes that average stars undergo. How do these relatively extreme, compact objects evolve from stars such as our sun? Stellar evolution theory describes the process of star formation up to the main sequence stage, the slow evolution away from the *zero age* main sequence, and the various evolutionary paths that stars then can follow depending on their initial chemical composition, masses and mass-loss rates at different lifetimes. To end up as a 0.6 $M_\odot$ white dwarf, a 10 $M_\odot$ main sequence star obviously loses a very substantial fraction of its initial mass, which emphasises the important role of late stages of stellar evolution (including the initial-final mass relations it predicts) for the galactic circuit of matter. At an age of $\sim$6 Gyr, the sun is about half-way on its long journey from the zero age main sequence to the turn-off point, where it will have exhausted the hydrogen supply in its core, forcing the hydrogen burning zone to move outwards. Shifting the fusion zone towards higher layers results in an expansion of the stellar outer envelope, thereby turning the star into a red giant, while the burnt-out core grows in mass and contracts until helium fusion is ignited.

For sun-like stars, this happens in a violent event referred to as the helium flash, which brings the star onto the horizontal branch. Here helium core and hydrogen shell burning proceed calmly for a longer period of time (of the order of 0.1 Gyr for a solar-mass star) before fuel exhaustion occurs once again, this time forcing the helium burning zone into a shell, and triggering the next, agitated phases. On its way along the asymptotic giant branch (AGB) towards regions of high luminosities, the star undergoes strong mass-loss through radiatively-driven winds. The subsequent stages are referred to as post-AGB evolution.

These late stages of stellar evolution comprise the processes up to the point where

[3] 1 $L_\odot$, i.e. the solar luminosity, corresponds to $3.90 \cdot 10^{33}\,{\rm erg\,s^{-1}}$.

the star eventually pivots onto the white dwarf cooling sequence. At the top of the AGB, a formerly sun-like star undergoes alternating phases of helium and hydrogen shell burning, and these thermal pulses lead to further mass-loss. The luminosity reaches a high value of $\sim 10^4\,\mathrm{L}_\odot$, then remains constant while the surface temperature quickly rises within only $\sim 10\,000$ yr, since the rapidly contracting hot core starts to shine through the expanding and dissipating envelope. Due to this contraction and the gradual loss of its envelope, corresponding to a sharp decline in the stellar radius, the remaining object is much more compact. The stellar wind accelerates due to the increased escape velocity, sweeping into and compressing the previously expelled material in the process.

The expelled material is ionised by the ultraviolet photons emitted from the increasingly hot object at its centre and starts to re-radiate at visible wavelengths, rendering it detectable as a planetary nebula. The nuclear fusion processes in the shell of the central star of the planetary nebula (CSPN) eventually cease, marking the now "dead" star's entry onto the white dwarf cooling sequence. According to the sequence of processes outlined here, standard stellar evolution theory hence predicts a white dwarf consisting of a carbon-oxygen core[4], surrounded by a helium layer, surrounded by an unprocessed hydrogen envelope. The thickness of this hydrogen envelope had been the subject of two competing theories for a while (known as the thick/thin layer discussion): The discussion seems to have converged to the statement that a whole (more or less continuous) range of envelope masses is required to explain the observations.

In addition to this, a non-negligible fraction of white dwarfs does not show such a hydrogen envelope at all. A late thermal pulse in a young white dwarf can bring it back onto the AGB, so that it is re-born as a star, hence the name "born-again" scenario for such an event. In this case, mixing processes draw the envelope material deep into the nuclear burning layers, where the remaining hydrogen supplies are being used up, leaving the star hydrogen-deficient when it approaches the top of the cooling sequence a second time.

Another peculiar variant in this listing of white dwarf feeder channels are stars that somehow already lose all but a tiny fraction of their hydrogen envelope as they reach the horizontal branch state. While they go through helium core burning just as normal horizontal branch stars do, their thin hydrogen envelopes are completely inert and make them appear as relatively hot, so-called extreme horizontal branch (EHB, spectral classification sdB, short for subdwarf B) stars. These objects do not have the means to spectacularly shed off large amounts of envelope material for simple lack of it, and instead follow a short-cut directly to the white dwarf graveyard.

Regardless of "details" in the surface composition, the final result of the evolution of low- and medium mass stars is usually a white dwarf with a carbon-oxygen core.

[4]More precisely, the outer part of the carbon-oxygen core is expected to be depleted in oxygen due to the temperature – and hence depth – dependency of the $^{12}\mathrm{C}(\alpha,\gamma)^{16}\mathrm{O}$ reaction rate during helium burning.

For a small range of initial masses around 10 $M_\odot$ (the exact numbers are still under discussion), theory predicts the possibility of oxygen-neon-magnesium cores instead, provided that the core mass growth during carbon burning is halted through envelope loss to prevent a subsequent core collapse. This should then result in massive white dwarfs of $\sim$1 $M_\odot$, with little envelope material left that is possibly strongly enhanced in neon. In contrast to this, very low mass stars should instead evolve into helium core white dwarfs, since they never attain the central densities required for helium burning. However, as the long evolutionary time scales for very low mass stars exceed the age of today's universe, this evolutionary channel has not had a chance yet to produce the helium core objects observed along the white dwarf cooling sequence. They instead exist because in binary systems, a close companion can draw off material from an ageing star when it starts to expand – up to the point where the core mass is reduced to below what is needed for the ignition of helium burning. In such a scenario the stellar ashes from only one instead of two main nuclear burning cycles make up the stellar remnant.

Just as the universe is too young to have produced helium core white dwarfs from isolated stellar evolution yet, it is also not old enough to allow for a cooling and hence fading in luminosity of nearby white dwarfs beyond the detection limit of large telescopes. The current low-temperature record stands at $\sim$2 200 K (Bergeron & Leggett 2002). Interpreted as an evolutionary effect, the observed cut-off in the cooling sequence of white dwarfs in our neighbourhood therefore provides a constraint for the galactic disk's age. Similarly, age and distance determinations from white dwarf cooling sequences can be attempted for open and globular clusters. Using a method that involves white dwarfs indirectly as progenitors in type Ia supernovae, they even serve in distance determinations on a cosmological scale. Understanding the underlying processes – all the way from the white dwarf(s) involved to the exact temporal and spectral dependency of the energy output during such an explosion – is an objective that, if fully achieved, would greatly improve the confidence in the reliability of this method.

More generally speaking, this implies that – in order to make use of white dwarf observations as tools in the quest for answers to other fundamental questions – one first has to understand the physical processes that link different evolutionary stages. Such continuous evolutionary sequences cannot be observed directly, they rather must be constructed from snapshots of individual stars at different ages. Stellar ages are generally only accessible through a detailed modelling of the star as a system that evolves through time according to given laws of physics. Other physical parameters such as the effective temperature, surface gravity or mass, radius and luminosity may be more readily accessible, but their precise determination also requires very detailed numerical simulations. An indispensable tool for such parameter determinations via spectral analysis methods are model atmosphere calculations: All processes deemed relevant

to the formation of the emergent spectral energy distribution of a star are mapped into a simulated model of the light-emitting atmosphere. A comparison of simulated with observed spectra then allows to draw conclusions about the exact physical conditions necessary to produce the observed spectrum. Besides a variety of fundamental stellar parameters that can be obtained from spectral analysis, the evaluation of if and how the integrated (or sometimes even dispersed) light from a star varies with time can yield further independent measurements, e.g. in binary systems or for pulsating stars.

A good understanding of the complete structure and outside appearance of a star still does not equal an understanding of its full history and future. To aquire insight into these, time-dependent stellar evolution models are needed. Here, in addition to being an indispensable tool in spectral analysis work, stellar atmosphere models play a crucial role by providing outer boundary conditions for these structural and evolutionary models. In particular, differences in the opaqueness of white dwarfs' atmospheres (due to the layer thickness) cause different cooling rates, just as the transition from radiative to convective energy transport leads to changes in the cooling rates which are otherwise determined by structural evolution in the core (diffusion, gas/liquid and liquid/solid transitions).

In many current applications, the evolutionary models used are those by Wood (1995).

The following Sect. 1.2 presents an inventory of the observed spectral properties of white dwarfs, which the entirety of both atmospheric and structural/evolutionary models will eventually have to reproduce and explain. Thereafter Sect. 1.3 details some demands to be made on stellar atmosphere models, and shows where this present work may be able to contribute an improvement. [5]

1.2 White dwarf atmospheres and diffusion

There are now more than two thousand white dwarfs compiled in the Villanova Catalogue of Spectroscopically Identified White Dwarfs by McCook & Sion (1999). The observational and physical information on white dwarfs it contains has been made available in an online version, which is also the primary source for the data maintained (and presented with some enhancements over the McCook & Sion 1999 online version) in the regularly updated electronic white dwarf database[6]. A large fraction of the objects currently appearing in the catalogues were discovered in large blue and ultraviolet (UV) excess surveys such as the Palomar-Green (PG, Green et al. 1986), Montreal-Cambridge-Tololo (MCT, Demers et al. 1986; Lamontagne et al. 2000) and

[5] The contents of this section partly rely on ideas collected in the Koester (2002) white dwarf review paper.

[6] http://procyon.lpl.arizona.edu/WD/

the Edinburgh-Cape (EC, Stobie et al. 1997; Kilkenny et al. 1997) surveys, as well as in the Hamburg Quasar and the Hamburg/ESO objective prism surveys (HQS, Hagen et al. 1995 and HES, Wisotzki et al. 1996; Reimers & Wisotzki 1997; Wisotzki et al. 2000).

With the Sloan Digital Sky Survey (SDSS), the number of photometrically detected white dwarfs is expected to rise by an order of magnitude (Fan 1999). On its way to achieving these additions through colour identification (and possibly follow-up spectroscopy), the SDSS First Data Release (Abazajian et al. 2003, following the Early Data Release, Stoughton et al. 2002) has already nearly doubled the number of spectroscopically identified white dwarfs (Kleinman et al. 2004). As a primer to what can be expected from the full SDSS once completed, Harris et al. (2003) have published WD numbers for a small area of sky.

Their compilation of exemplary observed spectra also constitutes a nice review of the different WD spectral types, from the very common to the rather unusual ones. Based on classification in the optical, the spectral types (all denoted starting with a D for *degenerate*) fall into two major categories: the hydrogen-rich DA and the helium-rich DB white dwarfs. The DA sequence is characterised by strongly pressure-broadened Balmer lines, while the non-DA sequence shows He I lines in case of DBs, and additional He II lines in case of the much rarer DOs, which extend the helium-rich sequence to high temperatures. Both the DA and the non-DA white dwarfs exhibit a quasi-mono-elemental chemical composition. Given that, in the scenario sketched earlier, white dwarfs should either end up with an unprocessed hydrogen envelope (making them DAs) or an exposed helium layer (generally making them DOs or DBs), the strongly sub-solar metallicity in their practically pure hydrogen or helium atmospheres would seem to contradict the general expectation of metal-enrichment with increasing stellar age.

The basic mechanism for this purification of white dwarf envelopes was first explained by Schatzman (1945, 1958): the strong gravitational field (typically, $\log g \simeq 8$ in cgs units) on the surface of WDs yields a steep pressure gradient, and hence pressure-driven diffusion separates the elements according to their atomic weight. This process is generally referred to as *gravitational settling* or sedimentation. Besides white dwarfs, where the sinking time scales are shortest in comparison, element segregation also affects the atmospheres of horizontal branch B stars, causing their helium and metal deficiency (Greenstein et al. 1967; Michaud et al. 1983), and is responsible for the chemical peculiarities observed in some A main sequence stars (Michaud 1970).

These diffusion processes cause perhaps the most obvious spectral evolutionary effects seen in WDs. They alter the atmospheric composition from complex patterns still observed beyond the AGB to just two mono-elemental variants. The strict separation of both sequences is due to diffusion. The initial effectiveness of diffusion is not

completely independent of temperature (as will be shown later) and hence also undergoes evolutionary change. Several other changes in appearance such as the evolution of the overall flux level, colours, or ionisation equilibria can also be directly linked to the continuing cooling. The ranges of effective temperatures assumed by DA WDs are simply parametrised by a spectral index from 1 to 7, calculated as 50 400 K / $T_{\rm eff}$ [K], and are reflected by the increasing strength of the Balmer lines with decreasing effective temperature. Just as the gradual recombination of ionised hydrogen to atomic hydrogen characterises the DA sequence, the recombination of He II to He I marks the transition from the hotter DOs to the cooler DBs, defined by the spectral lines observed from the predominant ionisation stage.

In addition to this easily explained break in the helium-rich sequence (due to the presence of more than one ionisation state, clearly reflected by a change in name), the helium sequence is also interrupted by the so-called "DB gap" (Liebert et al. 1986). A common explanation for the lack of any helium-rich objects in the temperature range between 45 000 K (coolest DOs) and 28 500 K (hottest DB) goes as follows: The upwards diffusion of any remaining traces of hydrogen is eventually enough to cover the helium layer – corresponding to the high-temperature end of the gap where helium-rich objects (DOs) therefore are effectively turned into DAs. Once convection due to helium ionisation becomes efficient it dilutes any thin diffusive hydrogen layer; mixing occurs and turns a fraction of the DAs back into DBs (presumably mostly the "hidden" former helium-rich ones, but the fraction of non-DAs versus DAs does not recover the ratio above the gap). However, there is as yet neither theoretical nor observational evidence which unambiguously confirms this scenario (or any alternative ones brought forward until now).

Towards cooler temperatures, first the helium and then the hydrogen lines substantially weaken and finally vanish when the energy necessary to excite the transitions ceases to be available. When no features can be discerned in such a WD, it is called a DC type. In some cooler WDs, however, photospheric carbon can be detected, believed to be brought to the surface from the (stratified) C/O core by dredge-up processes. Such WDs with carbon features are classified as DQs. Metal lines observed in a cool WD, on the other hand, make it a DZ. The tendency to purification is in this case not disturbed by convective mixing or dredge-up processes, but possibly by accretion from interstellar matter. Both DQ and DZ white dwarfs usually have helium-rich atmospheres, which are more transparent in the optical and therefore allow for the detection of smaller amounts of metals (including carbon) than hydrogen-rich ones. Aside from the white dwarf spectral classifications DA, DO, DB, DC, DQ and DZ, hybrid types are known. Though rare, they are often key objects to investigate possible evolutionary links between the classes. Finally, whenever polarisation due to magnetic fields has been measured, the classification is annexed by the letter P, and the corresponding spectra can appear heavily distorted.

In the relatively pure, opacity-poor hydrogen or helium atmospheres, additional absorbers can have a substantial impact on the atmospheric structure and the spectral distribution of the emergent flux. In the case of the types discussed above, the effects are remarkable enough to result in different classifications for the objects. But the very common DA white dwarfs (followed in number by DBs, with DA : DB $\approx$ 7:1), with the high degree of purification in their atmospheres brought about by diffusion, also continue to hold their surprises in this respect. In hot WDs with $T_{\rm eff} \approx 40\,000$ K upwards, the diffusion process is disturbed by the radiation pressure that elements experience, depending on the overlap of their wavelength-dependent opacities with the maximum spectral flux. The overlap of the maximal spectral intensity with the region of maximal opacity yields a considerable radiative acceleration on heavier elements in WD atmospheres, provided the luminosity is high enough (theoretical calculations by Vauclair et al. 1979; Fontaine & Michaud 1979, and later Morvan et al. 1986; Vauclair 1987, 1989 as well as Chayer et al. 1989, 1991, 1994, 1995a,b). Luminosities $L/L_\odot > 1$ are sufficient to sustain photospheric elements other than hydrogen with abundances no higher than 10^{-4} relative to hydrogen.

In *optical* spectra of hot white dwarfs, these trace pollutants become directly visible only when great effort is put in the detection of individual lines (Dupuis et al. 2000a), but can influence the accurate determination of effective temperatures and surface gravities. Through resonance lines in the UV and even more through the sheer number of lines in the extreme ultraviolet (EUV), these spectral ranges can be strongly affected.

The flux deficit caused by the additional opacity in the EUV as compared to pure hydrogen atmospheres, hinted at already by earlier data (Mewe et al. 1975; Hearn et al. 1976; Lampton et al. 1976; Margon et al. 1976; Shipman 1976), became more and more evident as the quality of observations improved with the HEAO 2 (Einstein), EXOSAT and ROSAT satellites (Kahn et al. 1984; Petre et al. 1986; Jordan et al. 1987; Paerels & Heise 1989; Barstow et al. 1993a; Jordan et al. 1994; Wolff et al. 1996). In particular, after ROSAT had found many fewer hot WDs than expected from predictions based on pure hydrogen atmospheres, both the levitation mechanism as well as the identification of the elements involved were turned into foci of research interest.

While EXOSAT (Vennes et al. 1989) and various ROSAT observations revealed that the opacity must be mainly due to absorbers other than helium, only observations with EUVE made a more detailed investigation of the nature of absorbers possible. Since then, first IUE and then subsequently HST have continued to place tight and sometimes contradictory constraints on the picture that starts to emerge. The application of radiative levitation theory to determine and explain the photospheric metal abundances in hot DA white dwarfs is the topic of this thesis. The remaining part of this introduction therefore compiles the most important results from previous work relevant to this field.

1.3 Line formation and spectral analysis

The atmospheres of WDs exhibit a quasi-mono-elemental composition because a large fraction of all heavy elements has disappeared from the outer layers due to gravitational sedimentation. Traces of metals may however be sustained by radiative levitation provided the radiation field is intense enough to supply substantial momentum transfer. Analysis of larger samples of hot white dwarf EUVE spectra by Barstow et al. (1997) and Wolff et al. (1998) have shown that this is the case in most DAs hotter than $T_{\rm eff} \approx 40\,000\,{\rm K} - 50\,000\,{\rm K}$.

Photospheric abundances can only be obtained through comparisons with detailed synthetic spectra, requiring a realistic modelling of stellar atmospheres. Using state-of-the-art non-LTE (NLTE) and LTE atmosphere models (see also the following chapter on modelling), both Barstow et al. and Wolff et al. derived a metal mix scaling factor for each object in their respective DA sample. Barstow et al. use this single scaling factor per object to adjust metal abundances predicted for its combination of effective temperature and surface gravity by Chayer et al. (1995a,b), whereas Wolff et al. use relative metal abundances which they derived for the well-studied standard star G 191–B2B as a typical metal mix and give the appropriate scaling factor that they call *metallicity* for each of their sample objects. The theoretical work by Chayer et al. (1995a,b) assumes an equilibrium condition for the interplay between gravitational settling and radiative levitation to obtain photospheric abundance values for various metals from a pre-computed atmospheric structure and its corresponding radiation field. The current state of similar calculations using equilibrium radiative levitation theory to attempt to explain observed surface abundance patterns in DO and DA white dwarfs has been summarised by Dreizler & Schuh (2003). Recent related work for different types of stars includes studies concerning the photospheres of horizontal branch stars (Hui-Bon-Hoa et al. 2000) and Ap/HgMn main sequence stars (Hui-Bon-Hoa et al. 2002; Budaj & Dworetsky 2002). Studies that additionally incorporate the effects of mass-loss in the modelling of both white dwarf and sdB star envelopes were last presented by Unglaub & Bues (1998, 2000, 2001).

Since the radiative acceleration is exerted on the trace element by a non-local radiation field through the element's local opacity, it can vary strongly with depth, leading to a chemically stratified atmospheric structure. In the model atmospheres used in the analyses by both Barstow et al. (1997) and Wolff et al. (1998), the distribution of the metals was assumed to be homogeneous, i.e. abundances were treated as being the same in all atmospheric depths (a standard assumption in stellar atmosphere modelling). As the effects of sedimentation and radiative levitation lead to a chemical gradient, fitting the emergent flux with homogeneous atmosphere model spectra has its limits, and true consistency cannot be achieved if the real WD atmosphere is stratified. Barstow et al. (1999) first succeeded in providing observational evidence for

such an abundance gradient when their attempt to include the impact of a chemical gradient via an ad hoc stratification of iron could better reproduce the EUVE spectrum of G 191–B2B. An improved model by Dreizler & Wolff (1999) with a much more sophisticated stratification pattern convincingly confirmed these findings for this single object. Using the same type of advanced stratified models, Schuh (2000) then obtained first results for a larger sample, again comprising the available EUVE observations of hot DAs.

The EUV spectral range is of particular importance here because the presence of trace metals strongly affects the emergent flux in the short wavelength regimes where hydrogen has become mostly transparent. Line blanketing effects redistribute the flux, sometimes up to a complete blocking of light in the short EUV/X-ray range. Since different spectral energy bands emerge from different atmospheric depths, metal abundances varying with depth have the strongest impact on the flux distribution in the EUV. Hence the pseudo-continuum is distorted in the spectral regions of maximum energy output, although observationally these are always subjected to interstellar absorption of varying degree due to hydrogen and helium.

In addition to these effects, a chemical gradient also has the potential to affect the line profiles of the element in question. Heavy line blending in combination with the limited spectral resolution makes it hard to identify individual metal lines in EUVE spectra, and impossible to examine their profiles in detail. The UV and far-UV (FUV) spectral ranges, currently covered by the HST and FUSE observatories, are not as severely affected by line blending and usually only suffer from more subtle interstellar absorption effects. Due to the possibility of extracting detailed information from individual lines, photospheric abundance studies have started to shift primarily towards these windows. Evidence for chemical stratification of nitrogen in the atmosphere of RE J1032+535 was found from unusual line profiles observed with HST by Holberg et al. (1999a). Chayer et al. (2003) also claim to require oxygen stratification in order to simultaneously fit HST, FUSE and EUVE data of Lan 23, GD 984, RE J1032+535 and RE J2156−543. To reach their conclusions, Holberg et al. (1999a) again used an ad hoc stratification, while Chayer et al. (2003) made use of the profiles provided by Schuh (2000).

Despite this growing evidence for important stratification effects, abundance analyses of larger samples of stars (Barstow et al. 2003c; Dupuis et al. 2003) still resort to homogeneous atmosphere models: Beyond the few special cases just discussed, more appropriate models have not been available. The derived abundances are then often compared to the numerical results by Chayer et al. (1995a,b).

It is questionable, however, whether such comparisons can be meaningful at all: The potential consequences of fitting spectral features resulting from highly stratified absorber patterns with such from homogeneously distributed absorber patterns are schematically illustrated in Fig. 1.1. A fixed amount of absorbing line forming mate-

rial is placed at different optical depths in a surrounding gas slab in high concentrations (grey areas in right-hand panels). The corresponding homogeneous abundance, obtained by evenly spreading the total absorber content over the given optical depth range, would be the same and equal to 1 in all cases (not shown). Comparing the line profiles calculated for the concentrated material with those calculated for various homogeneous distributions (i.e. abundance values smaller or greater than 1, not shown) gives a different result. The line profiles from the unevenly distributed patterns (grey lines in left-hand panels) can generally not be matched with profiles from abundance patterns without gradients. Upper and lower limits to the homogeneous abundances required to approximately fit the line profiles can be derived by matching the line cores and the line wings separately (black lines in both panels: line profiles left, abundance limits right). It can clearly be seen that these limits for the effective homogeneous abundances are not only systematically shifted towards lower or higher values in comparison to the corresponding mean homogeneous abundance, but also that they are not correlated with the peak value of the stratified abundances either.

These complications, potentially only made worse when going from the above academic example to a more realistic situation, suggest that direct comparison of abundance measurements obtained with homogeneous atmospheres to radiative levitation theory predictions should be interpreted with caution. Although the disagreement often seen in such comparisons has regularly been attributed either to shortcomings in the models by Chayer et al. (1995a,b) – such as the missing feedback of the additional absorbers' opacity on the atmospheric structure, or to the non-applicability of pure radiative levitation theory without the inclusion of further, so far unidentified physical processes – this fundamental difficulty must also be appropriately considered.

The incapability of even the current complex NLTE, fully line-blanketed atmosphere models, incorporating virtually any desired element, to reproduce the finer details of hot DA spectra is hard to overcome with models using an externally imposed depth-dependent stratification. Dreizler (1999) avoided the addition of numerous further adjustable parameters associated with such approaches, replacing them with physically meaningful profiles instead, by introducing self-consistent diffusion models. The depth-dependent abundances for any metals in these full-grown WD atmosphere models are calculated assuming equilibrium between radiative elevation and gravitational settling, with the coupling between the chemical stratification and the radiation field taken into account self-consistently through an iterative scheme. An inherent property of the equilibrium condition used is that the metal abundances are not free parameters as they would be in an homogeneous model, but determined at every single depth point for each of the metal species included, effectively reducing the free parameters for the model atmosphere calculation to the effective temperature and surface gravity only. By significantly reducing the dimension of parameter space in the fitting process, this approach also formally reduces the chances of finding the best

fit otherwise accessible through careful fine-tuning of (preferably depth-dependent!) abundance parameters. The requirement to describe the physics forming the chemical stratification as realistically as possible is therefore extremely stringent. Failure to avoid important systematic errors in the modelling, or to recognise and include all relevant physical processes, is likely to result in synthetic spectra that cannot reproduce observations at all (as opposed to reproducing observations at distorted stellar parameter combinations). For the new diffusion models, Dreizler & Wolff (1999) and Schuh (2000) have shown that they are capable of correctly predicting the general trends in the metal content and stratification in hot DA white dwarf atmospheres. Based on a preliminary analysis of EUVE spectra with a rudimentary set of models, these successful demonstrations of overall agreement proved the remarkable potential of the underlying principle, but still left many questions unanswered. Therefore, the objectives of this thesis are:

- to provide a full grid of diffusion models complete with abundance tables and high-resolution spectra;
- to repeat the analysis of EUVE spectra based on this larger grid and using improved visual magnitudes;
- to quantify possible systematic errors in the models by comparing the results to earlier diffusion calculations, as well as to new models with more extensive atomic input data (resulting in an improved treatment of the radiative accelerations);
- to quantify the contribution of systematic effects to the inconsistencies arising when comparing predicted equilibrium abundances to abundance measurements obtained with homogeneous models from extensive UV/FUV data;
- to explore the magnitude and possible correlation with stellar parameters of remaining discrepancies (after consideration of the issues above) which must be due to physical processes such as mass-loss, mixing, or accretion, all ignored so far in the models;
- based on the lessons learned from the investigations above, to provide guidelines on how the models can be productively used in systematic multi-wavelength analyses to understand the spectral evolution of WDs in a broader context.

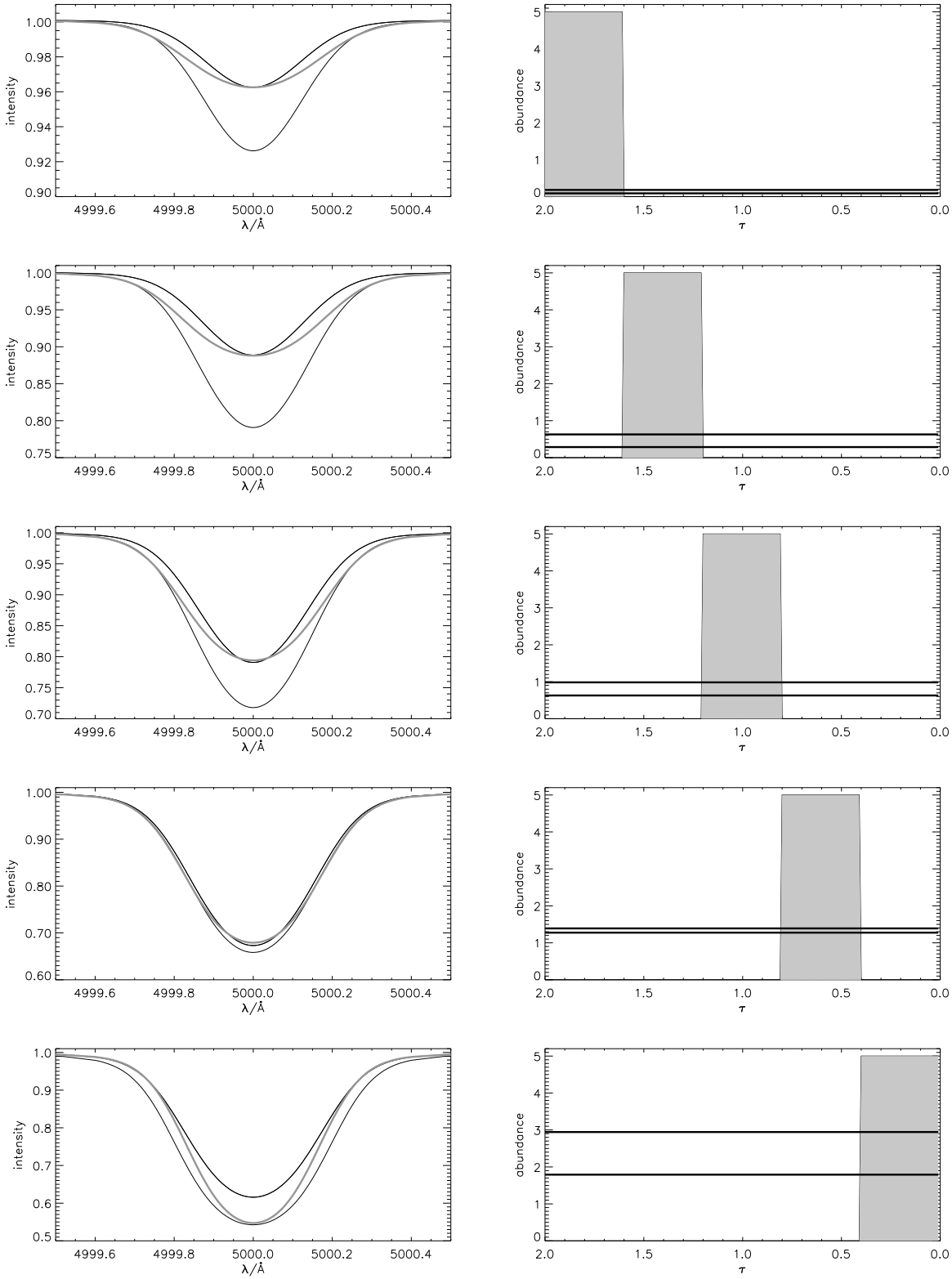

Figure 1.1: Line profiles (left panel) for homogeneously distributed (black) and stratified (grey) absorber contents in a gas slab (right panel) with a temperature gradient. Note the non-uniform axis ranges for the spectral flux intensities, otherwise see text for details, and Sect. 2.1.1 for a description of the calculations.

CHAPTER 2

Computational method

2.1 Radiative transfer

2.1.1 Basic equations

A star is not in thermodynamical equilibrium with its surroundings: The energy it produces is eventually radiated away into space through its atmosphere. For hot stars, the most efficient way to transfer energy through their atmospheres are radiative processes. The solution of the radiative transfer problem is hence one important ingredient in the construction of any stellar atmosphere model, extensively treated elsewhere, which is why only a few basic principles (from Dreizler 2002, partly based on Rutten 1997) are reiterated here.

In a simple one-dimensional configuration, the change of intensity dI along a segment dx at a given frequency ν is given by the attenuation of I due to the opacity κ and the added contribution through the emissivity η:

$$\frac{dI_\nu}{dx} = -\kappa_\nu I_\nu + \eta_\nu = -\kappa_\nu \left(I_\nu - S_\nu\right), \tag{2.1}$$

where the source function S has been introduced using the definition $S = \eta/\kappa$. An optical depth scale τ can be defined as

$$d\tau_\nu = \kappa_\nu \, dx, \tag{2.2}$$

allowing the expression of geometrical dependencies in units of the mean free path for photons. In the case of local thermodynamic equilibrium (LTE), where the electron temperature and the radiation temperature of the plasma are so strongly coupled through frequent collisions that they can both be described by one single value T, the source function may be approximated by the Planck function B, yielding

$$\frac{dI_\nu}{d\tau} = -I_\nu + S_\nu \approx -I_\nu + B_\nu. \tag{2.3}$$

For a given incident intensity I_ν at the location x_0, the solution to this radiative transfer equation along a segment $\delta x = x - x_0$ can then be written as

$$I_\nu(x) = I_\nu(x_0)\, e^{-\tau_\nu(x)} + \int_{\tau_\nu(x_0)}^{\tau_\nu(x)} B_\nu(T(\tau'_\nu))\, e^{-(\tau_\nu - \tau'_\nu)}\, d\tau'_\nu. \tag{2.4}$$

The optical depth is frequency-dependent since the opacity κ generally is a complex, frequency-dependent function of atomic properties. For some problems however, it is desirable to define a frequency-independent mean optical depth scale, such as the one based on the Rosseland mean opacity:

$$\tau_{\text{ross}}(x) = \int_{x_0}^{x} \kappa_{\text{ross}}\, dx' = \int_{x_0}^{x} \left(\frac{\int_0^\infty \frac{\partial B}{\partial T}\, d\nu}{\int_0^\infty \frac{1}{\kappa_\nu} \frac{\partial B}{\partial T}\, d\nu} \right) dx'. \tag{2.5}$$

For such a hypothetical "grey" opacity κ_{ross}, the optical depth scale becomes independent of frequency and can be thought of as if it described geometrical distances.

Generally speaking, opacity can result from photon absorption or stimulated emission in atomic (or molecular) level transitions (bound-bound transitions), photoionisation (bound-free transitions), free-free, or scattering processes. One basic and important contribution to κ is the line opacity in the case of an exemplary two-level system (the opacities are additive when more levels are included). For an atom featuring a *lower* and an *upper* state, its opacity would be determined by the cross section σ for the transition and the level population n according to

$$\kappa_{lu}(\nu) = \sigma_{lu}(\nu)\, n_{low}. \tag{2.6}$$

The cross section σ can be described by the classical cross section value for an electron in an electromagnetic field corrected by a quantum mechanical correction term (oscillator strength f), and the frequency-dependent contribution separated into a profile function ϕ, so that with

$$\kappa_{lu}(\nu) = \frac{\pi e^2}{mc}\, f_{lu}\, n_{low}\, \phi(\nu), \tag{2.7}$$

κ essentially becomes a function of the level population and the profile function for a given atomic line. The profile function will be a convolution of all broadening mechanisms at work, and as such potentially depend on temperature, pressure, magnetic field strength, micro turbulence, and large-scale movements such as convection, currents on the stellar surface, or rotation. The dominant effects of temperature and

pressure[1] in environments relevant to non-magnetic classical stellar atmosphere modelling can be described through the damping parameter a and a parametrisation in the dimensionless frequency variable v of the Voigt function $V(a, v)$. If this Voigt function is used as a typical profile function, the frequency dependency of an optical depth scale may be written as

$$\tau(v) = \tau_0 \, V(a, v), \tag{2.8}$$

where

$$v = v(\nu) = \frac{c \, (1 - \frac{\nu}{\nu_0})}{\sqrt{2\mathrm{k}T/m}}, \tag{2.9}$$

and where τ_0 shall be chosen so as to represent an arbitrary line opacity at the rest frequency of the line centre.

Given the two exemplary representations for τ in Eqs. 2.5 and 2.8, the corresponding effects on I_ν according to Eq. 2.4 can be illustrated using a simple two-temperature model. In what is known as the Schuster-Schwarzschild model, a plane parallel, isothermal gas slab is irradiated by a Planck function of any other temperature. The incident intensity is exponentially attenuated for increasing optical depths, and for $\tau = 1$ drops to $\frac{1}{e}$ of its initial value. The fractional contribution of the source function in the emergent intensity increases with increasing optical depths; for any frequency-independent optical depth, the effects of the source function quickly become completely dominant. The emergent intensity is then solely determined by the temperature of the gas slab, independent of what incident intensity it is being irradiated with, as long as this irradiation is not allowed to change the temperature of the gas itself. The situation is different for a transparent continuum modified only locally (in frequency) by an optically thick line. For this other extreme, the continuum contribution will be the unchanged incident radiation, since it can neither be attenuated nor can a gas slab with zero optical depth contribute to the intensity at those frequencies. The line centre, on the other hand, will again be dominated by the source function of the gas slab alone, so that the maximum possible line depth is given by the ratio of the source functions of the irradiating and the irradiated material. When the source functions are Planck functions as in the above example, it is immediately clear that an irradiation of a gas slab with a temperature below the radiation temperature of the incident field will lead to absorption, while a gas slab hotter than the irradiating field will cause emission. For equal temperatures, the attenuation is exactly balanced by the contributions of the source function in the material crossed.

In real situations, the optical depth will be a complex function of both continuum and line opacities. Furthermore, neither the temperature nor the opacity and emissivity will usually be constant throughout a macroscopic gas slab, but also vary with

[1] They obviously also can have a strong influence on the level population at the same time.

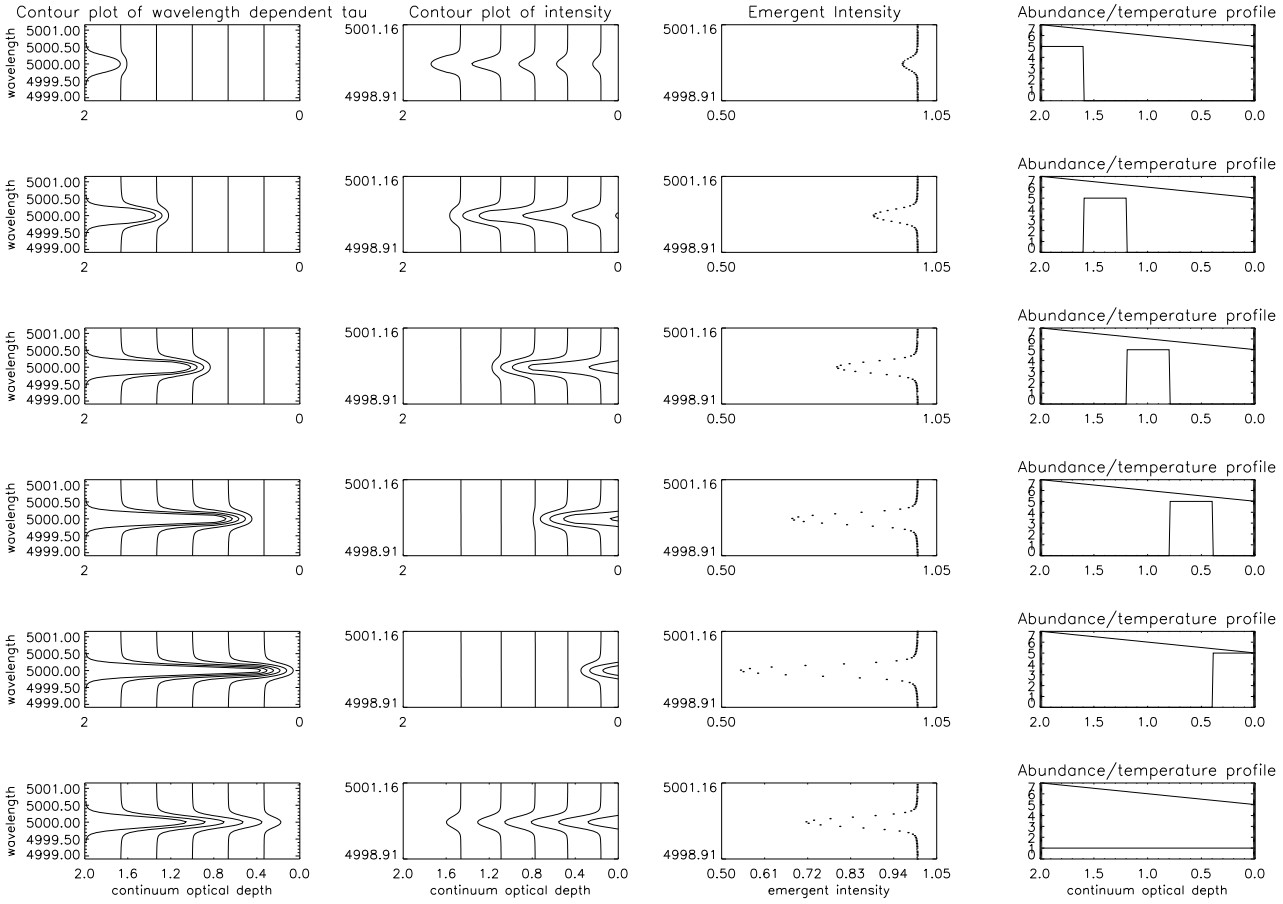

Figure 2.1: Radiative transfer quantities for an absorber stratified according to the distribution shown in the rightmost column: contour representation of the corresponding wavelength-dependent optical depth over continuum optical depth (left), wavelength-dependent intensity over continuum optical depth (second from left), and plot of the wavelength-dependent emergent intensity at a continuum optical depth of zero (third from left). The ordinate values for the right column characterise both the abundance distribution function $s(x)$ as well as the temperature in kK.

depth. To account for this, the optical depth must generally be determined according to Eq. 2.2.

2.1.2 Line formation in the case of inhomogeneous abundances

To illustrate the effects of compositional stratification on the emergent spectrum of radiating material, a simple case of one-dimensional radiative transfer through a plane parallel gas slab with a given temperature gradient will now be explored. At the geometrical depth $x = 0$, the gas slab is irradiated by a Planck function corresponding to a given blackbody temperature (7 000 K in this example), and its temperature $T(x)$ linearly decreases in the outward direction (to 5 000 K at the outer edge). The continuum opacity κ^c is assumed to be constant throughout the material, which allows one

to define a mean optical depth scale $\tau^c(x)$=$\kappa^c \cdot x$ (from τ^c=0 at x_0 to τ^c=2 at $x_{\max}$) that is regular in geometrical depth. Additionally, the frequency-dependent opacity of a single line (centred at 5 000 Å) is introduced as $\kappa^l \cdot V(a, v(x, \nu))$. The purpose of this line opacity is to simulate an absorbing element[2], which can be distributed in any desired depth intervals within the gas slab by means of the depth-dependent function $s(x)$. The full frequency-dependent optical depth scale is then of the form

$$\tau_\nu(x) = \int_{x_0}^{x} \kappa_\nu(x')\, dx' = \int_{x_0}^{x} \Big(\kappa^c + \kappa^l \cdot V\big(a, v_\nu(x')\big) \cdot s(x')\Big)\, dx' \tag{2.10}$$

which for κ^c=κ^l=1 (arbitrarily chosen for simplicity) transforms into

$$\tau_\nu(\tau^c) = \int_{\tau_0^c}^{\tau^c} \Big(1 + V\big(a, v_\nu(\tau^{c\prime})\big) \cdot s(\tau^{c\prime})\Big)\, d\tau^{c\prime}\ . \tag{2.11}$$

While the damping parameter for the Voigt function V can be assigned a typical value of a=0.1 everywhere, the dimensionless frequency parameter v is re-evaluated at each depth to take into account the non-zero temperature gradient.

Given the above optical depth scale, the intensity of the radiation transferred through the gaseous material can again, as in Eq. 2.4, be calculated as

$$I_\nu(\tau^c) = I_\nu(\tau_0^c)\, e^{-\tau_\nu(\tau^c)} + \int_{\tau_0^c}^{\tau^c} B_\nu(T(\tau'))\, e^{-(\tau_\nu - \tau_\nu')}\, d\tau'\ . \tag{2.12}$$

Rewritten for a discrete depth grid, this can equivalently be formulated as

$$I_\nu(\tau_n^c) = I_\nu(\tau_0^c)\, e^{-\tau_{\nu,n}} + \int_{\tau_0^c}^{\tau_n^c} B_{\nu,\mathrm{n}}\, e^{-(\tau_{\nu,n} - \tau_{\nu,\mathrm{n}})}\, d\tau_\mathrm{n}\ . \tag{2.13}$$

This approach allows one to solve for the intensity at any desired n immediately, in principle without having to calculate intensities at intermediate depth values n. Known as "long characteristics" treatment, it tends to suffer from numerical integration inaccuracies, unless special attention is given to a good choice of integration

[2]Due to its very small extent in frequency, this additional opacity source would not significantly influence the mean optical depth scale even if one of the more rigorous common definitions such as the Rosseland scale were used here.

weights. While there exist absolutely adequate solutions to this, the "short characteristics" method offers an alternative where the intensity obtained for a depth n uses the intensity obtained previously at $n-1$ as the boundary condition for the subsequent integration. Hence, in the respective variation of Eq. 2.13, the integral only spans one step on the depth grid, so that τ_0^c is to be replaced by τ_{n-1}^c and $I_\nu(\tau_0^c)$ by $I_\nu(\tau_{n-1}^c)$. The focus is on an appropriate choice of the integration weights for this contribution (as first given by Kunasz & Olson 1988). Using the definitions

$$\Delta_\nu(x_n) = \tau_\nu(x_{n-1}) - \tau_\nu(x_n) \tag{2.14.a}$$

$$w_\nu^a(x_n) = 1 + \frac{(e^{\Delta_\nu(x_n)} - 1)}{\Delta_\nu(x_n)} \tag{2.14.b}$$

$$w_\nu^b(x_n) = -\Delta_\nu(x_n) - \frac{(e^{\Delta_\nu(x_n)} - 1)}{\Delta_\nu(x_n)} \tag{2.14.c}$$

and provided that $I_\nu(\tau_{n-1}^c)$ is given, Eq. 2.13 may then be rewritten as

$$I_\nu(\tau_n^c) = I_\nu(\tau_{n-1}^c) \cdot e_\nu^\Delta(x_n) + w_\nu^a(x_n) \cdot S_\nu(x_n) + w_\nu^b(x_n) \cdot S_\nu(x_{n-1}) \; . \tag{2.15}$$

Both of the radiative transfer solutions have been used in the construction of models calculated for this work (see later, Sects. 2.2, 3.3, and 2.5). They are mathematically identical in a one-dimensional formulation, and may only differ numerically, so that obviously either approach is equally well suited to obtain the results displayed in Fig. 2.1. The rightmost column is similar to the one in Fig. 1.1, except in that it additionally contains the temperature profile, and has one extra row for a homogeneously distributed absorber profile. The first column from the left illustrates how the absorber profile modifies the wavelength-dependent optical depth in the vicinity of the line centre as a function of the continuum optical depth, the second how the radiation field intensity changes according to its effects. In these first two column panels, the line height contour decreases from left to right. Together, they demonstrate to what extent the line centre in particular samples different areas in depth depending on the absorber distribution. The resulting equivalent line widths implied by the emergent intensities (at a continuum optical depth of zero) in the third column's plots naturally underline the strong influence of the depth where an absorber is placed rather than just its total amount among a line of sight. Moreover, a comparison of the detailed line profiles (as presented more clearly in Fig. 1.1) reveals the non-equivalence of a homogeneous and a concentrated slab of line-forming material, and the highly non-trivial relations between "representative" and "true" absolute abundances.

2.1.3 Radiative transfer under realistic conditions

In a plane parallel approximation, the change of intensity of the radiation field along a line of sight x at an angle θ to the radial direction is $dI/dx = \cos\theta\, dI/dr$. With the standard abbreviation $\mu = \cos\theta$, the radiative transfer equation then takes the general form given in Eq. 2.16. To solve for the radiation field, the "long characteristics" method of a Feautrier solution scheme was implemented to construct the model grid presented in Sect. 3.3, while the "short characteristics" were used in the version for the newer ("improved", see Sect. 2.5) models. In contrast to the simplified example just discussed, where a very straightforward integration is possible, realistic situations imply a much more complex κ and η. In particular, when Thomson scattering is included (then κ is usually renamed χ) in addition to bound-bound, bound-free, and free-free processes, the solution requires either a Feautrier scheme (Feautrier 1964, in the long characteristics approach) or an iteration scheme (for the short characteristics approach, Olson & Kunasz 1987).

2.2 Atmospheric structure

In the classical stellar atmosphere problem, the radiative transfer needs to be solved self-consistently with the energy balance and hydrostatic equilibrium conditions, and the equations describing atomic level population (under NLTE conditions, the rate equations, which enforce statistical equilibrium). Further constraints are the mass and charge conservation within the atmospheric structure.

The Tübingen model atmosphere program PRO2 in its standard form approximates stellar atmospheres as plane parallel, chemically homogeneous atmospheres in radiative, hydrostatic and statistical equilibrium. The solution of rate equations in full NLTE for sophisticated atomic data makes PRO2 especially suitable for application to hot compact stars. Restriction to the one-dimensional, plane parallel geometry is justified whenever the extent of the atmospheric layer is small compared to the stellar radius, which is indeed particularly well fulfilled in compact objects. Atmospheres are in radiative equilibrium when alternative methods of energy transport, notably convection, are considerably less efficient than radiative transfer, and when energy production does not occur in these layers. Hot stars do have such radiative atmospheres. Hydrostatic equilibrium, on the other hand, only holds as long as a star does not suffer significant mass-loss, which implies potential limitations since radiatively driven winds are more important the hotter an object is.

A recent comprehensive description of the physics and numerical solution schemes implemented in PRO2 has been given by Werner et al. (2003), superseding an earlier overview by Werner & Dreizler 1999. The review articles are complemented by a user's guide (Werner et al. 1998), the work by Nagel (2003) which records aspects

concerning some of the latest updates that are also partly relevant to the modelling presented here, and a series of several earlier publications often concentrating on selected topics within the overall problem as referred to in Werner et al. (2003).

Several extensions to this general concept have been recently or are currently being implemented (in addition to the references above, see Dreizler 2003; Rauch & Deetjen 2003; Deetjen et al. 2003; Schuh & Dreizler 2003; Nagel et al. 2003). To correctly describe the chemically stratified atmospheres of hot white dwarfs and possibly sdB stars, modifications which allow the self-consistent prediction of depth-dependent abundance profiles have been implemented (Dreizler 1999 and later; see the following Sect. 2.3). For an up-to-date overview of the status of NLTE atmosphere modelling as well as related, current topics of more general interest to this field, two proceedings publications on Stellar Atmosphere Modelling from recent conferences in Tübingen and Uppsala (Hubeny et al. 2003; Piskunov et al. 2004) each provide an excellent reference.

Since this literature collection describes the various aspects of the techniques necessary for the construction of metal-line-blanketed model atmospheres under the above-mentioned set of assumptions in a much more comprehensive and detailed way than would be appropriate here, only a few central points are repeated here. The one-dimensional radiative transfer equation reads

$$-\mu \frac{dI_{\nu\mu}(r)}{dr} = \eta_\nu(r) - \kappa_\nu(r) I_{\nu\mu}(r). \tag{2.16}$$

The condition of hydrostatic equilibrium, meaning that gravitational pull is balanced by the total (gas, radiation and turbulent) pressure gradient, takes the form

$$\frac{dP(r)}{dr} = -g\rho(r) \qquad \text{where} \quad g = \frac{GM}{R^2}\,. \tag{2.17}$$

The energy balance, or radiative equilibrium, requires that the overall flux is conserved from one depth to another, or else that the total energy absorbed per unit volume and time is the same as that emitted, which in an integral formulation is equivalent to

$$0 \stackrel{!}{=} \int_0^\infty \kappa_\nu (S_\nu - J_\nu)\, d\nu \qquad \left(= \int_0^\infty (\eta_\nu - \kappa_\nu J_\nu)\, d\nu \right). \tag{2.18}$$

J_ν is the quantity obtained by angle integrating $I_{\nu\mu}$. Statistical equilibrium can be expressed through a set of rate equations where the rates *into* each level l from all other levels u and *away* from level l into any other level u will on average cancel out

to yield time-independent population numbers n_l:

$$0 \stackrel{!}{=} \frac{\partial n_i}{\partial t} = n_l \sum_{l \neq u} P_{lu} - \sum_{u \neq l} n_u P_{ul}. \tag{2.19}$$

For an index l which runs through all levels of all ions of all elements, particle conservation may be written as

$$n_e + \sum_l n_l = N \tag{2.20}$$

and charge conservation (with Z_l referring to the charge of the current ionisation stage j) as

$$n_e = \sum_l n_l Z_l = \sum_j n_j Z_j \tag{2.21.a}$$

$$P_e = \sum_l P_l Z_l = \sum_j P_j Z_j \tag{2.21.b}$$

respectively. Since Z_l is the same for all levels of one ionisation stage j, and the population of this stage j is composed of the individual NLTE and LTE levels that model it[3], the right-hand side expression (corresponding to a summation over the population numbers of all ionisation stages of all elements only) is also sufficient. Furthermore, for electron and ion gas temperatures that are indistinguishable, particle densities may be replaced with partial pressures using the ideal gas law, yielding an equivalent variant of the charge conservation as given by 2.21.b (this will be needed in Eq. 2.34).

A complete linearisation (CL) of this highly coupled, non-linear set of equations yields a system whose numerical solution is still beyond current possibilities for reasonably large numbers of atomic levels. An iterative approach is therefore necessary to partly remove the strong depth and frequency coupling. The Lambda iteration procedure achieves this by basically separating the radiative transfer from the rate and constraint equations solution. For a given source function S (essentially determined by the level populations n, approximately known from a previous iteration step $k-1$), an updated radiation field J can then formally be determined by applying a Lambda operator on S:

$$J^k = \Lambda\, S^{k-1}\ . \tag{2.22}$$

[3]This can be expressed through $n_j = \sum_{l=1}^{\text{NLTE}} n_l + \sum_{l=1}^{\text{LTE}} n_l^*$.

A re-determination of the remaining solution vector in the next step then relies on that fixed J from the formal solution, resulting in an extremely slow overall convergence behaviour. It is more effective to insert the yet-to-be determined population numbers entering the radiative transfer equation into the structure solution part via a more sophisticated expression for J. This is feasible through the following split, at the heart of the so-called Accelerated Lambda Iteration (ALI):

$$J^k = \Lambda^* S^k(n^k) + [\Lambda - \Lambda^*] S^{k-1}(n^{k-1}) \; . \tag{2.23}$$

If the Approximate Lambda Operator Λ^* (ALO) is chosen such that it avoids the re-introduction of excessive depth coupling, the first part of Eq. 2.23 can be substituted into the full Eq. 2.22 for an up-to-date S, while the second part corrects for the deviations caused by this approximation, which can be calculated from quantities of iteration $k-1$ before introducing Eq. 2.23 into

$$[A(J^k)]n^k = b^k \; . \tag{2.24}$$

In the case of convergence, quantities^k approach quantities^{k-1} so that from a mathematical point of view the exact form of Λ^*, although it actually differs from the true Λ, becomes irrelevant. The problem of constructing a numerically stable ALO has for example been solved by Olson & Kunasz (1987).

2.3 Diffusion

Diffusion is a transport phenomenon based on stochastic thermodynamic processes. Random microscopic movements may result in a macroscopic change of state variables if concentration (C), temperature (T) or pressure (P) gradients are present. In a generalisation of Fick's first law, the mean diffusion velocity is proportional to these gradients in the form given by

$$v_D = -\frac{1}{C} D(\nabla C + k_T \nabla \ln T + k_P \nabla \ln P) \tag{2.25}$$

(Kippenhahn & Weigert 1990) for a diffusion coefficient D, and coefficients k_j for T and P, respectively (see also Chapman & Cowling 1970). Diffusion then occurs on characteristic time scales of

$$\tau_D \approx \frac{C}{k_j} \frac{H^2}{D} \; , \tag{2.26}$$

where H represents the typical scale height for the respective gradient, and τ_D the approximate time to reach a stationary state where the mean diffusion velocity tends

to zero. The transport phenomenon hence tends to cause the gradient that drives it to vanish, but in a situation where a gradient or a set of gradients is kept up by external forces, these instead rather dictate the constraints under which diffusion proceeds. In other words, a pressure gradient - acting as an external force - can impose the formation (not the disappearance) of a concentration gradient in order for the overall system to reach a stationary state.

This is what is happening in white dwarf atmospheres. Koester & Chanmugam (1990) recapitulate the theoretical background for this situation, where the large pressure gradient (implying a short pressure scale height) completely dominates the diffusion velocity, leading to short diffusion time scales of the order of months[4]. Any contributions from the temperature gradient, for which time scales are longer and scale heights larger (i.e. the resulting effects less pronounced), will be neglected in the following.

For a given element species i of atomic weight μ_i, the related pressure scale height H_P is given by

$$H_{P_i} = -\frac{dr}{d\ln P_i} = -P_i \frac{dr}{dP_i} \overset{(a)}{=} \frac{P_i}{g\rho_i} \overset{(b)}{=} \frac{RT}{g\mu_i}, \tag{2.27}$$

if the conditions of hydrostatic equilibrium (a) and the ideal gas equation (b) are used. Under the assumption of an isothermal ideal gas (T = const., unrealistic in stellar atmospheres), the solution to the differential equation for P_i implied by 2.27

$$\frac{dP_i}{dr} = -\frac{1}{H_{P_i}} P_i \tag{2.28}$$

is of the form

$$P_i = P_{i0} \cdot e^{-\frac{r}{H_{P_i}}} \tag{2.29}$$

and equivalent to

$$\rho_i = \rho_{i0} \cdot e^{-\frac{r}{H_{P_i}}} \tag{2.30}$$

since $P \propto \rho$ in the isothermal case. Qualitatively, a roughly exponential decline of the density ρ_i for a species i on scale heights that decrease with increasing atomic weight μ_i means that the density of heavier elements will fall off quicker along the direction of a negative pressure gradient than that of lighter ones. Heavier elements therefore ”sink” into denser regions, while the lightest one ”floats” on top. The scale heights in white dwarfs on which the decline happens are small compared to the geometrical

[4]”Short” in this context means in comparison to the respective stellar evolutionary time scale.

extension of the atmosphere, and the drop-off regions are located at different depths for different species, so that the resulting elemental distribution may be considered as relatively well-defined, separated layers.

A more exact description of partial pressure and density distributions can be obtained from a balance of forces acting on each element species solved simultaneously with the full set of stellar atmosphere equations. A substantial simplification in the case of white dwarf atmospheres results from the fact that a detailed description can make use of the general results obtained from both observational evidence as well as the qualitative discussion above: The lightest element floats on top of all others, and since this is at the same time also the most abundant one in the atmosphere, its partial pressure mostly dominates the hydrostatic structure while all other species are only present in traces and can be treated as perturbations.

This remains true if, in addition to the gravitational settling, radiative acceleration is considered in the overall balance of forces. The levitation effect of momentum transfer by radiative acceleration hence pollutes the white dwarf atmosphere with heavier elements, but cannot substantially alter the abundance of the main constituent. Under the assumptions that no processes competing with diffusion and levitation are present *and* that diffusion time scales are short, the distribution of trace elements in a stellar atmosphere can then be expected to take on an equilibrium state, as proposed by Chayer et al. (1995a,b) and implemented for NLTE situations by Dreizler (1999). The solution of an equilibrium condition for each atomic species yields equilibrium abundances. For a plane parallel model atmosphere in hydrostatic equilibrium, those are solely determined by the photospheric parameters $T_{\rm eff}$ and $\log g$, in other words, the photospheric abundances are no longer free parameters.

In such a stationary situation, mean diffusion velocities of all elements (i) with respect to the main constituent (1) would be zero everywhere in the atmosphere, due to an exact balance of the sum of gravitational, radiative, and electrical forces. Neglecting thermal and concentration diffusion, a detailed formulation of this condition

$$m_1 a_1 - m_i a_i \stackrel{!}{=} 0 \tag{2.31}$$

for polluting elements (i) in a hydrogen (or helium) plasma (1) yields (following Dreizler 1999)

$$m_1 a_1 = -A_1 m_p g + Z_1 e E \tag{2.32.a}$$

$$m_i a_i = -A_i m_p g + Z_i e E + A_i m_p g_{{\rm rad},i} \ . \tag{2.32.b}$$

The $m_i a_i$ are the forces acting on element (i), A_i are the atomic weights, Z_i are the mean electrical charges, E is the electrical field caused by the separation of electrons and ions, m_p is the proton mass, and $g_{{\rm rad},i}$ is the radiative acceleration acting on element (i). The following modified hydrostatic equilibrium conditions for the

partial pressures are valid (where $A_e \ll A_i, A_1$ and $Z_e = -1$ are used in the last approximation):

$$\frac{1}{P_1}\frac{dP_1}{dr} = -\frac{A_1 m_p g}{kT} + \frac{Z_1 eE}{kT} \tag{2.33.a}$$

$$\frac{1}{P_i}\frac{dP_i}{dr} = -\frac{A_i m_p g}{kT} + \frac{Z_i eE}{kT} \tag{2.33.b}$$

$$\frac{1}{P_e}\frac{dP_e}{dr} = -\frac{A_e m_p g}{kT} + \frac{Z_e eE}{kT} \approx -\frac{eE}{kT}\,. \tag{2.33.c}$$

Since $P_{i\neq 1} \ll P_1$, and again $Z_e = -1$, charge conservation (from Eq. 2.21.b) yields

$$P_e = \sum_i P_i Z_i \approx P_1 Z_1 \tag{2.34}$$

where both sides may be logarithmised then differentiated with respect to r to obtain

$$\frac{1}{P_e}\frac{dP_e}{dr} = Z_1 \frac{1}{P_1 Z_1}\frac{dP_1}{dr}\,. \tag{2.35}$$

Expressions 2.33.a and 2.33.c inserted into 2.35 give

$$-\frac{eE}{kT} = -\frac{A_1 m_p g}{kT} + \frac{Z_1 eE}{kT} \tag{2.36}$$

from where the electric field can be calculated to be

$$eE = \frac{A_1 m_p g}{Z_1 + 1}\,. \tag{2.37}$$

Inserting this into Eq. 2.31 (with the contributions given by Eqs. 2.32.a and 2.32.b)

$$\begin{aligned}
m_1 a_1 - m_i a_i &= (A_i - A_1) m_p g - (Z_i - Z_1) eE - A_i m_p g_{\mathrm{rad},i} \\
&= (A_i - A_1) m_p g + (Z_1 - Z_i) \frac{A_1 m_p g}{Z_1 + 1} - A_i m_p g_{\mathrm{rad},i} \\
&= A_i m_p \left(g - \frac{A_1}{A_i} g + \frac{A_1}{A_i} \frac{Z_1 - Z_i}{Z_1 + 1} g - g_{\mathrm{rad},i} \right) \\
&= A_i m_p \left(g - \frac{A_1 (Z_i + 1)}{A_i (Z_1 + 1)} g - g_{\mathrm{rad},i} \right) \\
&= A_i m_p \left(g - g_{\mathrm{el},i} - g_{\mathrm{rad},i} \right) \\
&= A_i m_p \left(g_{\mathrm{eff},i} - g_{\mathrm{rad},i} \right) \\
&\stackrel{!}{=} 0
\end{aligned}$$

leads to the balance of accelerations term

$$g_{\mathrm{eff},i} = g_{\mathrm{rad},i} \,. \tag{2.38}$$

The effective gravitational acceleration on the left-hand side has been introduced above according to the definition in 2.39, while the right-hand side quantity, the radiative acceleration, must be calculated according to 2.40:

$$g_{\mathrm{eff},i} = \left(1 - \frac{A_1 (Z_i + 1)}{A_i (Z_1 + 1)} \right) g \tag{2.39}$$

$$g_{\mathrm{rad},i} = \frac{1}{\rho_i} \frac{4\pi}{c} \int_0^\infty \kappa_{\nu,i} H_\nu d\nu \,. \tag{2.40}$$

Here, ρ_i is the mass density of the element (i), $\kappa_{\nu,i}$ is the frequency-dependent absorption coefficient which includes all contributions of this element at the frequency ν, and H_ν is the Eddington flux. To generalise the formulation of g_{eff} for an element i in *different* ionisation stages j, which is a more realistic situation, one needs to define its effective charge Z_i^{eff} which replaces Z_i (including Z_1; the mass numbers remain unchanged) in Eq. 2.39:

$$Z_i^{\mathrm{eff}} = \frac{\sum_j Z_j n_j}{\sum_j n_j} \left(= \frac{\sum_j \sum_k Z_j n_{jk}}{\sum_j \sum_k n_j k} \right) \,. \tag{2.41}$$

Similarly, $g_{\rm rad}$ must then be constructed from the individual contributions of all j ionisation stages of element i as

$$g_{{\rm rad},i} = \sum_j g_{{\rm rad},ij} \quad . \tag{2.42}$$

Following this discussion, one recognises that requiring diffusion velocities to be zero by cancelling relative forces is equivalent to asking for the accelerations caused by effective gravitational settling and radiative levitation to cancel each other. With the amendments above in mind, one can finally rewrite Eq. 2.38

$$\left(1 - \frac{A_1(Z_i^{\rm eff}+1)}{A_i(Z_1^{\rm eff}+1)}\right) g = \frac{1}{\rho_i}\frac{4\pi}{c}\int_0^\infty \kappa_{\nu_i} H_\nu \, d\nu \tag{2.43}$$

from where it becomes clear that $g_{{\rm rad},i} = g_{{\rm eff},i}$ can only be fulfilled by fixed values for ρ_i. This equilibrium solution for ρ_i is depth-dependent, leading to a chemically stratified atmosphere. As there exists an intimate coupling between the abundances, the opacities and the flux, the whole system has to be solved self-consistently, which, in contrast to Chayer et al. (1995a,b) who neglected this aspect, is achieved here by iteration (Dreizler & Wolff 1999; Dreizler 1999; Schuh 2000).

2.4 Peculiarities of subsequent numerical implementations used

During the course of the analysis presented in Chapter 5, it will become clear that while superior to homogeneous models in the EUV range, the first generation of stratified models is not elaborate enough to simultaneously reproduce all of the very abundance-sensitive metal lines in the UV spectral range. A number of possible improvements therefore appear desirable, and could partly be adopted from developments in parallel to this study. The changes with respect to the old models fall into two categories: A generally more efficient stellar atmosphere code in conjunction with a new implementation of the opacity sampling method for the iron group elements, and a different set-up of the model atmosphere calculations by extending them to include more elements than previously used.

The improved efficiency of the code results from switching the radiative transfer from the Feautrier method to short characteristics (as treated earlier in Sect. 2.1.3), in conjunction with the use of a linear variation of the ALI and a refurbished temperature correction scheme. The advances in the formulation of the code are as detailed in Dreizler (2003): Generally, an update of the temperature structure in a model may either be obtained through a constraint implementation by requiring energy conservation, or through an Unsöld-Lucy temperature correction scheme (Lucy

Table 2.1: Summary of "old" model atoms. Super-levels (marked by *) comprise hundreds to thousands of atomic levels. Line transitions between these super-levels (marked by $^+$) are composed of all transitions between the individual levels comprising the super-levels (see Werner & Dreizler 1999 for details).

	H	He	C	N	O	Si	Fe	Ni
NLTE levels	17	54	70	50	24	25	28*	29*
NLTE lines	56	106	218	114	35	53	77^+	44^+

1964) generalised to NLTE conditions. Both have already been implemented in an earlier version, but the latter was mostly used for difficult cases where convergence could only be reached with regular temperature correction after several iterations of Unsöld-Lucy correction. In conjunction with the linear method introduced for ALI and the short characteristics radiative transfer, the Unsöld-Lucy scheme was adapted to that and used exclusively. The new implementation goes by the name of NGRT (Next Generation Radiative Transfer) to distinguish it from PRO2.

Both code-inherent as well as set-up related changes in the use of model atoms are the subject of the following section.

2.5 Model atoms

A self-consistent solution of the chemical stratification within state-of-the-art, fully line-blanketed NLTE stellar atmospheres with many elements will only be meaningful if detailed model atoms are incorporated. To this end, input from line lists by Kurucz (1991) and Opacity project data (Seaton et al. 1994) is used. NLTE occupations can only be calculated for a limited number of levels, so that a selection has to be made. The predominantly populated levels in elements slightly beyond the CNO group can be chosen as a subset from a direct mapping of atomic levels to the model atom. In contrast to this, the iron group elements which feature orders of magnitudes more levels and lines must be treated with a procedure to merge numerous individual levels to several super-levels, with lines described as NLTE inter-level and LTE intra-level transitions. The principles underlying the opacity sampling for the iron group elements along with the relevant earlier references can be found in Werner & Dreizler (1999) and Rauch & Deetjen (2003).

Opacity sampling for iron group elements was used in both general types of models calculated for this work, but since the sampling employed by Dreizler & Wolff

Table 2.2: Summary of "new" model atoms, symbols have the same meaning as in Table 2.1. In this listing, Ca and Ti have not been included since they were omitted in the test calculations used for comparison with models based on Table 2.1. The reasons for this omission are further explained in the text.

H	He	C	N	O	Si	Sc	V	Cr	Mn	Fe	Co	Ni
17	34	116	128	31	40	29^{*}	30^{*}	36^{*}	33^{*}	28^{*}	28^{*}	29^{*}
56	79	433	466	185	65	84^{+}	84^{+}	129^{+}	108^{+}	68^{+}	71^{+}	69^{+}

(1999) a more comfortable implementation to prepare model atom input data for `PRO2` or `NGRT` from the Opacity project and Kurucz tables has become available. The modernised opacity sampling offered by `IrOnIc` (Rauch & Deetjen 2003) allows inclusion of additional elements that are considered important with less effort than before.

Table 2.1 summarises the model atoms used in the "old" models, where the Fe and Ni models were taken from Dreizler & Wolff (1999). Table 2.2 lists the input for newer test calculations as described further in the next two chapters. There actually exist variants of models based on Table 2.2 with {H – Si, Fe, Ni}, with {H – Si, Sc – Ni without Ca and Ti}, and {H – Si, Ca – Ni including Ca and Ti} (the latter two are not listed in Table 2.2).

In a continued effort to push the models to a more sophisticated level, first all of the iron group elements from Ca to Ni were additionally taken into account due to their significant opacities (before considering further additions such as P and S). In fact, both the opacities as well as the theoretical equilibrium abundances of the two elements Ca and Ti turned out to be particularly high. The resulting abundance stratifications had an unrealistically strong impact on the emergent flux as well as a non-negligible feedback on the atmospheric structure which substantially altered the results for all other elements, too. Ca and Ti therefore were excluded from further test calculations (see Sect. 4.3).

The Stark broadening for hydrogen is calculated from the Lemke (1997) tables (based on the theory by Vidal et al. 1973). The broadening for He I is based on the BCS theory (Barnard et al. 1969; Griem 1974), that for He II on Schöning & Butler (1989a,b). Level dissolution is treated according to the Hummer-Mihalas formalism (Hummer & Mihalas 1988).

In the set of spectra calculated with `SYNSPEC` from the"extended" model grid (Sect. 3.3 and 3.3.3), the full Kurucz line list for all elements included in the model calculations is used.

CHAPTER 3

Model grids and high resolution spectra

3.1 Overview

Applications to hot DA white dwarfs in Chapter 5 show that synthetic spectra derived from chemically stratified models can quantitatively describe the EUV spectra observed from these objects. The model calculations (Sect. 3.2) used for the analysis of EUVE spectra by Schuh et al. (2002) have since been extended to a larger model grid (Sect. 3.3). To investigate whether remaining discrepancies are due to limitations in the way the models have been set up, or arise mainly from additional physical processes in the stellar atmosphere not so far incorporated in the modelling process, tests for improvements of the models in Sect. 3.3 have been carried out and are presented in Sect. 3.4.

3.2 The model grid used for the EUV analysis

3.2.1 Parameter range, atomic data and computational details

The model grid used for the analysis in Chapter 5 spans the $T_{\rm eff}$ and $\log g$ plane as suggested by the results from Wolff (1999): The effective temperatures cover a range from 38 000 – 70 000 K in 2 000 – 3 000 K steps, and the logarithmic surface gravity a range from 7.2 – 8.3 in 0.1 – 0.2 dex steps. The grid used in the analysis was an incomplete subset of the models shown in Fig. 3.1 and predominantly concentrated around the previously found parameter combinations for the objects listed in Table 5.1. It must be emphasised once more that the total absorber content, i.e. the entire depth-dependent distribution of each individual trace element, is solely defined by the $[T_{\rm eff}, \log g]$ – combination of the models, which makes $T_{\rm eff}$ and $\log g$ the *only* free parameters. The elements included in the model calculations are the same as those used by Wolff et al. (1998) for the definition of their metal mix, which in turn are those that they were able to identify in HST-GHRS data of the standard

star G 191–B2B. Other elements were assumed to be present in abundances too low to significantly contribute to the EUV opacity, although stratification may possibly invalidate this assumption. While other elements than those used in Wolff's and this analysis have been identified in UV spectra of some of the sample stars, including G 191–B2B itself, the low abundances of $2.5{\cdot}10^{-8}$ for phosphorus and $3.2{\cdot}10^{-7}$ for sulfur, for example, as reported from the analysis of ORFEUS spectra by Vennes et al. (1996a), confirm that the opacities of these elements will presumably not contribute significantly to the total EUV opacity. To investigate the possible effects of several additional elements, further analyses have been conducted (Sect. 3.4). For this analysis, the aim was to compare the results to a previous analysis in the EUV, as mentioned before. Consequently, the list of elements considered besides H reads He, C, N, O, Si, Fe and Ni. Differences remain with regard to the number of atomic levels and with regard to the LTE/NLTE population of these levels. Details of the model calculations presented here are summarised in Table 2.1. Note that the model atoms used for the solution of the atmospheric structure and for the solution of the equilibrium condition are identical, which implies that the relatively high accuracy required for the correct evaluation of the radiative acceleration slows down the atmospheric structure calculation.

The time it takes a model with the specified atomic data to converge depends primarily on the stratification of the input model. For homogeneous input models with abundances derived from the published metallicities as a first guess, roughly $5\text{x}10^6$ CRAY-CPU seconds are required, while for converged stratified models with photospheric parameters that are somewhat off the desired ones, convergence requires some $5{\cdot}\,10^5$ CPU seconds. Due to this particularly large CPU time demand per model, the convergence criterion for the models was set to be a less than 5% change in the model flux, which means that the maximal relative correction at *any* frequency point is no larger than that limit, compared to the result from the previous *diffusion* iteration step. Only individual lines (usually two or three He lines) are actually affected by these larger variations, the continuum flux itself is much more exactly determined and easily complies to the usual "$< 10^{-4}$" criterion.

As to the uniqueness of a particular solution, tests indicate that the results agree to within the error limits regardless of the extremely different stratification of diverse start models, making a strong case at least for the stability of the result. One can therefore trust that, no matter what the initial conditions in the start model are, the final abundances in the converged model will always be the same.

3.2.2 Spectra

The emergent fluxes used for comparison with the observations have been calculated (with PRO2) from the model atmospheres on a frequency grid optimised for the EUV spectral range. This grid covers $\lambda = 50$–700 Å in detail and contains more than 30 000

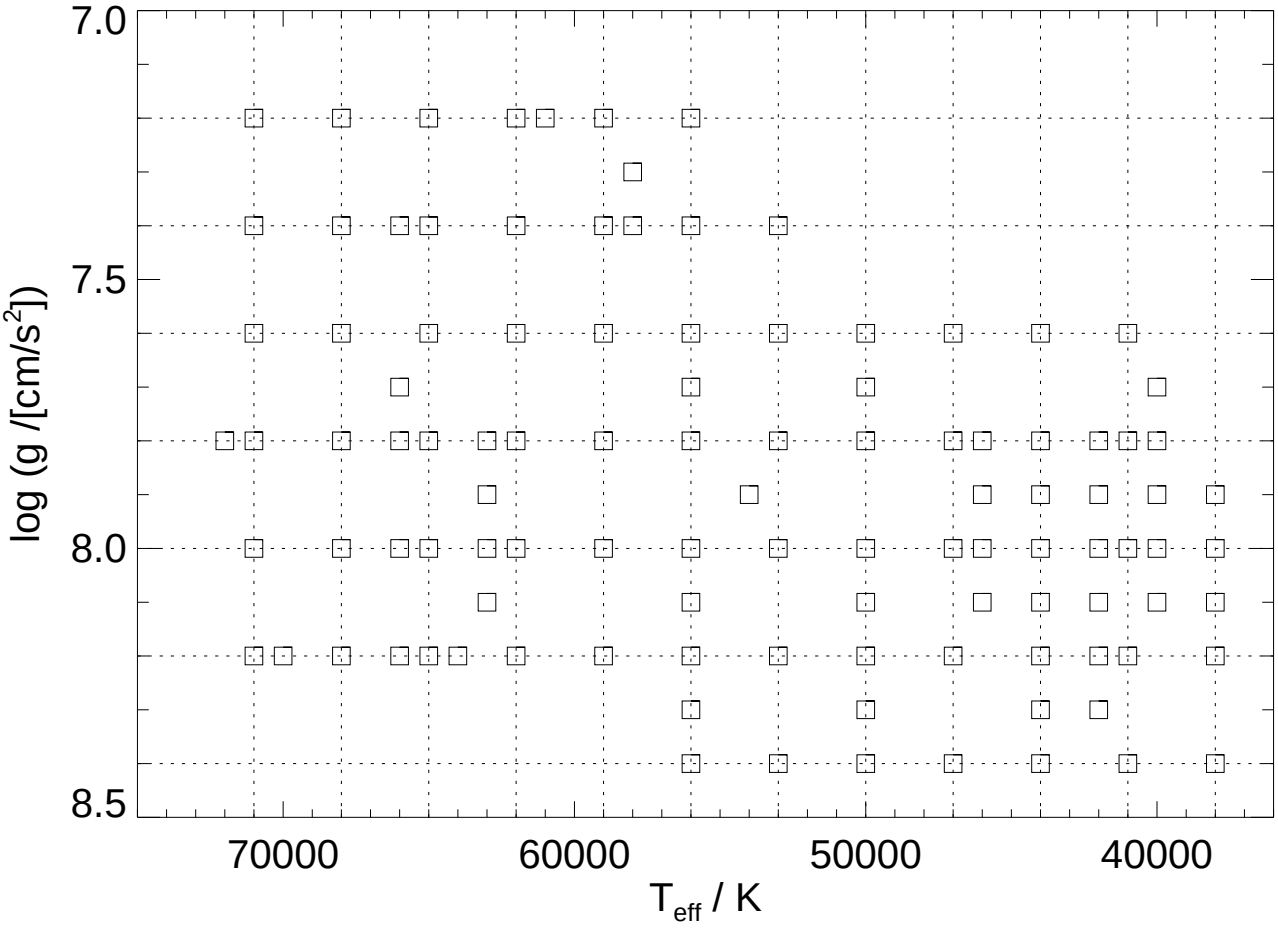

Figure 3.1: Representation of the extended model grid.

frequency points in total. Separate UV and optical spectra are also available.

3.3 Extended model grid

3.3.1 Parameter range and computational details

The full model grid of chemically stratified stellar atmospheres for hot DA white dwarfs is presented in Fig. 3.1. The grid limits are those imposed by the implications of the discussion in Sect. 5.3.2, i.e. it should be physically meaningful to calculate diffusion models within these limits. They are basically the same as in the previous section, but the grid itself is more regular and complete. As above, the results are for the elements He, C, N, O, Si, Fe and Ni in a hydrogen plasma in the effective temperature range of $T_{\rm eff} = 30\,000$ K to 72 000 K and for surface gravities from $\log g = 7.2$ to 8.4. The model atoms here are still identical to those in Table 2.1, the numerical implementation used was the one described under "old" models in Sect. 2.4

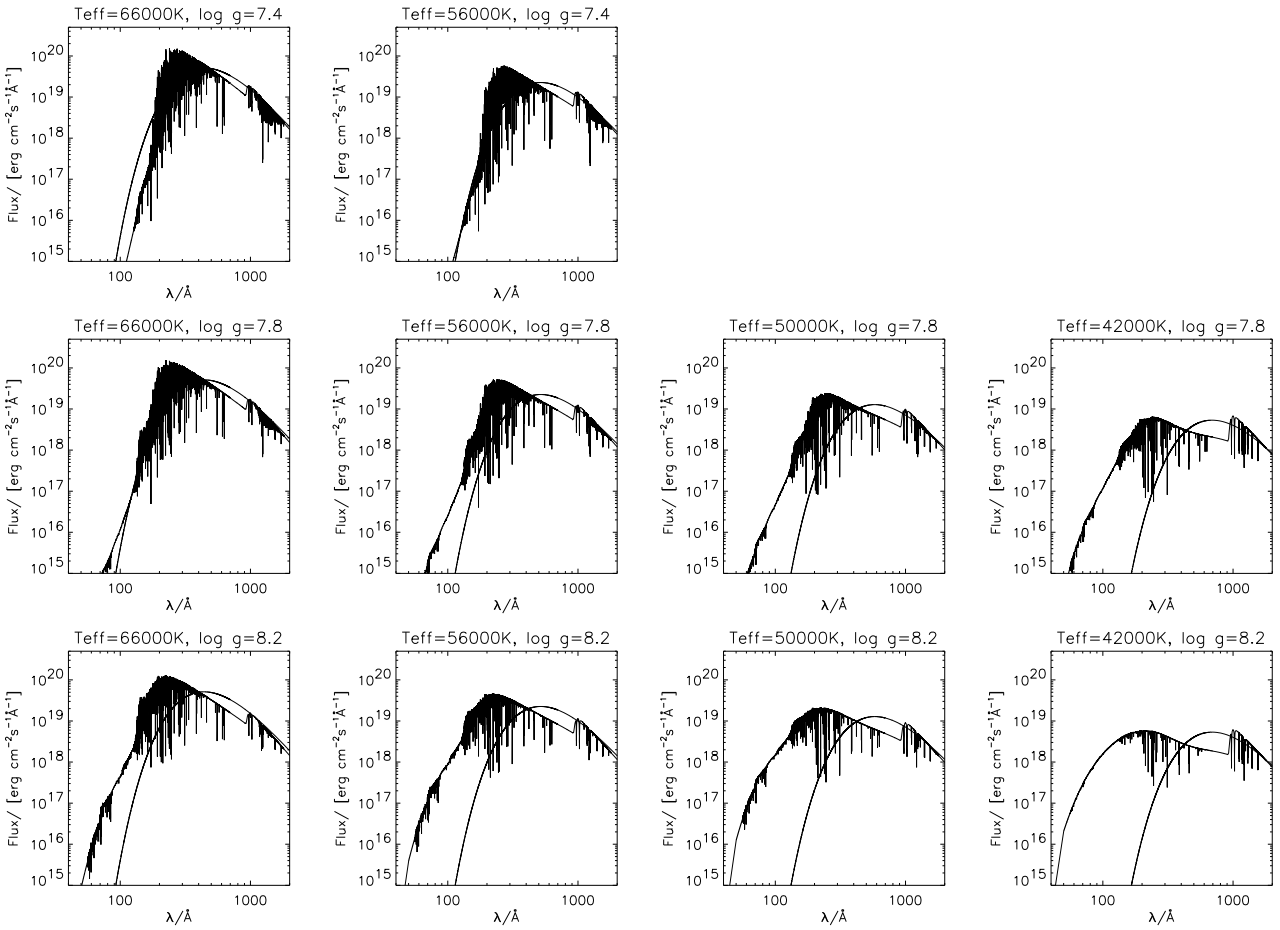

Figure 3.2: Emergent fluxes for selected parameters $T_{\rm eff}$ and $\log g$.

and calculations were performed on the Kiel CRAYs.

For fitting purposes, rectangular sub-grids with regular spacing in the fundamental parameters can be extracted from the full model grid. Properties of the models related to the depth-dependent abundance stratification for all elements included in the calculations are presented in more detail in Sects. 4.1 and 4.2 of Chapter 4, but it is briefly discussed how the presence of traces of metals in hydrogen-rich atmospheres affects the emergent flux in the following.

3.3.2 Example results: spectral features

Figure 3.2 shows the emergent fluxes for a few of the self-consistently solved, chemically stratified stellar atmosphere models at different parameter combinations: The emergent spectra (with lines) result from the full NLTE solution, while the overplotted spectral distributions represent the blackbody flux for the given effective temperature. Obvious effects are the decrease of the overall flux level and the strengthening of the Lyman jump with decreasing temperature, as well as the shift of the

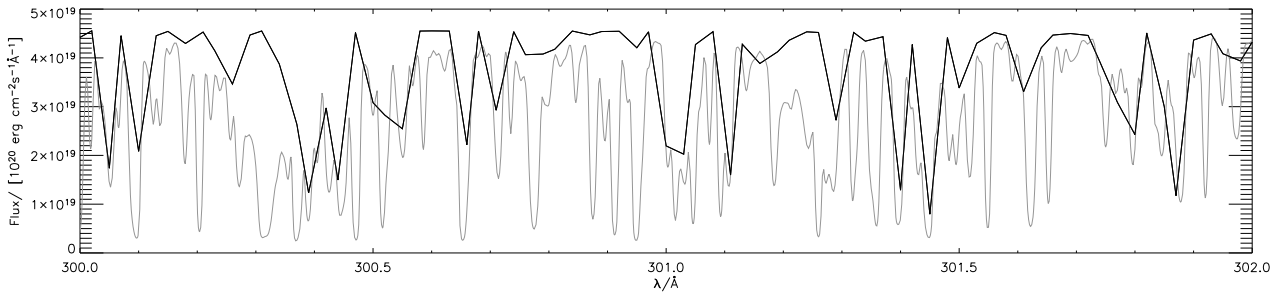

Figure 3.3: Detail of EUV spectra from PRO2 (black) and SYNSPEC (grey).

maximum flux towards longer wavelengths for the blackbody radiation. This last effect is not seen in the NLTE models. This peculiarity ultimately derives from the fact that the metal abundances in all these models are not free parameters but are a function of the effective temperature and the surface gravity. The decrease of the total absorber content with decreasing effective temperature and increasing surface gravity becomes obvious through the number of lines visible in the individual spectra. For stars at parameter combinations where a high effective temperature yields a strong radiative acceleration and a low surface gravity yields a comparatively weak gravitational acceleration, the absorber content is so high that any flux at the shortest wavelengths is totally blocked. For lower effective temperatures or increased surface gravities, this blocking is more and more lifted as more absorbers are being drawn into deeper layers, resulting in a flux redistribution.

3.3.3 Spectra from SYNSPEC

A few modifications to the spectrum synthesis program SYNSPEC[1] have been made to allow its use with stratified models from PRO2 or NGRT. SYNSPEC allows radiative transfer calculations through a given atmosphere structure using the full Kurucz line list, and for any desired elements (including additional ones not included in the structure calculation, giving up on full self-consistency in the process). Radiative accelerations can therefore readily be calculated with more extended atomic data. This could eventually allow one to separate the model atmosphere solution from the determination of updated equilibrium abundances in the sense that customised atomic data can be used for each of the two different iteration steps. Iteration between model atmosphere calculation and the very detailed radiative transfer including radiative accelerations possible with SYNSPEC has in the meantime been implemented for TLUSTY models by Hubeny & Barstow (priv. comm.).

Currently, the benefit derived from the first step of this SYNSPEC implementa-

[1]The most recent overview for TLUSTY and SYNSPEC is from Hubeny & Lanz (2003). Hubeny & Lanz (2000) make available a user's guide on the Web. Version 48 has been used in this work.

tion for the extended model grid discussed here is a series of high-resolution spectral grids. For these, atomic input data has been prepared in SYNSPEC-readable format, identical in content to the data used for the calculation of the stratified model grid. The Lemke (1997) broadening tables for hydrogen Lyman and Balmer lines were used. There are three grids, for the EUV (25 – 900 Å), UV (900 – 3 000 Å) and optical (3 000 – 10 000 Å) ranges, all at a minimum of 0.005 Å resolution. Figure 3.3 compares the emergent fluxes in a small section of the EUV wavelength range for spectra calculated according to Sect. 3.2.2 with those synthesised here.

3.4 New models: Test calculations

The next generation of models benefits from major improvements of the model atmosphere code that reduce the CPU time drastically. Test models have been calculated with the new code with atomic data prepared as similarly as possible as in the old models, in particular including only the elements that were also used there.

Further tests have included different atomic data for a model at $T_{\rm eff} = 56\,000$ K and $\log g = 7.6$: First all elements from Ca to Ni were added to the existing list. The atomic data were prepared with IrOnIc, for details refer back to Table 2.2. However, this immediately resulted in hefty absorption edges in the EUV, incompatible with observations. The equilibrium abundances of both Ca and Ti were at levels well above those of Fe and Ni, which does not appear reasonable. A model with only the lighter elements plus Ca showed that the strong absorption edge was mainly due to Ca, but nevertheless both Ca and Ti were removed in the final model to obtain the results in Sect. 4.3. Along with these results, the procedure of removing Ca and Ti is also further discussed and justified in Sect. 4.3.

All of these models were calculated on PCs in Tübingen.

CHAPTER 4

Abundance tables

4.1 Characteristics of the models

Based on the model grid presented in Sect. 3.3, abundance predictions are tabulated for optical depths ranging from $0.01 < \tau_{\rm ross} < 10$ for models covering the range of $38\,000\,{\rm K} < T_{\rm eff} < 71\,000\,{\rm K}$ and $7.2 < \log g < 8.4$. For each $[T_{\rm eff}, \log g]$ – combination, a separate table exists with, in the first column, the Rosseland optical depth, and in the following columns, the relative abundances with respect to hydrogen for all elements contained in the model. Appendix A displays an essential part of the information from these tables compiled in graphical representations. The most noticeable trends are illustrated in this section.

The models show the general properties as expected from diffusion theory, i.e. the overall trace element abundances usually decrease with lower $T_{\rm eff}$ and higher $\log g$ values. Accordingly, the emergent spectra approach the flux distributions of those of pure hydrogen model atmospheres at sufficiently evolved parameters on the cooling sequence. Iron and nickel dominate the opacity in the EUV, where the flux of hot white dwarfs peaks. Though their dominant effect on the EUV opacity is partly due to the many lines these elements exhibit, it is equally important that their abundances are, over a wide parameter range, simply larger than those of the CNO elements. Of course these two effects are tightly correlated, since more lines directly translate into a stronger radiative acceleration, which in this case easily compensates for the higher atomic weights and thus a stronger response to gravity.

As in previous calculations (Dreizler 1999; Dreizler & Wolff 1999), the iron group element abundance can reach solar values or more, with nickel being at virtually the same level as the iron abundances. While the behaviour of iron is by and large consistent with results obtained from EUV analyses (see Chapter 5), the incompatibility with observation in the UV of an iron to nickel ratio close to unity must be addressed again in Sect. 6.3.

Using the example of iron, Figs. 4.1 and 4.2 show that the iron abundance varies

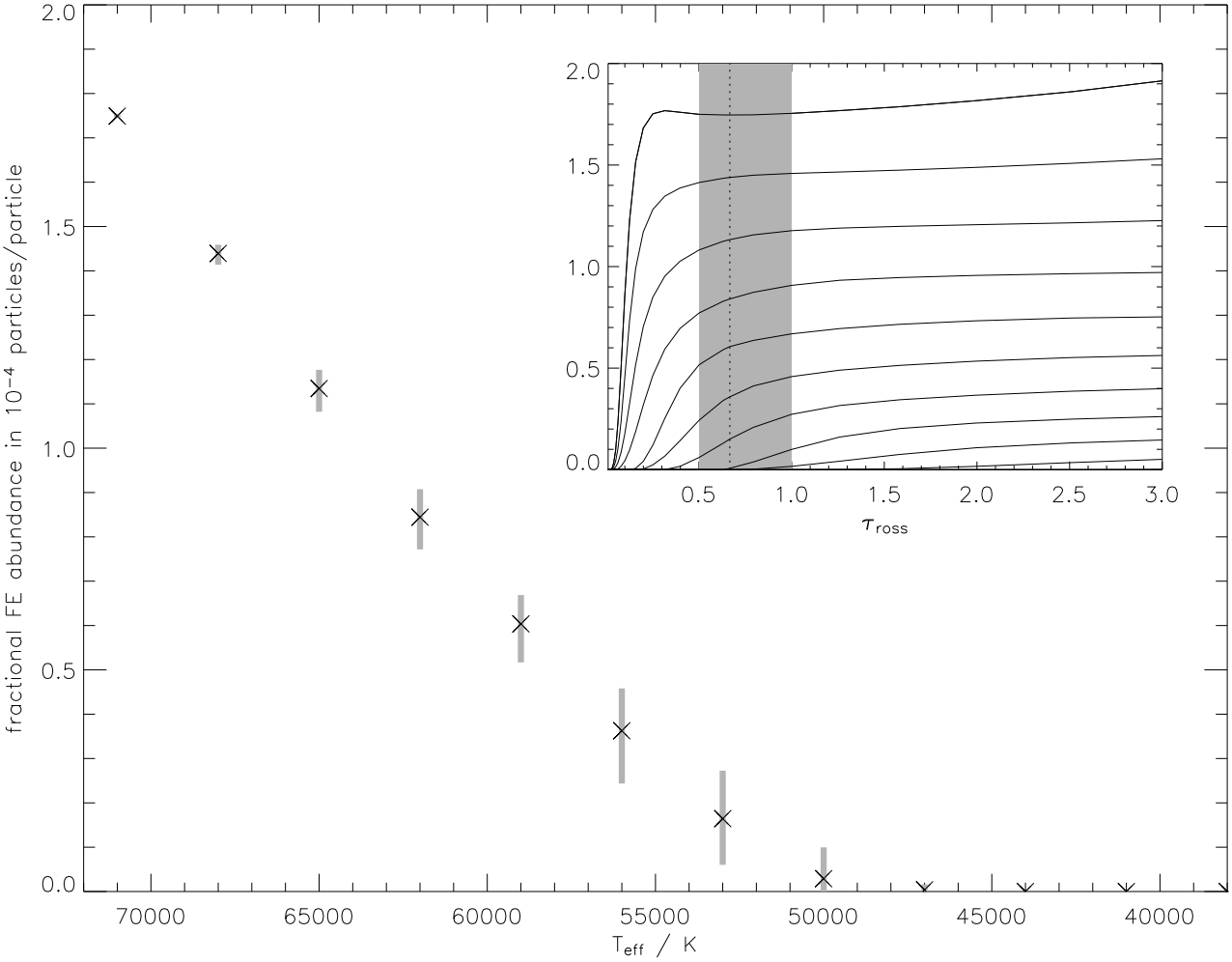

Figure 4.1: Iron abundances at $\tau_{\rm ross} = \frac{2}{3}$ as a function of effective temperature at a fixed surface gravity of $\log g = 8.0$. The inset figure shows the depth-dependent iron abundance profiles for the underlying models at the different effective temperatures used to obtain the data points in the main plot; the shaded area marks region between $\tau_{\rm ross} = 0.5$ and 1.0. The abundance variation in that area translates to "error bars" in the main graph.

with the atmospheric parameters as expected. The first figure (4.1) shows the decrease of the iron abundance at $\tau_{\rm ross} = \frac{2}{3}$ with decreasing effective temperature at a fixed surface gravity of $\log g = 8.0$. The inset figure shows the depth-dependent iron abundance profiles for the different models; the shaded area marks the approximate line formation region between $\tau_{\rm ross} = 0.5$ and 1.0. The effect of abundance variations in that area is translated to "error bars" in the main graph. The second figure (4.2) shows the decrease of the iron abundance at $\tau_{\rm ross} = \frac{2}{3}$ with increasing surface gravity at a fixed effective temperature of $T_{\rm eff} = 56\,000\,{\rm K}$; the inset figure is similar to the one in Fig. 4.1. All abundances are relative fractions with respect to the total particle number.

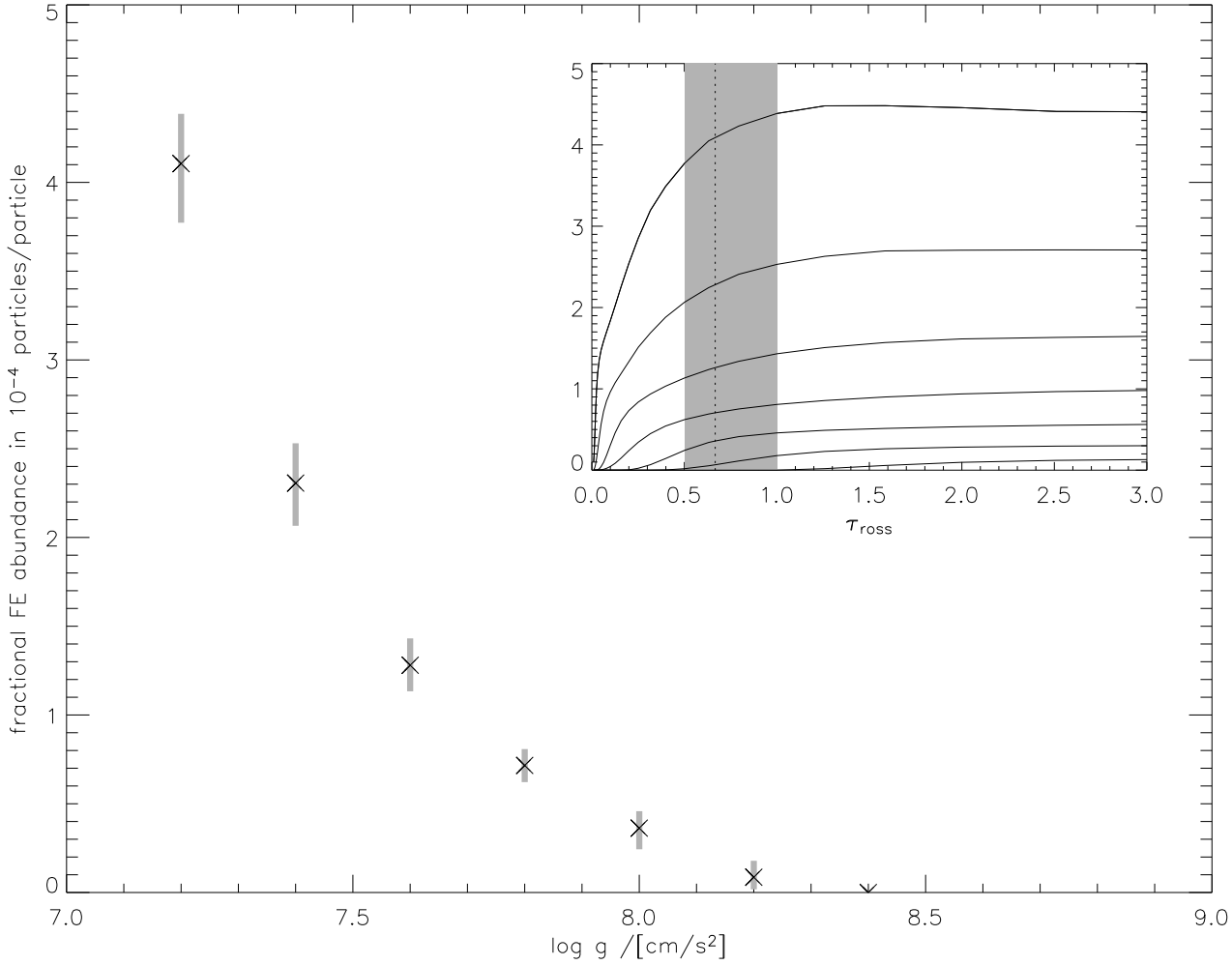

Figure 4.2: Iron abundances at $\tau_{\rm ross} = \frac{2}{3}$ as a function of surface gravity at a fixed effective temperature of $T_{\rm eff} = 56\,000$ K; the inset figure is similar to the one in Fig. 4.1.

Analogue representations for silicon and nitrogen in Figs. 4.3, 4.4, 4.5 and 4.6 illustrate more complex structural properties of the models. In contrast to other elements in the effective temperature range considered, silicon shows the same ”anomaly” that had already been found (and explained) by Chayer et al. (1995a, in their section 3.1): In that particular temperature range Si predominantly exists in the Si V ionisation state which is a (Ne I-like) noble gas configuration. The radiative acceleration on ions in noble gas configurations is extremely small – a circumstance that leads to ”gaps” in the overall trend with effective temperature such as the one resulting for Si here.

Likewise, the vertical element distribution does not always follow the simple picture of monotonously increasing local abundances with depth, but is strongly affected by the respective radiative acceleration (see also Dreizler 1999, Schuh 2000, or Dreizler & Schuh 2001 for further example graphical representations). In particular, gradients may change signs repeatedly, meaning this can in principle be brought

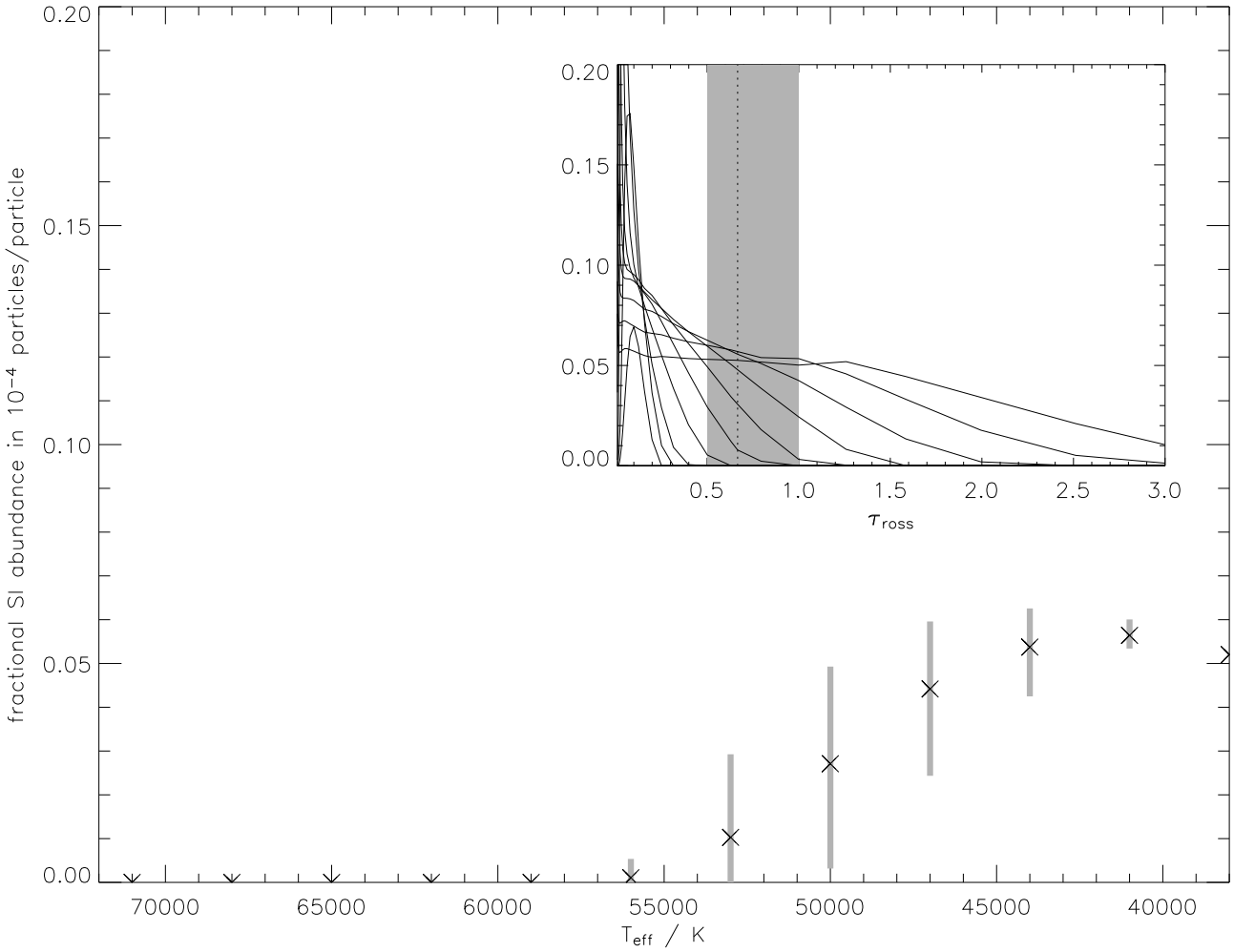

Figure 4.3: Silicon abundances for different effective temperatures, similar to Fig. 4.1.

about by diffusion processes alone. This is in contrast to other notions that additionally evoke mass-loss effects to explain increasing local abundances towards outer atmospheric regions. Notably, a nitrogen hump in the high atmosphere similar to the one Holberg et al. (1999a) required to explain their observations of RE J1032+535 may be considered. In the insets of Figs. 4.5 and 4.6, the location where the gradient reverses is located significantly outward from $\tau_{\rm ross} = \frac{2}{3}$, where the particle densities have dropped by more than 5 orders of magnitude with respect to their values at $\tau_{\rm ross} = \frac{2}{3}$. It is associated with a temperature inversion.

Consequently, it is somewhat questionable whether the reversed gradient claimed to be observed from nitrogen lines can actually be seen in the models, so that a verification requires a full quantitative analysis and further discussion has to be deferred to Sect. 6.2.1.

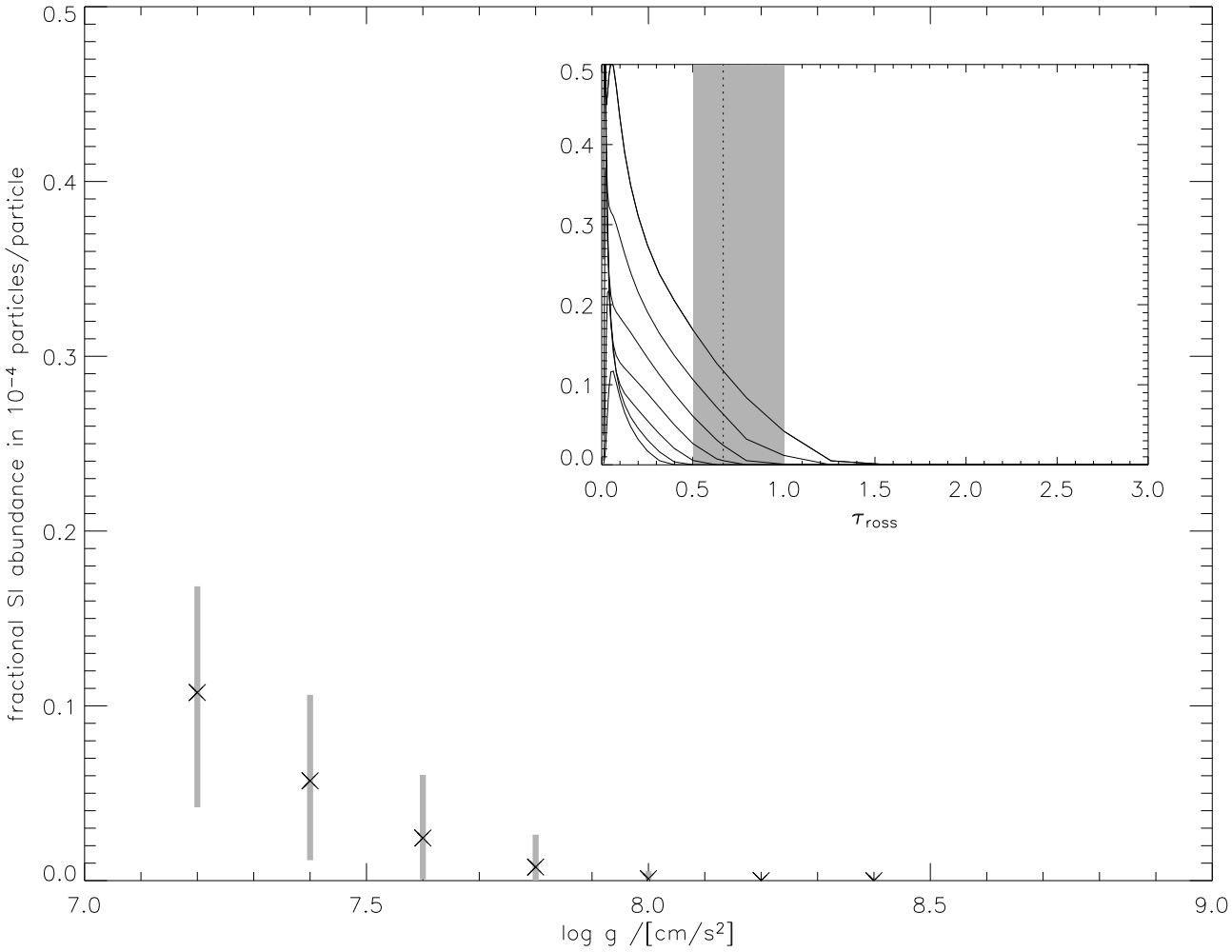

Figure 4.4: Silicon abundances for different surface gravities, similar to Fig. 4.2.

Due to the rough λ^3 dependency of the hydrogen opacity[1], the EUV originates from deeper layers than the UV or optical in a hydrogen-dominated atmosphere. The definition of the Rosseland optical depth scale provides a fixed point. Starting from the location of $\tau_{\rm ross} = \frac{2}{3}$, its relevance can be explored for different spectral ranges. Figure 4.7 displays the location of $\tau_{\rm ross} = \frac{2}{3}$ on the mass scale for models of different effective temperatures and gravities. In the left panel, the shift of the flux peak towards the EUV on the one hand and the reduced H opacity due to stronger ionisation on the other hand lead to a deeper view into the atmosphere ($\tau_{\rm ross} = \frac{2}{3}$ is located further in) with increasing effective temperature. From the consistency of this with the relation shown in the left panel, it follows that the iron (or, more generally, heavy

[1]The general λ^3 increase is discontinuously interrupted at the absorption edges, in particular the Lyman edge, and locally modified through lines. The mean dependency over a large spectral range averages to a lower overall value of about λ^2.

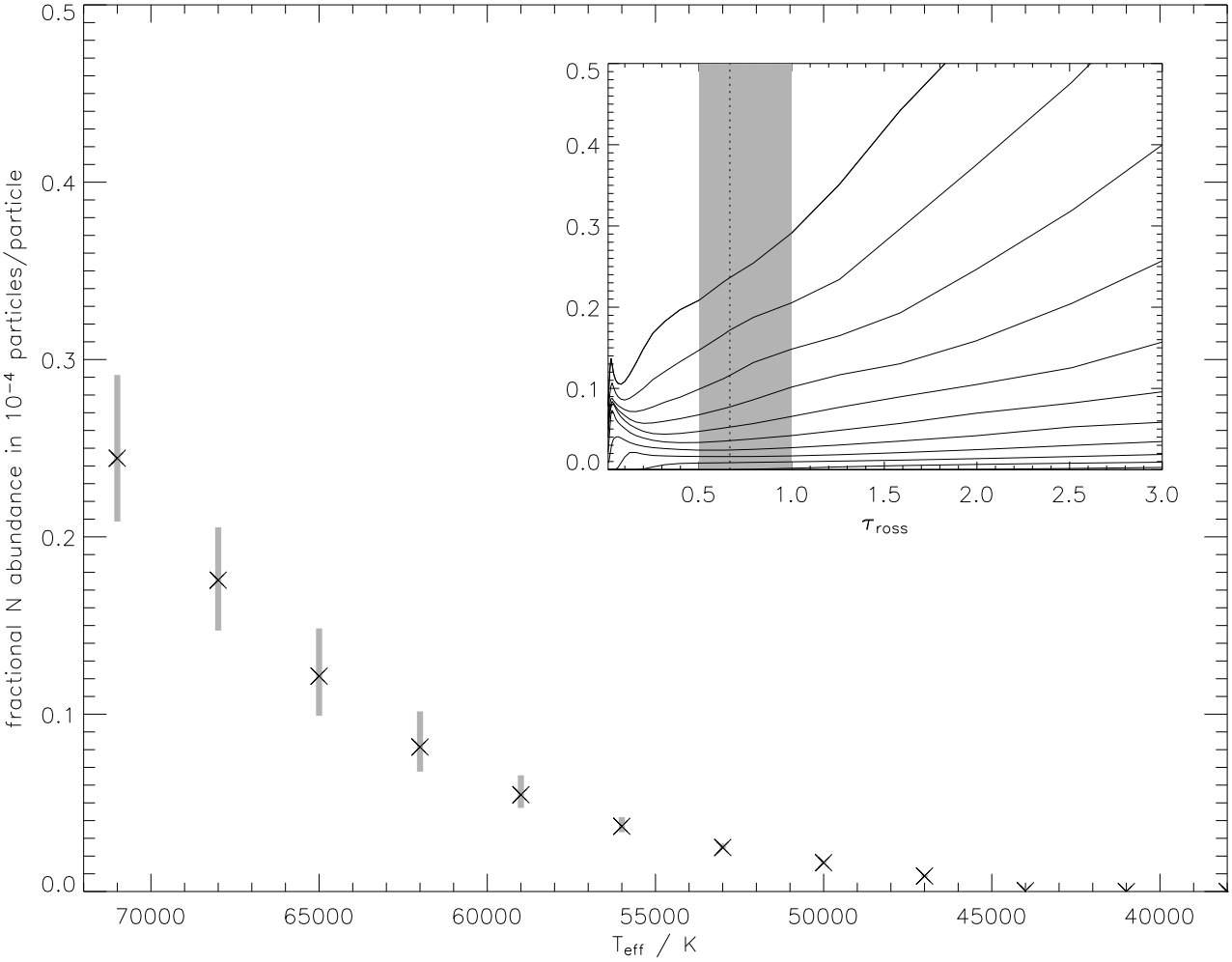

Figure 4.5: Nitrogen abundances for different effective temperatures, similar to Fig. 4.1.

element) opacity – which increases with shorter wavelengths and with increasing $T_{\rm eff}$, and hence should move $\tau_{\rm ross} = \frac{2}{3}$ further outward – does not have a dominating effect on the location of $\tau_{\rm ross} = \frac{2}{3}$. In the right panel, the decreasing density with decreasing $\log g$ leads to higher transparency and again a deeper view into the atmosphere ($\tau_{\rm ross} = \frac{2}{3}$ is located further in). The increasing iron (or heavy element) abundance with decreasing $\log g$ is not dominant enough to reverse this trend. Despite the fact that the heavy element (in particular iron) opacity is highest in the EUV[2], comparisons based on the assumption that shorter-wavelength ranges originate from deeper layers than longer-wavelength ranges generally remains valid, as long as possible complications through the Lyman edge can be either neglected or are appropriately considered.

[2]Although the effect is minimal, the high heavy element abundances can also be "seen" particularly well at high $T_{\rm eff}$ and low $\log g$, while the heavy elements at low $T_{\rm eff}$ and high $\log g$ are – in addition to their low absolute abundances – also better "hidden" by the increased mean hydrogen opacity.

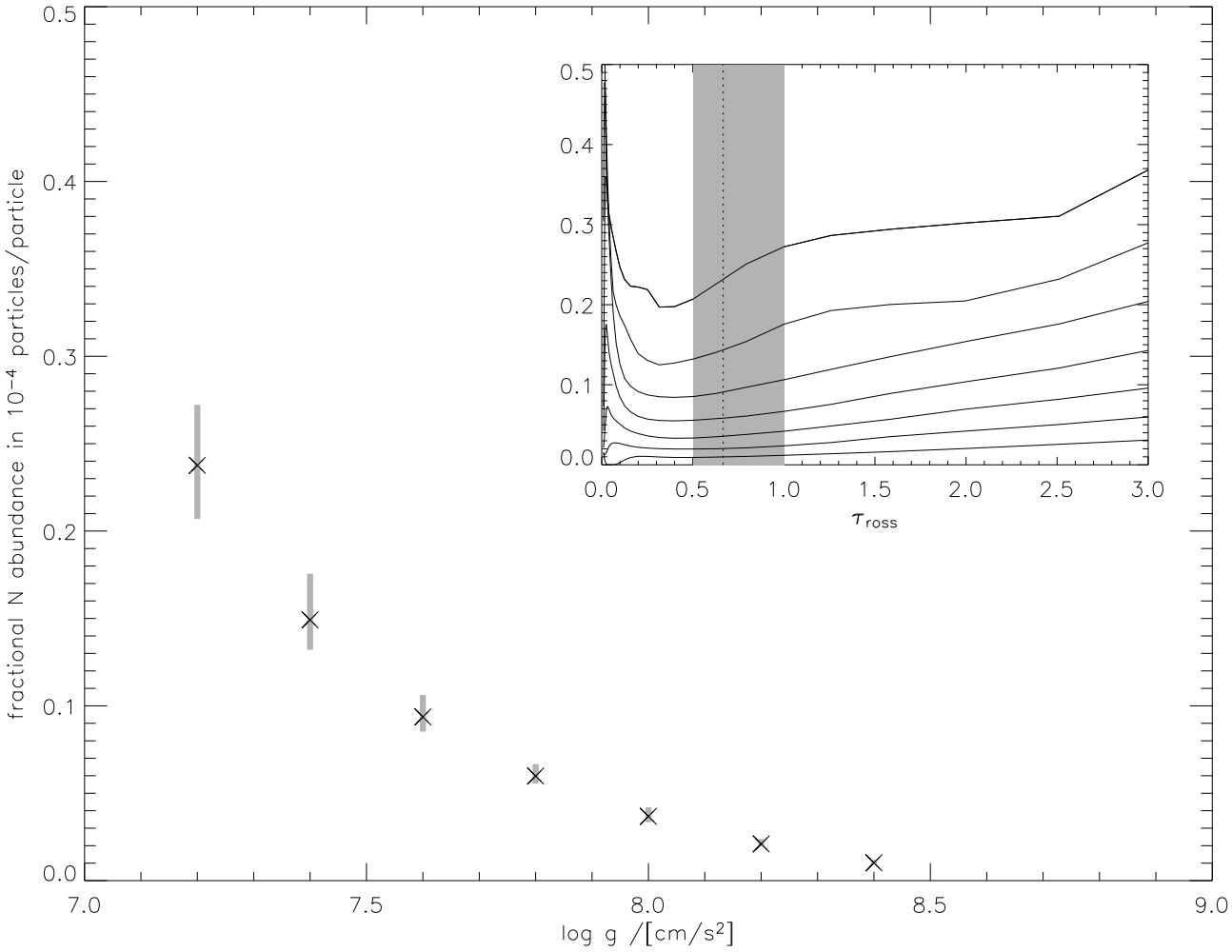

Figure 4.6: Nitrogen abundances for different surface gravities, similar to Fig. 4.2.

The reasoning by Holberg et al. that an observed nitrogen abundance that is higher in the UV than in the EUV should result from a nitrogen slab located in the outer regions of RE J1032+535's atmosphere therefore is valid even though it remains to be seen if the increased N abundance in the models presented here can provide a quantitative explanation. As a summary, it can be stated at this point that even equilibrium calculations yield rather non-trivial abundance distributions.

In Appendix A, the approach to display the information for all parameters and all elements is in principle very similar as in the plots just shown for iron, silicon and nitrogen. Instead of displaying selected cuts through the model grid at fixed surface gravities and effective temperatures, predicted abundances are displayed as a function of $T_{\rm eff}$ for all parameters $\log g$, and as a function of $\log g$ for all parameters $T_{\rm eff}$. Despite the obvious redundancy, this is useful to estimate the margins within which one of the parameters can, or must, be varied for various comparisons. The

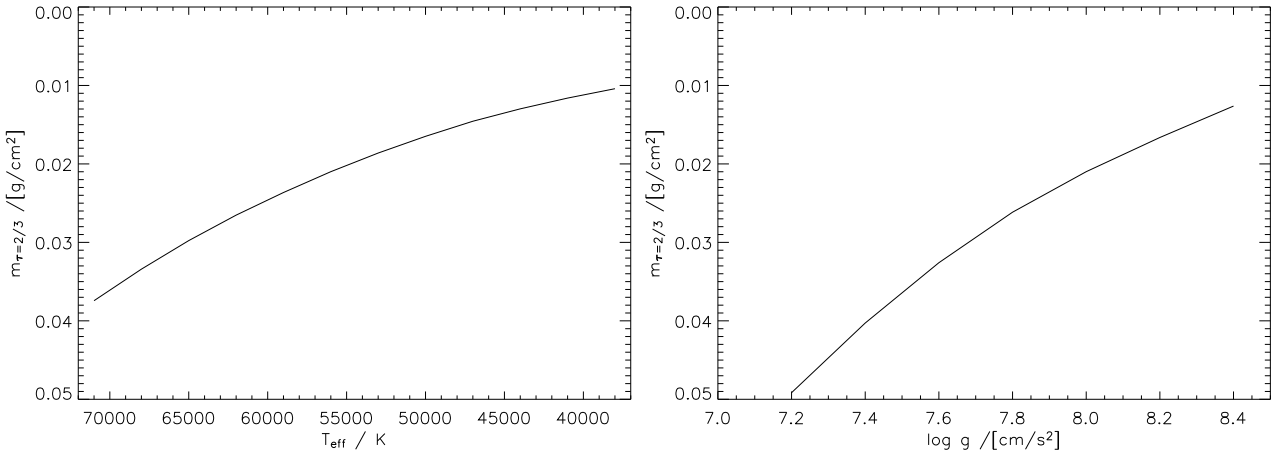

Figure 4.7: Location of $\tau_{\rm ross} = \frac{2}{3}$ on the mass scale as a function of effective temperature (for a fixed surface gravity of $\log g = 8.0$, left panel) and surface gravity (for a fixed effective temperature of $T_{\rm eff} = 56\,000$ K, right panel).

uncertainties in these representations, as above, are obtained from the variation of the respective abundance with optical depth.

4.2 Comparison to earlier models

The above results are compared to the calculations by Chayer et al. (1995b). Both investigations are based on a model atmosphere approach, Chayer et al.'s in LTE and this work in NLTE. Dreizler & Werner (1993) made a good case for the necessity of NLTE treatment of hot white dwarf atmospheres. Chayer et al., in addition to a few intermediate steps since Chayer et al. (1994) and Chayer et al. (1995a), mainly present a "big" and a "small" grid. Both contain equilibrium calculations for all heavy elements contained in the TOPBASE[3] atomic data base, i.e. {C, N, O, Ne, Na, Mg, Al, Si, S, Ar, Ca, Fe} – in contrast to {He, C, N, O, Si, Fe, Ni} here. Both Chayer et al. grids consider momentum redistribution (improved according to Gonzalez et al. 1995), which the newer models do not. In the "big" grid, equilibrium abundances are calculated from an existing model atmosphere structure and its radiation field from pure hydrogen opacity; in the "small" grid, a representative fixed mixture of {C, N, O, Fe} provides an additional background opacity (as opposed to full consideration of all modelled elements simultaneously including the atmospheric structure's reaction to their presence here). Due to the "small" grid's very limited coverage of the $[T_{\rm eff}, \log g]$ plane, the following comparison is done with results from the "big" grid. In that case, the superiority of the newer models with respect to

[3]Cunto & Mendoza (1992), based on Opacity project data (Seaton et al. 1992; Seaton 1992).

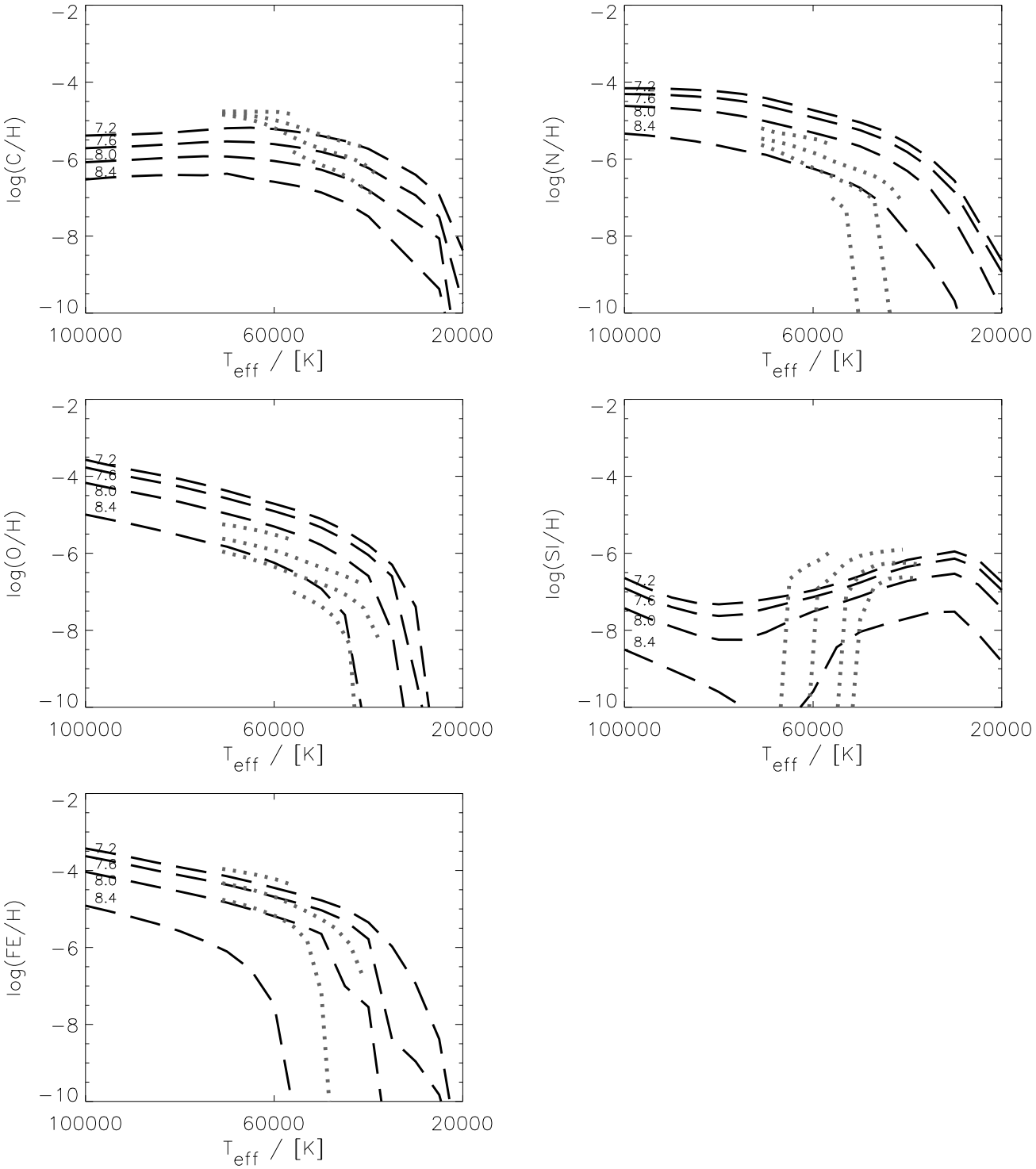

Figure 4.8: Comparison of predicted elemental abundances (grey dots) to Chayer's abundances (black dashed) as a function of temperature for different surface gravities: see annotations.

self-consistency is even more distinct.

Figure 4.8 compares the predicted equilibrium abundances at $\tau_{\rm ross} = \frac{2}{3}$ as a func-

tion of $T_{\rm eff}$ for a range of $\log g$ values. The parameters shown were chosen such that the overlap range covered by the Chayer "big" grid and this work's "extended" grid was maximised and the diagrams could be done without interpolation. All elements considered in both calculations simultaneously are shown: C, N, O, Si, and Fe.

Although overall trends are generally recovered, the magnitude of deviations can be up to about 1.7 dex in relative abundance (in regions where gradients are not exceptionally strong). This can alternatively be expressed as corresponding to shifts in $\log g$ of up to 1.5 dex (up *or* down!) that would be necessary to better match individual predictions to each other. The location of edges where abundances drop off dramatically is best described as offset in effective temperature, where significant discrepancies up to 25 000 K occur (albeit for un-observably small absolute abundance values).

The case of Si is special; the reversed gradient below $\approx 80\,000$ K described earlier is recovered in both cases, but the newer models do not reproduce the rise above that temperature predicted by the earlier ones. Various solutions found by Chayer et al. during the refinement process of their models also differ from each other because the silicon abundance in that parameter range is very sensitive to slight changes. This is due to the Si V noble gas configuration which is predominantly populated but does not contribute significantly to the levitation; the momentum transfer rests on the small fractions of silicon in lower ionisation states. Since in the new models no ionisation states higher than Si V were included, the recovery of the silicon abundance towards the upper end of the grid at $\approx 70\,000$ K due to higher ionisation states cannot be reproduced here.

Altogether, the differences from one grid to the other show no fundamental trend for the common elements; the deviations can go in both directions. Since "extra opacity may reduce or increase (through redistribution) the flux available to across the line spectrum of an element" (Chayer et al. 1995b), the reaction of an individual element to changes in the respective background opacity (if interpreted as such) can be quite different, and the rather unpredictable character of this behaviour seems to show here. The conditions under which the compared calculations were performed involve a whole range of differences; together they perhaps allow to estimate the current maximum systematic errors in radiative levitation calculations. Similarly, this exercise may be continued with the more detailed calculations in the next section.

4.3 Discussion of test calculations with more opacities

In a continued effort to push the models to a more sophisticated level, models from Sect. 3.3 were subjected to refinements according to Sect. 3.4. The main quest is to include more elements. Due to their significant opacities, the missing iron group ele-

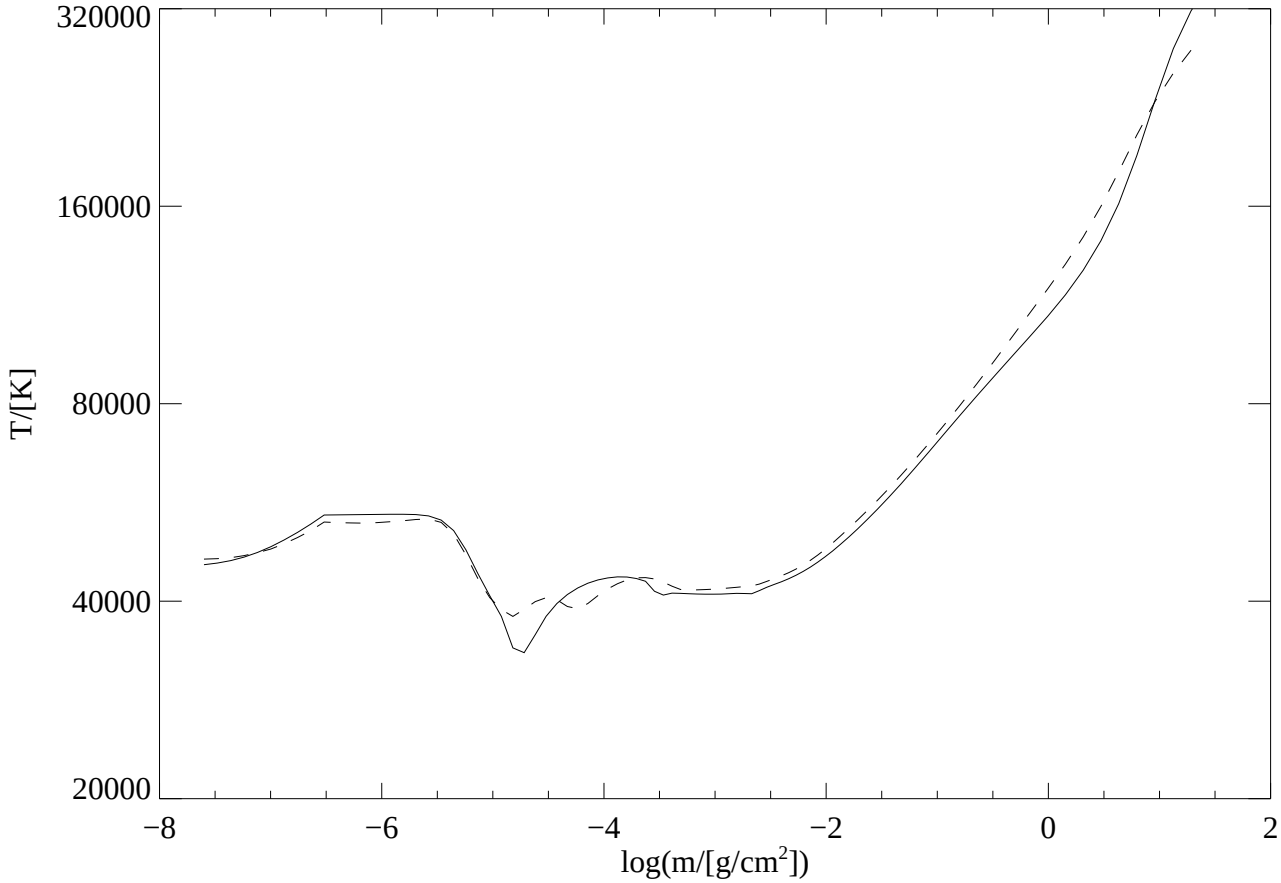

Figure 4.9: Temperature stratifications with the ”old” (full line) and ”new” (dashed) codes.

ments from Ca to Ni were additionally taken into account first; this section discusses the effects.

When the impact of the extension to the full iron group elements is explored, the main differences in the atmospheric structure are caused by two of the newly added elements that display surprisingly large equilibrium abundance values: Ca and Ti. Both additionally reach the artificially introduced upper limits of a mass fraction of 10^{-2} in the outmost parts of the atmosphere. Such high abundances are not corroborated by observations as reported for example by Barstow et al. (2003c).

It is one possibility to interpret the outward increase as the sign of a selective wind – not covered by the present static model – which might in principle help to decrease the excessive overall abundance of the affected elements. A more elegant interpretation could be available by adopting results from Fontaine & Chayer (1997) for He in sdB stars, who included weak mass-loss in their models and find that equilibrium profiles tend to be maintained in the atmosphere until the reservoir is emptied from bottom up, at which point the element quickly disappears. Using equilibrium profiles when an element is obviously present in a specific object, and completely discarding it

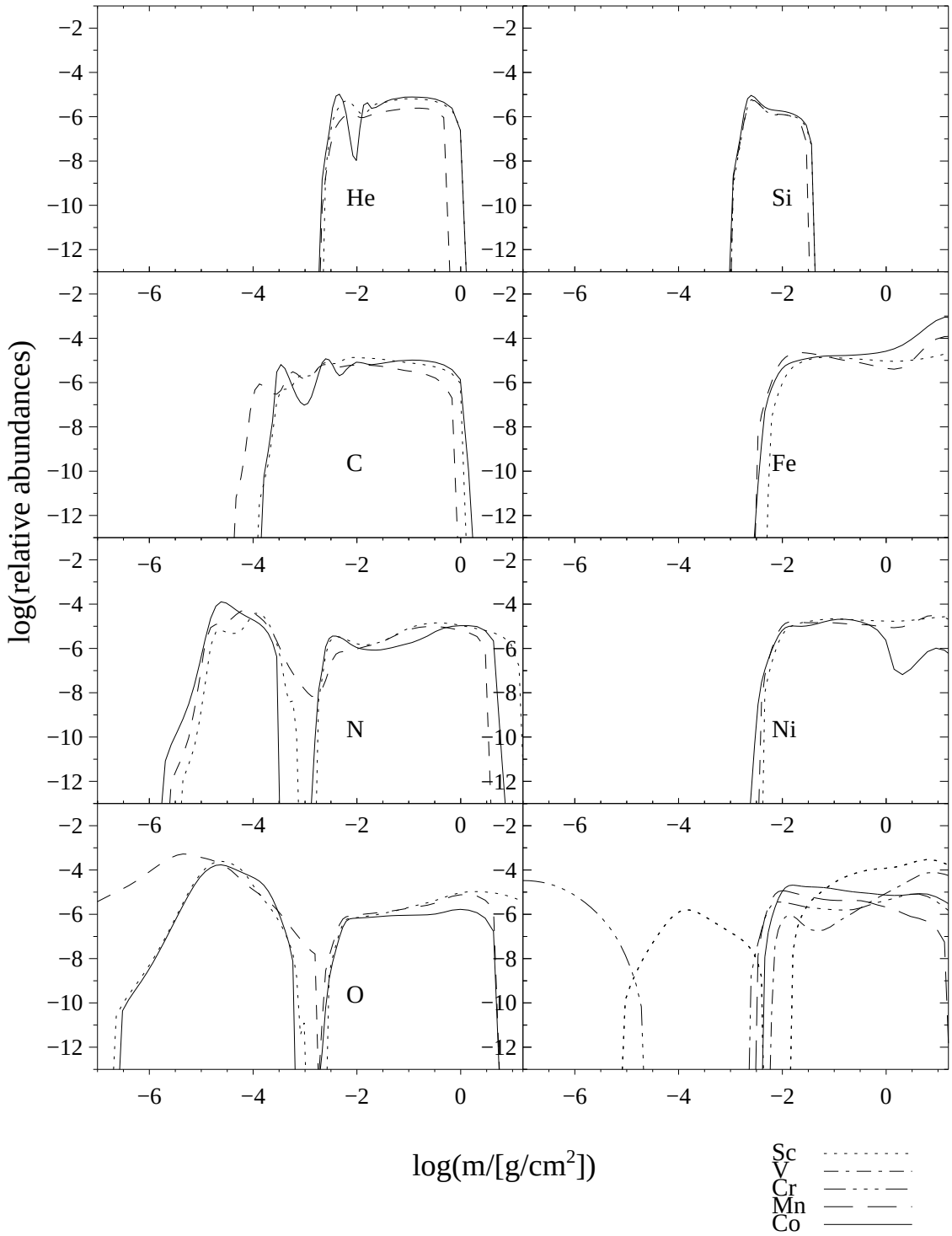

Figure 4.10: The first seven panels show the abundance stratifications predicted by a model calculated with the old code and containing fewer elements (full line), and by a model calculated with the new atmosphere and sampling codes but containing the same restricted number of elements (dotted line), in comparison to the ones predicted by a model calculated with the new codes and containing more elements (dashed line), with the respective element name indicated directly in the appropriate panel. The last panel shows the predictions of that last new model for the additional elements included there, with a code to the individual species printed on the lower right-hand side.

otherwise, may therefore be an acceptable choice.

Based on such considerations the addition of more elements was restricted to the iron group elements without Ca and Ti for the time being. This modification leads to changes in the structure of the test model such as the slight alteration of the temperature structure shown in Fig. 4.9 and results in new abundance profiles as illustrated by Fig. 4.10. All results are for models with $T_{\rm eff} = 56\,000\,{\rm K}$ and $\log g = 7.6$: one taken directly from Sect. 3.3 for comparison (old code, old model atoms; "old" model represented by a full line), one calculated with the new code and partially modified atomic data (but with no further elements included; dotted line), and one with additional elements as discussed above ("new" model represented by a dashed line). This key is valid for the elements common to all three models, while the abundance predictions for the add-on elements as shown in the last panel of Fig. 4.10 are labelled individually.

Since the new code has been thoroughly tested to give identical results for unchanged input data, the impact of the first step (compare the full and the dotted lines) must be attributed to the different methods of preparation of atomic input data (for the same list of elements; details were given in Sect. 2.5).

The effect of adding more elements in the second step leads to the differences in predicted equilibrium abundances as shown using dashed lines. While for all elements that are common to the three models the shapes of the equilibrium profiles are fairly similar in all cases, the absolute abundances in numbers at a given depth point can differ substantially, mainly due to the steep gradients involved. It will therefore depend heavily on the formation region of any given line how much its shape will be affected.

The inclusion of further heavy elements does not affect the stratification profiles of those previously considered in a straightforward manner. In particular, the notion that additional elements with important opacity over a large wavelength range might lead to considerable flux blocking, reducing the relative abundance of similar species so that only the total of heavy elements supported remains at a given level, proves to be wrong. The effects of flux redistribution do not lead to a "saturation", instead every new element reaches approximately the same level as those already present (see last panel) and basically adds to the total opacity.

By comparing all results and evaluating the scale of the deviation, "systematic" errors can be derived that amount to up to 2 dex uncertainty (plus a much larger deviation for O in the outmost regions). This value is of the same order of magnitude as in the last section, where Chayer et al. models were compared to current results. It reflects the degree to which the predictions can perhaps be considered trustworthy, by estimating the influence from various modelling-dependent effects.

CHAPTER 5

Analysis of spectroscopic EUVE data

The following is largely based on Schuh, Dreizler & Wolff (2002), with a few enhancements in the contents, and with some subsections omitted or moved to other parts in this thesis where they fit better. The contributions of the co-authors to this work were the data reduction of the EUVE spectra performed by B. Wolff, while S. Dreizler provided the diffusion code used to calculate the model grid. In comparison to the analysis by Schuh (2000), this full reanalysis is based on a more complete model grid (although not identical to the "extended" model grid) and improved visual magnitudes for the objects (taken from the literature).

5.1 Introduction

The basic physical mechanisms leading to the element stratification have long been known, so their actual modelling appears preferable to an ad hoc approach. Chayer et al. (1995a,b) were the first to calculate an extensive model grid for white dwarfs predicting the chemical stratification assuming equilibrium between gravitational settling and radiative levitation. An improvement has now been achieved through the introduction of self-consistent NLTE model atmospheres which account for the coupling between chemical stratification and the radiation field (Dreizler 1999). The successful application of these models to the EUVE spectrum of G 191–B2B (Dreizler & Wolff 1999) has motivated a more systematic analysis of a larger sample of hot DA white dwarfs which we present here.

The investigation in this chapter exploits EUVE spectra and discusses the results with respect to parameter determinations in the optical. The following Chapter 6 will deal with the UV wavelength ranges and give detailed metal abundance pattern predictions. The availability of EUVE spectra defines, as in Wolff et al. (1998), the overall sample, which is more thoroughly introduced in Sect. 5.2. The observations and particular considerations concerning the interstellar medium are shortly described there as well. Sect. 5.3 recapitulates the principle of the model calculations as discussed at some length in Chapter 2; for characteristics of the model grid computed

for comparison with the sample on hand we refer back to Chapters 3 and 4. The methods and results from fitting the new class of theoretical spectra to the observations are presented in Sect. 5.4. The implications of these results are discussed in Sect. 5.5.

5.2 EUVE observations of hot DA white dwarfs

5.2.1 The EUV selected DA sample

Generally speaking, the maximum spectral flux of hot WDs lies in the extreme ultraviolet (EUV). The fact that the main opacity of heavy elements at these temperatures tends to lie in the same range means that radiative acceleration can sustain traces of them in the atmosphere, but it also implies that the EUV is the best suited spectral range for the detection of these elements. Consequently, we start by surveying EUVE spectra, even though the spectral resolutions of its instruments are not high enough to identify individual lines. The element-by-element identification is best deferred to high-resolution UV or FUV studies. The new models do not a priori require line identification, although it would in principle be desirable to be able to do that even in the EUV. They impose no need for the use of a pre-defined metal mix (as used by Wolff et al. 1998), nor do they require the adjustment of a scaling factor as in Barstow et al. (1997), as the abundances are not free parameters but are derived from an equilibrium condition (see Sect. 5.3). As the EUV flux is very sensitive to the chemical composition of the photosphere, a comparison in this regime is extremely useful to test the predictions of the diffusion models. Interpreting the repeated analysis as a test case for the models, it is reasonable to start out by following previous investigations as closely as possible. For this reason, we chose to use the 26 DAs previously analysed by Wolff (1999).

This sample comprises all hot ($T_{\rm eff} > 40\,000$ K) DA white dwarfs with EUVE observations, which were mostly taken from the EUVE public archive (now available at the multi-mission data archive at STScI). The data sets and the reduction procedures are described elsewhere (Wolff et al. 1998; Wolff 1999); those publications also show the reduced spectra in the form used here, i.e. flux calibrated SW, MW and LW[1] data concatenated to yield a single spectrum.

The effective temperatures of the sample stars lie above $T_{\rm eff} = 40\,000$ K, where photospheric metal abundances are still large enough to be detectable. Above $T_{\rm eff} = 70\,000$ K, mass-loss effects might start to disturb the expected equilibrium between gravitational and radiative acceleration (Unglaub & Bues 1998), but the sample contains no stars hotter than that. Wolff et al. (1998) have grouped the objects into

[1] SW (short-wavelength spectrometer, 70 Å – 190Å, 0.5 Å resolution), MW (medium-wavelength spectrometer, 140 Å – 380Å, 1.0 Å resolution), and LW (long-wavelength spectrometer, 280 Å – 760Å, 2.0 Å resolution) refer to data from three different instruments on-board the EUVE satellite.

four different categories. The first set consists of G 191–B2B like objects, where the high metallicity yields a steep flux drop towards short wavelengths, beyond the interstellar He II absorption edge. The second group includes GD 246 and similar objects which contain fewer photospheric metals, but still more than those in the third group whose spectra Wolff et al. could fit with pure hydrogen atmospheres. A fourth rather inhomogeneous set compiles the remaining objects. For details, especially on the effective temperature, surface gravity and metallicity region in parameter space covered by the different groups, we refer once more to Wolff (1999).

5.2.2 Treatment of the ISM

The interstellar medium (ISM) considerably attenuates the stellar flux in the EUV. The most important features are the H I, He I and He II bound-free ground state absorptions with edges at 911.7 Å, 504.3 Å and 227.8 Å, respectively. This is being accounted for in the same way as in Wolff et al. (1998): The effect of given interstellar column densities on the theoretical fluxes is modelled and applied following Rumph et al. (1994). The derivation of H I column density depends on the effective temperature of the model used, and the He I and He II column densities on its absorber content. Due to the interrelation of $T_{\rm eff}$ and N(H I) and the fact that the Lyman edge lies outside the range observed by EUVE, Wolff et al. (1998) have started from optically determined effective temperatures (by Finley et al. 1997), and additionally have retained surface gravities from that analysis unchanged. In the present approach, we start from the effective temperatures from Wolff (1999) and adopt his H I column densities unalteredly whenever possible.

Even though the He I and He II column densities have to be constantly modified during the fitting procedure depending on the assumed photospheric parameters, all interstellar contributions will in the following be treated as a secondary effect on the stellar light that can be dealt with independently of the analysis of the source itself, disregarding the fact that an appropriate correction can only be made *after* a set of photospheric parameters has been adopted. As the interstellar absorption is more important at longer wavelengths while the absorption by photospheric metals increases towards shorter wavelengths, the different contributions can partly be separated.

5.3 Equilibrium abundances from stratified model atmospheres

5.3.1 Diffusion models

Our self-consistent diffusion models have been introduced in the previous chapters. Chayer et al. (1995a,b) have presented extensive results of similar calculations for white dwarfs. Their predicted equilibrium abundances were not quantitatively consistent with observations. This might be partly due to the fact that the observations

were analysed with chemically homogeneous model atmospheres, meaning that homogeneous abundances were compared to predictions for stratified atmospheres, or arises because the feedback of the modified abundances on the radiation field was not accounted for.

The self-consistent solution of the equilibrium condition and the atmospheric structure has first been presented by Dreizler (1999). In addition to this newly introduced coupling, it is also a novelty that the calculations are being performed under NLTE conditions. This has turned out to be a crucial point (Schuh 2000; Dreizler & Schuh 2001). The code itself relies on an iteration scheme that alternates between the determination of new equilibrium abundances and the corresponding solution for the atmospheric structure (we remind the reader of Chapter 2 and Werner & Dreizler (1999) for a description).

5.3.2 Scope of application

It remains to be justified why the white dwarfs in our sample will presumably obey the presented equilibrium condition. Processes eligible to disturb or prevent its adjustment can be mass-loss, accretion from the interstellar medium, convection or mixing through rotation. As explained by Unglaub & Bues (1998), mass-loss would have the effect of homogenising a chemical stratification, but as has also been shown in the same paper, mass-loss rates drop below the critical limit ($10^{-16}\,\mathrm{M}_\odot$/yr) for DAs cooler than $T_{\mathrm{eff}} = 70\,000\,\mathrm{K}$ so that this phenomenon should not occur in any of the sample stars. Calculations of MacDonald (1992) that treat the interaction between accretion and the white dwarf wind reveal that WDs in our sample are not affected by accretion. It is prevented since $\mathrm{L_{WD}}/\mathrm{L}_\odot > 1$, so that at least a critical mass-loss rate of $3{\cdot}10^{-18}$ to $10^{-21}\,\mathrm{M}_\odot$/yr is sustained.

Convection would of course homogenise abundances, too. However, convective instability in the outer layers occurs only below $T_{\mathrm{eff}} = 12\,000\,\mathrm{K}$ for DAs, i.e. well below $T_{\mathrm{eff}} = 40\,000\,\mathrm{K}$. Rotation could lead to a mixing through meridional currents; but as most white dwarfs are very slow rotators (Heber et al. 1997; Koester et al. 1998), this is not likely to interfere either.

Even if it is left undisturbed, it takes an atmosphere a certain time to reach an equilibrium state. Due to the high surface gravities, diffusion time scales are of the order of months in the outer layers of white dwarfs (Koester 1989, based on diffusion coefficients by Paquette et al. 1986). This is nothing but an instant compared to evolution time scales ($\sim 10^7$ yr), and this is the reason why DA atmospheres in the effective temperature range between 40 000 K and 70 000 K can be regarded to have their photospheric abundances set to equilibrium values at any time of their evolutionary stage. In the temperature range above 40 000 K the flux maximum still lies in the EUV, i.e. in the same range where multiple lines of heavier elements provide substantial opacity, making radiative levitation an efficient mechanism for sustaining absorbers. It

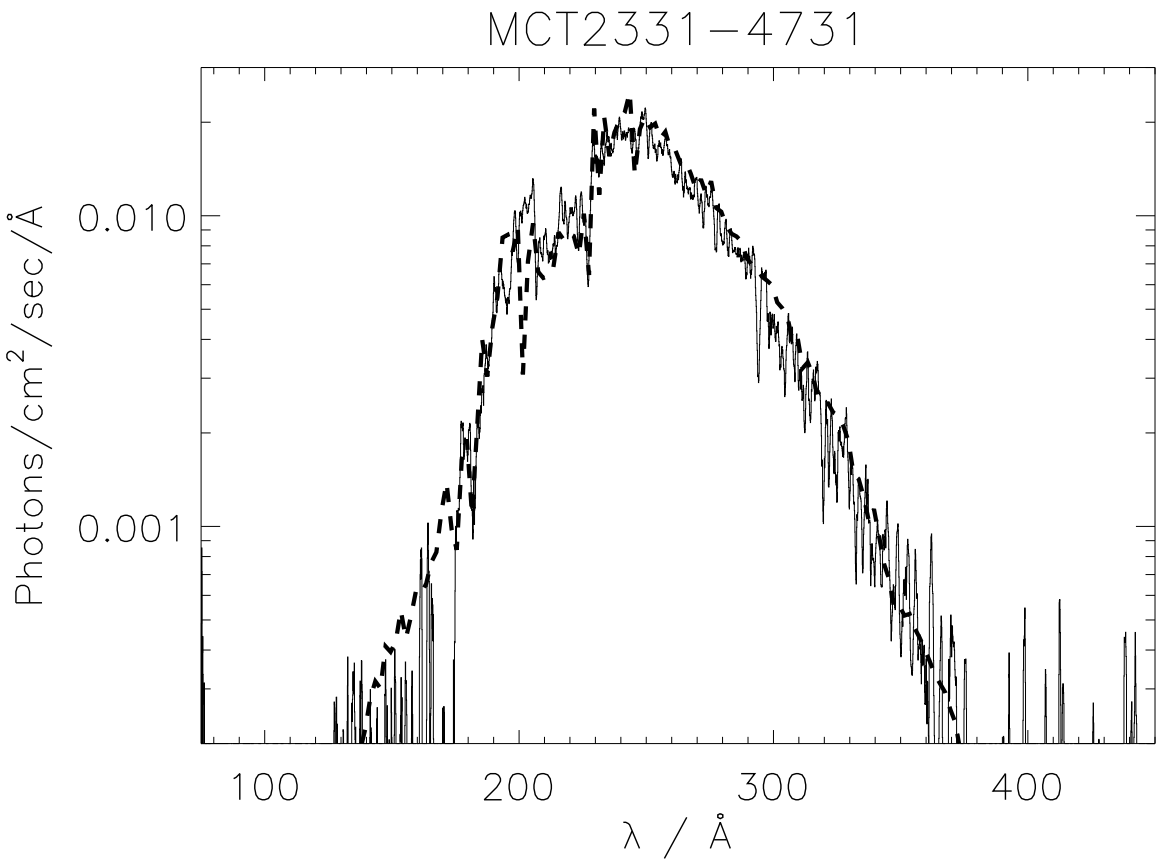

Figure 5.1: EUVE spectrum of MCT 2331−4731 with the best-fit model at $T_{\rm eff} = 56\,000$ K and $\log g = 7.7$ overlaid (dashed). The photon flux is displayed on a logarithmic scale.

should in this context also be noted that the evaluation of the equilibrium abundances does not include the contributions of thermal and concentration diffusion, which have much longer time scales.

5.4 Testing the diffusion models and re-analysing the DA sample

5.4.1 Comparison of theoretical and observed spectra

To directly compare a theoretical flux distribution with the observed one, it is first rebinned in wavelength and normalised to the observed visual magnitude. The values for m_V have been chosen using the compilation of McCook & Sion (1999) and are listed with their individual references in Table 5.1. Then the effect of interstellar absorption is calculated as sketched in Sect. 5.2.2. The model matching was performed on the grid mentioned in Sect. 3.2 which did not in all parameter ranges correspond to a tight mesh, and no interpolation was used. The quality of an individual fit was eval-

uated by eye. Of course, changing the interstellar He column densities seemingly has a big impact on the overall shape of the spectrum. However, the region most sensitive to metal abundances lies at least partly beyond the He II absorption edge, so once this and the lower energy edges are fitted all remaining deviations have to be due to either a different flux level as caused by the effective temperature or a different amount of absorber content as regulated by the surface gravity in the equilibrium models.

5.4.2 Revised atmospheric parameters

The present model matching led to new atmospheric parameters where mainly the surface gravities differ from former specifications. The improvement of many of the individual fits (see Fig. 5.3) as compared to fits with homogeneous models (in Wolff et al. 1998; Wolff 1999; Dreizler & Wolff 1999) vindicates these adjustments.

With homogeneous models, discrepancies were encountered especially for higher metallicity stars in the shorter wavelength regimes, which could not be adjusted by a different metallicity value as this would have deteriorated the quality of the fit at other wavelengths. This difficulty is resolved with the new models, as they offer different abundances at different formation depths. Consequently they can often better reproduce especially these formerly delicate regions. Figure 5.1 shows an example.

Figure 5.3 displays all observations with the best-fit model spectra over-plotted, both shown at 1 Å resolution. Table 5.1 lists the parameters of the best-fit model for each object, along with the interstellar column densities used to produce the plots. The latter are to be regarded as very preliminary as fitting improved models to the spectra may yet again yield different values. High He II column densities, found throughout the sample, may be an indication that in particular short-wavelength opacities are still missing. The table additionally lists a quantity denoted mi, which stands for the *metal index* that is introduced next.

5.4.3 Metal index

With depth-dependent abundances, it is difficult to quote one representative value for each element (although problematic, we mostly retreat to using values at $\tau_{\rm ross} = \frac{2}{3}$ in Chapter 4 and for the UV analysis in Chapter 6). To evade this problem here, we have introduced a *photospheric parameter*-dependent quantity that relies entirely on the predictions by diffusion theory. As explained above, the absorber content of the models is determined from the equilibrium between the radiative and the gravitational forces. The radiative acceleration scales with $T_{\rm eff}^4$ due to the occurrence of the Eddington flux in Eq. 2.40, the effective gravitational acceleration scales with g as is evident from the upper expression in the same equation. The absorber content should thus be comparable along lines of constant $T_{\rm eff}^4/g$. To map this ratio onto a

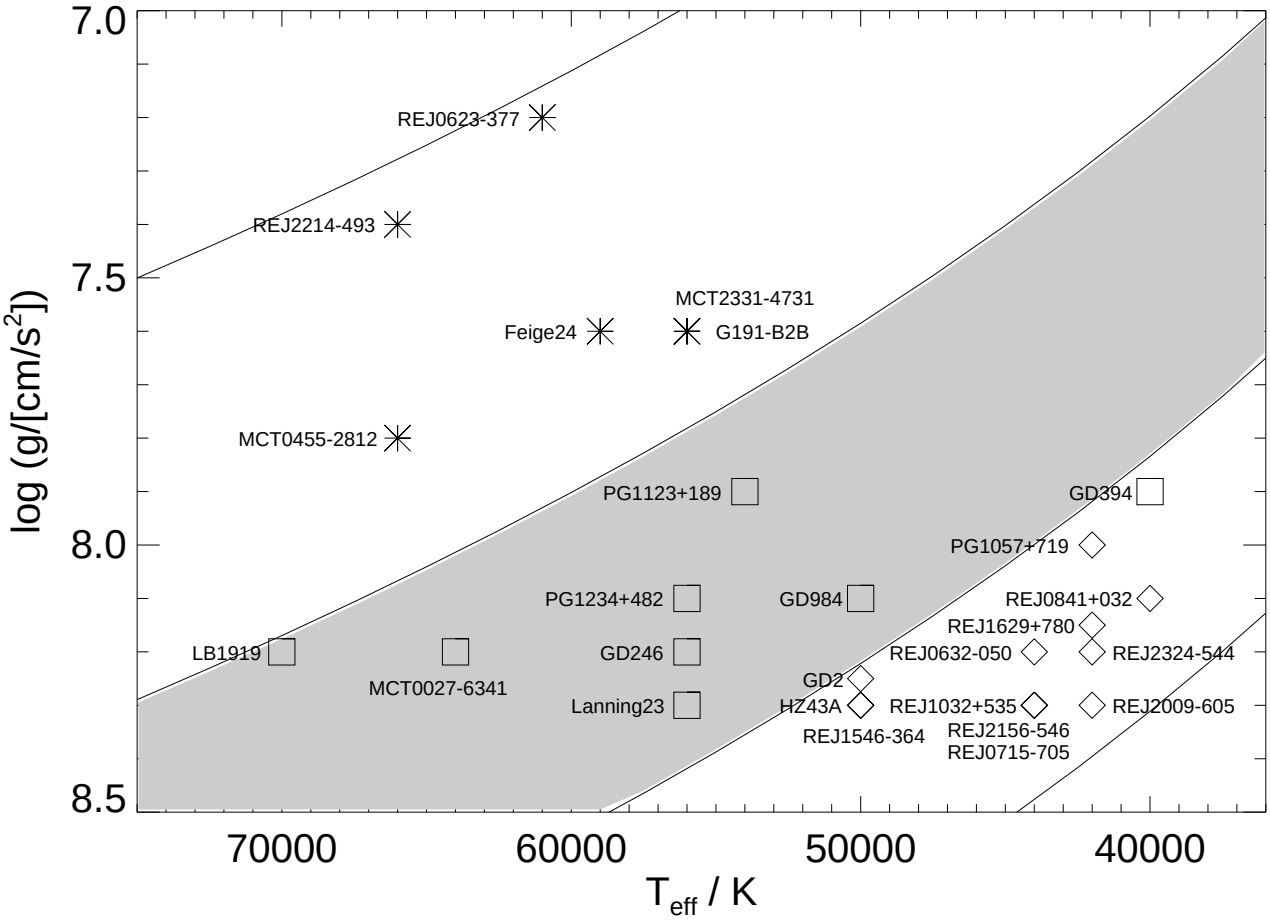

Figure 5.2: Revised parameters of the program stars in the [$T_{\rm eff}$, $\log g$] plane. Lines indicate constant values of the metal index as defined in Sect. 5.4.3, $mi = 4.$, 0.65, 0.15, 0.05, respectively. The shaded area indicates the metallicity of DA white dwarfs of the GD 246 group of Wolff et al. (1998). These as well as the objects classified as irregular fall into this regime and are marked by squares. Stars above that region belong to the G 191–B2B-group (identified by starry symbols), stars below to the pure-hydrogen-group (marked by diamond-shaped symbols). See also Sect. 5.2.1.

dimensionless and small-number parameter, we define

$$mi = 4 \cdot 10^{-12} \cdot T_{\rm eff}^4/g \ \ /[{\rm K}^4{\rm s}^2/{\rm cm}] \tag{5.1}$$

where the leading factor has been chosen to yield a result of the order of one for the photospheric parameters of the standard star G 191–B2B. Lines of constant mi are displayed in Fig. 5.2.

It should be emphasised that this quantity is not derived from the actual calculated equilibrium abundances in the models. It is based on a much simpler evaluation of just the same idea that underlies the construction of the models. Knowing this, it is

Table 5.1: New and previous results (Wolff et al. 1998) of the EUV analysis ordered by decreasing metal index mi. N_H is given in $10^{18}cm^{-2}$. See Section 5.4.3 for an explanation of the theoretical metal index mi.

WD–N^o	Name	m_V		N_H log g [[cgs]] log g [[cgs]]	He I/H T_{eff} [K] T_{eff} [K]	He II/H mi m	(new) (new) (old)
WD 0621−376	RE J0623−377	12.089	[1]	5.0	0.09	0.15	
				7.2	61000	3.49	
				7.27	58000	2.0	
WD 2211−495	RE J2214−493	11.7	[1]	5.8	0.07	0.15	
				7.4	66000	3.02	
				7.38	66000	4.0	
WD 0232+035	Feige 24	12.56	[2]	2.72	0.068	0.25	
				7.6	59000	1.22	
				7.17	58000	1.0	
WD 0455−282	MCT 0455−2812	13.95	[3]	1.3	0.063	0.3	
				7.8	66000	1.20	
				7.77	66000	1.0	
WD 0501+527	G 191–B2B	11.79	[2]	2.05	0.071	0.3	
				7.6	56000	0.99	
				7.59	56000	1.0	
WD 2331−475	MCT 2331−4731	13.1	[4]	8.5	0.08	0.1	
				7.6	56000	0.99	
				8.07	56000	0.75-1.	
WD 1056+516	LB 1919	16.8	[4]	16.0	0.04	0.05	
				8.2	70000	0.61	
					69000	0.1	
WD 1123+189	PG 1123+189	14.13	[1]	11.9	0.09	0.052	
				7.9	54000	0.43	
				7.63	54000	0.4	
WD 0027−636	MCT 0027−6341	15.0	[4]	21.5	0.068	0.06	
				8.2	64000	0.42	
				7.96	64000	0.2	
WD 1234+482	PG 1234+482	14.38	[5]	11.7	0.09	0.05	
				8.1	56000	0.31	
				7.67	56000	0.2	
WD 2309+105	GD 246	13.09	[2]	18.0	0.05	0.03	
				8.2	56000	0.25	
				7.81	59000	0.25	
WD 0131−164	GD 984	13.98	[6]	22.0	0.068	0.035	
				8.1	50000	0.20	
				7.67	50000	0.2	
WD 2247+583	Lanning 23	14.26	[7]	40.0	0.068	0.03	
				8.3	56000	0.20	
				7.84	59000	0.25	

WD 0004+330	GD 2	13.85 [2]	82.4	0.068	0.01
			8.25	50000	0.14
			7.63	49000	< 0.1
WD 2111+498	GD 394	13.09 [8]	6.5	0.07	0.15
			7.9	40000	0.13
			7.94	39600	0.25
WD 1314+293	HZ 43A	12.914 [9]	0.9	0.06	0.0
			8.3	50000	0.13
			7.99	50800	0.0
WD 1543−366	RE J1546−364	15.81 [10]	50.4	0.068	0.03
			8.3	50000	0.13
			8.88	45200	0.0
WD 1057+719	PG 1057+719	14.68 [1]	20.7	0.068	0.052
			8.0	42000	0.12
			7.90	41500	0.1
WD 0630−050	RE J0632−050	15.537 [1]	30.1	0.01	0.055
			8.2	44000	0.09
			8.39	44100	0.0
WD 1631+781	RE J1629+780	13.03 [11]	35.0	0.068	0.0
			8.15	42000	0.09
			7.79	44600	0.05
WD 0838+035	RE J0841+032	14.48 [1]	16.0	0.068	0.052
			8.1	40000	0.08
			7.78	38400	0.0
WD 2321−549	RE J2324−544	15.2 [1]	9.5	0.05	0.06
			8.2	42000	0.08
			7.94	45000	0.05
WD 1029+537	RE J1032+535	14.455 [1]	7.5	0.005	0.04
			8.3	44000	0.08
			7.77	44000	0.0
WD 2152−548	RE J2156−546	14.44 [1]	7.0	0.04	0.04
			8.3	44000	0.08
			7.91	44000	0.0
WD 0715−703	RE J0715−705	14.178 [1]	21.9	0.068	0.015
			8.3	44000	0.08
			8.05	44000	0.0
WD 2004−605	RE J2009−605	13.6 [1]	17.5	0.06	0.015
			8.3	42000	0.06
			8.16	41900	0.0

[1] Marsh et al. (1997a) [2] Kidder et al. (1991) [3] Barstow et al. (1994d) [4] Pounds et al. (1993) [5] Green (1980) [6] Wesemael & et al. (1995) [7] Vennes et al. (1997) [8] Bergeron et al. (1992) [9] Bohlin et al. (1995) [10] Vennes et al. (1996b) [11] Schwartz et al. (1995)

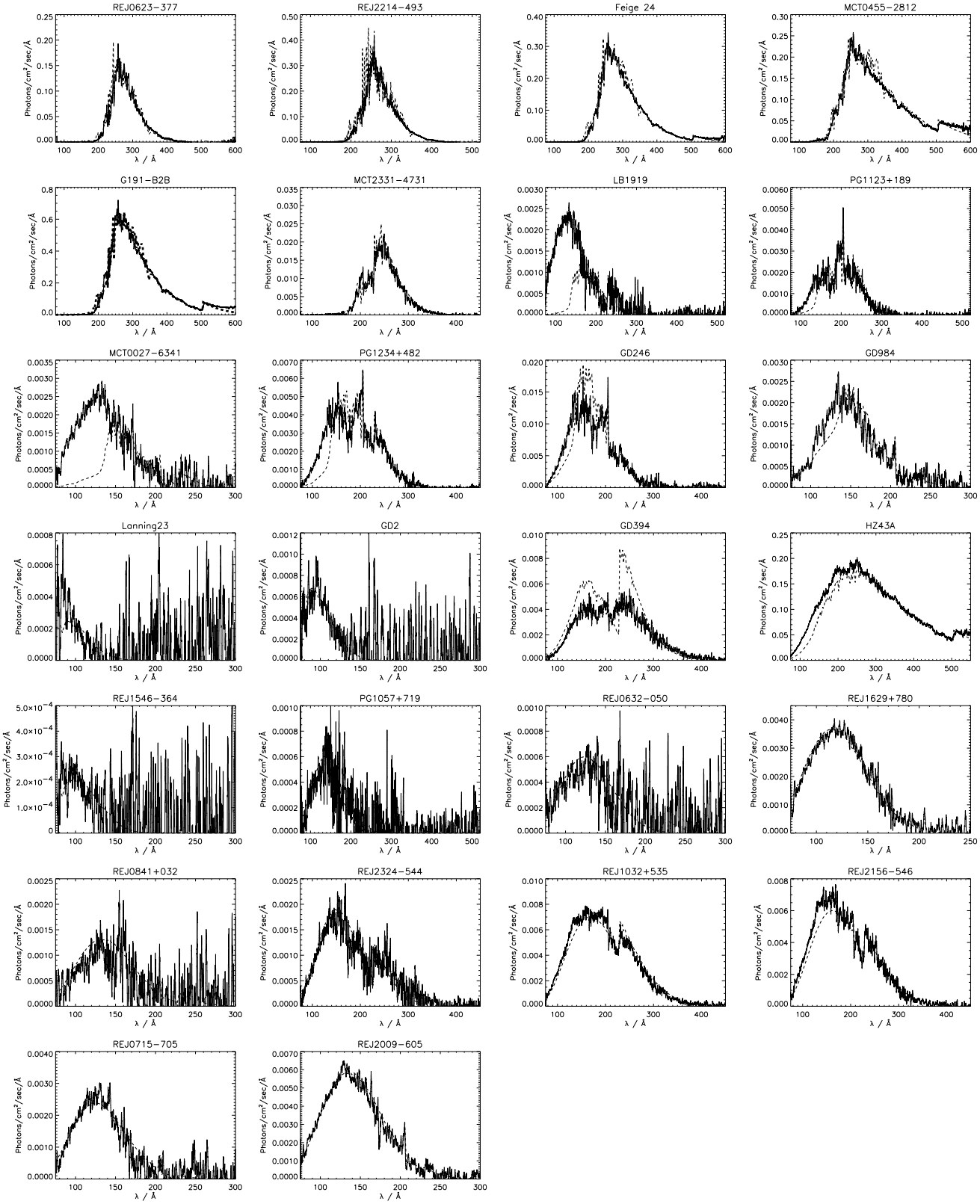

Figure 5.3: EUVE spectra of the program stars with theoretical spectra overlaid (dashed), ordered by decreasing metal index mi. We only show the spectral range with significant signal. Parameters of the models as well as interstellar column densities for hydrogen and helium can be found in Table 5.1.

all the more surprising how well the metal indices mi at the newly determined parameters match the metallicities m that Wolff (1999) has derived for the objects.

5.5 Discussion

5.5.1 Summary

The new diffusion models can reproduce the observed EUV spectra of the majority of the hot DA white dwarfs in the sample. Since the models predict the chemical composition from the equilibrium between sedimentation and radiative acceleration, the number of free stellar parameters is drastically reduced to the effective temperature and surface gravity only. The good agreement is a strong evidence that the interplay of these two processes defines the chemical composition and stratification. The agreement is, however, not in all cases better than with chemically homogeneous models, which requires a more detailed discussion.

Stars similar to G 191–B2B (the group one from Wolff et al. 1998) can be reproduced significantly better with our self-consistent stratified models. This result is not surprising since the first and successful application of these models to G 191–B2B (Dreizler & Wolff 1999) motivated this work in the first place. Our new models can also reproduce the stars classified as pure hydrogen (group three from Wolff et al. 1998), demonstrating that the vanishing of trace amounts of metals is correctly reproduced. Within this group, however, the surface gravity had to be increased by up to 0.5 dex in order to achieve a good fit (see also Table 5.1, and the discussion in Sect. 5.5.2).

The fits of PG 1123+189, GD 246 and GD 984 are not completely satisfying but deviations are of the same order as compared to fits with homogeneous models. The fits for HZ 43A, RE J1032+535, RE J2156−546 and RE J2009−605 are not quite as good as the ones which could be achieved with spectra derived from the grid of homogeneous models. In four cases (LB 1919, MCT 0027−6341, PG 1234+482, and GD 394), using the new models results in a worse fit than before. These significant individual deviations between models and observation could have physical reasons. As discussed in Sect. 5.3.2, competing processes can disturb the equilibrium between radiative acceleration and gravitational settling. As is evident from the overall good fit of our models, these are unimportant in general but individual exceptions are possible. In the case of LB 1919 for example, an unusually high rotation rate has been suspected (Finley et al. 1997).

5.5.2 Remarks on g and $g_{\rm rad}$

As mentioned above, our surface gravities are in several cases higher than in earlier analyses. Those analyses had evaluated the Balmer line profiles for a determination

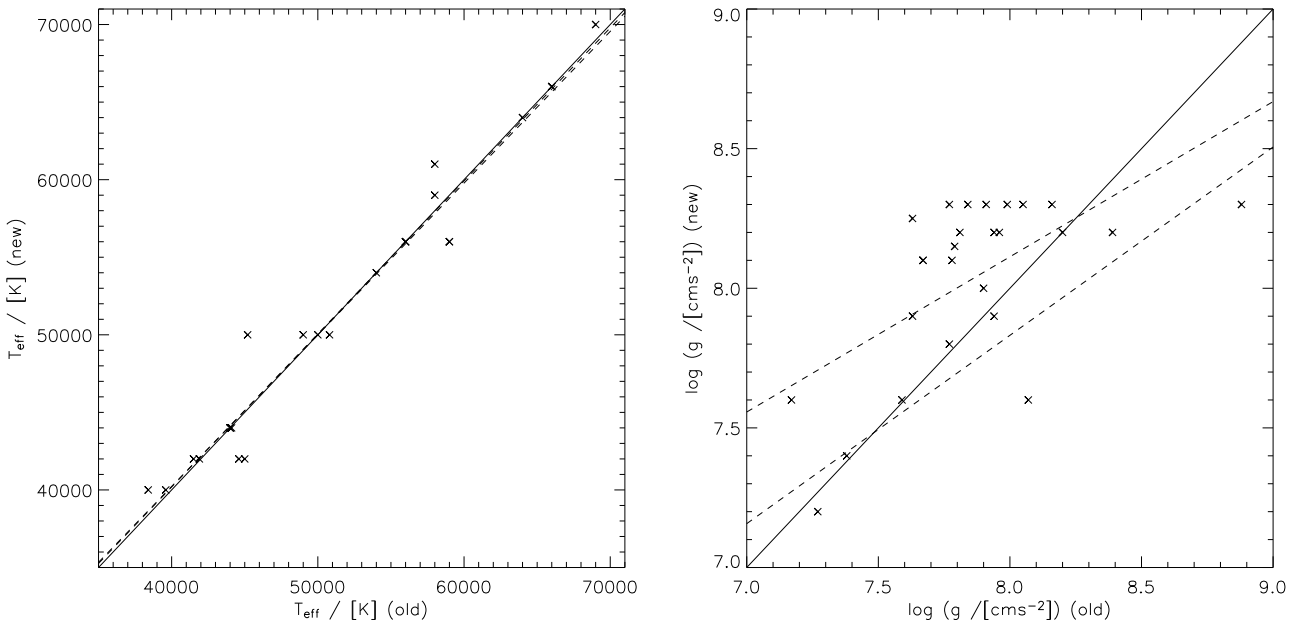

Figure 5.4: Comparison of old and new effective temperatures and surface gravities: Wolff et al. (1998) values versus those from this work as crosses in a $T_{\rm eff}$,$T_{\rm eff}$ and a $\log g$,$\log g$ diagram. The solid lines are the identity, dotted lines are linear least-squares fits to new as a function of old, and old as a function of new, values.

of the surface gravity. The analysis of optical spectra with our new stratified models would allow one to search for systematic effects in comparison to analyses with chemically homogeneous models. For now, we show the mostly reasonable correlation between the effective temperatures by Wolff et al. (1998) and ours, and the less consistent relation for the surface gravities taken from Finley et al. (1997) and ours, in Fig.5.4. In Fig.5.5, the agreement, on average, between metallicity and metal index mi pointed out earlier is visualised. The surface gravities in our work appear indeed biased towards higher values.

The uncertainties in the knowledge of fundamental atmospheric parameters are larger, however, than individual studies may suggest. Even for a well-studied standard star such as G 191–B2B, the ensemble of recent determinations of $T_{\rm eff}$ and $\log g$ implies a surprisingly large scatter, as demonstrated in Fig.5.6. Here, the EUVE observations result in a good mean positioning of the object within other measurements. Yet the overall scatter is not noticeably smaller than what must be noted for the bulk of sample objects in Fig. 5.4.

Another independent result might be worth considering in this context: Detailed parallax and gravitational redshift measurements with HST of the binary system Feige 24 (Benedict et al. 2000; Vennes et al. 2000) also yielded a higher surface gravity for the WD component than several optical analyses ($\log g = 7.2$–7.5). The con-

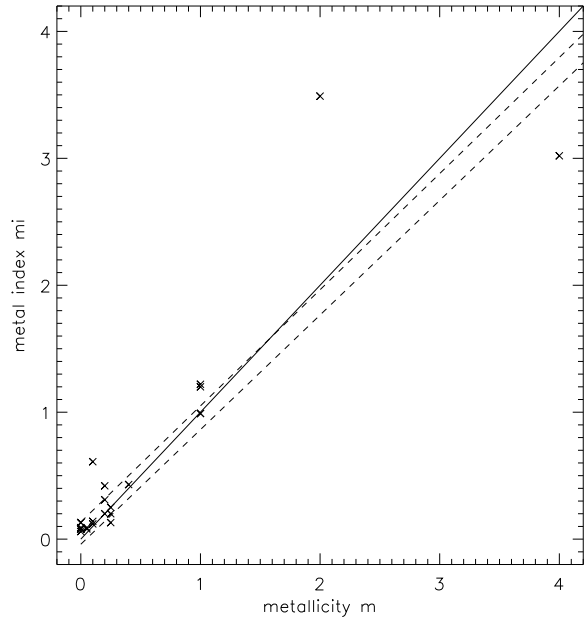

Figure 5.5: Comparison of different measures of the metal content: Wolff et al.'s (1998) metallicity versus the metal index mi, line styles have the same meaning as in Fig. 5.4.

sistency of our result ($\log g = 7.7$) with Vennes et al.'s ($\log g = 7.5$–7.7) might be interpreted as a hint that our current results, while they may certainly be subject to some inaccuracies, do not as a general rule suffer from exceedingly high $g_{\rm rad}$ values in the models that enforce the usage of higher $\log g$; part of the absolute deviation may as well be due to specific problems in other studies.

Should the surface gravities determined with our models prove to be reliable, they would open up a new possibility: The surface gravity governs the gravitational settling. Through the equilibrium condition, the amount of trace metals in the atmosphere is determined. In effect, we therefore evaluate the metal abundances in order to derive the surface gravity. Our proposed method would be a very sensitive indicator but it is, unfortunately, also sensitive to systematic errors in the calculation of the radiative acceleration. The shifts in $\log g$ necessary to obtain good fits for several of the objects consequently could indicate that the accuracy of the $g_{\rm rad}$ calculation needs to be further improved. New test models therefore aim at determining radiative accelerations with higher precision (see Sects. 3.4, 4.3).

Since the accuracy of the calculation of the radiative acceleration is a crucial issue, several possible improvements not yet implemented into our models can be considered that may help to resolve remaining discrepancies. Tests including more, and more detailed, model atoms have been presented earlier. The fine structure splitting of lines was considered for Fe and Ni in the Kiel atomic data, and is also considered

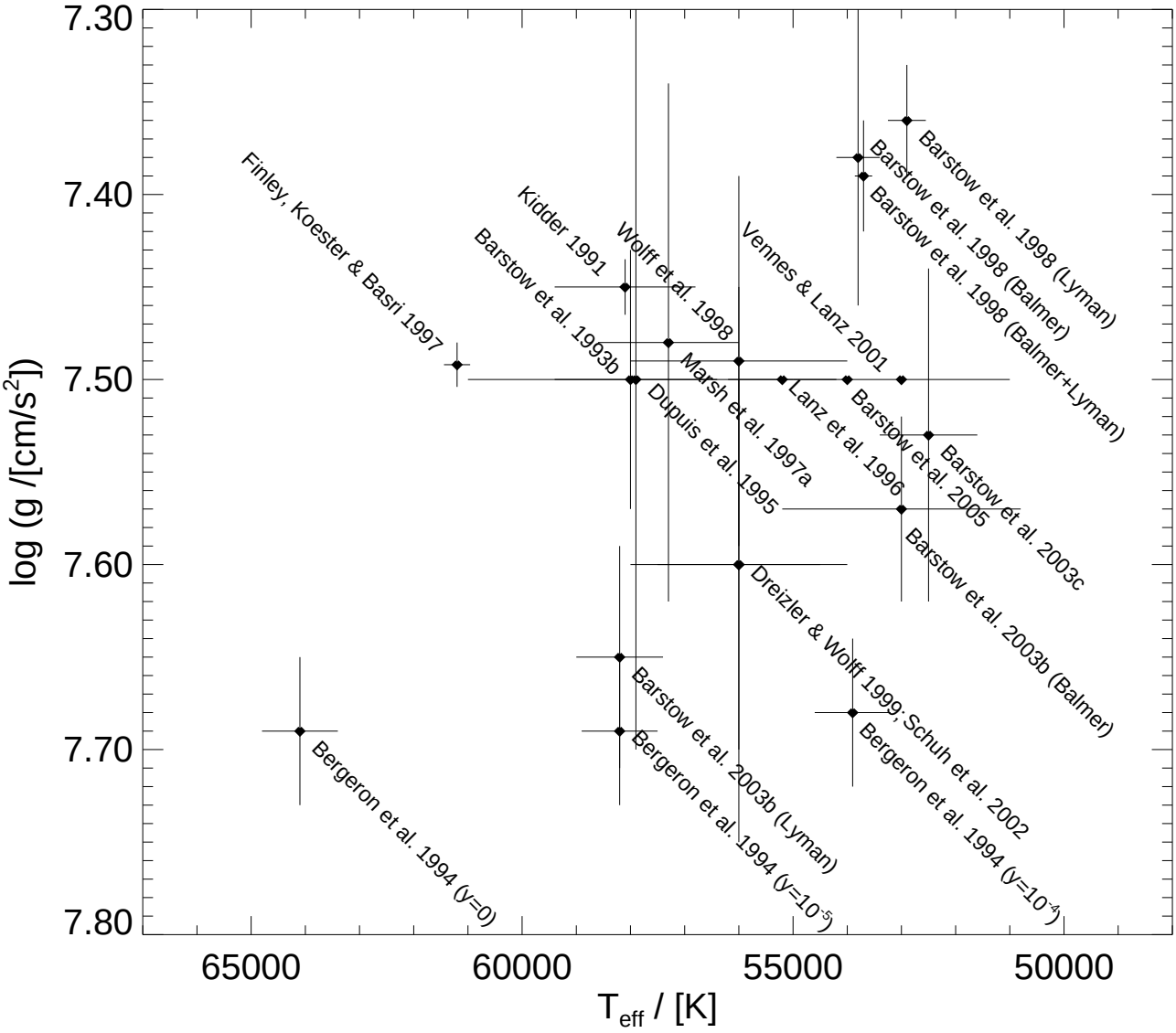

Figure 5.6: Parameters for G 191–B2B from different studies; only references from 1991 on have been considered. References with parameters adopted from one of the above analyses were not included. In the annotations added to some of the quotes, the abbreviations ”Balmer” and ”Lyman” mean that the parameters have been derived using the hydrogen Balmer or Lyman line series, while the mentioning of y values for Bergeron et al. (1994) parameters refers to different He contents of the models explored in that paper.

in all data prepared with `IrOnIc` according to the Kurucz data. The inclusion of fine structure (as suggested by Chayer et al., who also tested the effect for Fe and Ni) adds further opacity and usually leads to higher equilibrium abundances. The fine structure splitting has not been taken into account (except for appropriate weighting) for CNO elements and Si.

The momentum redistribution according to Montmerle & Michaud (1976) is also still missing.

5.5.3 Outlook

We have presented our chemically stratified model atmospheres describing the chemical composition through the equilibrium between gravitational settling and radiative acceleration self-consistently. The application to 26 EUVE spectra of hot DA white dwarfs has revealed an overall good agreement, demonstrating the potential of these new models.

In Chapter 6, we will discuss the derived parameters for individual objects in the context of an analysis of the metal lines observable in UV spectra. This will also be an important test for the consistency of atmospheric parameters derived from different parts of the spectrum, which often poses a problem. While analyses with chemically homogeneous models may be biased due to systematic errors introduced through the neglect of stratification, the parameters presented here may be subject to systematic errors due to the fixed photospheric abundances and might also not stand on exceptionally firm ground yet.

Likewise, the determination of the interstellar column densities has to be regarded as preliminary, since these cannot be determined independently from the theoretical spectra.

CHAPTER 6

Abundance analysis in the UV

6.1 Graphical representation of the results

In this chapter, the abundance values predicted by the diffusion models in a given photospheric layer are compared to results from analyses using established model matching techniques applied to abundance determinations from UV observations. This comparison uses photospheric parameters for a 25-object sample analysed and published by Barstow et al. (2003c) that, with 14 common stars, partly overlaps the EUVE sample in Chapter 5. Effective temperatures, surface gravities, and metal abundances were derived from IUE, HST, and FUSE spectra using a χ^2 fitting technique. For 7 objects only IUE spectra, for 3 objects only HST-GHRS spectra were available, while for the bulk of 14 objects HST-STIS spectra could be used. Both types of HST spectra were in five cases supplemented by IUE data for better spectral coverage. For one object a FUSE spectrum was used (PG 1342+444, based on Barstow et al. 2002). A comprehensive determination of metal abundances from all FUSE spectra obtained for hot DA white dwarfs is work in progress (Barstow et al. 2001b, 2003a; Dupuis et al. 2003).

Barstow et al. (2003c) calculated both pure hydrogen and heavy element blanketed NLTE models, with homogeneous abundances of $\{\mathrm{He},\ \mathrm{C},\ \mathrm{N},\ \mathrm{O},\ \mathrm{Si},\ \mathrm{Fe},\ \mathrm{Ni}\}$ fixed at the values measured for G 191–B2B for the blanketed models, to determine $T_{\rm eff}$ and $\log g$ from Balmer line fitting to optical spectra. Theoretical spectra with variable abundances for the purpose of model fitting of the UV spectra were obtained by calculating formal solutions with the modified abundances based on the existing model structures for one element at a time (using the element list above). The $[T_{\rm eff}, \log g]$ parameters from Balmer line fitting were restricted to these values within narrow bounds during the abundance determination from the UV spectra.

In the following, the equilibrium abundances predicted by diffusion models at the $T_{\rm eff}$ and $\log g$ parameters given by Barstow et al. (2003c) are compared to their abundances measured by model matching. The first set of figures (6.1 – 6.24, starting on

page 71) shows the results for one object per plot. The x-axis is used to represent the different ions or elements considered, the y-axis shows four abundance types that the following symbols stand for:

Black dots represent the abundances as measured by Barstow et al. (2003c) with error bars in abundances that are the formal fitting errors obtained by these authors. Items where only the error bar without a dot is plotted denote upper limits.

Grey dots are diffusion model predictions at $\tau_{\rm ross} = \frac{2}{3}$ interpolated for $T_{\rm eff}$ and $\log g$ of each object. The error bars for the abundances are obtained by evaluating the maximum abundance variation due to the given uncertainties in $T_{\rm eff}$ and $\log g$ (the latter, as above, are Barstow et al.'s formal fitting errors).

Dark grey diamonds repeat the same exercise for the predictions from diffusion models by Chayer et al. (1995b), but without errors assigned.

Dotted lines visualise the cosmic abundances of the elements considered (according to Wilms et al. 2000) and are therefore obviously the same in all figures.

The objects are sorted by decreasing effective temperature (as in the discussion below, where they are however first split into two groups). The second set of figures (6.29 – 6.42, starting on page 104) compiles the results obtained for all objects on an element-by-element basis. The upper plot on each left-hand page shows all measurements for one element as function of effective temperature, with part of the scatter observed[1] due to the scatter in $\log g$, the lower plot shows the same measurements as a function of surface gravity so that here part of the scatter is due to the scatter in $T_{\rm eff}$; the upper plot on right-hand pages displays the measurements as a function of the metal index mi. The meaning of the symbols is almost identical to what has been described above:

Black dots are the measurements by Barstow et al., with errors bars in $T_{\rm eff}$, $\log g$ and abundances that are their formal fitting errors (errors for the derived quantity mi are obvious). Items without a dot denote upper limits.

Grey dots are the predicted abundances from diffusion models at $\tau_{\rm ross} = \frac{2}{3}$ using the objects' given $T_{\rm eff}$ and $\log g$ values. The $T_{\rm eff}$ or $\log g$ errors are also directly from Barstow et al. here, while the error bars for the abundances are obtained as above by evaluating the abundance variation due to the given uncertainties in $T_{\rm eff}$ and $\log g$ (and similarly for the errors in mi).

Dark grey diamonds still stand for Chayer et al. predictions, without errors assigned.

Dotted lines represent the cosmic abundance of the element in each plot.

[1] "Observed" here refers both to the actual observations as well as to the model abundances.

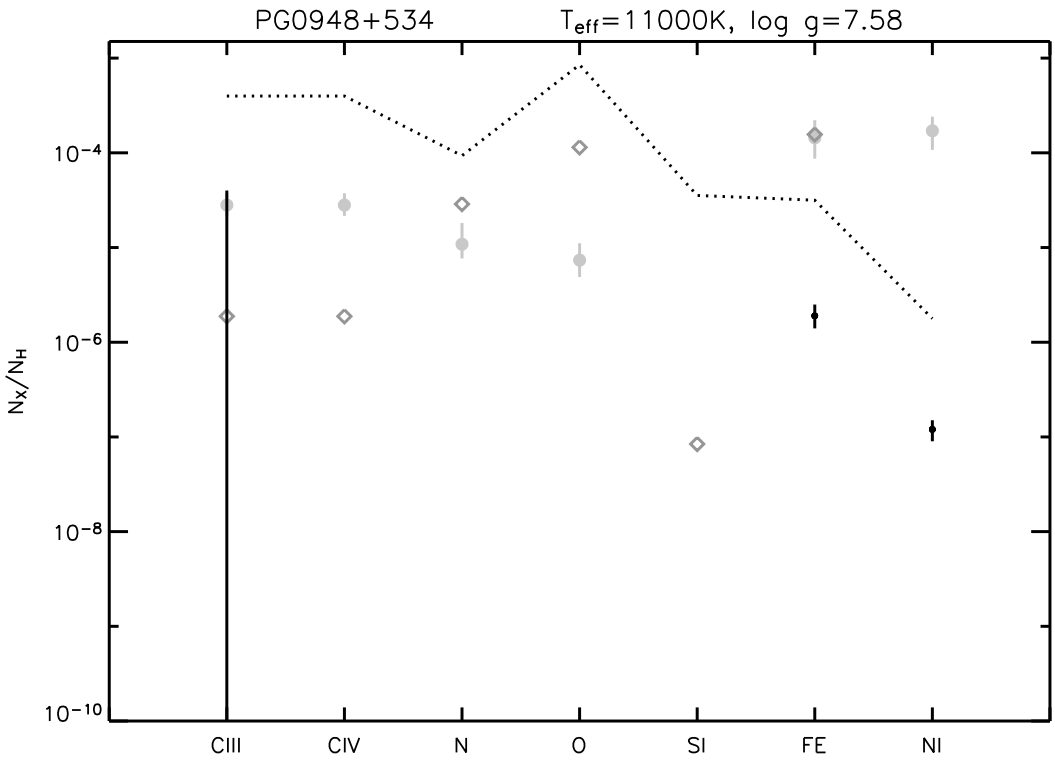

Figure 6.1: Comparison of UV elemental abundances, see text.

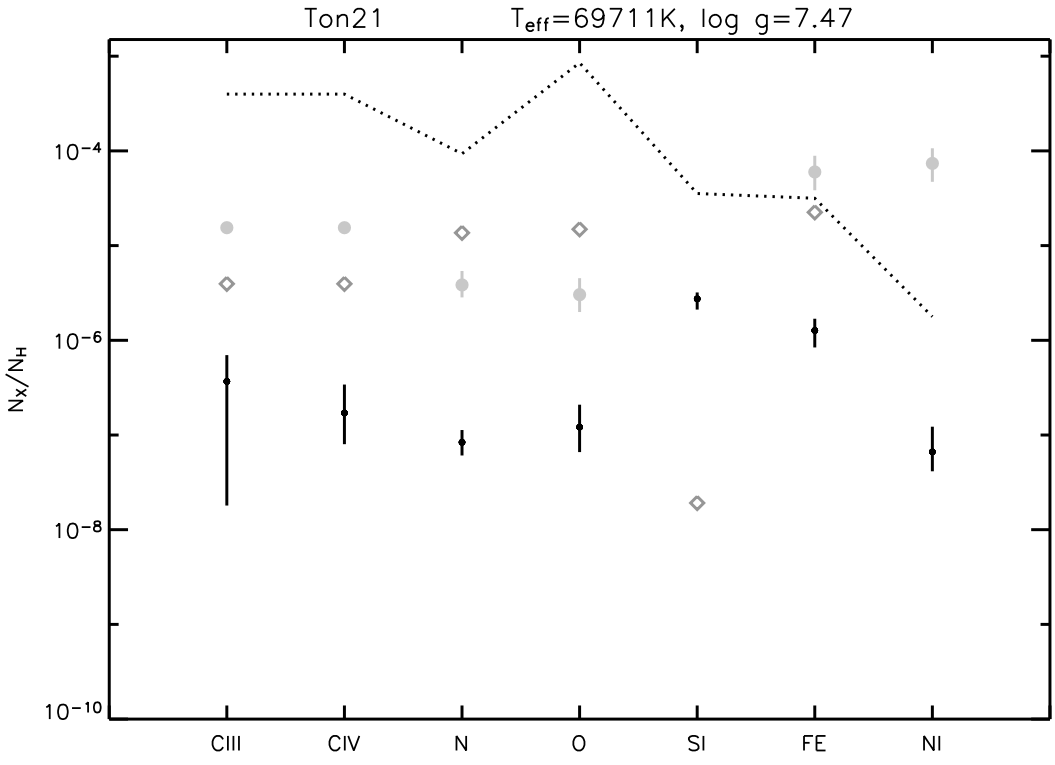

Figure 6.2: Comparison of UV elemental abundances, see text.

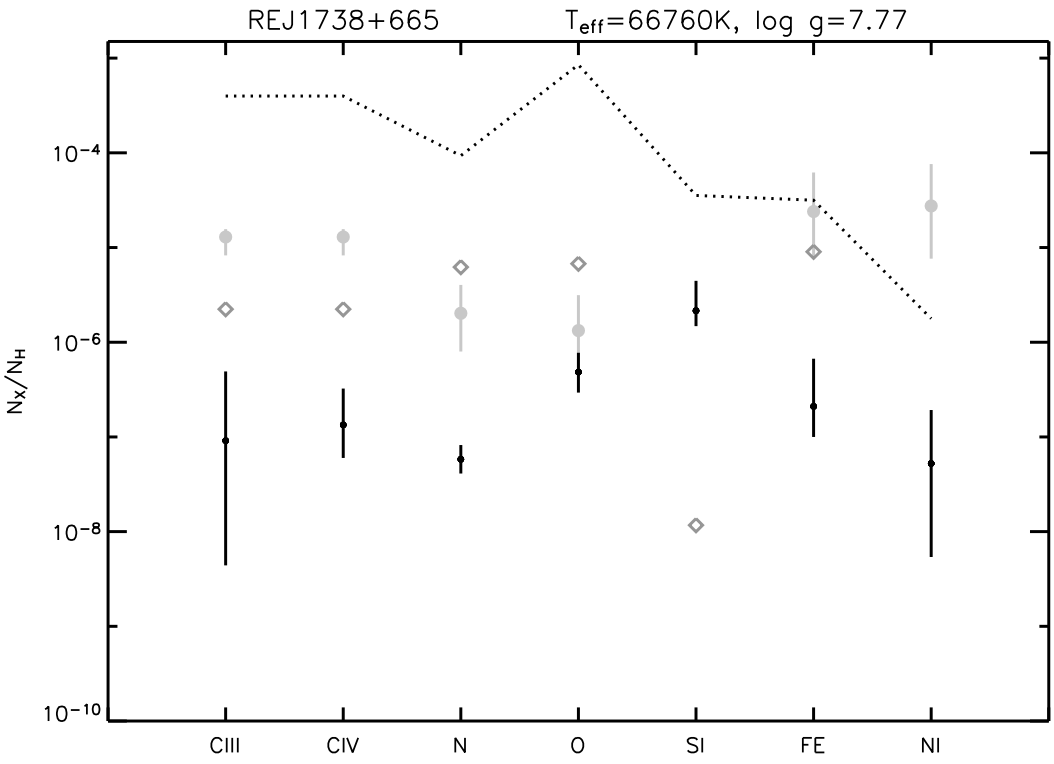

Figure 6.3: Comparison of UV elemental abundances, see text.

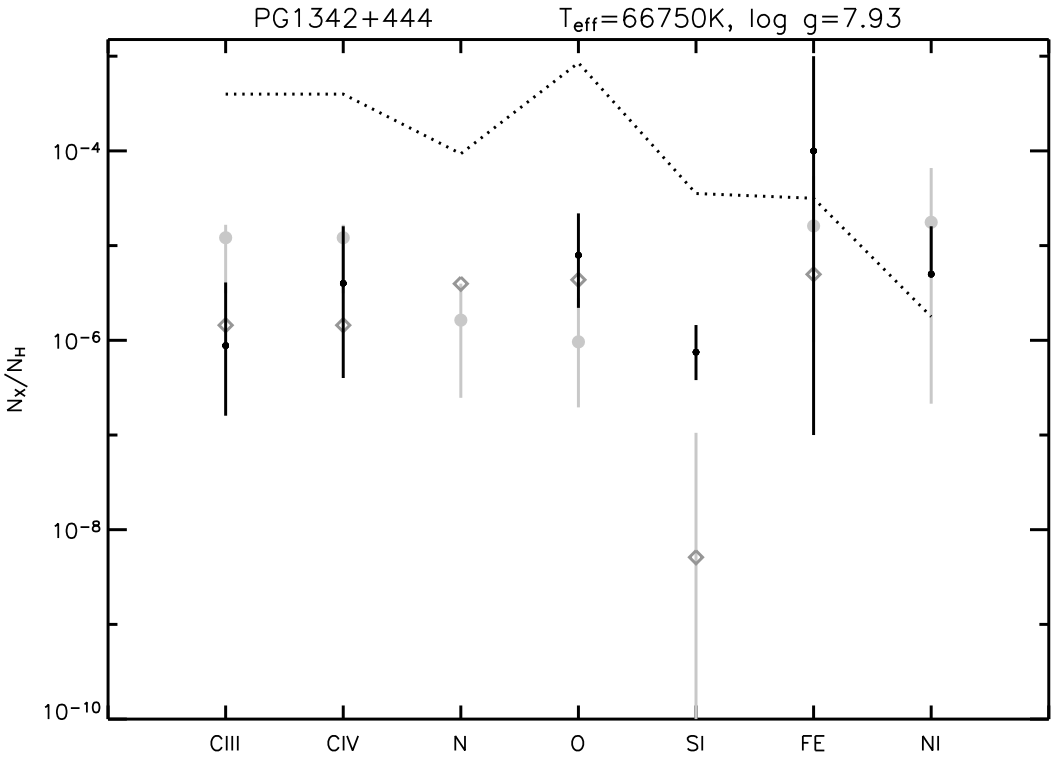

Figure 6.4: Comparison of UV elemental abundances, see text.

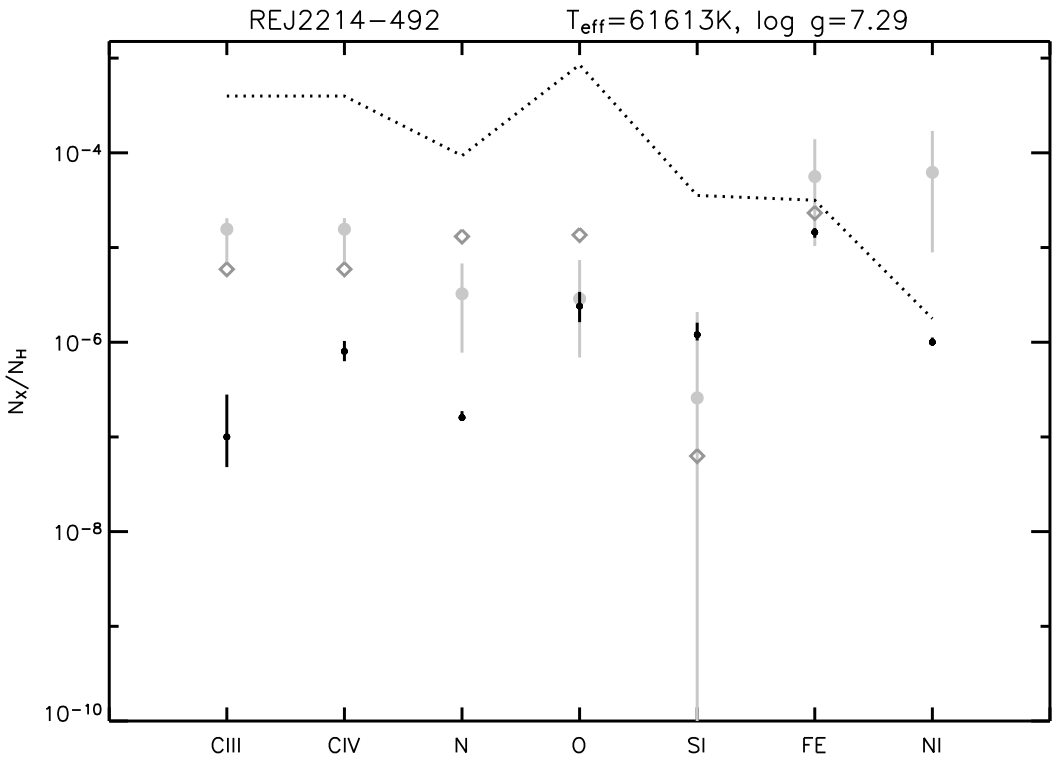

Figure 6.5: Comparison of UV elemental abundances, see text.

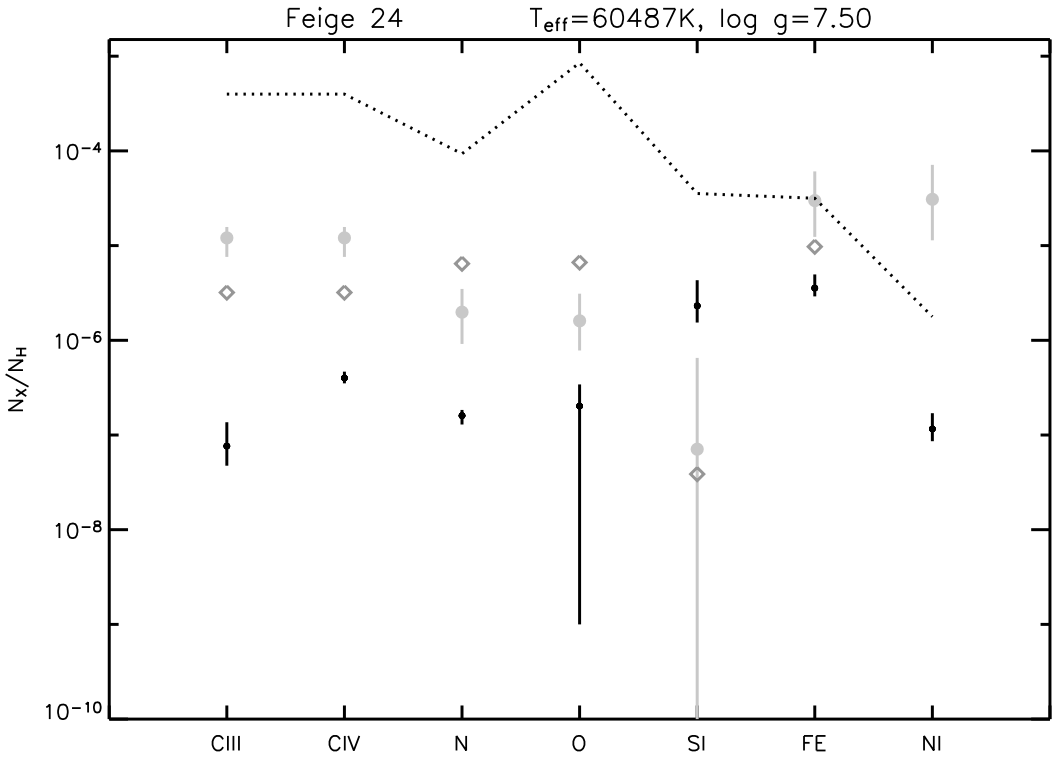

Figure 6.6: Comparison of UV elemental abundances, see text.

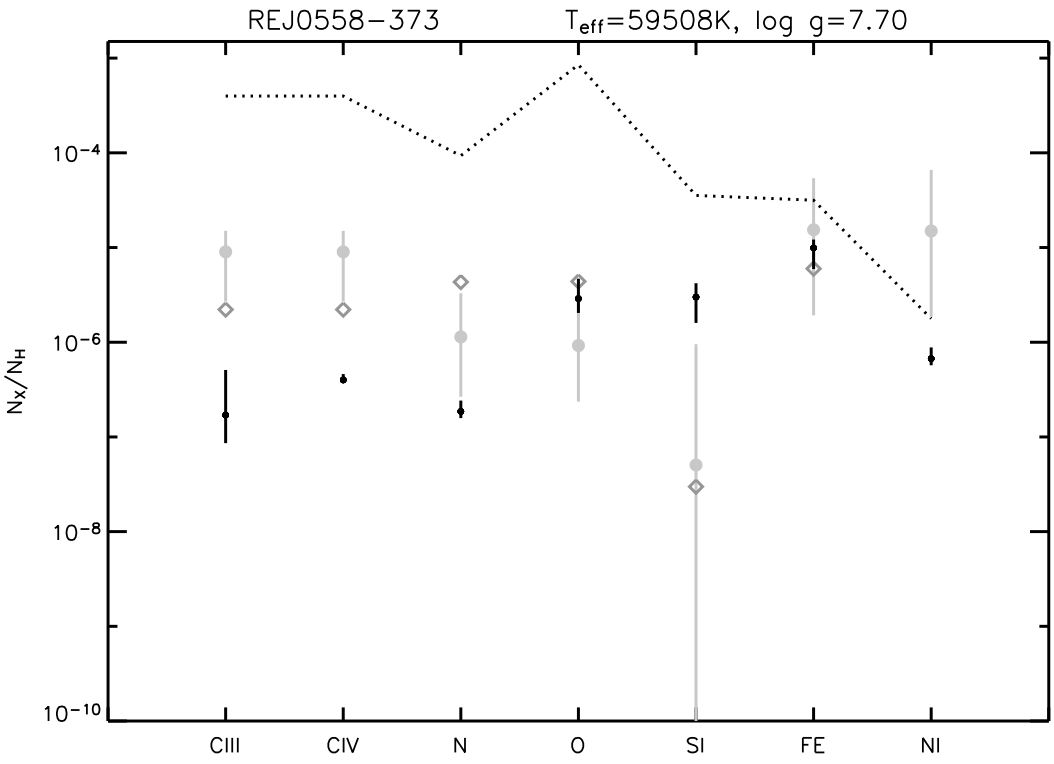

Figure 6.7: Comparison of UV elemental abundances, see text.

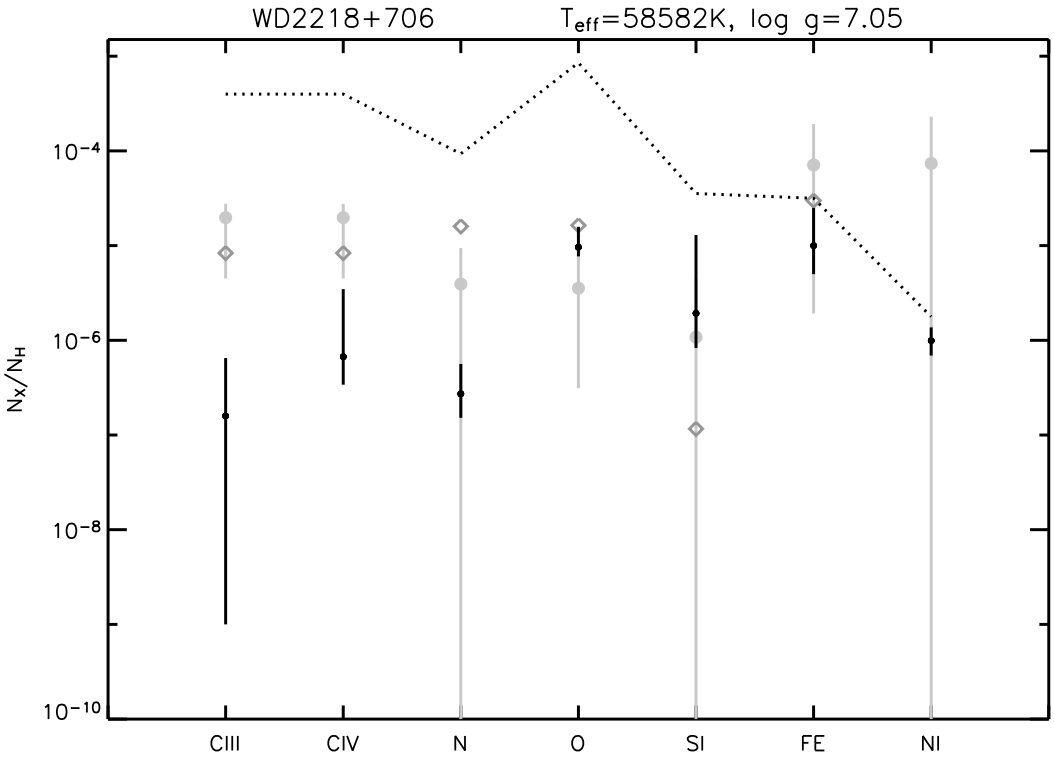

Figure 6.8: Comparison of UV elemental abundances, see text.

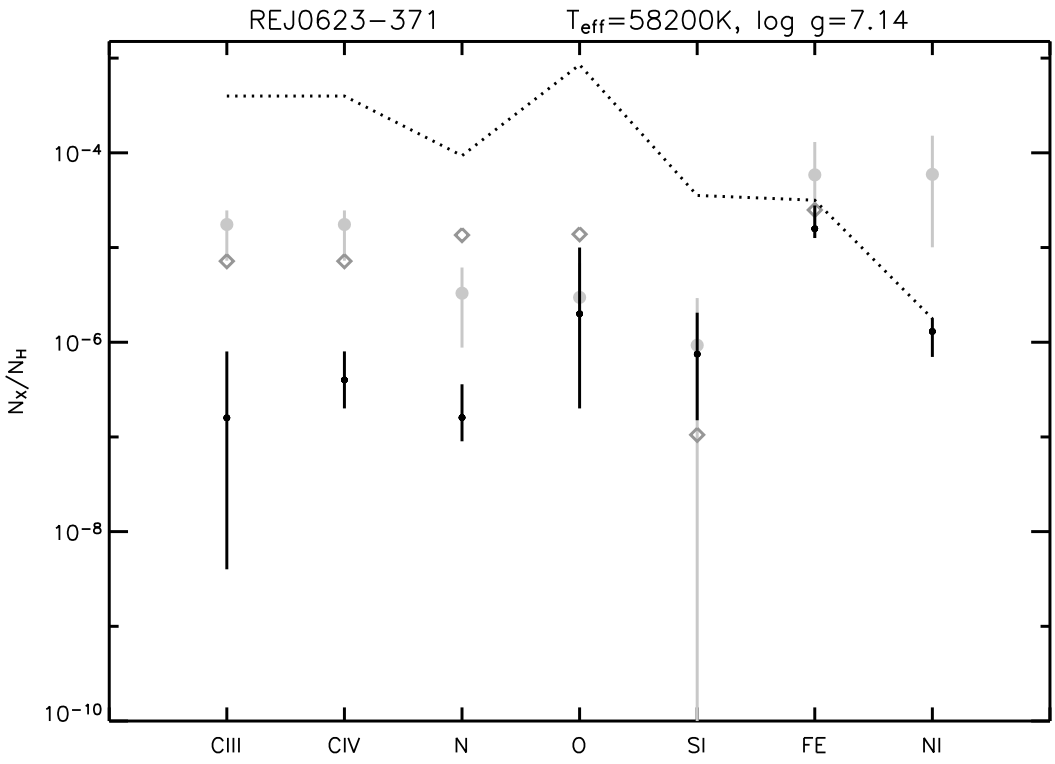

Figure 6.9: Comparison of UV elemental abundances, see text.

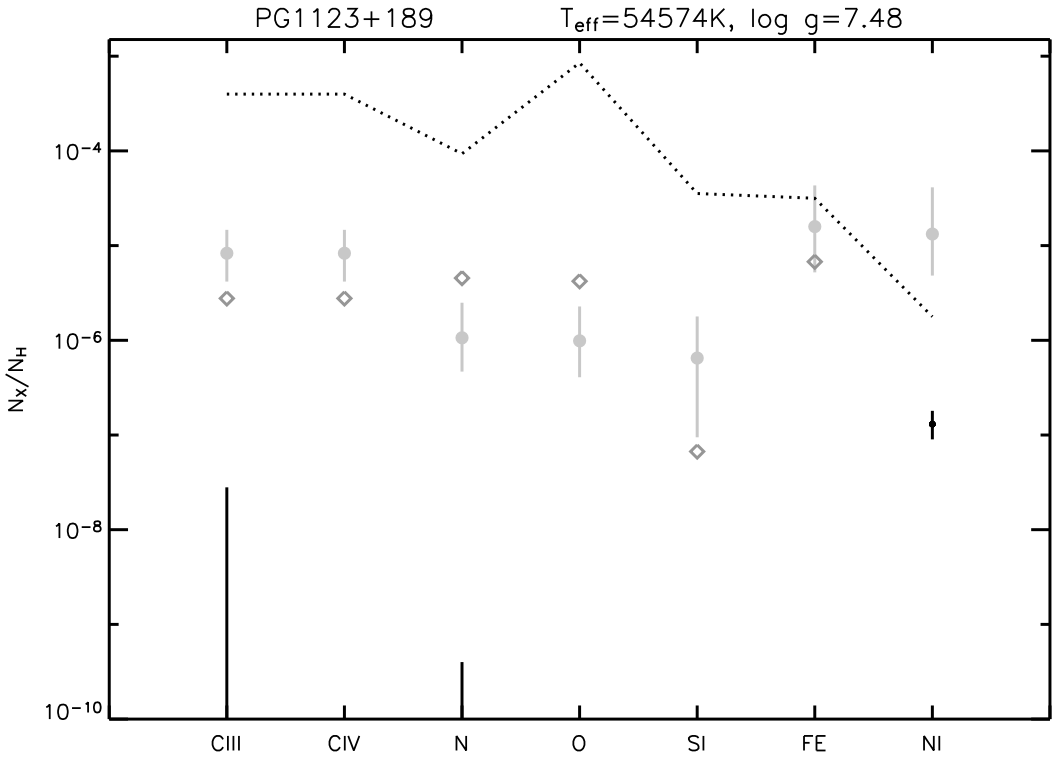

Figure 6.10: Comparison of UV elemental abundances, see text.

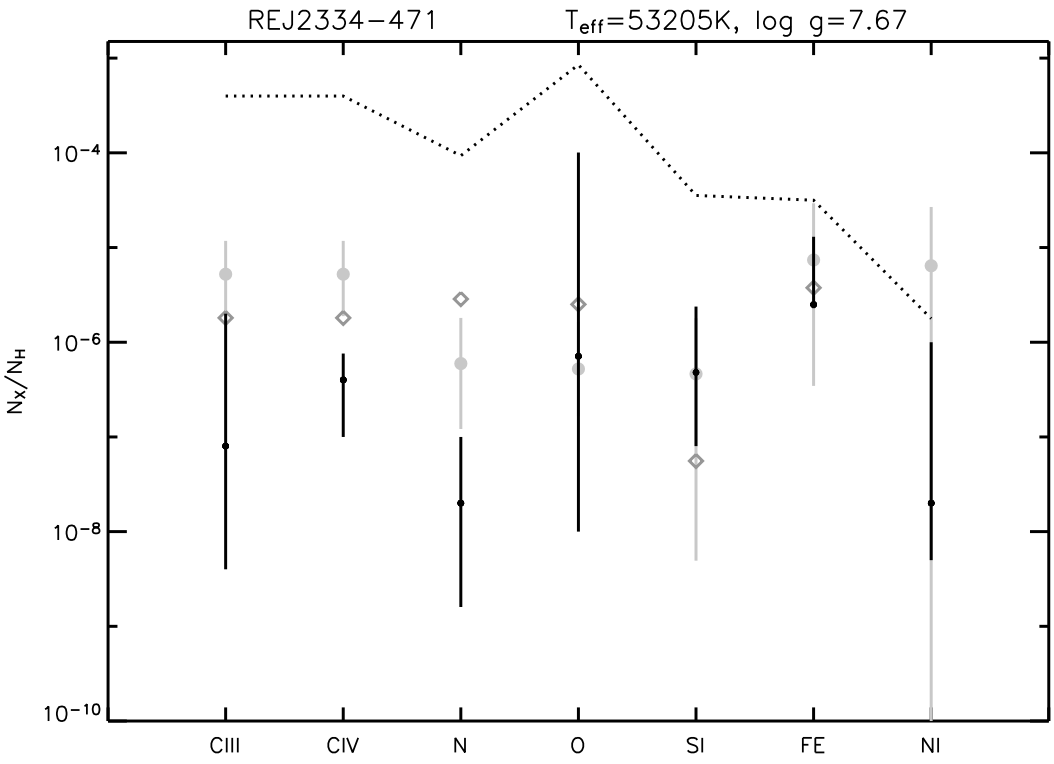

Figure 6.11: Comparison of UV elemental abundances, see text.

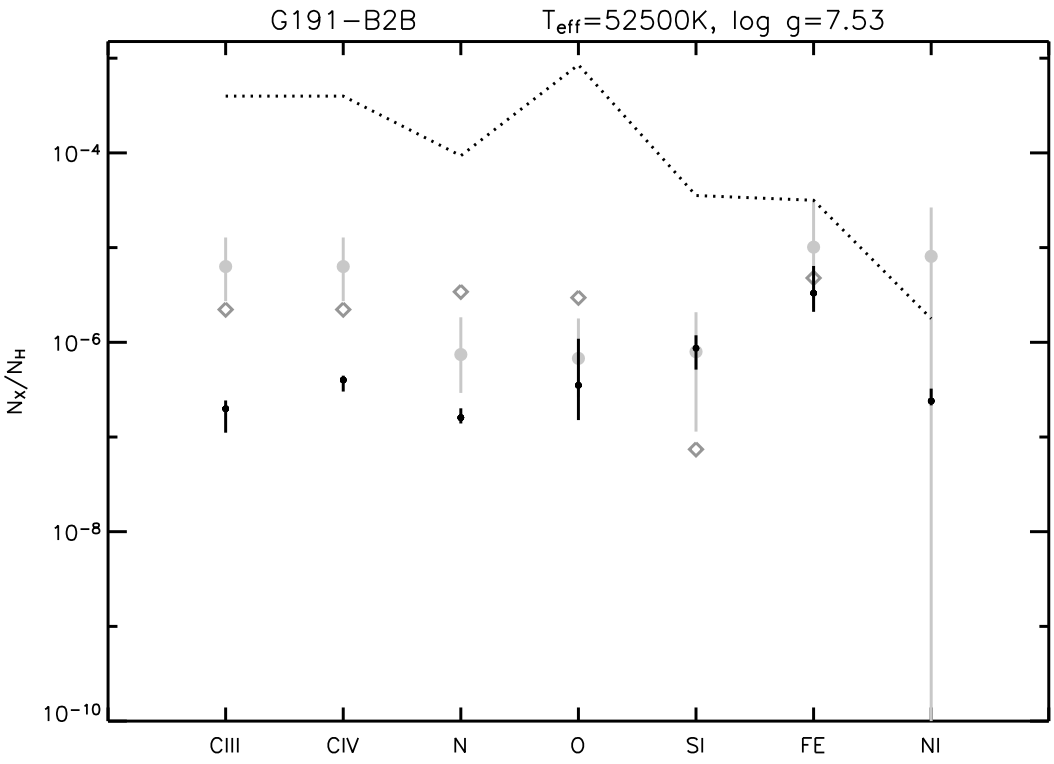

Figure 6.12: Comparison of UV elemental abundances, see text.

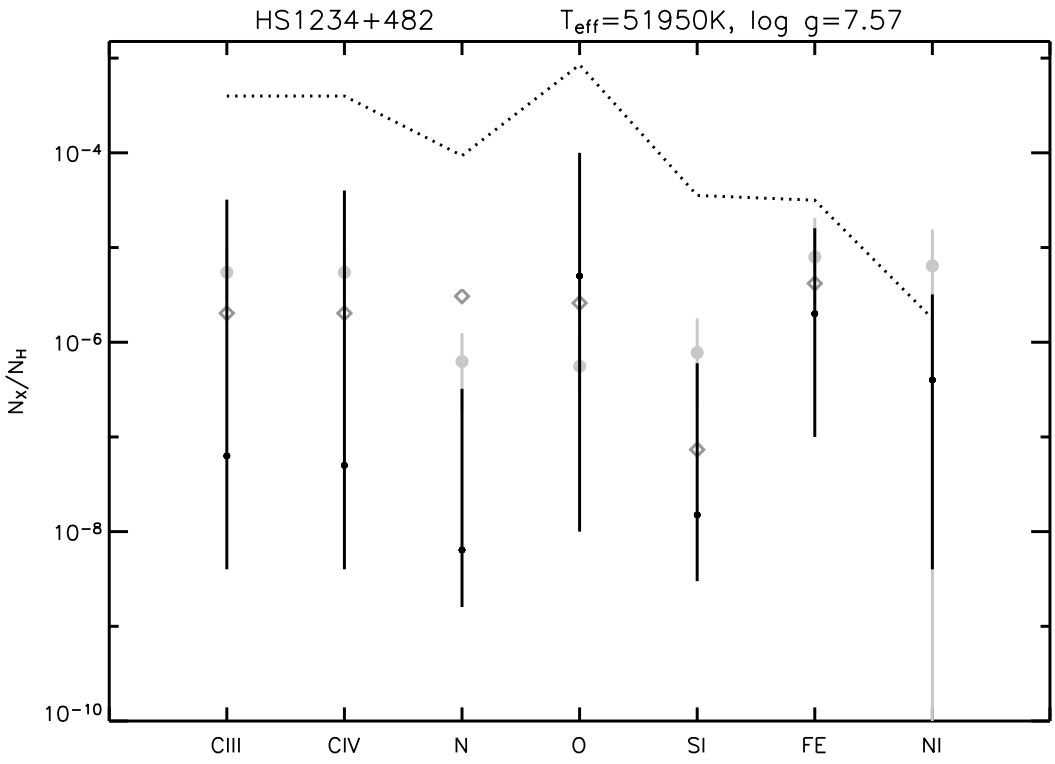

Figure 6.13: Comparison of UV elemental abundances, see text.

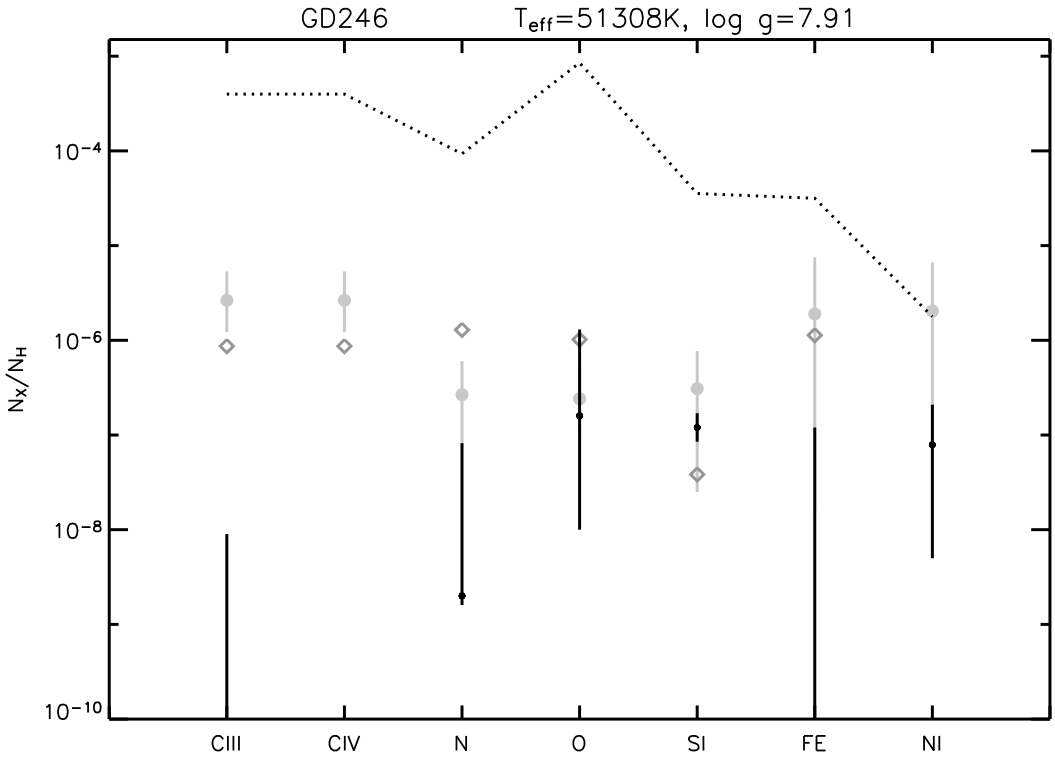

Figure 6.14: Comparison of UV elemental abundances, see text.

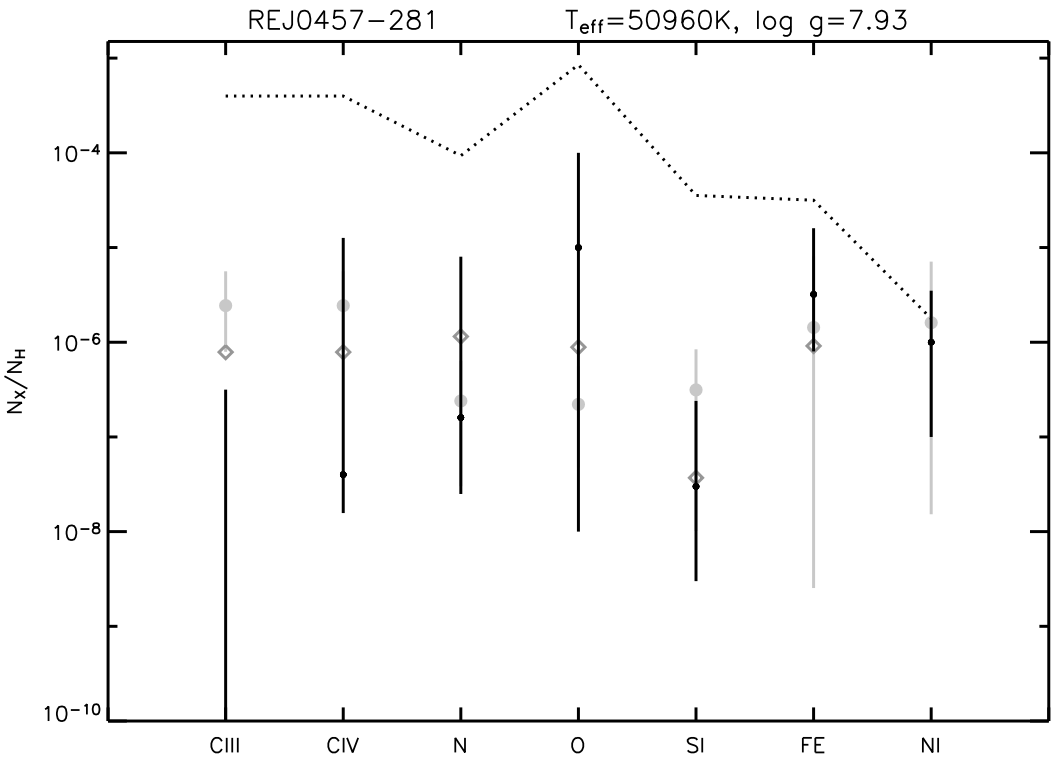

Figure 6.15: Comparison of UV elemental abundances, see text.

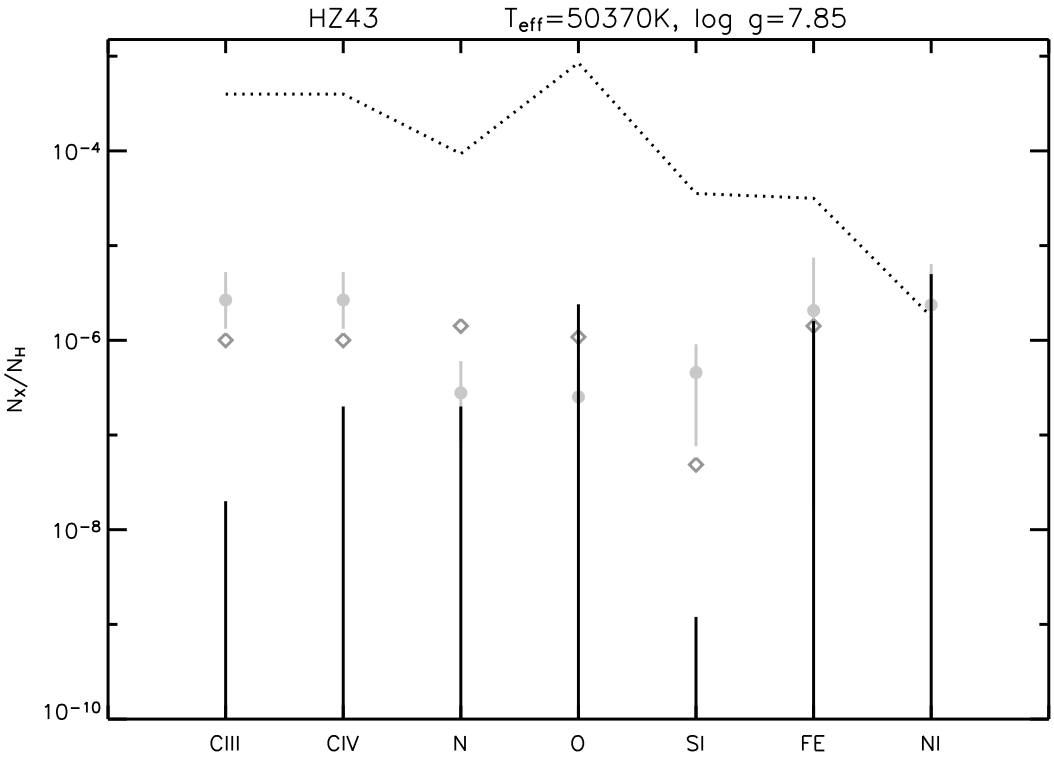

Figure 6.16: Comparison of UV elemental abundances, see text.

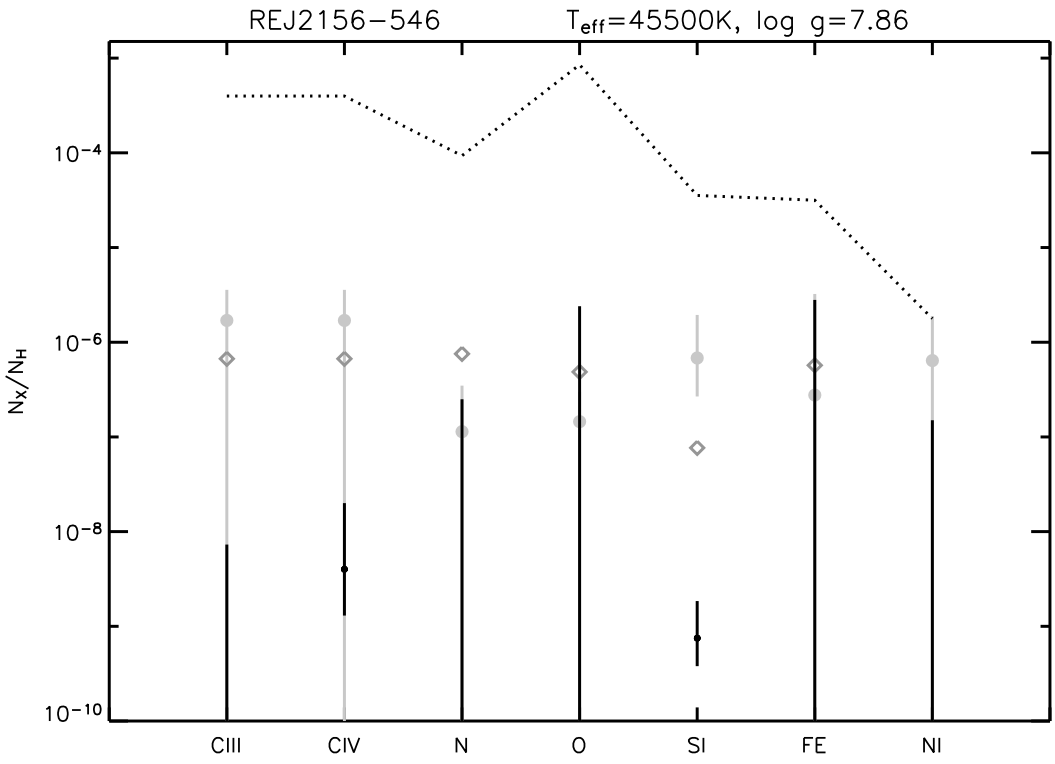

Figure 6.17: Comparison of UV elemental abundances, see text.

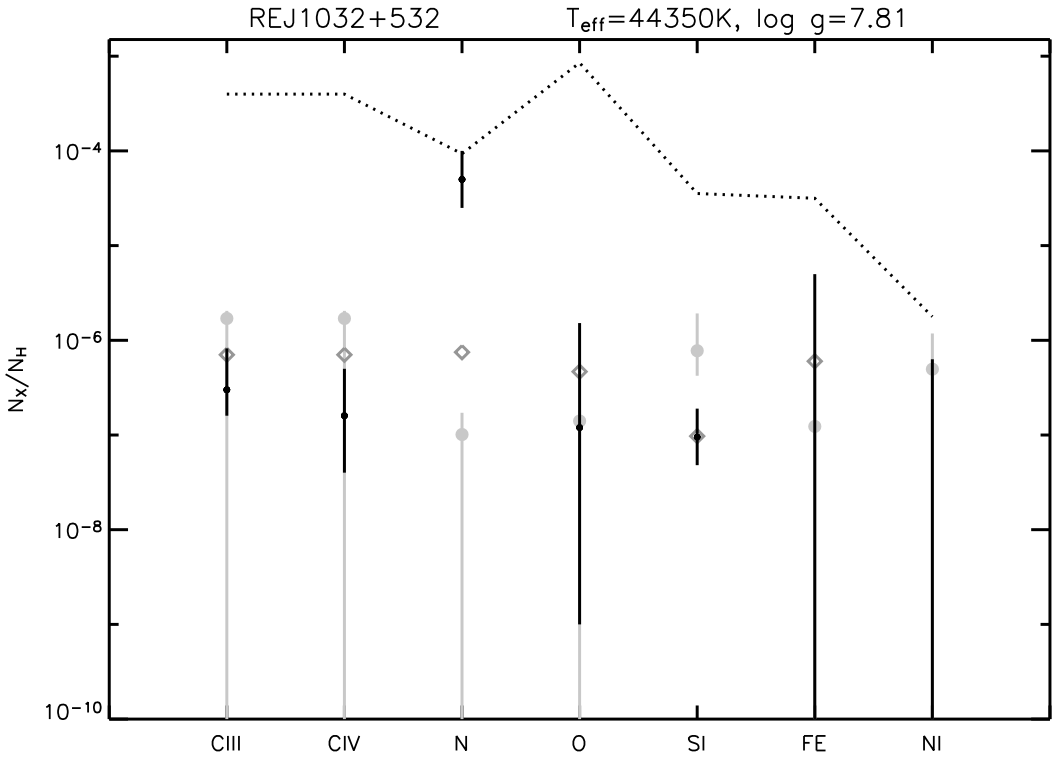

Figure 6.18: Comparison of UV elemental abundances, see text.

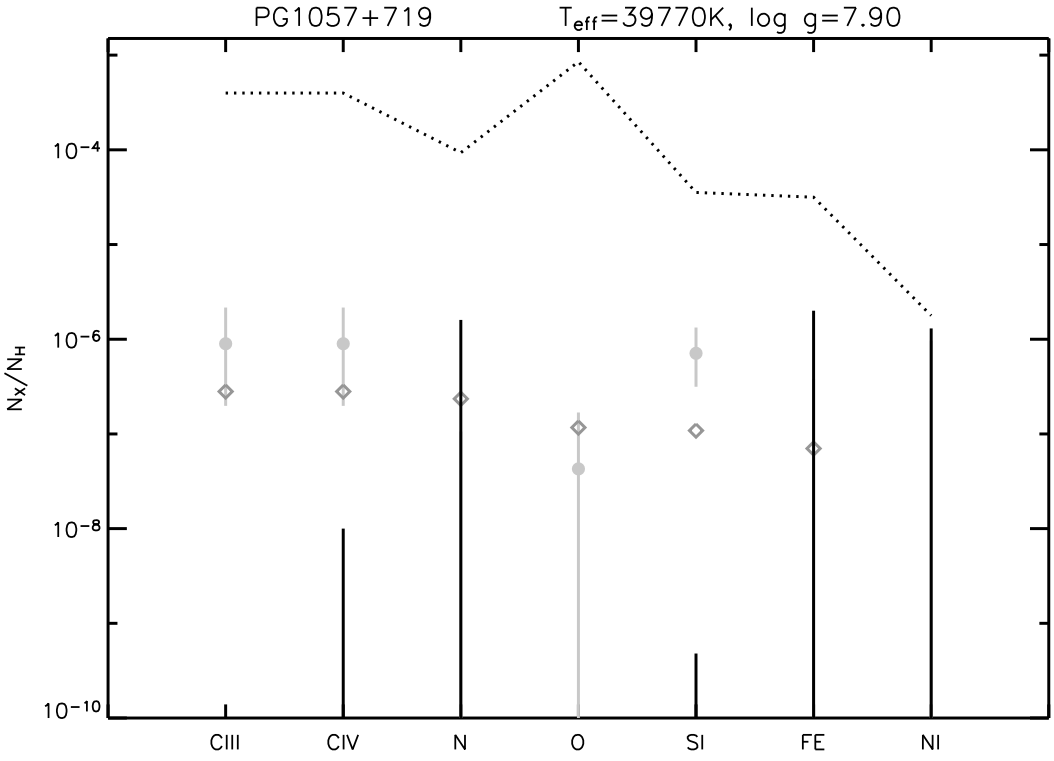

Figure 6.19: Comparison of UV elemental abundances, see text.

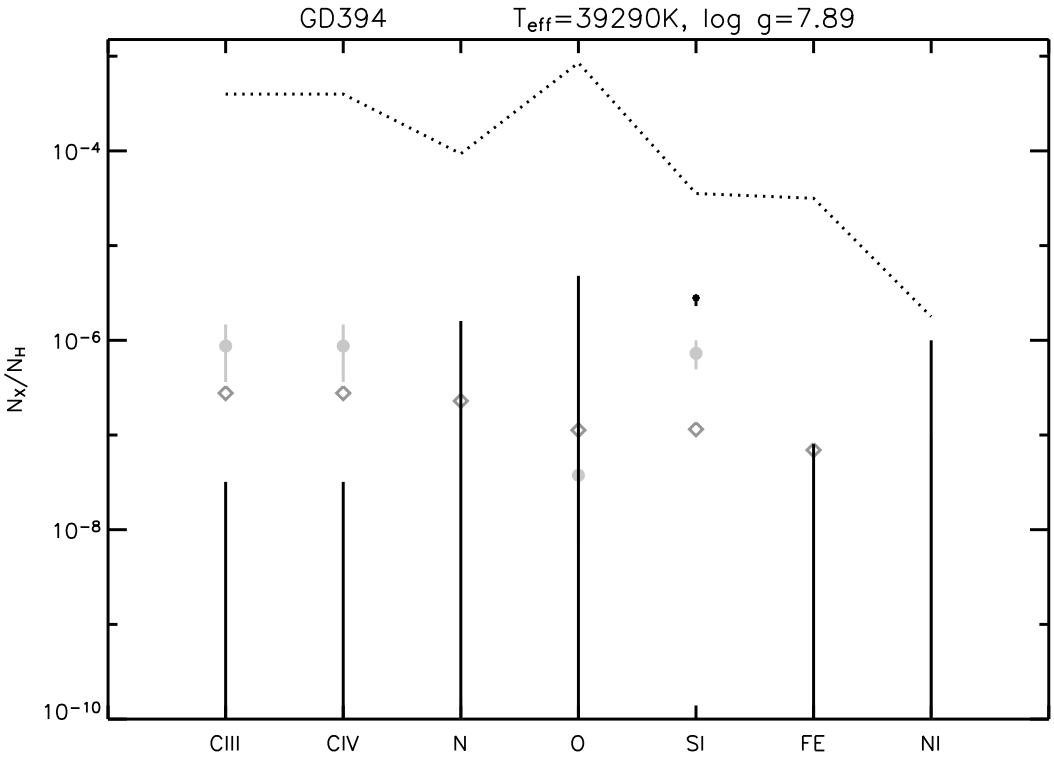

Figure 6.20: Comparison of UV elemental abundances, see text.

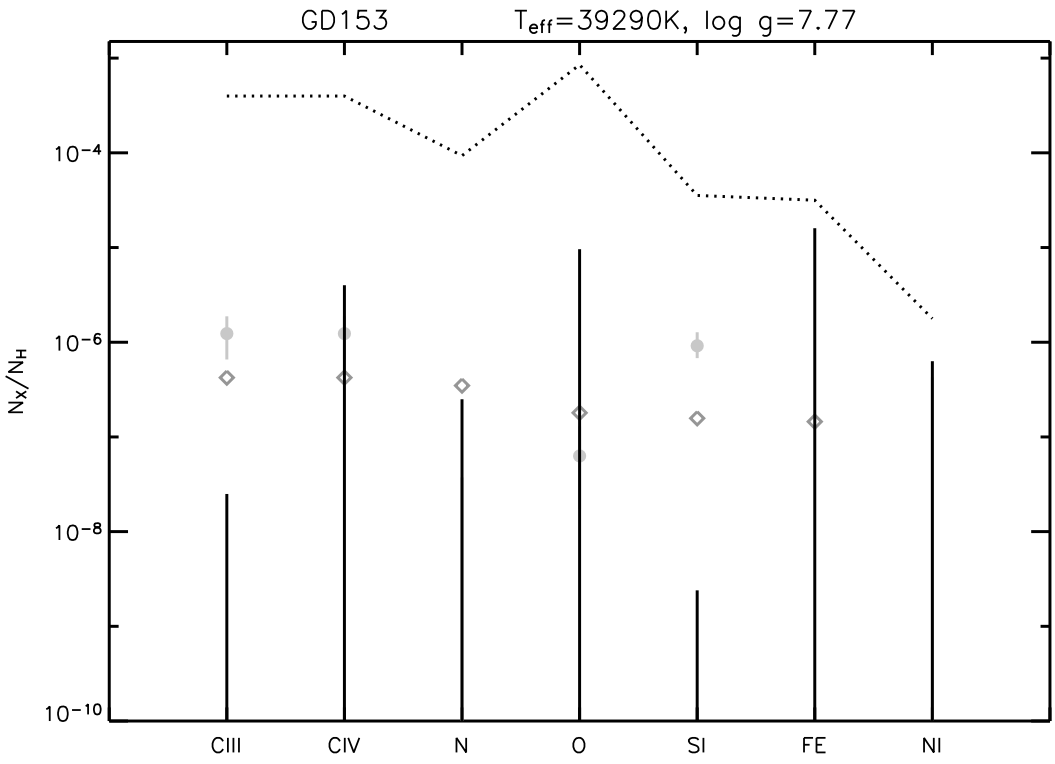

Figure 6.21: Comparison of UV elemental abundances, see text.

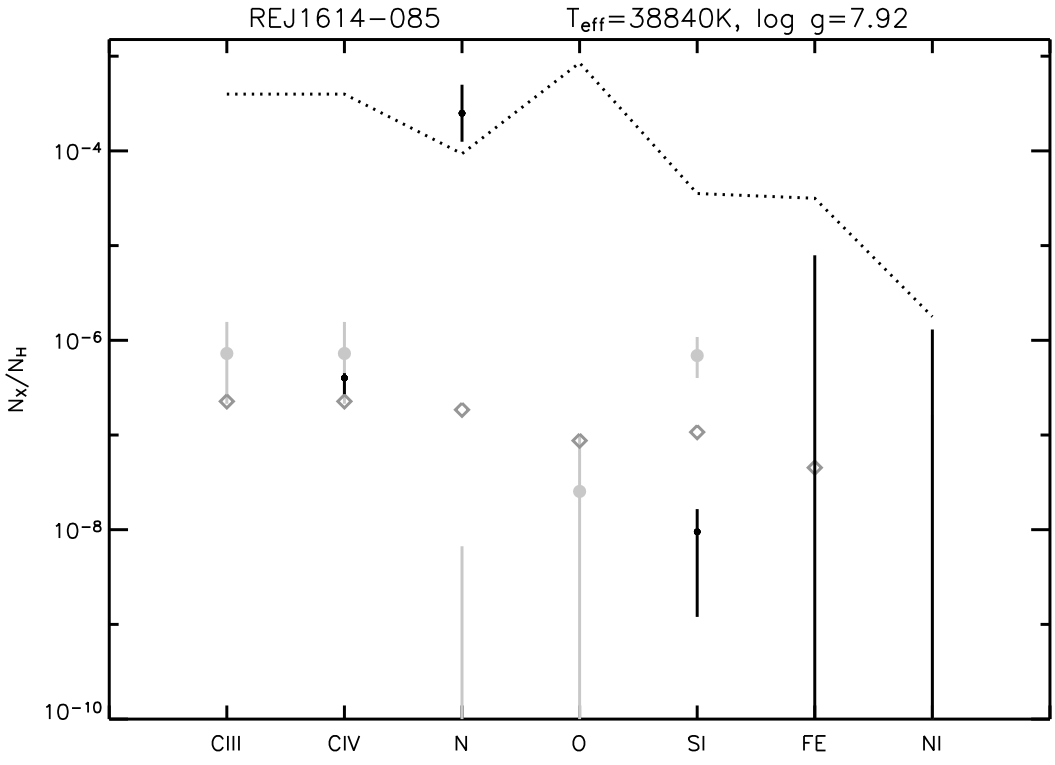

Figure 6.22: Comparison of UV elemental abundances, see text.

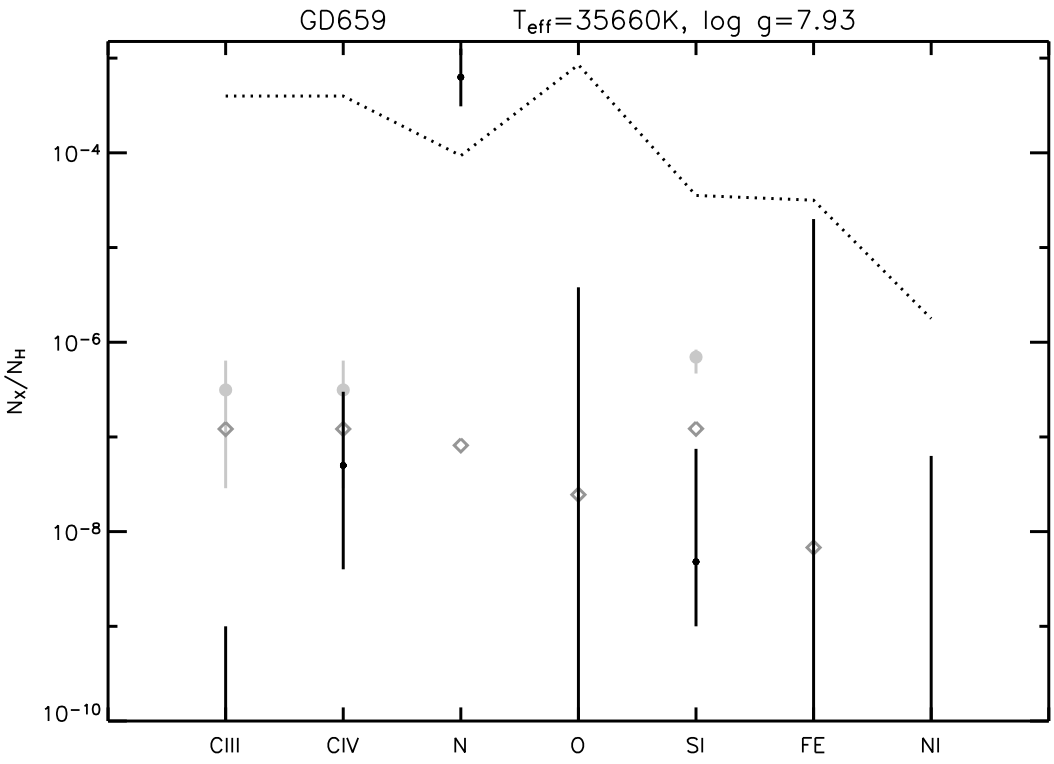

Figure 6.23: Comparison of UV elemental abundances, see text.

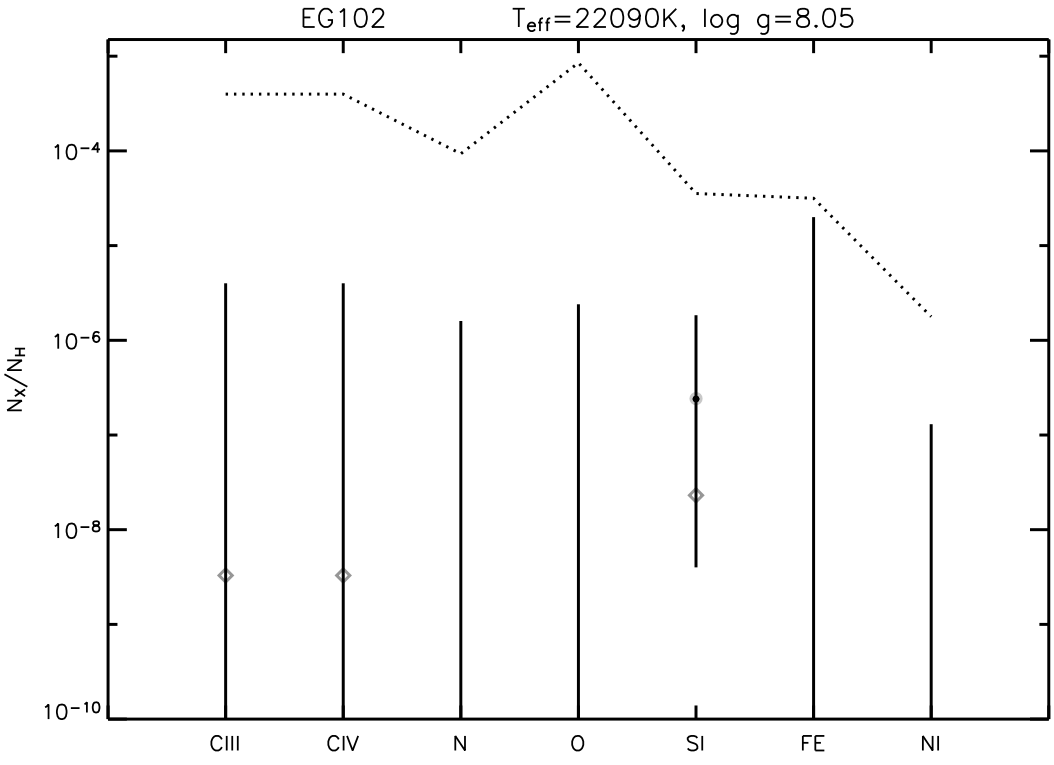

Figure 6.24: Comparison of UV elemental abundances, see text.

6.2 Object-by-object discussion

Prior to going into the discussion of the substantial contents of the object plots, a brief summary of observations and resultant publications relevant to the determination of photospheric abundances is given for each object. In the references compiled for each object, the following types of publications have generally been excluded deliberately: Publications from before 1993 (because no NLTE metal-line blanketed atmospheres were available for analyses before that time: the first such modelling goes back to Dreizler & Werner 1993, Hubeny & Lanz 1995 and Lanz & Hubeny 1995); publications that have already been extensively cited in this or the previous chapter that represent comprehensive studies of the whole sample (see below); publications concerned with the determination of fundamental parameters from Balmer or Lyman lines (optical: Bergeron et al. 1994, Finley et al. 1997, Marsh et al. 1997a; including a comprehensive table of known hot DAs: Napiwotzki 1999[2]; optical analysis of X-ray selected objects: Vennes 1999; comparison optical versus FUV: Barstow et al. 2001c, 2003b); publications concerned with the analysis of the interstellar medium for which the white dwarf only acts as a background light source; usually publications that are not much more than abstracts especially if full-fledged refereed articles with similar contents are available; and publications that predominantly compile or repeat results published elsewhere, as for example in review papers. Those references treating a significant sub-sample of objects are usually not listed under the individual objects again. These exceptions include the bulk analyses of ROSAT pointed observations by Barstow et al. (1993a), Jordan et al. (1994) and Wolff et al. (1996), the IUE survey by Holberg et al. (1998), and the examination of EUVE samples by Dupuis et al. (1995), Barstow et al. (1997), Marsh et al. (1997b), Wolff et al. (1998) and Barstow et al. (1998).

Further references of general interest here are the HIPPARCOS parallaxes available from Vauclair et al. (1997), the disentanglement of photospheric from circumstellar features (Bannister et al. 2003) and of course the comprehensive analysis of heavy element abundances by Barstow et al. (2003c) on which the comparison in this chapter is based.

6.2.1 Objects contained in the EUVE sample

RE J2214−493 After its discovery by ROSAT, RE J2214−493 was observed by the IUE satellite and the spectra obtained were among the first to be analysed with NLTE models treating the line-blanketing effects from iron and nickel lines. Additionally, C, N, O, Si, and Al are detected.

[2]The literature compilation by Napiwotzki (1999) provides a full list of hot DAs down to 30 200 K with a total of 130 objects (of those, less than two thirds lie within this work's model grid limits). Napiwotzki et al. (1999b) furthermore provide a LTE to NLTE corrections map for such analyses.

The Fe abundances determined by Holberg et al. (1993) and Werner & Dreizler (1994) were based on the same model grid and compared well with each other ($\log(\mathrm{Fe/H}) = -4.25 \pm 0.25$). The Ni abundances published by Holberg et al. (1994, TLUSTY models: $\log(\mathrm{Ni/H}) = -5.5$) and Werner & Dreizler (1994, PRO2 models: $\log(\mathrm{Ni/H}) = -4.4 \pm 0.3$), on the other hand, differ by 1 dex. At a value of 0.4 – 5 of the Fe/Ni abundance ratio in the latter case, a clear enrichment compared to the solar value of ≈ 20 is implied that the authors attribute to radiative levitation. Both the value of $\mathrm{Fe/Ni} = 20 \pm 10$ by Holberg et al. (1994) as well as the current results represented in Fig. 6.5 ($\mathrm{Fe/Ni} = 14 \pm 3$ in numbers, differing from the older results by a re-determination of effective temperature and surface gravity from new optical data, and new abundances found on the basis of the IUE final data set – Barstow et al. 1998; Holberg et al. 1998) disagree with this. The issue remains to be settled and is perhaps symptomatic for the remaining uncertainties due to modelling issues, in particular concerned with the accuracy and completeness of atomic data.

Taking the results in Fig. 6.5 at face value, the measured abundances of O in particular, but also, to a lesser extent, of Fe and, just within the error bars, Si, are matched by the predictions. C, N and Ni are over-predicted by various degrees. It is remarkable that the iron and nickel abundance values appear close to what looks like a limit set by the cosmic abundances.

The fit to the EUV spectrum in Chapter 5 is reasonably good and does not require to twist the fundamental parameters found in earlier studies. However, since those earlier parameters imply an effective temperature almost 10% higher than that used in the above comparison, the sole fact that predicted and measured (UV) iron abundances are not too different in this comparison does not immediately signify consistency with the EUV results.

A FUSE spectrum exists, but has so far only been explored for studies of the ISM (e.g. Hébrard et al. 2002).

Feige 24 Besides being a secondary photometric standard star, the Feige 24 system is the prototype of a close binary that has just emerged from a common envelope phase and is likely to evolve into a cataclysmic variable[3]. Fundamental stellar and binary system parameters derived by Vennes & Thorstensen (1994) from optical and IUE data favour a low mass and a helium core for the hot white dwarf, a scenario further refined through modelling and interpretation in

[3]From Vennes & Thorstensen (1994): "Feige 24 is the prototype of a class of young, EUV-emitting, binary systems comprising a late main sequence secondary and a hot H-rich white dwarf; the class is characterized by optical and ultraviolet photospheric He II absorption, circumstellar C IV ($\lambda = 1550$Å) absorption, and by the presence of EUV-induced, phase-dependent Balmer fluorescence. These young systems present the best opportunity to constrain theory of common-envelope evolution."

Vennes et al. (1995), only to be disputed by Benedict et al. (2000) who suggest a carbon core based on HST Fine Guidance Sensor 3 data. This conclusion was also adapted by Vennes et al. (2000) after they obtained revised atmospheric parameters from HST-STIS observations.

The HST-STIS data complement or partly supersede observations, among other, by ROSAT, IUE, EUVE (e.g. Barstow et al. 1994b), and earlier HST instruments. The IUE spectrum was used by Werner & Dreizler (1994) to measure photospheric abundances, the EUVE spectrum was analysed by Dupuis et al. (1995). EUV model spectra were also presented by Lanz & Hubeny (1995). Based on the HST-STIS spectrum first published by Vennes et al. (2000), Vennes & Lanz (2001) give photospheric abundances for C, N, O, Si, S, Fe, and Ni. After removing part of an apparent ionisation imbalance for oxygen by applying NLTE models, Vennes et al. (2000) note a residual ionisation imbalance that they attribute to either faulty atomic data for oxygen or chemical stratification. These considerations, also maintained in Vennes & Lanz (2001), could however not be solved in favour of the stratification hypothesis for Feige 24 so far.

Similar as for RE J2214−493, the abundances now determined tend to lie below the predictions, again with the exception of Si.

A good EUVE fit could be obtained for a surface gravity value higher than previously determined ones, but in return consistent with the results by Vennes & Lanz (2001).

RE J0623−377 Variously known as RE J0623−374, RE J0623−377, or simply RE J0623−37, and systematically called RE J0623−371 in publications by Barstow et al., the object unambiguously identified by its white dwarf number as WD 0621−376 was first discovered by ROSAT (Holberg et al. 1993). The IUE spectrum was analysed by Werner & Dreizler (1994), and is of course included in the studies by Holberg et al. (1998) and Barstow et al. (2003c).

In comparison to results from the latter, the predicted C and N abundances are too high, while O and Si are very well, Fe reasonably well matched. For Ni, the same discrepancy as for RE J2214−493 and Feige 24 is observed: The prediction is at the same level as Fe, the measurement is more than one order of magnitude smaller. This is just barely within the limits suggested by Werner & Dreizler (1994) who found $\mathrm{Fe/Ni} = 0.5-10$ for this object.

The EUVE spectrum is very well reproduced at parameters consistent with those that different studies generally seem to agree on.

A FUSE spectrum exists, but has so far only been explored for studies of the ISM (e.g. Lehner et al. 2002).

PG 1123+189 As an ultraviolet-excess object, ROSAT, IUE and EUVE source, the spectroscopic binary PG 1123+189 is included in the major survey papers and additionally features in Napiwotzki et al.'s (1999a) NLTE optical parameter re-determination.

The EUVE spectrum cannot be fitted well with diffusion models even with an increased surface gravity value. This fits with the picture in Fig. 6.10, based on an otherwise unpublished HST observation with limited spectral coverage: The upper limits for C and N are far below the prediction, the Ni measurement is two orders of magnitude below the prediction.

RE J2334−471 Tentatively classified as a DA already by Hill & Hill (1966), RE J2334−471 or MCT 2331−4731 was observed by ROSAT, EUVE and IUE. An LTE analysis of the FUSE spectrum was presented by Wolff et al. (2001). Their work adds P and S to the list of elements observed in the photosphere of this star, and reports abundance values for Si, P, S and Fe including $\log(\mathrm{Si/H}) = -6.22$ and $\log(\mathrm{Fe/H}) < -5.3$.

Both of these values are consistent with the results here (but obtained assuming different fundamental parameters, see below), which in turn agree with the predictions. Despite large error bars, the agreement is also very good for the best values for O. This is not true to the same degree for C, N and Ni, with the measurement for the latter almost three orders of magnitude smaller than predicted.

At the chosen set of parameters, the EUVE spectrum is well fitted by the model; however, an impressive range of effective temperatures and surface gravities is still being suggested by various authors depending on the particular observation analysed. Values range from 53 000 K to 62 000 K in T_{eff} and 7.6 to 8.1 in $\log g$.

G 191–B2B At a visual magnitude of m_v=11.79, and correspondingly bright blue and UV colours, this spectrophotometric standard star is very well observed and frequently used for calibration purposes, in particular of UV instruments (e.g. HST: Colina & Bohlin 1994; Bohlin et al. 1995; Stone 1996; Bohlin 1996, and HST-STIS in particular: Bohlin 2000; Bohlin et al. 2001). In a review article, Kruk (1998) explains the essential role that reliable spectral modelling of the flux standard plays for the successful calibration of observational instruments.

G 191–B2B has been observed by, or used for the calibration of, HUT Astro 1 (Kimble et al. 1993a; Smith et al. 1996; Kruk et al. 1997), HUT Astro 2 (Kruk et al. 1999), EUVS (Extreme Ultraviolet Spectrograph, Wilkinson et al. 1993), the ORFEUS SPAS I+II missions (Dixon et al. 2002), extreme-ultraviolet rocket spectroscopy experiments such as the Extreme Ultraviolet Opacity Rocket (EOR, Gunderson et al. 2001) and J-PEX (Cruddace et al. 2002), the

X-ray observatory XMM (Chen et al. 2004 suggested G 191–B2B for XMM's wavelength calibration), and large optical telescopes such as Keck or VLT.

The extensive data allow a detailed modelling and parameter determination of this "prototype" hot DA, resulting in knowledge about the object which is in turn required to fulfil the calibration needs. The remaining uncertainties in the modelling as documented in Fig. 5.6 might appear surprising in this context: The host of values for $T_{\rm eff}$ and $\log g$ found from optical (Balmer line series) and Lyman line analyses (see the short compilation at the beginning of this section and Fig. 5.6 for the corresponding references) frame the various values used in or derived from UV and FUV studies. Besides systematic effects attributable to poorly understood effects from one wavelength range to another, and uncontrollable random scatter from one observation to another, the discrepancies amount to a large extent from different approximations in the models. The usage of NLTE versus LTE models, the inclusion of He and/or metals and their exact composition, and the degree to which the imperative of self-consistency is observed all play a role. The efforts to explain the spectral energy distribution of G 191–B2B in particular reflect the overall increasing complexity of the atmosphere models utilised to understand the composition and physics in any hot DA atmosphere. New concepts were often first tested on this star, due to stronger constraints from new observations, numerously obtained for this target:

Barstow et al. (1993a,b) were unable to obtain an acceptable fit to ROSAT data with H models. The first NLTE line-blanketed models with Fe were presented by Dreizler & Werner (1993) for comparison with EUV and IUE data, and subsequently used in studies by Holberg et al. (1994) and Werner & Dreizler (1994) who determined Fe and Ni abundances from the IUE spectrum. Similarly sophisticated model atmospheres were then computed by Lanz & Hubeny (1995), and used in Lanz et al. (1996) to create a model specifically for G 191–B2B that resulted in the determination of a lower effective temperature, and heavy element abundance measurements (still based on the IUE and additional EUV data). Vidal-Madjar et al. (1994) detected N, Si, and Fe lines in an HST-GHRS spectrum, Vennes et al. (1996a) P and S in an ORFEUS spectrum. Barstow et al. (1994b) presented the first EUVE spectrum that Dupuis et al. (1995) then used to determine a suitable $T_{\rm eff}$ and analyse the ISM along the line of sight towards G 191–B2B. However, the EUVE observation continued to elude successful modelling (Barstow & Hubeny 1998: H+He stratified model including heavy elements) until Barstow et al. (1999) suggested a stratified Fe slab model. The diffusion model by Dreizler & Wolff (1999) delivered the justification for such an approach and correctly predicted the Fe opacity required

to match HST-STIS and EUVE spectra simultaneously.

Recently, Vennes & Lanz (2001) have published a comparison of Feige 24 and G 191–B2B based on HST-STIS spectra, of which Holberg et al. (2002) offer a co-added, high signal-to-noise version. There have been efforts to separate photospheric from circumstellar metal line contributions (Bruhweiler et al. 1999 mention such a component for C; the major works on this topic have been listed in the introduction). FUSE observations (e.g. Lemoine et al. 2002, ISM analysis) await a detailed investigation as announced in Barstow et al. (2003a). A flight of the J-PEX instrument has targeted G 191–B2B, resulting in a new high-resolution spectral observation in the extreme-ultraviolet (Cruddace et al. 2002; Barstow et al. 2005).

As for several other objects assigned to the so-called G 191–B2B-group, the agreement between predicted and measured value for Fe is relatively good; it is excellent for Si and of only slightly lesser quality for O. A decreasing coincidence must be noted for N, C, and Ni in this order, with a large deviation for Ni. Owing to the well-matched Fe profile, the fit to the EUVE spectrum, at an accepted pair of fundamental parameters, is good, as has been previously proven in Dreizler & Wolff (1999).

PG 1234+482 Wolff et al. (1994) and Jordan et al. (1996) reported the detection of Fe in the EUVE spectrum, and Homeier et al. (1998) have provided an independent optical parameter determination. Apart from a measurement of Fe, the new attempt only cites upper limits for other elements, all with large error bars due to the noisy IUE spectrum. The non-detection of most heavy elements roughly fits with the notion that absorbers are missing in the short-wavelength part of the EUVE spectrum that would bring down the observed spectrum to the lower flux level of the diffusion model, which has already been boosted considerably by increasing the surface gravity.

GD 246 Napiwotzki et al. (1999a) give a NLTE optical parameter determination for this faint spectrophotometric standard (Bessell 1999, UV normalisation; Hawarden et al. 2001, large optical telescopes; Smith et al. 2002, SDSS standard-star network).

The star has IUE and EUVE spectra that Vennes et al. (1993) used to prove the existence of interstellar He II for the first time; one of the more recent ISM studies based on a FUSE spectrum is, for example, Oliveira et al. (2003).

FUSE observations are also reported by Wolff et al. (2001) and Chayer et al. (2001). Wolff et al. (2001) identify C, N, O, Si, S, Ar and Fe and measure photospheric abundances of Si, S and Fe. The Fe abundance is actually an upper limit of $\log(\mathrm{Fe/H}) < -4.7$, but Dupuis et al. (2000b) and Vennes & Dupuis

(2002) write about the presence of Fe in a CHANDRA spectrum that they relate to the missing opacity in the EUV.

The diffusion models fail in fact to reproduce the EUVE spectrum; this is one of only two cases where the predicted flux is too high at intermediate EUV wavelengths despite a lowered effective temperature. At short EUV wavelengths, the situation is reversed, and cannot be reconciled by the increased surface gravity employed.

The latter is in accord with the finding for Fe in the comparison shown (based on IUE and HST-STIS spectra, Holberg et al. 2000): The upper limit measured lies far below the prediction. The same is true for most other elements except O and Si, where some agreement can be noted.

MCT 0455−2812 Identified with simultaneous discoveries by Barstow et al. (1992), MCT 0455−2812 was ultimately published as a new ROSAT white dwarf RE J0457−281 by Barstow et al. (1994d).

NLTE analyses of optical spectra are available from Napiwotzki et al. (1999a) and Koester et al. (2001, SPY); the latter cites a larger $T_{\rm eff}$ than used here.

Apart from IUE and EUVE spectra, MCT 0455−2812 also has an ORFEUS I spectrum (1993 flight) that reveals the presence of S and P (Vennes et al. 1996a; Barstow et al. 1998). An analysis of the FUSE spectrum was presented by Wolff et al. (2001); similar to GD 246, C, N, O, Si, P, S and Fe are found. An upper limit of $\log({\rm Fe/H}) < -5$ is cited.

The EUVE can be reproduced fairly well, at a significantly higher temperature than even found in Koester et al. (2001), so that a direct comparison of results in the EUVE versus those in the UV makes little sense. Nevertheless, both Fe and Ni are well matched, although the iron measurement is higher than the prediction, in contrast to the systematics emerging so far. At the higher temperature suggested by the EUVE fit, this would probably appear reversed again. The remaining elements show a gaudy scatter in the direction of deviations, in conjunction with large error bars.

HZ 43 A Despite its red companion, HZ 43 A is a very popular spectrophotometric standard. The wide common proper motion pair are separated by about 3”, so that depending on the seeing and the spatial resolution of the telescope the dMe component will or will not contaminate an optical spectrum. It can be easily separated with HST, and its contribution to shorter wavelength observations is negligible.

Napiwotzki et al. (1993) and Heber et al. (1997, determination of an upper limit for the rotational velocity) have presented good optical spectra in addition to the

familiar standard works. The binary nature of the system can be exploited to study, within a larger sample, evolutionary channels in non-interacting binary systems (Barstow et al. 1994a), population membership via the radial velocity and metallicity of the un-evolved companion (Silvestri et al. 2002), and gravitational redshifts (Reid 1996, allowing an independent determination of $\log g$).

HZ 43 A is one of four primary white dwarf standards used as a spectrophotometric reference for various HST instruments (Bohlin et al. 1995, Bohlin 1996, Bohlin 2000, Bohlin et al. 2001). It is treated in Kruk's 1998 review about UV calibration, prominently features in the Hopkins Ultraviolet Telescope Astro-1 and Astro-2 calibration (Kruk et al. 1997, 1999), and supplied the in-flight calibration of ORFEUS-SPAS II (Hurwitz et al. 1998; Dixon et al. 2002). Further, it is used in Massa & Fitzpatrick's (2000) re-calibration of IUE NEWSIPS, in the FUSE calibration (Sahnow et al. 2000), XMM-Newton's (Jansen et al. 2001) and also CHANDRA's low-energy calibration (see also Vennes & Dupuis 2002).

After having established a set of fundamental photospheric parameters in 1993, Napiwotzki et al. exclude HZ 43 A from their 1999a analysis but state that systematic errors of 0.3 dex in $\log g$, as found between Napiwotzki et al. (1993) and Finley et al. (1997), are not so serious in the light of their new results.[4] Although the smaller shifts in effective temperature warrant correspondingly fewer discussions, it is noteworthy that the work by Bessell (1999) on spectrophotometric standards uses $T_{\rm BB} = 35\,000$ K, a blackbody temperature, that obviously deviates strongly from the accepted effective temperature of about 50 000 K. Generally, of course, the discussion is not between blackbody versus LTE H models, but between LTE H models (as used in virtually all of the calibration works) versus NLTE models, and with various traces of He or metals.

Undisputedly, HZ 43 A exhibits an unusually pure H atmosphere. Regularly, spectra from new instruments only place upper limits on heavy element abundances. Modelling efforts have therefore concentrated, among other things, on NLTE models (also for spherical symmetry) for various He/H compositions, or LTE model atmospheres with comptonisation (Madej 1998) which contributes some additional opacity that however only has an effect on the emergent X-ray spectra when the atmosphere contains no He.

The series of observations that have failed to detect photospheric metals in

[4] From Napiwotzki et al. (1999a): "Therefore, we conclude that the accuracy is not limited by the noise for good spectra, and we suggest that other effects, such as details of the extraction or fluxing and normalisation procedures, contribute more. Considering these systematic uncertainties, the 0.3 dex difference between the gravity determinations of Finley et al. (1997) and Napiwotzki et al. (1993) for HZ 43 A is only a 1.5 σ deviation and therefore not as serious as considered by Finley et al. (1997)."

HZ 43 A includes Kimble et al. (1993b, HUT); Barstow et al. (1995, including a constraint of $\log(\mathrm{Fe/H}) < -6.5$, from EUVE spectra); Dupuis et al. (1998, ORFEUS-SPAS II); and Kruk et al. (2002) who, within an ISM analysis with FUSE data, amended by HST-GHRS and EUVE, once more report that no heavy elements are detected in the photosphere.

Likewise, Fig. 6.16 shows only upper limits from IUE and HST-STIS measurements; although those for N, O, Fe and Ni remain marginally consistent with the predictions. The ORFEUS spectrum actually places tighter limits on the C and N abundances, definitely destroying any consistency for N. The limiting abundances for Fe and Ni remain high however and are instead further constrained by the EUVE spectrum: Irrespective of the above Napiwotzki et al. (1993) / Finley et al. (1997) discussion, the $\log g$ required to purify the atmosphere to the observed degree is higher by yet another 0.3 dex at least than those values, reminiscent only of the historical value by Holberg et al. (1986) from a Lyman line analysis (not confirmed in the newer work by Barstow et al. 2003b).

Fuhrmeister & Schmitt (2003) set the flare flag in the tabulated results of their ROSAT variability study, although they mention in the paper text that they have used HZ 43 A as a stable reference to test their methods.

RE J2156−546 First observed in the Einstein IPC slew survey (Elvis et al. 1992), this object is also a ROSAT (e.g. Chu et al. 2004), EUVE (ISM paper: Wolff et al. 1999), HST and FUSE (ISM paper: Lehner et al. 2003) target. In their SPY survey, Koester et al. (2001) find a slightly higher T_{eff} and lower $\log g$ (46 700 K, 7.65) than cited in Chapter 5 (44 000 K, 7.91), while both the T_{eff} and $\log g$ used for the comparison here (45 500 K, 7.86) lie in between those values.

Although generally classified as another pure hydrogen-object, RE J2156−546 surprisingly shows oxygen lines in the FUSE range; from a combination of this finding with STIS and EUVE data, Chayer et al. (2003) conclude that O must be stratified in this (and three further) stars. Their modelling is based on a stratification profile taken from this work for a model with $T_{\mathrm{eff}} = 46\,00$ K and $\log g = 7.8$.

While for their H+O NLTE models the EUVE spectrum can apparently be reproduced, the fit here is not completely satisfactory for the full models including other elements, and even this can only be achieved if $\log g$ is increased by 0.4 or 0.5 dex.

For most elements, the STIS spectrum only allows to derive upper limits; although those for N, O and Fe are consistent with the predicted values, at least

Fe is probably quite a bit lower than predicted. C and Si are detected, but at much lower levels than expected.

RE J1032+535 Holberg et al. (1999a,b) discuss the STIS spectrum of RE J1032+535 in conjunction with the EUVE spectrum. One of their conclusions is that N must be stratified in this star; this issue is disputed by Chayer et al. (2005, in press), and further discussed in some detail in Sect. 6.2.3. From the FUSE data (Welsh et al. 2002, ISM), on the other hand, Chayer et al. (2003) deduce an oxygen stratification. Barstow et al. (2003c), finally, suspect a stratification of carbon based on the line profiles observed in the STIS spectrum.

The EUVE fit, similarly to RE J2156−546, requires a $\log g$ increased by about 0.5 dex, while other parameter determinations exhibit less scatter in $T_{\rm eff}$ and $\log g$.

The problems with the EUVE fit probably result from too high values for Fe and Ni in the equilibrium model. Although their predicted values are consistent with the upper limits shown in Fig. 6.18, the actual values could be significantly lower. C, O and Si are also predicted somewhat too high, in stark contrast to N: The use of the stratified profile from Holberg et al. (1999a) results in a particularly high value. This apparent N superabundance leads to the definition of a group that also encompasses RE J1614−085 and GD 659.

For the ROSAT data, Fuhrmeister & Schmitt (2003) set the "flare" flag (as for 5 more out of the 13 white dwarfs they detect).

PG 1057+719 ROSAT and EUVE data for this object suggest it has a pure hydrogen atmosphere. Holberg et al. (1997b) also find no evidence of heavy elements in this object's HST-GHRS spectrum; consequently, Fig. 6.19 displays upper limits for C, N, Si, Fe, Ni based on the wavelengths covered by the GHRS observations. In particular, PG 1057+719 does not show nitrogen lines.

The EUVE spectrum appears strongly absorbed; it can be fitted at generally accepted parameters.

Fuhrmeister & Schmitt (2003) find everything from flare activity to periodicity and a trend in the ROSAT data.

GD 394 Given how complex the object GD 394 has turned out to be, it must have been a challenge for some applications to use it for calibration purposes, as carried out for example in Finley et al. (1984, IUE), Kruk et al. (1999, HUT), and again Smith (2001, test of IUE wavelength calibration). The star appears confusing enough to merit to be featured in Trimble & Aschwanden's "Astrophysics in 2000" review (2001).

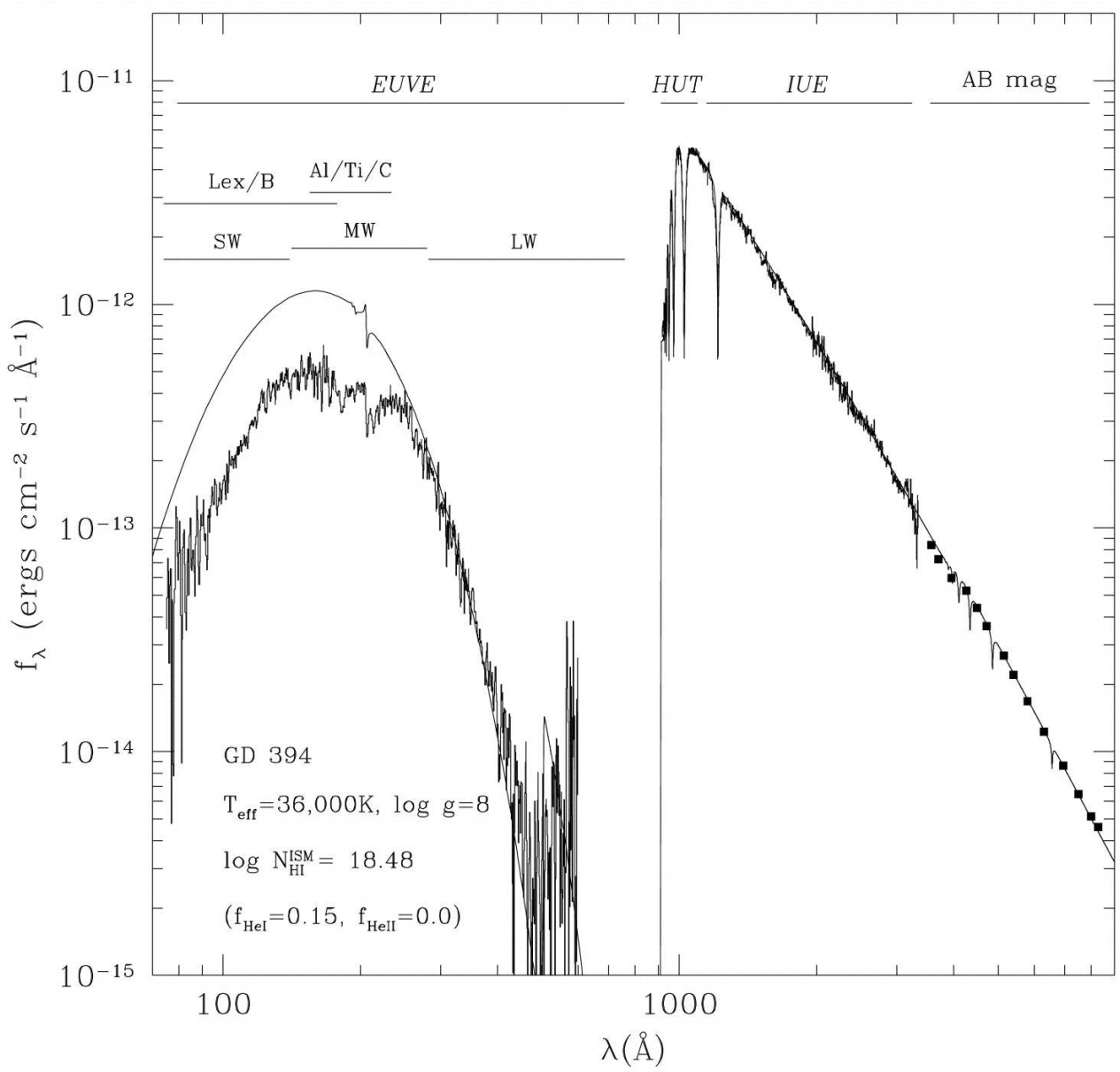

Figure 6.25: This representation of observations of GD 394 has been taken from Dupuis et al. (2000a) and illustrates the ”complete spectral energy distribution including data from EUVE (80-400 Å), HUT (911-1950 Å), IUE (NEWSIPS LWP 20211 and SWP 41457; 1150-3250 Å), and AB magnitudes from Greenstein & Liebert (1990), along with a representative pure-hydrogen model. The IUE flux scale was adjusted by +4%.”

A Si versus C overabundance was already reported from IUE spectra in Bruhweiler & Kondo (1983), where GD 394 was also re-classified from DO to DA. From EUVE spectra, Shipman & Finley (1994) reached the same conclusion as Barstow et al. (1993a) from ROSAT, namely that the significant EUV opacity observed cannot result from He.

The HST-GHRS spectra have first been analysed by Shipman et al. (1995). They assigned a circumstellar origin to a number of Si lines that Barstow et al. (1996) subsequently classified as photospheric within a combined analysis of IUE, HST-GHRS, EUVE and optical data. In Holberg et al. (1997b), GD 394 HST-GHRS spectra are directly contrasted to those of the pure hydrogen object RE J1614−085.

Dupuis et al. (2000a) compile optical, IUE, HST-GHRS, HUT, EUVE observations for the most recent in-depth analysis of GD 394. Figure 4 in their paper, reproduced in Fig. 6.25, shows a nice overview of all these observations that together produce a fairly complete spectral energy distribution. In the optical Echelle spectroscopy, Si is detectable, once more implying a large, and apparently variable, abundance. Furthermore, GD 394 turns out to be variable in the extreme ultraviolet (EUV) with an amplitude of 25% and a period of 1.150 ± 0.003 days. The same periodicity has now been found in ROSAT data by Fuhrmeister & Schmitt (2003). Since the time difference between both observations amounts to 5 years, the variability must be caused by a non-transient phenomenon. The proposed spot, resulting from assumed accretion onto a magnetic pole and causing the variations through stellar rotation, would have to be stable on such time scales.

To the element Al measured by Dupuis et al. (2000a) after it had been reported in Holberg et al.'s co-added IUE spectrum (1998), Chayer et al. (2000) add the detection of P and Fe in the FUSE spectrum.

Although this direct verification of the presence of Fe in GD 394 confirms earlier models, the diffusion models that incorporate Fe obviously cannot explain the observed abundance. There is too little overall opacity in the diffusion models, in contrast to most other objects, and the attempted match to the EUVE spectrum is by far the worst in the whole sample. If the accretion scenario is correct, this discrepancy is not surprising.

On the other hand, the measured Si abundance in the UV is not too far off the equilibrium predictions, and except for C, where tight upper limits can be set on the elemental abundance, the limits from measurements remain all the same consistent with predictions.

Due to the time-dependency and in the light of all other likely complications mentioned, any such survey-like results must be treated with extreme caution.

6.2.2 Other objects without EUVE spectra

PG 0948+534 At 110 000 K, PG 0948+534 lies far beyond the hot edge of the model grid, so that the theoretical abundances are extrapolations that should only be

read with extreme caution. Additionally, Barstow et al. (2003c) could not find satisfactory fits to the C IV, N V, O V and Si IV lines that are detected in the HST-STIS spectrum although they note values larger than about $10^{-4.5}$.

The extrapolated Fe and Ni abundances (both well beyond solar here) are too high by 2 and 3 dex, respectively, compared to the measurements.

Ton 21 Although Ton 21 is a spectrophotometric standard star (Massey et al. 1988), no FUSE spectra are available. The HST spectra are discussed in recent surveys mentioned in the introduction.

All predicted elemental abundances are too high, including Fe and Ni where the discrepancy becomes similarly large as for PG 0948+534. Crudely speaking, the offset scatters around a value of about 2 dex. It is higher for Ni which rather seems to be loosely constrained by the cosmic ratio. It is extremely large for Si, the most abundant element in the observation. This is probably due to missing higher ionisation stages that were not included in the model calculations.

RE J1738+665 This object was the hottest WD detected by ROSAT (Barstow et al. 1994c), a discovery even followed up by a discussion in Nature (Shipman 1994; Tweedy 1995). It might also still be surrounded by an old planetary nebula (Tweedy & Kwitter 1994). In contrast to the notion shortly after its discovery that it must have unusually low metal abundances to show the detected soft X-ray flux, its abundance patterns do not appear too peculiar in the light of newer parameter determinations (RE J1738+665 is included in the recent surveys analysing HST and FUSE spectra).

The abundance pattern and how it relates to the predictions is very similar to that of Ton 21.

PG 1342+444 As do Ton 21 and RE J1738+665, PG 1342+444 also lies near the hot edge of the model grid. A FUSE spectrum is the only available high-resolution observation in the UV (Barstow et al. 2002). It is one of the spectra that entered into the study comparing effective temperatures as derived from Balmer and Lyman lines by Barstow et al. (2001c, 2003b). The results displayed in Fig. 6.4 were also obtained based on that data.

The overall abundance pattern as obtained from the FUSE spectrum is (roughly) matched by the predictions better than for most other objects. But while the error bars continue to overlap, in detail the mean values actually do differ by one order of magnitude. In particular, the Si discrepancy mentioned for other objects above remains.

RE J0558−373 The EUVE spectrum of this object was not included in Wolff et al.'s (1998) sample.

In the element abundance determination, although the first impression again is not too bad, very small error bars on the measurements destroy compatibility in all but two cases. So the predictions only meet the values for O and Fe – this quite well.

WD 2218+706 WD 2218+706 is surrounded by an ancient planetary nebula (e.g. Acker et al. 1992); HST-STIS spectra of the central star have previously been analysed by Barstow et al. (2001a).

In the abundance pattern, the matches are not so good for C and N, and the apparent limit imposed on Ni by the cosmic abundance is also particularly striking and results in a mismatch. The measurement for O lies slightly above the prediction but very close to it.

GD 153 GD 153 is frequently used for calibrations. For this reason, a variety of observations exist, including, for example, observations from FAUST (Bowyer et al. 1993), HST-FOS (Bohlin et al. 1995), Astro-1 and Astro-2 of HUT (Kruk et al. 1997, 1999), IUE (Massa & Fitzpatrick 2000), HST-STIS and HST-NICMOS (Bohlin 2000; Bohlin et al. 2001), and XMM-Newton (Jansen et al. 2001).

ROSAT observations exist and were, in addition to the standard publications, also reported on by Thomas et al. (1998).

GD 153 is furthermore useful for ISM studies, as conducted using EUVE (Vennes et al. 1994), FUSE (Lehner et al. 2003) and HST-STIS observations (Redfield & Linsky 2004a,b).

Due to their global non-detection, the abundances from metal lines are all upper limits. Those are tight enough for C and Si only in order to disagree with the diffusion models.

RE J1614−085 Following up on Holberg et al. (1997b), Fig 6.22 presents revised abundance measurements from HST-GHRS spectra.

With respect to the equilibrium predictions, C is well matched, while the observed Si is lower and N is higher at an extreme value of more than 6 orders of magnitude. This causes it to be grouped together with RE J1032+535 and GD 659 by Barstow et al. (2003c).

The exceedingly large abundance of N in that group is disputed by results from Chayer et al. (2005, in press) that are shortly discussed again in the context of RE J1032+535 in Sect. 6.2.3.

GD 659 Early EUVE and ROSAT observations, presented by Finley et al. (1993) and Wolff et al. (1995), respectively, suggested a pure hydrogen atmosphere of this object. It is part of the MCT sample (Lamontagne et al. 2000) and of interest for ISM studies so that a FUSE spectrum is available (Lehner et al. 2003).

In their initial analysis of EUVE and IUE spectra, Holberg et al. (1995) found metals but favoured a circumstellar origin of the observed C, N and Si lines, that are now interpreted as photospheric in the IUE and HST-STIS observations. In comparison to the radiative levitation calculations, the observed irregular abundance pattern shows occasional consistencies but is generally lower than the predictions. The exception to this is again N, for which the highest abundance in the whole sample is reported.

For this member of the nitrogen-rich group, Chayer et al. (2005, in press) also obtain different results.

EG 102 This is another spectrophotometric standard star (Colina & Bohlin 1994, optical; Kaiser et al. 1998 and Bohlin et al. 2001, HST-STIS and HST-NICMOS; Smith 2001, IUE). A FUSE spectrum also exists (Hébrard et al. 2003).

The star has been reported to show lines of Si, Al and Mg (see for example Holberg et al. 1997a). Due to its low effective temperature, the presence of metals is attributed to accretion, which Debes & Sigurdsson (2002) speculate might come from a perishing planet. Zuckerman & Reid (1998) and Zuckerman et al. (2003) analyse the metal lines observations within a larger sample of cool objects.

The comparison shown for the Si measurement implies a risky extrapolation to low effective temperatures far beyond the actual model grid; funnily enough, the match is so perfect that the data points shown become indistinguishable. While no accretion would then be necessary to explain the presence of Si, Al and Mg remain unexplained. The upper limits given for all other elements are consistent with their absence in diffusion calculations due to complete settling.

Wolf 1346 Since this object has an even lower effective temperature than EG 102, and only Si – whose presence is also generally being attributed to accretion – could be measured (Holberg et al. 1996), this work refrains from displaying a plot with abundance comparisons.

6.2.3 A closer look at the nitrogen lines in RE J1032+535

The following analyses rely on the N V resonance line doublet at rest wavelengths of 1238.82 and 1242.80 Å observed in the HST-STIS spectrum. Holberg et al. (1999a) have used it in conjunction with EUVE data to derive a chemical stratification in

RE J1032+535 where large amounts of N are concentrated in the high atmosphere. Chayer et al. (2005, in press) have repeated the analysis of the same observation with homogeneous models and obtain a good fit at a significantly lower N abundance.

Here, the line profiles are first compared to the emergent fluxes from several diffusion models; then the diffusion models themselves are tested against the homogeneous grid by Chayer et al. (2005). All variations of depth-dependent N stratification, or level of the homogeneous abundance, assumed in the different works are summarised in Fig. 6.26.

The abundance profiles in Fig. 6.26 (in grey colour) and the theoretical fluxes (smooth grey curves) in Fig. 6.27 correspond to stratified models with the predicted equilibrium N abundance, and with that abundance profile scaled up by factors 10 and 10^2. There are potential problems with the two scaled-up versions since they are not self-consistent; the abundances were only scaled up and spectra were calculated with SYNSPEC, the models themselves were not re-converged. Figure 6.27 is for two different sets of atmospheric parameters: 46 000 K and $\log g = 8.0$ are used for the upper plot; and, following Barstow et al.'s values of $T_{\rm eff} = 44\,350$ K and $\log g = 7.81$, 44 000 K and $\log g = 7.8$ are used for the lower plot. Hence the lower two panels in Fig. 6.27 are at the $T_{\rm eff}$ and $\log g$ also shown in Fig. 6.27.

Table 6.1 summarises the results for the direct comparison of the spectra from the three models to the N V lines. The lowest abundance is favoured over the higher ones; the decision between the models with different effective temperature and $\log g$ is less clear but the overall best match is at the parameters also adopted in the other studies.

Next, the three stratified models at $T_{\rm eff} = 44\,000$ K and $\log g = 7.8$ were fitted with the H+N homogeneous NLTE grid by Chayer et al. (2005). P. Chayer derives representative homogeneous abundances that best fit the models at values of -6.21, -4.82, and -4.80 (see Table 6.2). Figure 6.28 demonstrates that while the fit quality is good for the lowest abundance pattern, it decreases for the scaled-up versions. The value determined for the original diffusion model coincides with the value Chayer et al. (2005) determine from the observation. The other two values are so close to each other that they are hard to distinguish. The less than perfect fits and the very similar results for abundances that in the underlying model differ from each other by one magnitude must perhaps be attributed to the lack of self-consistency. The obvious saturation of the line, or a genuine stratification effect that could have a larger impact at larger abundances, provide further potential explanations.

However, the by far most interesting case is the original model itself: The value derived by the fitting as its representative abundance is 0.8 dex higher than what the model's abundance is at $\tau_{\rm ross} = \frac{2}{3}$. On the other hand, this value is practically identical to the one Chayer et al. (2005) derive for RE J1032+535: This is consistent with the interpretation that the nitrogen in RE J1032+535 is stratified due to radiative levitation as predicted by the model, and that it is present at about the same overall

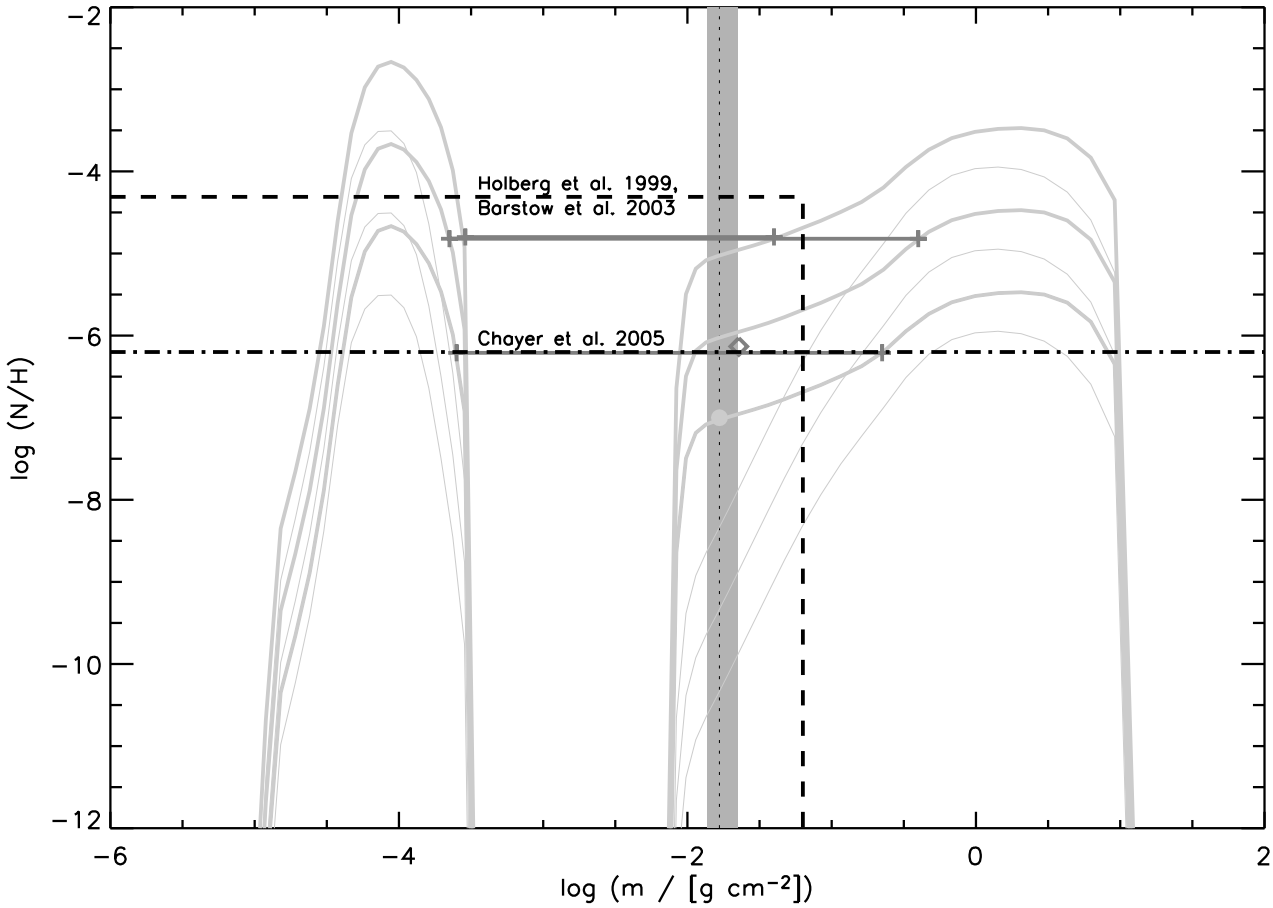

Figure 6.26: Different nitrogen stratification profiles assumed for RE J1032+535 at $T_{\rm eff} = 44\,000$ K and $\log g = 7.8$: The lowest of the three thick grey diffusion profiles is the stratification profile predicted from this work, the two similar profiles above this are scaled up by factors of 10 and 10^2, respectively. Thin grey lines denote the contribution of N V to the total N abundance in all three cases.
The location of $\tau_{\rm ross} = \frac{2}{3}$ on the logarithmic mass scale near -2 is indicated along with the range corresponding to $\tau_{\rm ross} = 0.5-1.0$, with the abundance measurement point entering into the "object" or "element" plot series marked by a dot. Similarly, the Chayer et al. (1995b) prediction is marked by a dark grey diamond and placed on the mass scale where $\tau_{\rm ross} = \frac{2}{3}$ in the Chayer et al. (1995b) models.
Also shown is the slab model proposed by Holberg et al. 1999a that Barstow et al. (2003c) use to obtain the nitrogen abundance value employed earlier (dashed line). A new determination by Chayer et al. (2005, in press: dash-dotted line) using H+N NLTE models yields a much lower abundance (as could perhaps be expected after considering Fig. 1.1 again).
Finally, synthetic spectra from the three stratified diffusion models were fitted with the same H+N NLTE grid by Chayer et al. as above. The values determined by P. Chayer (priv. comm., compare also Fig. 6.28 and Table 6.2) are added as dark horizontal lines bordered by plus signs that define the range around $\tau_{\rm ross} = \frac{2}{3}$ where these values are actually reached in the underlying stratified models. The value for the lowest-abundance diffusion model lies right on top of Chayer et al.'s 2005 value, the other two are barely distinguishable from each other.

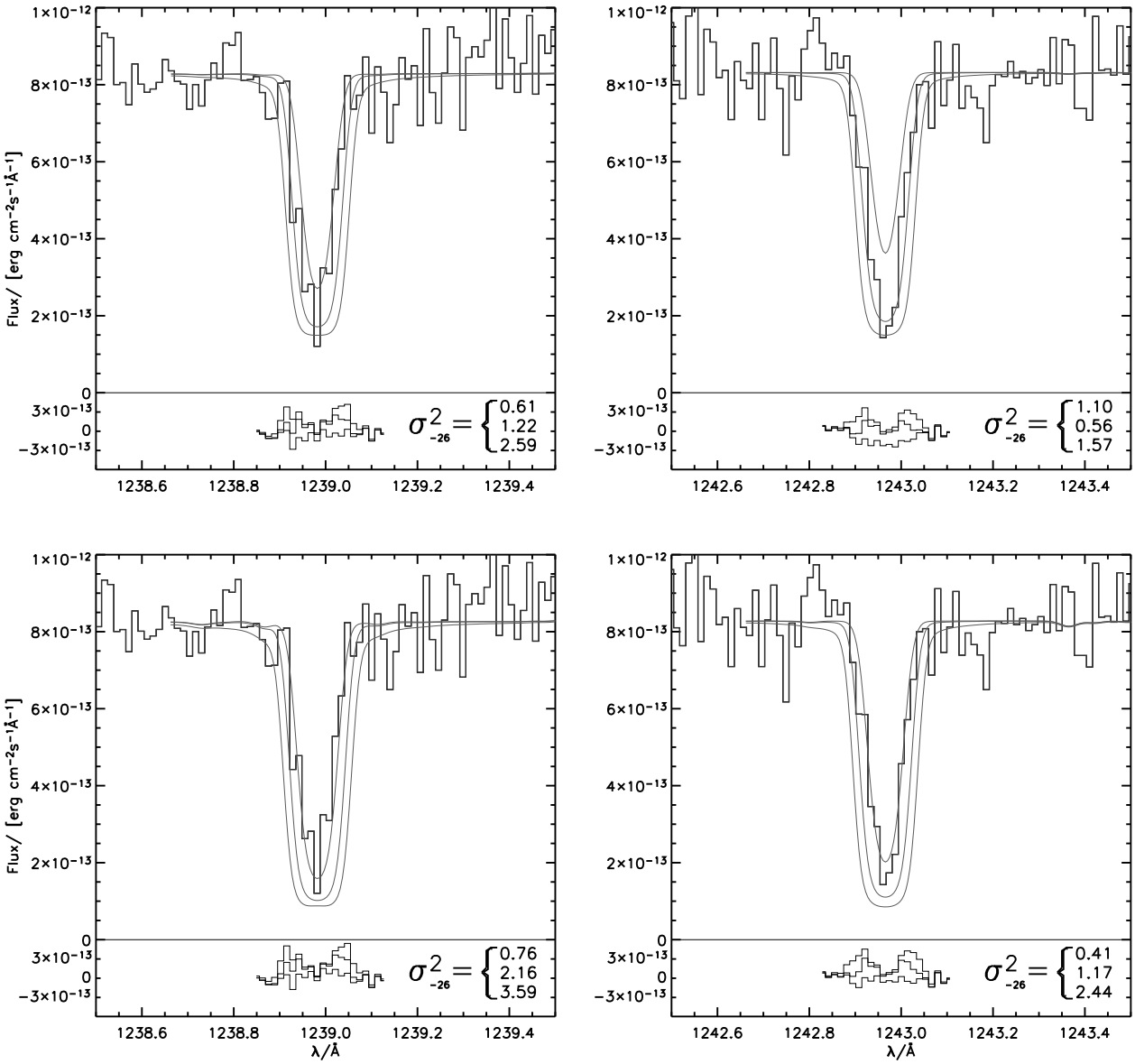

Figure 6.27: The N V doublet lines in RE J1032+535 from HST-STIS spectra in comparison to models with $T_{\rm eff} = 46\,000$ K and $\log g = 8.0$ (top) and $T_{\rm eff} = 44\,000$ K and $\log g = 7.8$ (bottom). Three emergent spectra for both models were calculated: one at the N abundance predicted from radiative levitation, and two with that equilibrium pattern scaled up by factors 10 and 10^2. The deviation of the models from the observation in each case are shown in the insets at the bottom of each plot. The quadratic sum of these deviations is also given (the index -26 for the σ^2 means that the value must be multiplied by 10^{-26} to yield the actual result; the absolute value however does not matter here). See also Table 6.1.

absolute level, so that the fit by P. Chayer to the observation gives the same result as the fit to the model. Although the direct comparison of the measured versus the predicted abundance at a given depth is very different, they would in fact describe an

Table 6.1: The N V doublet in RE J1032+535 from HST-STIS spectra compared to emergent spectra from diffusion models: The fit results are sorted by decreasing $\sum \sigma^2_{-26}$, which results in an almost simultaneous sorting in $\log(\mathrm{N/H})$ at $\tau_{\mathrm{ross}} = \frac{2}{3}$ except for the two best-fit models where the one with the T_{eff}, $\log g$ parameters closer to those published matches better.

T_{eff} [K]	$\log(g\,/\,[\mathrm{cm\,s^{-2}}])$	$\log(\mathrm{N/H})$	N V^{1238}: σ^2_{-26}	N V^{1242}: σ^2_{-26}	$\sum \sigma^2_{-26}$
44 000	7.8	−7.0	0.76	0.41	1.17
46 000	8.0	−7.2	0.61	1.10	1.71
46 000	8.0	−6.2	1.22	0.56	1.78
44 000	7.8	−6.0	2.16	1.17	3.33
46 000	8.0	−5.2	2.59	1.57	4.16
44 000	7.8	−5.0	3.59	2.44	6.03

identical situation. It is also remarkable that the fit in that case is very good, indicating that although the stratification is present in the model, there are no direct hints of it in the line profile.

The predicted stratification profile cannot be validated from the argument alone that it results in spectral lines that fit the observation, and that those spectral lines in turn behave the same as the observation when fitted with spectra from a homogeneous model. Nevertheless, the picture is consistent and the validity of the model is given further credibility by the fact that the stratification profile is not simply an educated guess, but relies on modelling the radiative levitation process. One important question is what the offset in representative versus actual abundance at $\tau_{\mathrm{ross}} = \frac{2}{3}$ in the model is due to. It cannot be a NLTE effect; it could be related to the H+N only composition (the diffusion model also has – too much – iron as well as H, He, C, N, O, Si and Ni). Or it could indeed be a stratification effect; then the bump at $\log m \approx -4$ would in fact play a role.

The lower N abundance around $\log m \approx -2$ should not result in a nitrogen absorption edge in the synthetic EUV spectrum that would become inconsistent with observations, since it also does not pose this problem at a corresponding abundance level in Chayer et al. (2005). The bump further out cannot have any effect on the EUV range. That bump may however contribute some opacity in the core of the N V lines even though the density is low in this region; this is in fact more plausible than to assume that the additional contribution needed for the model to look like it has an increased average abundance mostly comes from the $\log m \approx 0$ region.

Besides RE J1032+535, Chayer et al. find similar results for the other cool objects RE J1614−085 and GD 659. This does not resolve the question why the so-called "twin" objects RE J2156−546, PG 1057+719, GD 394 and GD 153 that have simi-

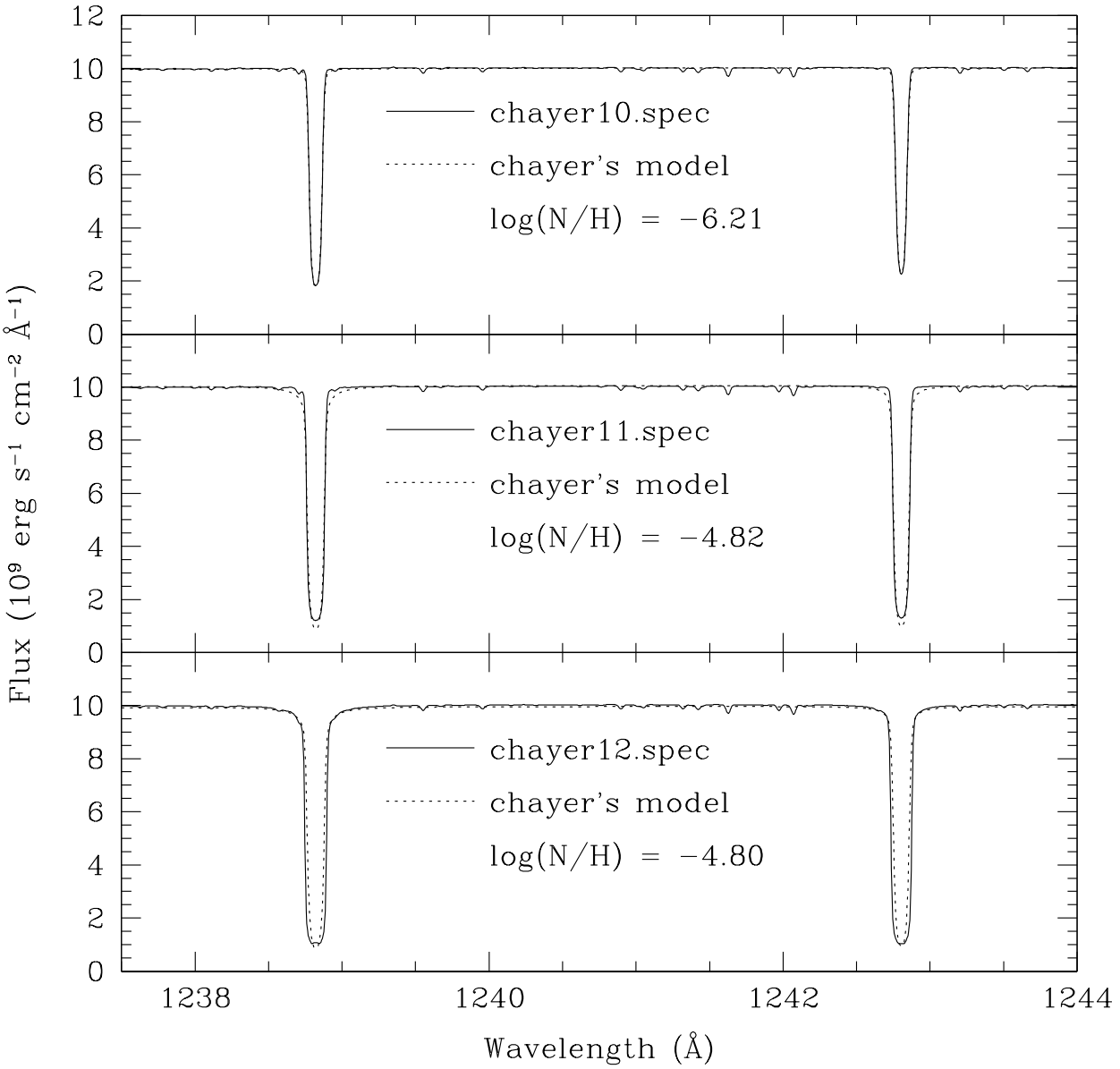

Figure 6.28: The N V doublet in the three diffusion models at $T_{\rm eff} = 44\,000$ K and $\log g = 7.8$ calculated for RE J1032+535 in comparison to the best-fit models at the same effective temperature and surface gravity by P. Chayer. The N abundance increases from top to bottom; see Table 6.2 for the identification of the diffusion models, and comments on each of the fits. The plots and table for this exercise are courtesy of P. Chayer.

lar atmospheric parameters do not show the N V doublet at all. The new homogeneous abundances are actually almost at the same level as the statistical upper limits Barstow et al. (2003c) give for these objects. This does not rule out the possibility that a group of stars with a particularly high N abundance exists, but the absolute

Table 6.2: The N V doublet in RE J1032+535 in the model with $T_{\rm eff} = 44\,000$ K and $\log g = 7.8$ at different N abundance levels, fitted by P. Chayer with his H+N homogeneous NLTE grid (from Chayer et al. 2005): results and details of the fit quality. The N abundance is encoded in the model names as follows: The index 10 in `chayer10.spec` stands for the diffusion model with a scaling factor of 10^0 (i.e. this corresponds to the un-scaled original profile), 11 stands for a scaling factor of 10^1 and 12 for 10^2.

Model (compare Fig 6.28)	best fit at $\log(\mathrm{N/H})$	comments
chayer10.spec	-6.21	very good fit
chayer11.spec	-4.82	the wings and core do not fit perfectly
chayer12.spec	-4.80	not a good fit; the wings fit well though

values that Holberg et al. (1999a) obtain from both a homogeneous distribution of the absorbing material within the atmosphere ($\log(\mathrm{N/H}) = -4.31$) as well as from the slab model (-4.3, the value also adopted by Barstow et al. 2003c) is surprising.

It is worrying that two groups who use the same model atmosphere program (TLUSTY together with SYNSPEC), and analyse the same observation with it, obtain values that differ by two orders of magnitude. The analysed star is relatively metal-poor, and both groups consistently forego the inclusion of iron group elements. The good agreement between the diffusion models in this work, and the H+N models (Chayer et al. 2005) with no metal-line blanketing at all, make it even more unlikely that the problem is due to metal-line blanketing.

In addition to the blatant discrepancy between the Holberg et al. (1999a) / Barstow et al. (2003c) and the Chayer et al. (2005) results, the finding that representative homogeneous abundances can be significantly lower than the $\tau_{\rm ross} = \frac{2}{3}$ value in stratified models should be kept in mind in order to prevent misleading conclusions. This effect might help to reconcile some, definitely not all, of the discrepancies apparent in the comparisons shown elsewhere in this chapter which should accordingly be interpreted with some caution.

6.3 Element species in the full grid

For most elements, the scatter due to different surface gravities in the model predictions alone for the plots as a function of $T_{\rm eff}$ can amount to one order of magnitude, and can be significantly larger in the plots as a function of $\log g$ due to the effective temperature range covered. This scatter in the models is, for all elements except Si,

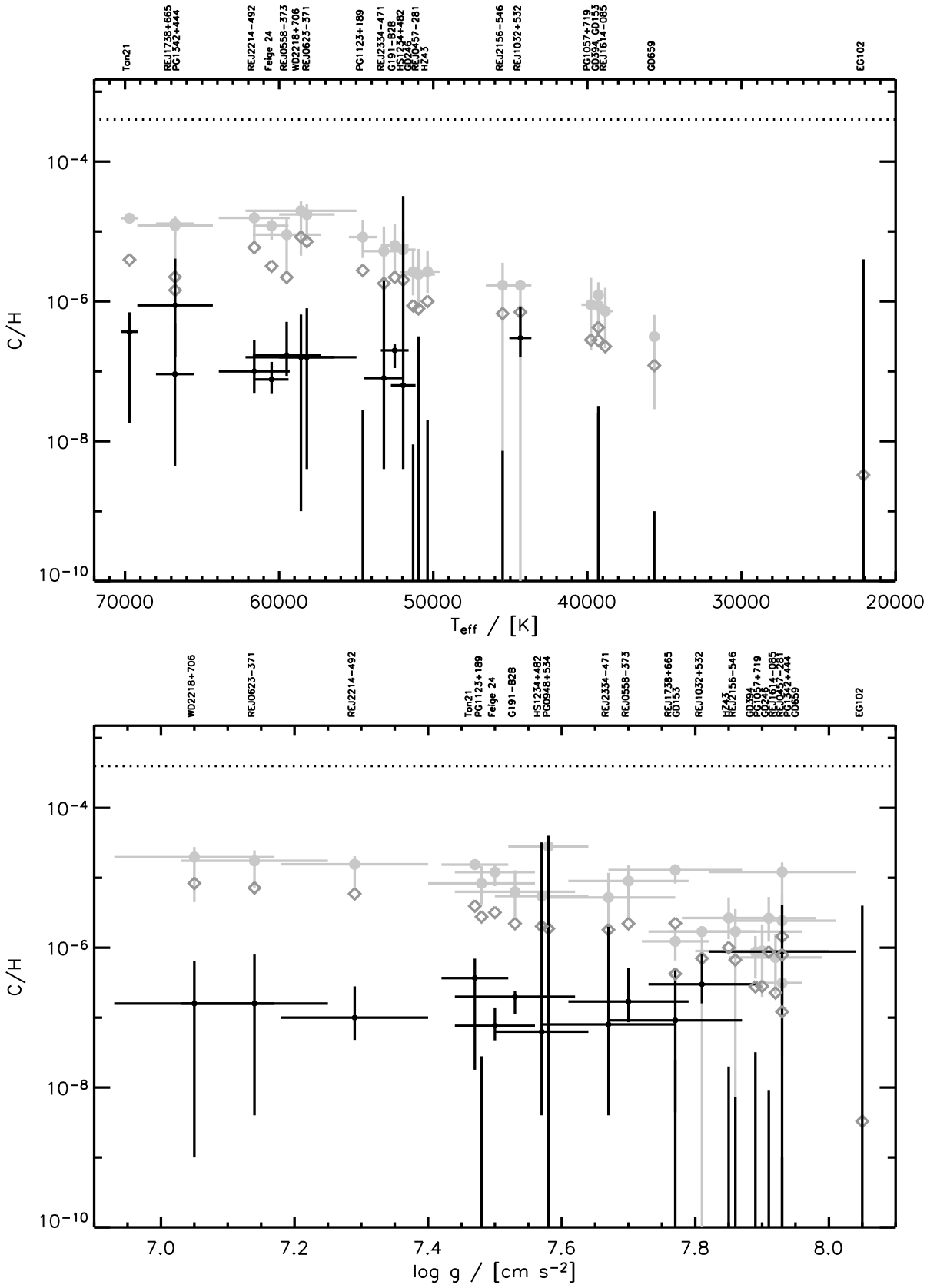

Figure 6.29: UV C III abundances as a function of T_{eff} and log g.

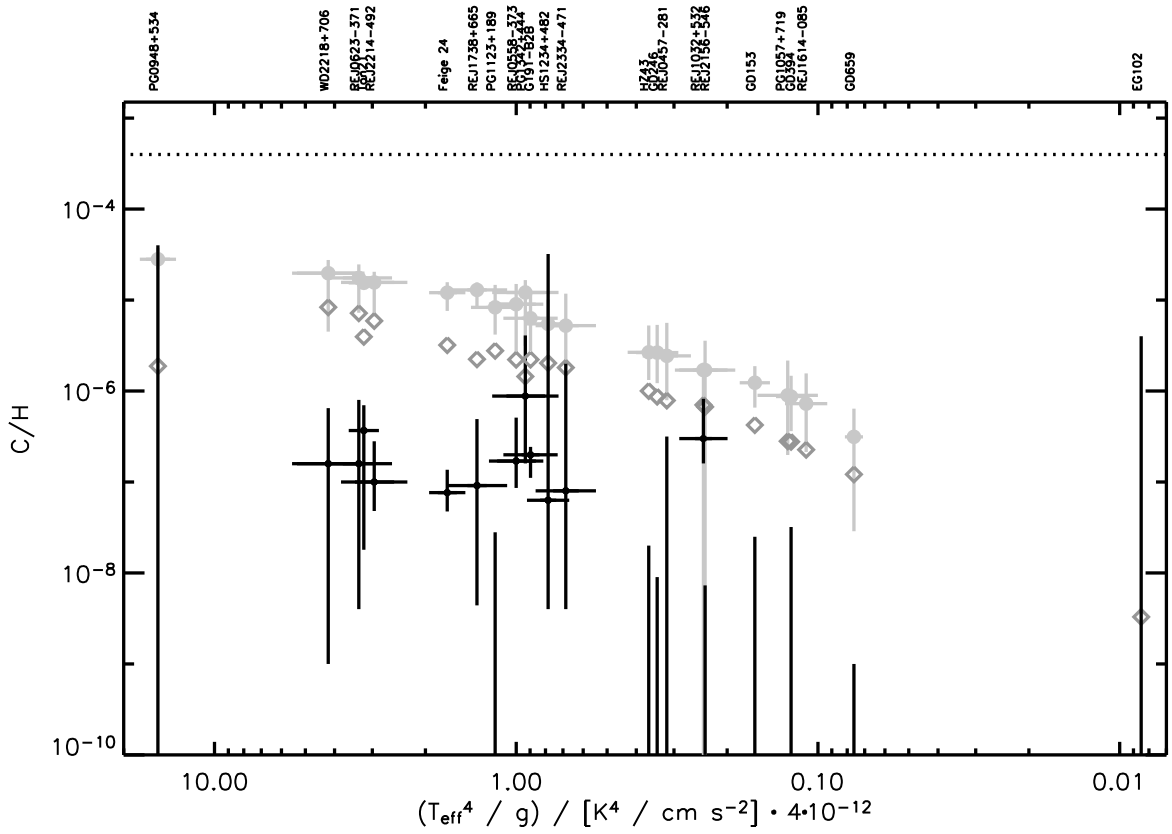

Figure 6.30: UV C III abundances as a function of the metal index mi.

drastically reduced in those plots where the results are shown as a function of the metal index mi.

This is true for both Chayer et al.'s (1995b) as well as for the current diffusion models. In a duplication of the results from Sect. 4.2, Figs. 6.29 to 6.42 show again that Chayer et al.'s predictions for C, Si, and Fe lie below, those for N and O above those of the new models. No overall systematic effect is evident.

The location of $\tau_{\rm ross} = \frac{2}{3}$ on the mass scale in Chayer et al.'s hydrogen models with respect to the diffusion models with potentially large amounts of heavy elements does not result in significant offsets that could distort the representation of the results. According to the data in Table 6.3, and an interpolation from the models in this work to the representative surface gravity cited there, it is obvious that this difference results in an offset in the $\tau_{\rm ross}$ scale no larger than 0.04 dex in $\log m$ over a large effective temperature range (as shown in Fig. 6.43). It is therefore unlikely that this produces any noticeable systematic differences. The larger offset in Fig. 6.26 results from a slightly wrong surface gravity used in the determination of the location of $\tau_{\rm ross} = \frac{2}{3}$ on the mass scale.

Is is also worth noting that with very few exceptions (objects belonging to the upper

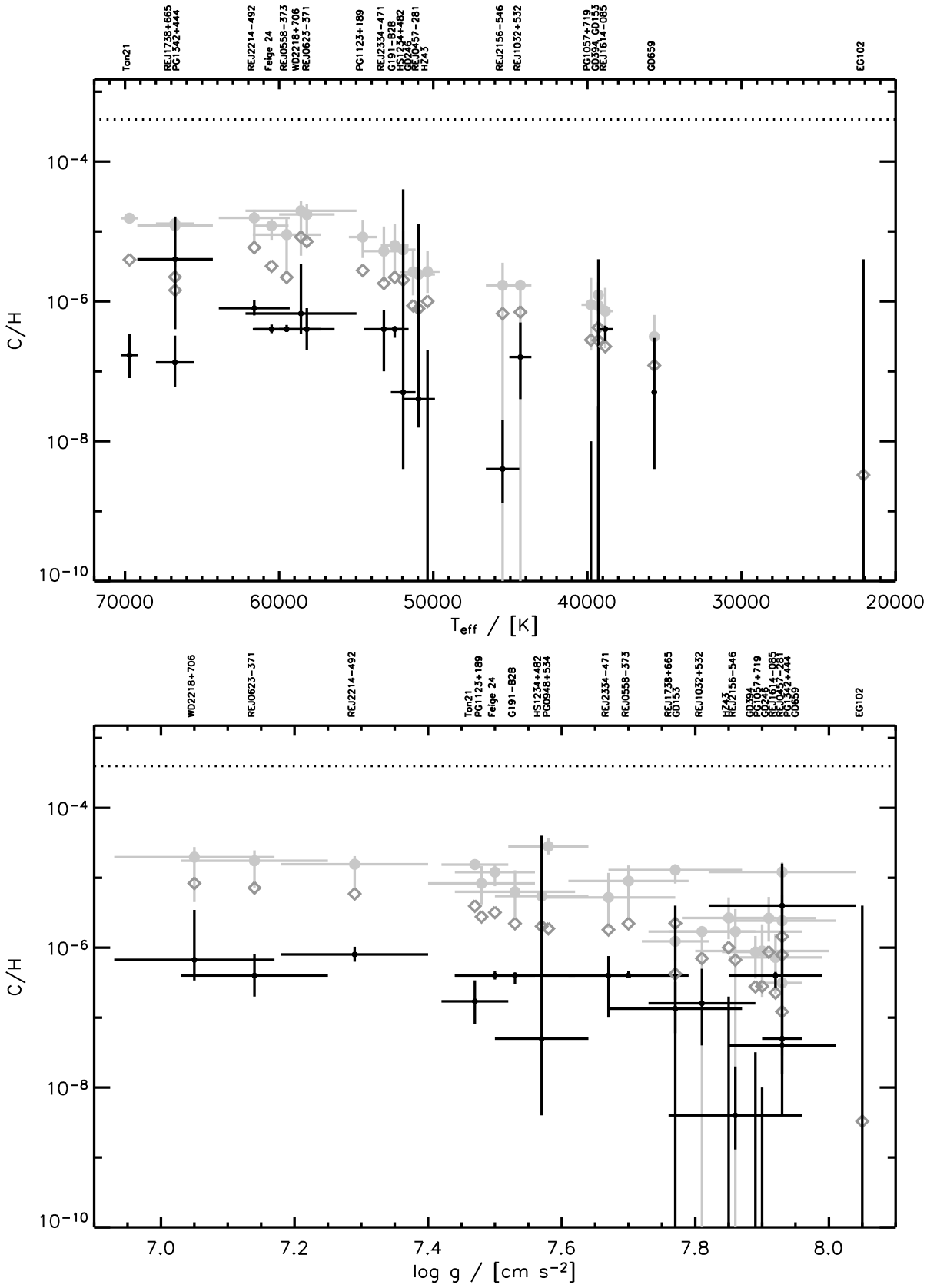

Figure 6.31: UV C IV abundances as a function of T_{eff} and log g.

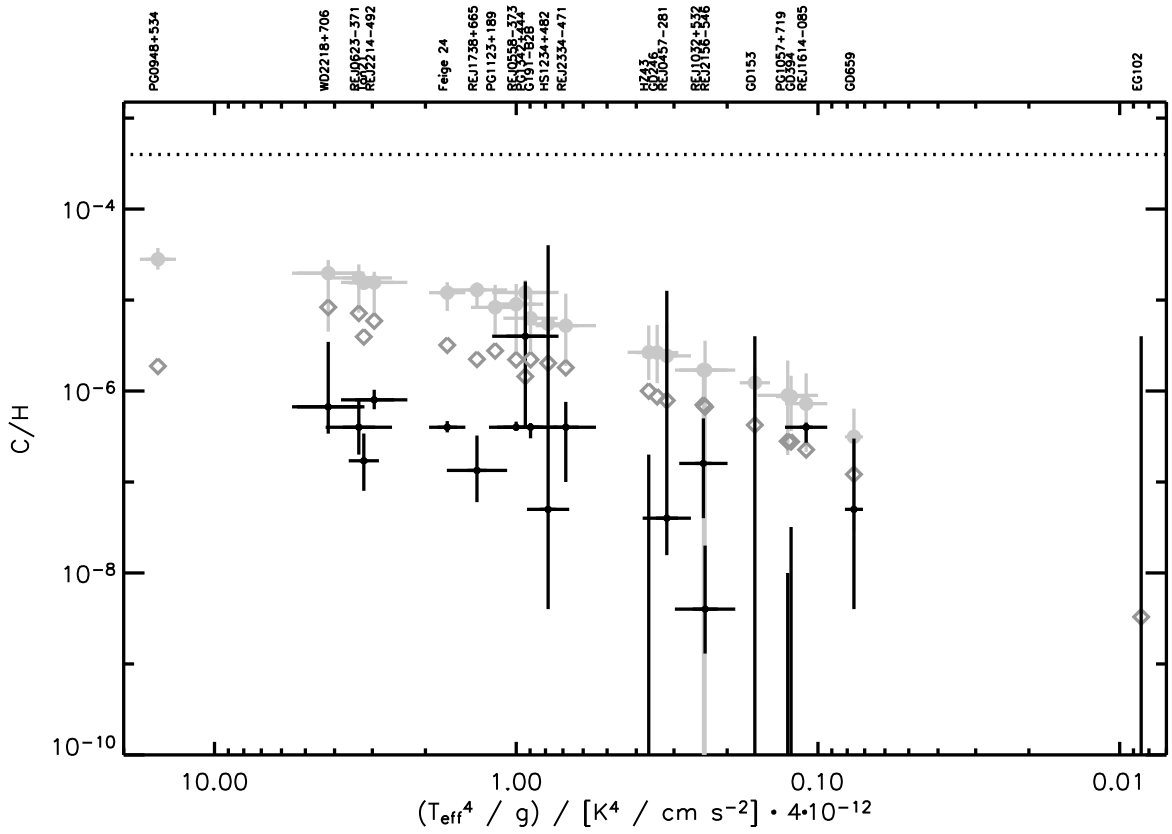

Figure 6.32: UV C IV abundances as a function of the metal index mi.

branch of nitrogen dichotomy, iron and nickel in PG 1342+444), all photospheric abundances seem to respect cosmic abundances as an upper limit.

Helium This element has been included in the model calculations and is therefore listed here for completeness. Since, by definition, the amount of He contained in DAs is un-detectably small, no measurements are available from Barstow et al. (2003c). Therefore no comparison plots, where only the predictions would appear, are shown. WD 2218+706 is an exception that shows a weak He II feature at 1640 Å (but no detectable He lines in the optical).

Carbon Both C III and C IV are consistently over-predicted. Theory and observations follow the same general temperature dependency but although theory nicely runs in parallel to the observations its level is too high. The gap is much smaller than average for C III in the case of RE J1032+535, and for C IV in the case of GD 659, RE J1032+535, PG 1342+444 and RE J1614−085.

For high surface gravities, the large scatter in effective temperature makes it hard to appreciate the better quality of agreement for these objects. Its high

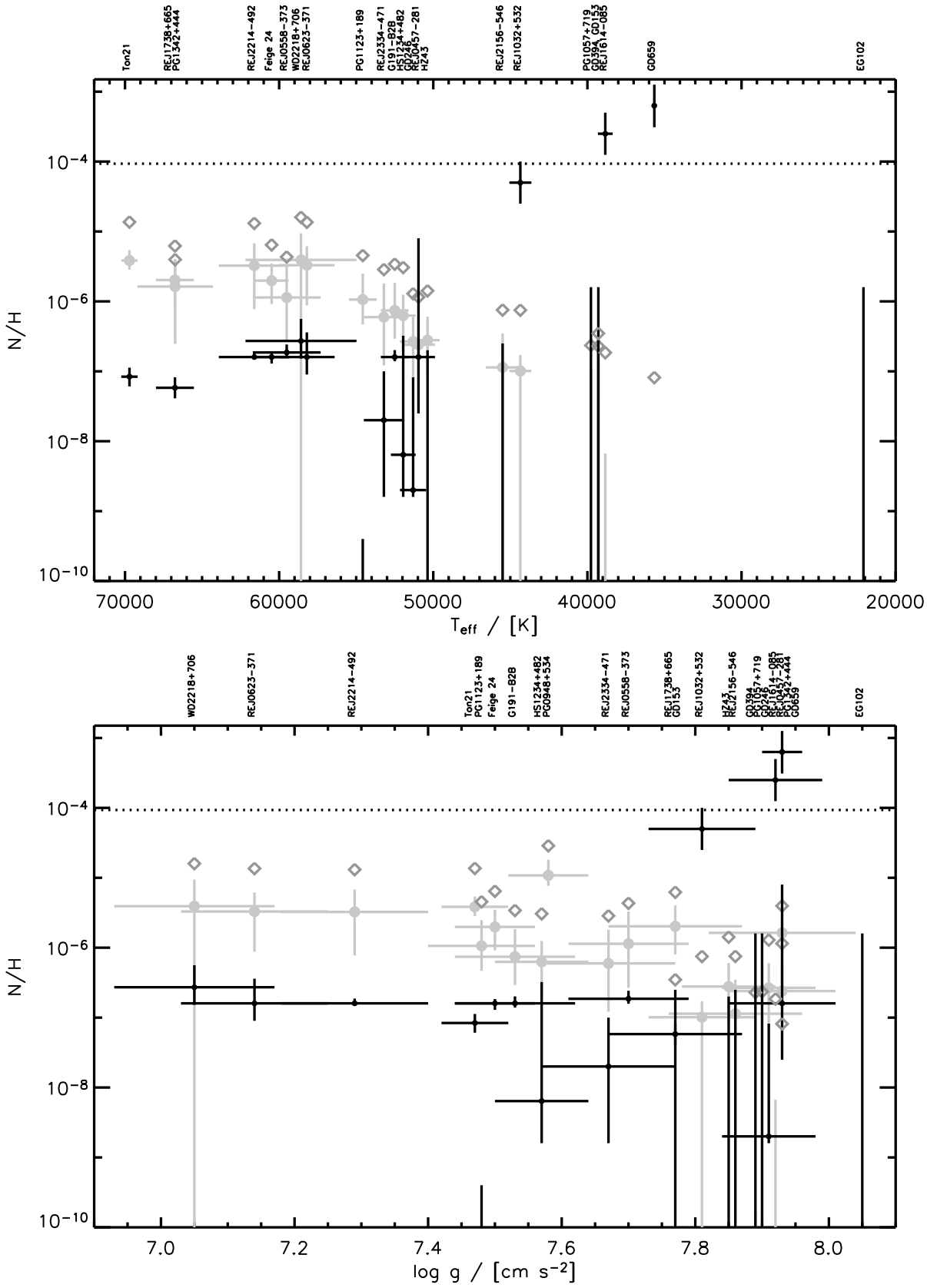

Figure 6.33: UV N abundances as a function of $T_{\rm eff}$ and log g.

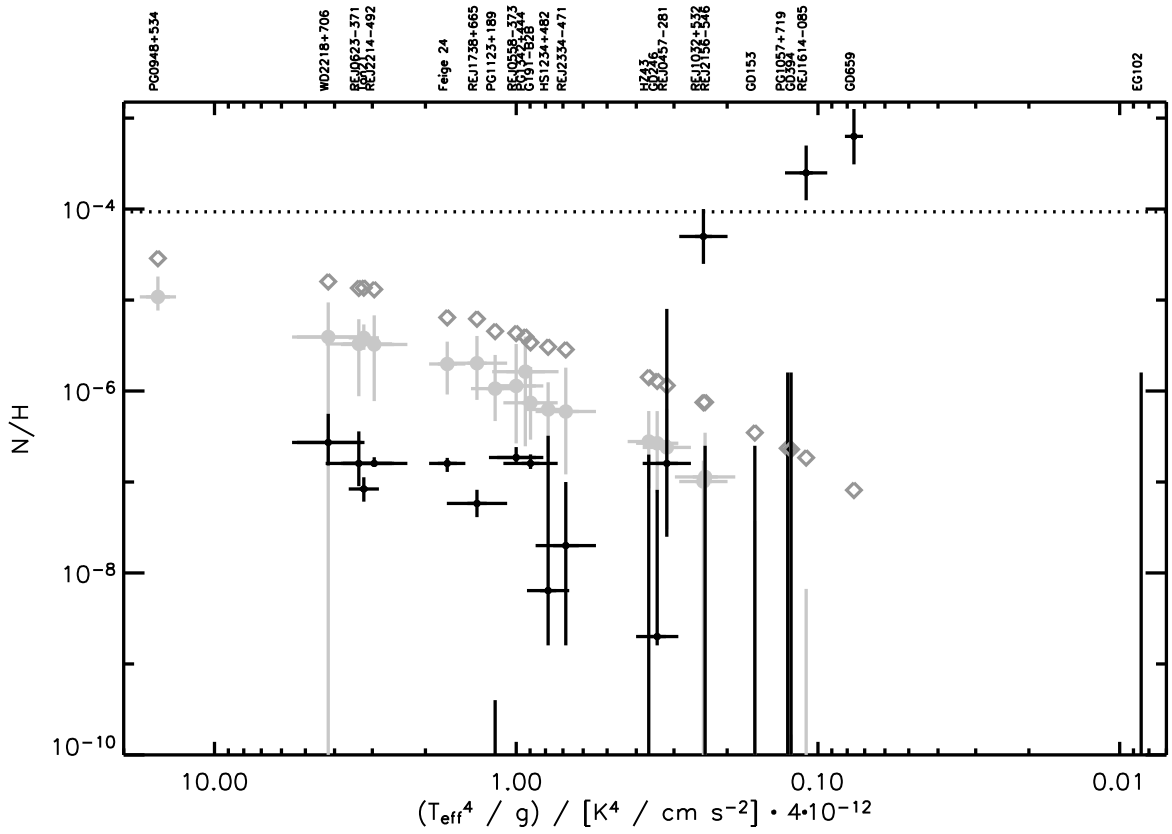

Figure 6.34: UV N abundances as a function of the metal index mi.

$T_{\rm eff}$ makes PG 1342+444 stand out from the overall trend where upper limits for measurements plunge in parallel to theory. It is also noteworthy that PG 1342+444 is the only objects were FUSE spectra were used.

Otherwise there is little formal agreement with predictions unless the measurement errors are very large.

Nitrogen Although not as clearly as for carbon, nitrogen is also over-predicted at higher temperatures. Towards lower temperatures, there is some agreement between $\approx 54\,000$ and 50 000 K while below that the measurements yield only upper limits (remaining compatible with predictions).

The general trend of the models is to run in parallel to what in both Figs. 6.33 and Fig. 6.34 appears as the lower branch of the observed dichotomy at low temperatures/high surface gravities/intermediate metal indices.

On the other hand, it has just been shown in Sect. 6.2.3 that the N V spectral lines of at least one object – RE J1032+535, clearly belonging to the upper branch – can be fit with the N abundance of a diffusion model. While

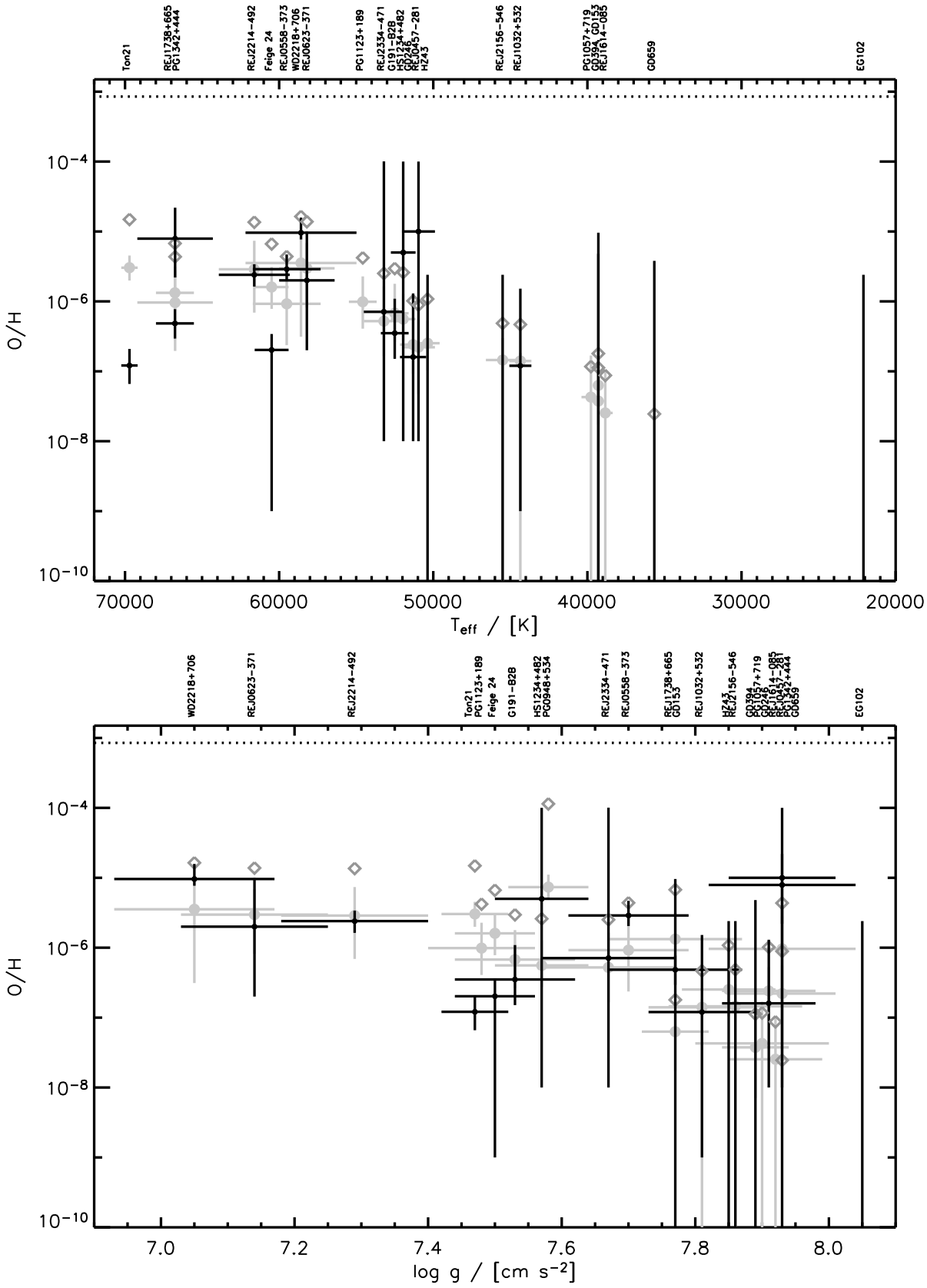

Figure 6.35: UV O abundances as a function of T_{eff} and log g.

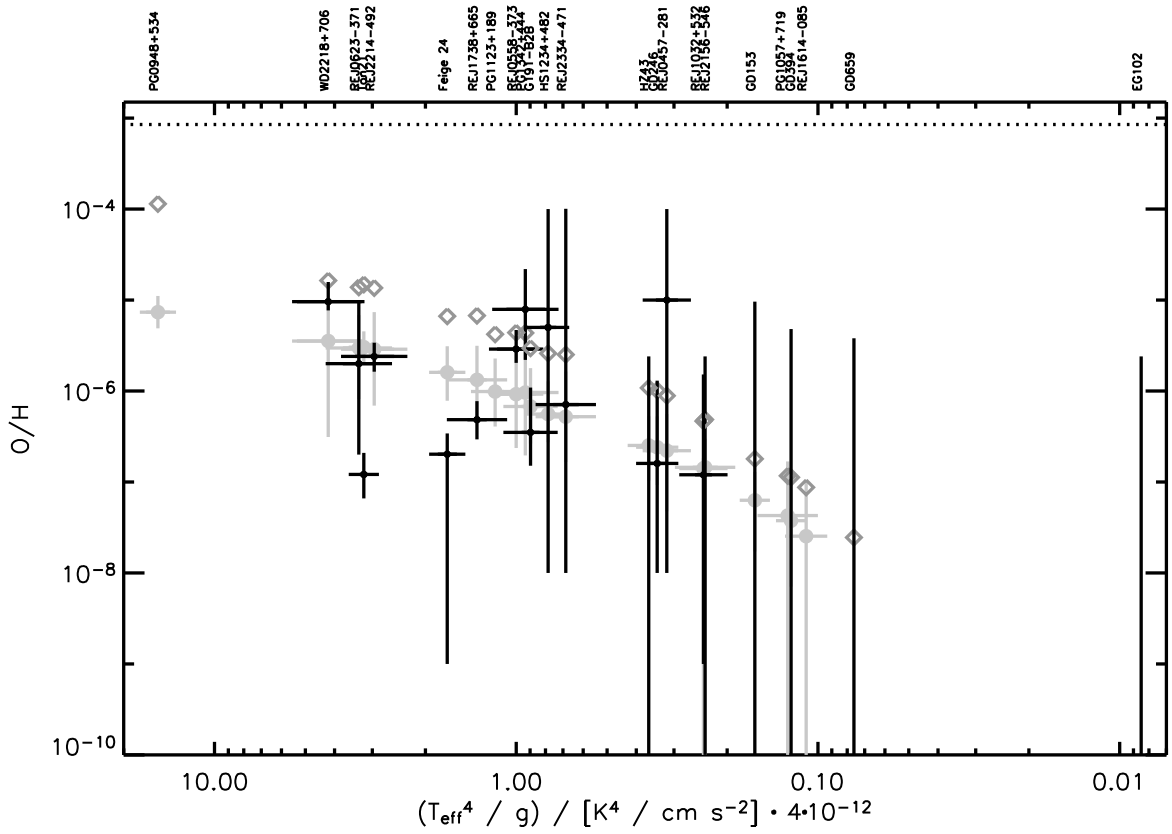

Figure 6.36: UV O abundances as a function of the metal index mi.

Holberg et al. (1999a) and Barstow et al. (2003c) obtain their best fit at a much higher level of $\log(\mathrm{N/H}) = -4.3$, the diffusion model implies a predicted abundance of -7.0 at $\tau_{\mathrm{ross}} = \frac{2}{3}$. This paradox is anything but resolved by Chayer et al. (2005, in press) who also derive a lower abundance, matching the equilibrium abundance very well, from the same HST spectrum.

In Chayer et al. (2005), lower abundances furthermore result for RE J1614−085 and GD 659. The observation that another group of objects at similar atmospheric parameters (RE J2156−546, PG 1057+719, GD 394 and GD 153) does not show nitrogen at all remains unexplained.

Oxygen The trend with effective temperature is generally well followed, and the absolute level of the predictions is also mostly consistent with the observational error bars. Therefore, a quite good overall agreement can be noted for this element.

This positive finding is further confirmed by the successful application of the theoretical stratified O abundance profiles from this work in a detailed analysis of Lanning 23, GD 984, RE J1032+535, and RE J2156−546 presented by

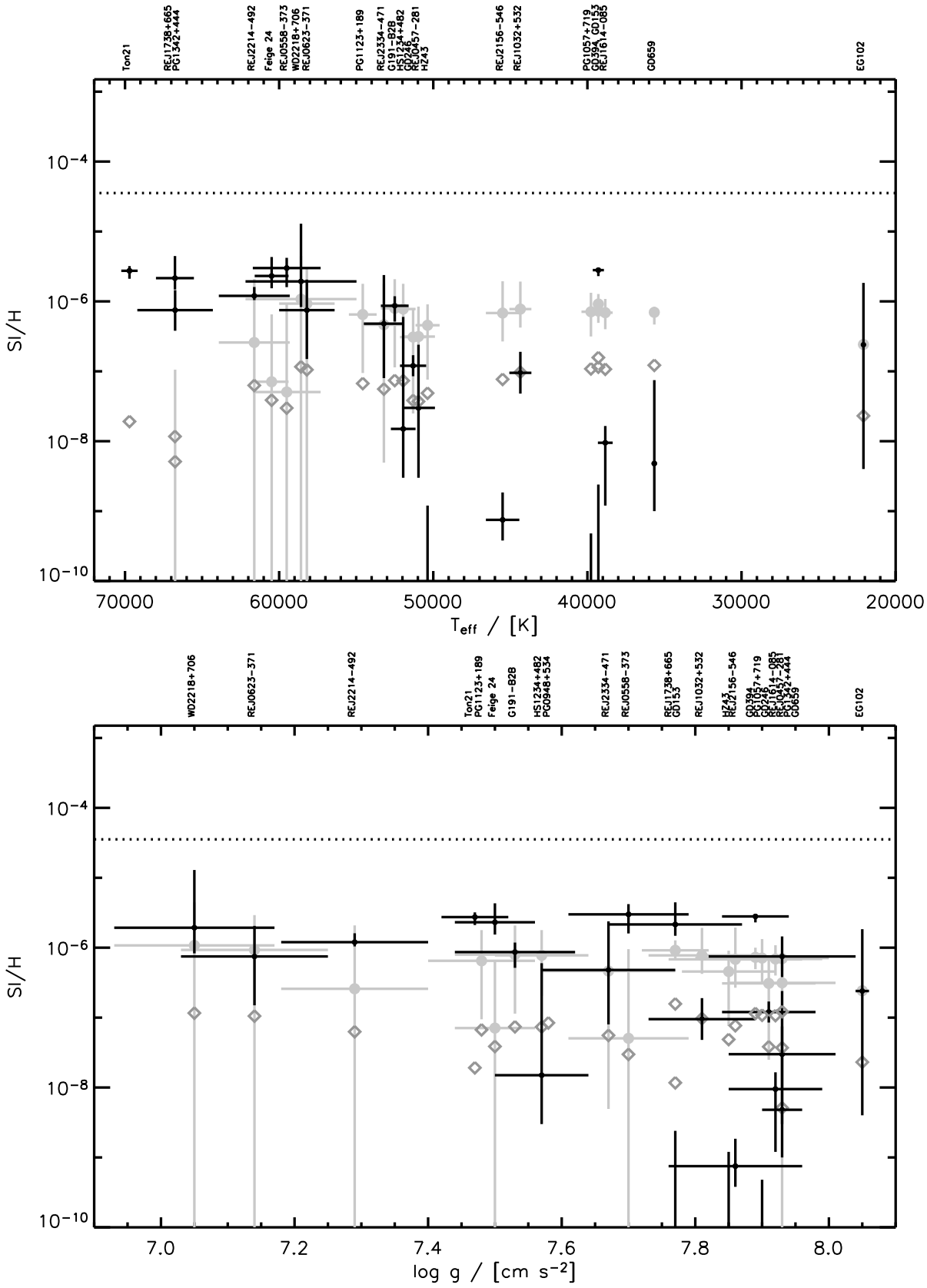

Figure 6.37: UV Si abundances as a function of T_{eff} and log g.

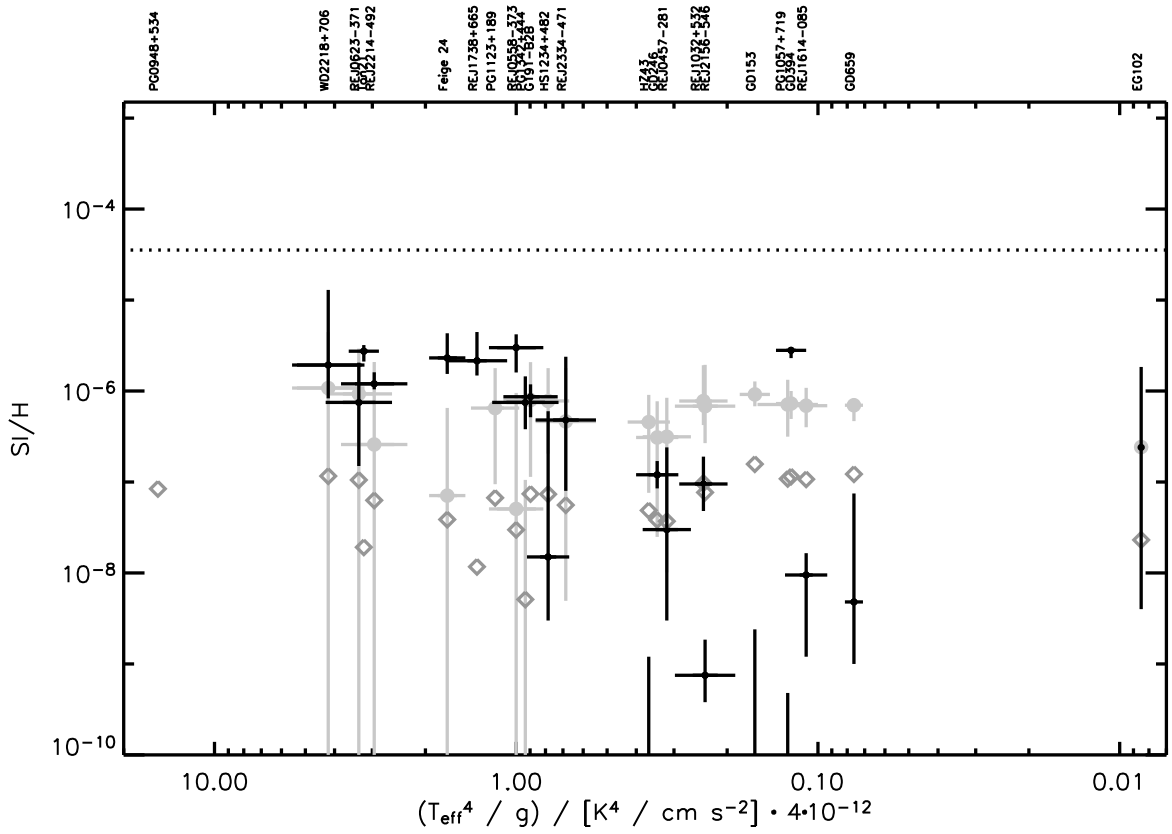

Figure 6.38: UV Si abundances as a function of the metal index mi.

Chayer et al. (2003).

Silicon In contrast to C and N, Si shows opposite gradients with respect to effective temperature in theory and observation, effectively leading to a similarly good agreement as for O in the cross-over area. The slight increase in the equilibrium abundance of Si with decreasing effective temperature is consistent within the theoretical results but leads to under-predictions at higher effective temperatures and over-predictions below $\approx 50\,000\,\mathrm{K}$ in comparison to the observations.

The "normal" behaviour with respect to $\log g$ and a reverted trend with effective temperature combine to prevent a clear sorting of the equilibrium abundances with respect to the metal index mi.

Interestingly, in the lower effective temperature range, the new equilibrium abundances come close to the absolute value observed in GD 394, usually considered to show an anomalously high silicon abundance. This agreement is consistent with the results by Chayer et al. (1997), although the special case of GD 394, as discussed in Sect. 6.2.2, in conjunction with an EUVE spectrum

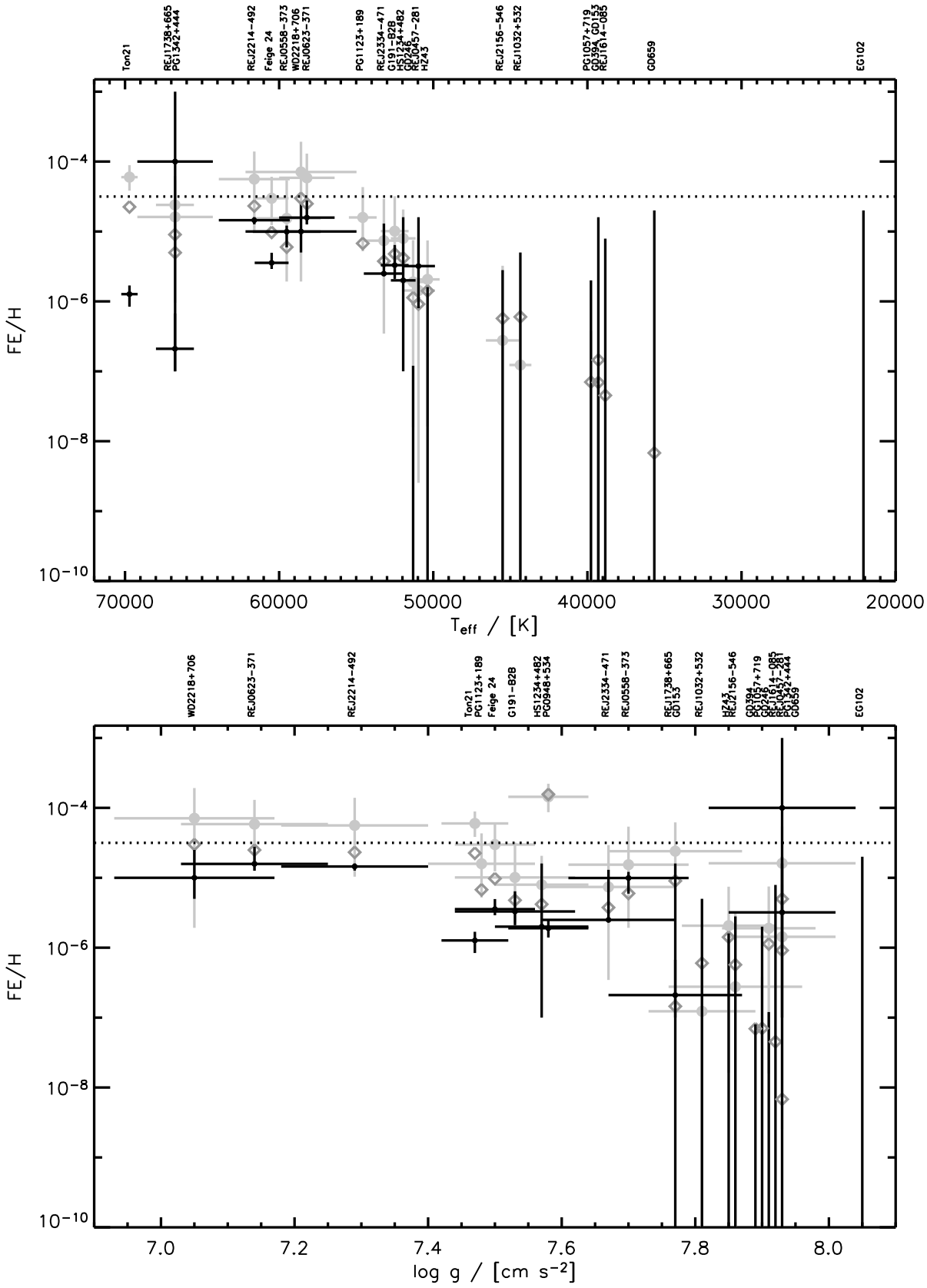

Figure 6.39: UV Fe abundances as a function of T_{eff} and log g.

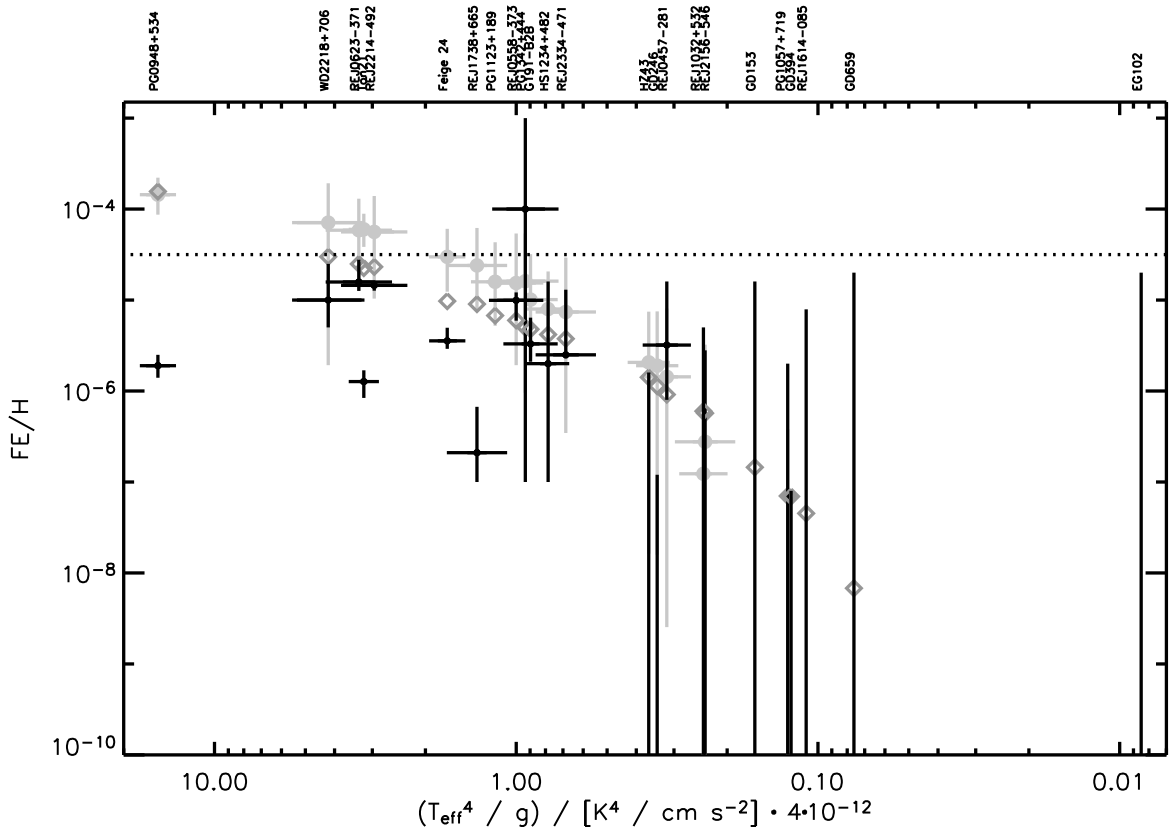

Figure 6.40: UV Fe abundances as a function of the metal index mi.

that cannot be explained by the models here, forbids to associate this with a successful prediction.

Iron The predicted iron abundances are consistent with observations on a star by star basis over practically the full the temperature range considered. On average across all stars, the iron abundance remains about a factor of tow higher than observed, a value of the order of the systematic error expected for the models.

This is in agreement with EUV observations (where Fe is the most important source of opacity) which can for the majority of objects successfully be reproduced with the stratified diffusion models.

The problem seen there for several objects, the necessity of an offset in surface gravity to reconcile theory and observations to further improve the match, is also apparent and can again be retraced here.

Nickel Within the framework of radiative levitation theory, Ni should behave similarly to Fe, which it effectively does, but this predicted behaviour is in disagreement with observations. The observed Ni is well below the prediction,

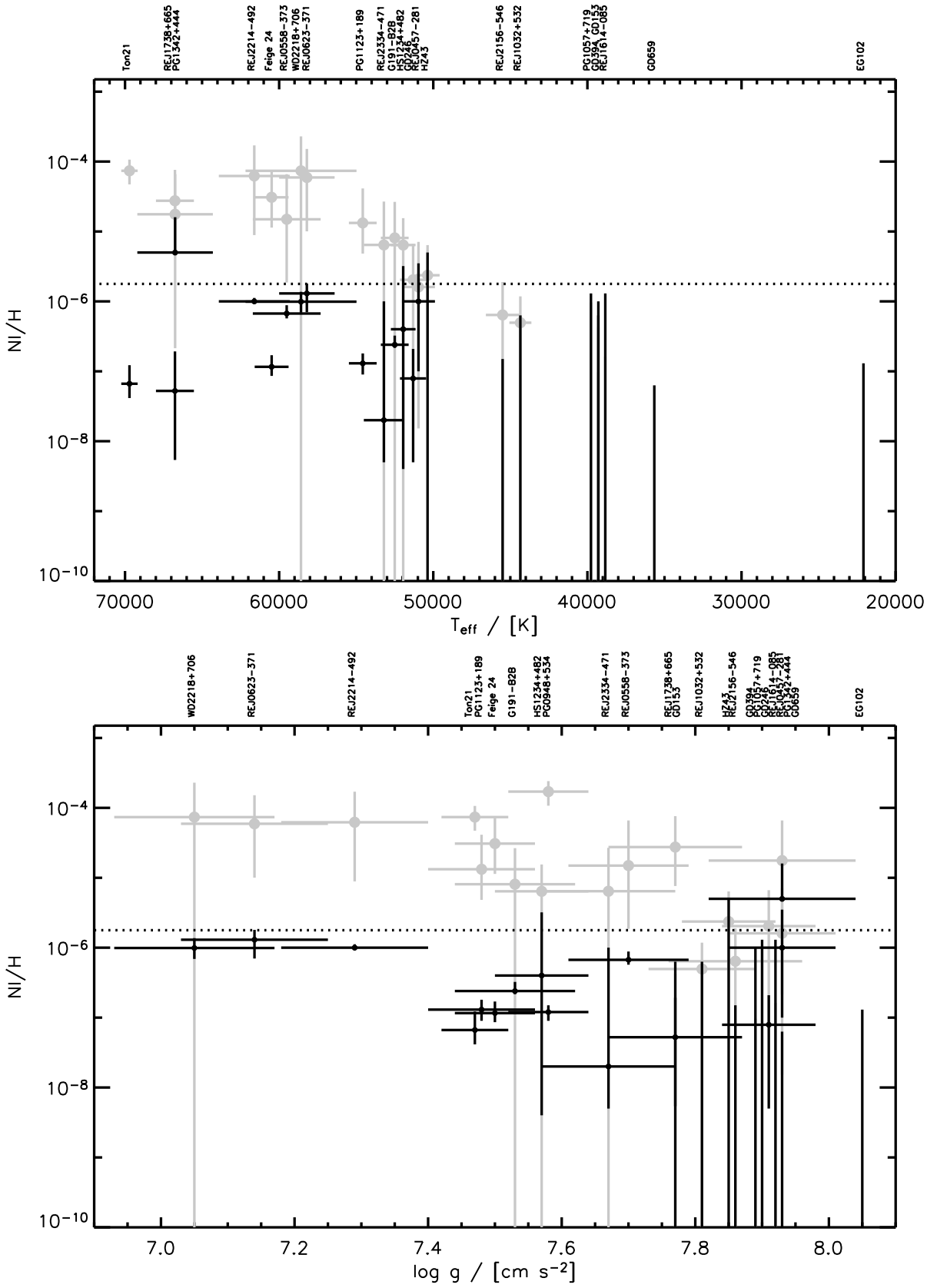

Figure 6.41: UV Ni abundances as a function of T_{eff} and log g.

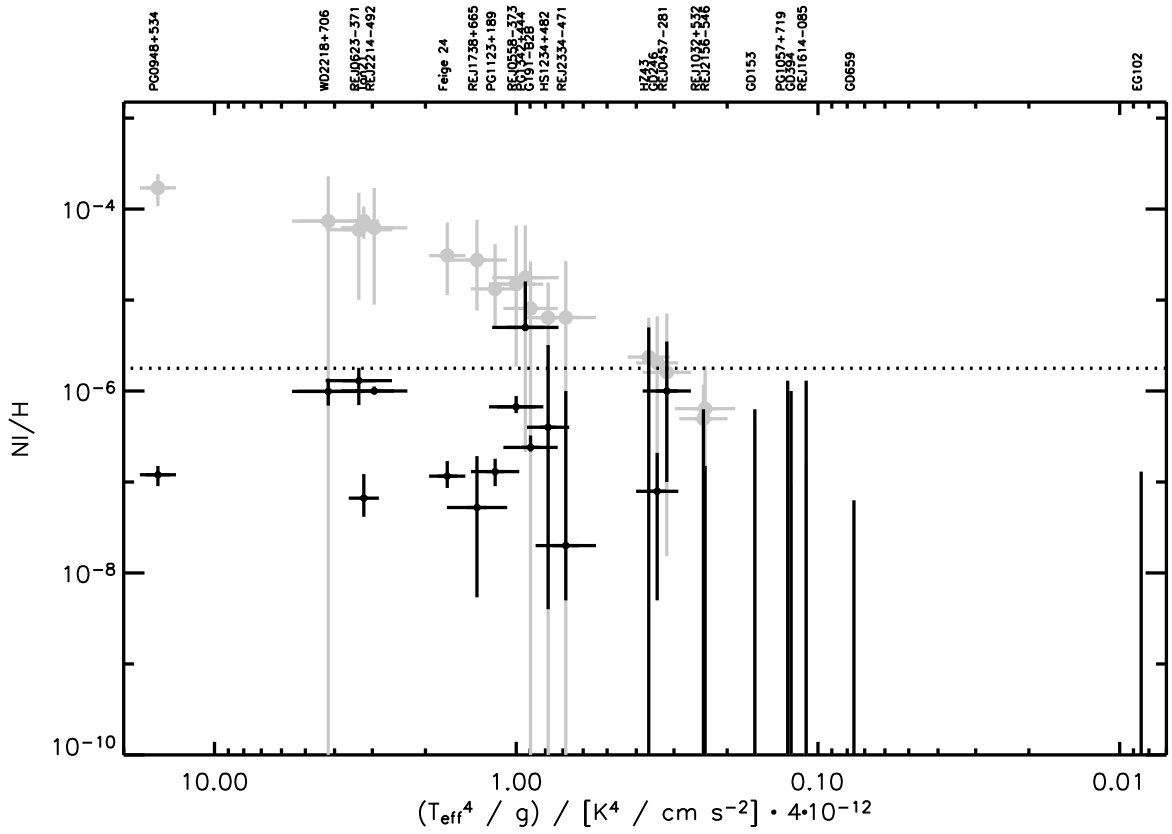

Figure 6.42: UV Ni abundances as a function of the metal index mi.

the over-prediction from the models is clearer than for iron.

So instead of $\frac{\mathrm{Fe}}{\mathrm{Ni}} \approx 1$, Fe and Ni are present in a roughly cosmic ratio – a result already obtained in Barstow et al. (2003c) through a direct comparison.

On the other hand, Werner & Dreizler (1994) have obtained Fe to Ni ratios for RE J0623−377 RE J2214−492, and to a smaller extent for G 191–B2B, and Feige 24 that are lower, indeed implying an enhancement of Ni with respect to Fe attributable to radiative levitation.

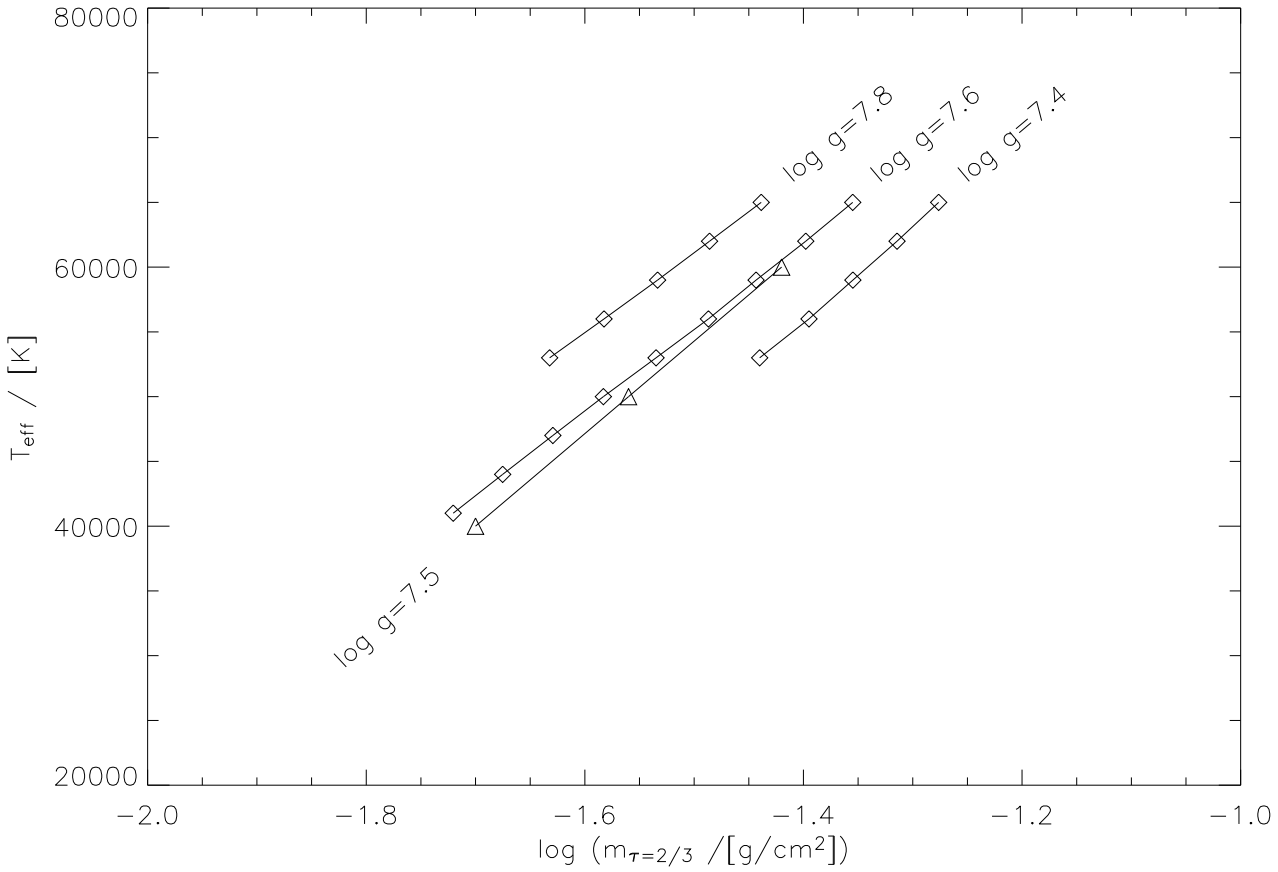

Figure 6.43: In order to estimate if the location of $\tau_{\rm ross} = \frac{2}{3}$ on the mass scale in the Chayer et al. (1995b) models differs significantly from that of the diffusion models in this work, the values in Table 6.3 are compared to similar data from the current model grid. Triangular data points correspond to the mass where $\tau_{\rm ross} = \frac{2}{3}$ in the Chayer et al. models (all at $\log g = 7.5$), diamonds represent the same information for the grid here at surface gravities of 7.4, 7.6, and 7.8. An interpolation of these values to $\log g = 7.5$ (not shown) proves that deviations remain below 0.04 dex for the accessible effective temperature range.

Table 6.3: The location of $\tau_{\rm ross} = \frac{2}{3}$ on the mass scale for Chayer et al. (1995b) models is available for one fixed surface gravity at three different effective temperatures. These values are used in Fig. 6.43.

$T_{\rm eff}$[K]	$\log\,(g\,/\,[\mathrm{cm\,s^{-2}}])$	$\log\,(m_{\tau=\frac{2}{3}}\,/\,[\mathrm{g\,cm^{-2}}])$
40 000	7.5	-1.70
50 000	7.5	-1.56
60 000	7.5	-1.42

CHAPTER 7

Conclusions

7.1 Status of modelling

Stellar atmosphere models have been calculated for the analysis of a sample of hot DA (= hydrogen-rich) white dwarfs. By coupling radiative levitation theory with state-of-the-art metal-line blanketed NLTE stellar atmosphere models and self-consistently solving the full system of equations, photospheric chemical abundance profiles can be predicted by this novel method for a given combination of effective temperature and surface gravity as the only input parameters. The evaluation of radiative accelerations requires a detailed modelling of atomic data. NLTE conditions, fully self-consistent diffusion, and an exhaustive treatment of iron group element atomic data have for the first time been combined to construct models detailed enough for a direct comparison of theoretical emergent fluxes with the high-resolution UV and EUV observations now available.

The main grid of diffusion models consists of atmospheric structures where the abundances of the elements $\mathrm{He}, \mathrm{C}, \mathrm{N}, \mathrm{O}, \mathrm{Si}, \mathrm{Fe}, \mathrm{Ni}$ as trace absorbers in a background plasma dominated by H are self-consistently predicted from an equilibrium condition between radiative levitation and gravitational settling. Abundance tables and high-resolution spectra for the optical, UV to FUV and EUV spectral ranges are available for the full grid. In comparison to Schuh (2000), this implies both a significant enlargement of the model grid as well as more extensive data products.

The main motivation for further developments is the desire for an improved treatment of the radiative accelerations. This can primarily be achieved with more extensive atomic input data, as explored in a few test models. By comparing the results to earlier diffusion calculations (LTE, not self-consistent), and by exploring the effects of improvements in the modelling, a quantitative estimate of the systematic errors inherent in the models is possible. While the internal error within one type of calculation is only about a factor of two, the variations from Chayer et al. (1995b) models to models in this work's major grid, and from those to test models with more elements

included, can amount to 2 dex in the respective equilibrium abundances, mainly due to the strong depth-dependency of the resulting profiles. While these discrepancies are understood to arise from the different conditions imposed on the modelling, it is not immediately clear which of them resemble reality most closely.

7.2 Recapitulation of results from EUV and UV observations

Based on this larger and more complete model grid, and using improved visual magnitudes, a re-analysis of EUVE spectra has been presented. When comparing the theoretical spectra to spectroscopic EUVE observations, the fits turn out to be of good quality for most of the sample stars, and in those cases often better than with chemically homogeneous stellar model atmospheres. The fraction of objects with good fits could be increased thanks to the improvements in the repeated analysis in comparison to Schuh (2000). From these results (published in Schuh et al. 2002), the current implementation of diffusion theory therefore seems to be able to quantitatively describe the processes taking place in moderately hot white dwarf atmospheres and can successfully reproduce observed EUV spectra. Exceptions to this, most prominently perhaps GD 394, have been discussed in the previous chapters.

The picture is more complex for the analysis of UV observations. In that case, instead of matching the spectra directly, abundances derived from individual lines in UV (IUE, HST-GHRS and HST-STIS) spectra with homogeneous models (Barstow et al. 2003c) have been compared to the equilibrium abundance predictions of the diffusion models. Overall the best agreement across the board for individual stars is obtained in the effective temperature range $\approx 50\,000 - 55\,000$ K. However, in strictly absolute values, the offset between observed and predicted abundance levels is often such that no formal agreement of the exact numbers is achievable anywhere on the full parameter range of the model grid. This suggests that an attempt of formally fitting UV spectra with diffusion models would only result in parameters at the edges of the model grid, because it would only be possible to compensate discrepancies in abundance by shifts in effective temperature and surface gravity. The usefulness of such a procedure at the present state is questionable and can currently not be recommended for large samples of stars. Instead, it is advisable to closely examine every object individually, and test various scenarios, to track down the particular reason for potential mismatches between predicted absorption lines and their observed counterparts. The description of the physics in white dwarf atmospheres through diffusion models is most likely still better than with homogeneous models, although those may, due to the significantly larger number of free parameters, currently yield better fits in a direct matching of spectral lines. Exceptions where the diffusion models do better straightaway exist.

One such example of an in-depth examination is the analysis of RE J1032+532.

Also, using the predicted stratification profiles, Chayer et al. (2003) succeeded in simultaneously reproducing the observed oxygen lines of different ionisation stages in FUSE and HST-STIS spectra of GD 984, RE J1032+532 and WD 2152−548.

Generally, the manageable amount of individual lines for most elements, and their good resolution in many UV observations, allows – and requires – one to differentiate more than in EUVE observations. In the element-by-element comparison between theory and measurements, there are cases where both gradients have the same sign as well as cases where they are opposite to each other, so that the required offset in fundamental parameters would even point in different directions, respectively.

Overall, measured photospheric abundances seem to respect cosmic abundances as an upper limit – which the equilibrium abundances do not where the radiative acceleration is large enough –, with very few exceptions: iron and nickel in PG 1342+444, and nitrogen in RE J1614−085 and GD 659 (nitrogen is also close to solar in RE J1032+535). Given that equilibrium radiative levitation theory ignores any evolutionary constraints, the subsolar photospheric abundances may be indicative of a "reservoir problem" (meaning there is no unlimited supply of all elements available) in the real stars.

A summary of all results of the comparison between predicted equilibrium abundances to abundance measurements obtained with homogeneous models from the UV data is shown in Figs. 7.1 and 7.2. Figure 7.1 combines the total of all measurements for all elements and for all stars (sorted by metal index mi; upper plot) and all corresponding predictions (lower plot). This representation does not take into account the errors assigned to these mean values, it just recapitulates the latter from the more detailed graphs in Chapter 6. Figure 7.2 condenses this information further by subtracting the numbers in the upper left from those in the lower left plot. In the upper panel of Fig. 7.2, this is done for the actual mean values. In the lower panel, the errors are now taken into account and the minimal residual differences allowed are shown for all values. Consistency of measurement and prediction within the error bars yields a deviation of zero in this case.

There are three possible sources for the remaining discrepancies still seen in the merged final results. The errors cited above are statistical errors, but from the comparison of different homogeneous analyses alone, the various results from several works imply that the hidden systematic errors must be at least of the order of ± 1 dex (see the examples of the nitrogen abundance for RE J1032+535, the nickel abundances for RE J0623−377 and RE J2214−492, or the fundamental parameters for G 191–B2B).

Besides these uncertainties in methods regarded as well established for the determination of abundances from the analysis of observations, successive generations of diffusion models that try to predict these results still disagree with each other by up to 2 dex. In the same spirit as above, this must be interpreted as the systematic errors

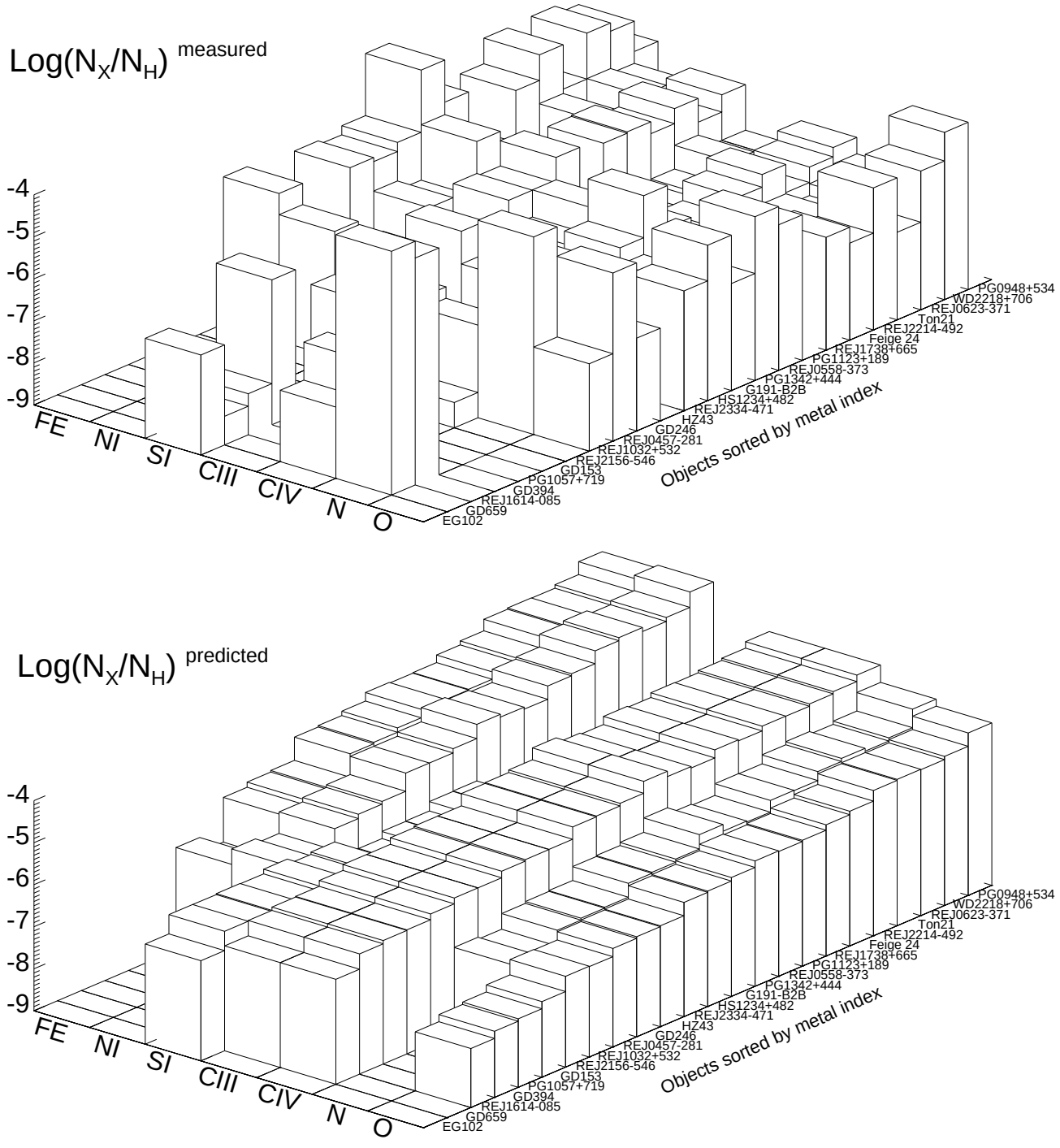

Figure 7.1: Summary of predicted (bottom) and measured (top) UV abundances for all objects for all elements. The elements are roughly sorted by overall equilibrium abundance level in the predictions, the objects are sorted by metal index mi. Zero values for which only upper limits exist are arbitrarily set to a value of 10^{-9}.

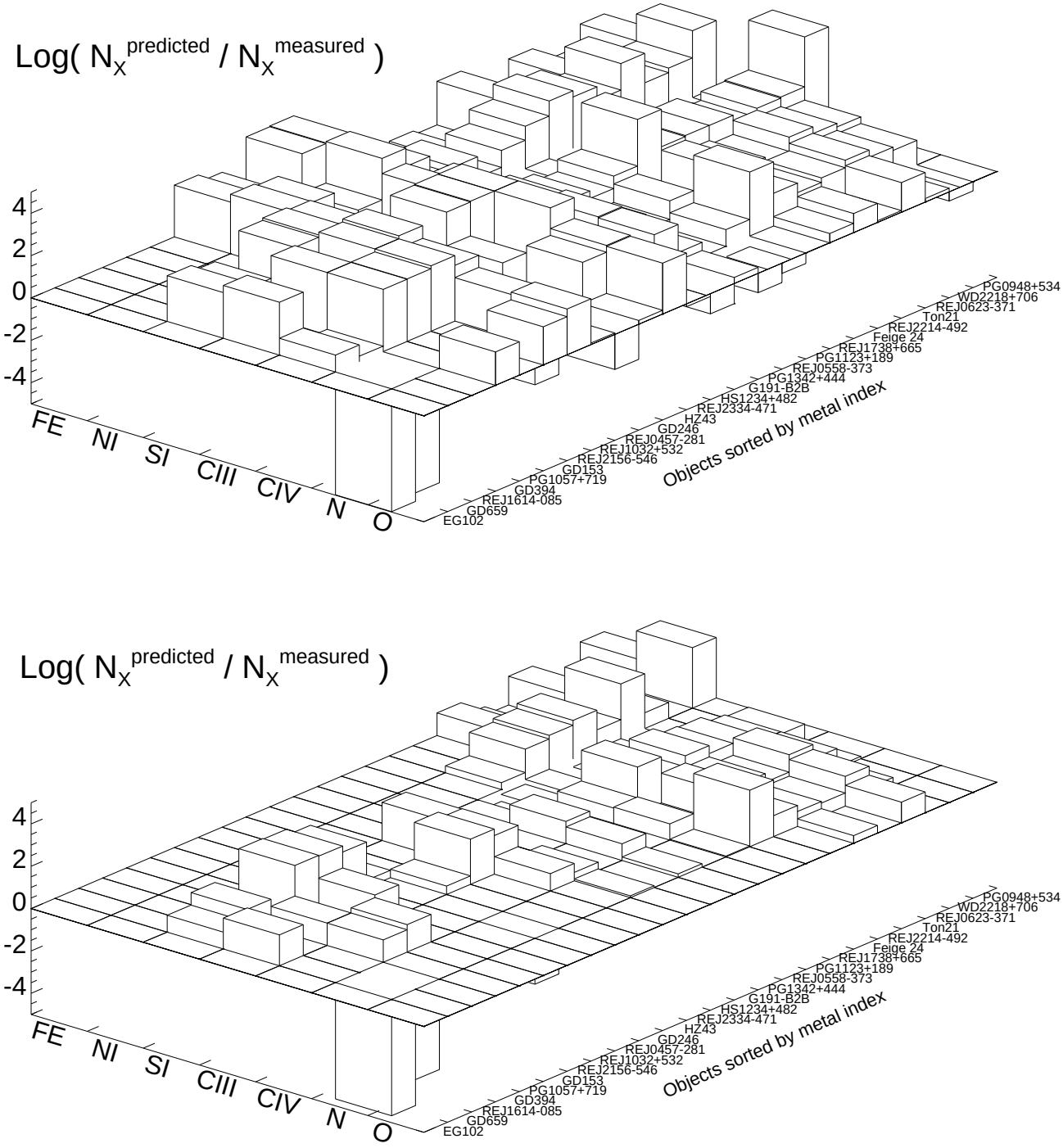

Figure 7.2: Summary of deviations between predicted and measured abundances: The upper panel is the difference between the lower and upper plots in Fig. 7.1, the lower panel takes into account the errors (or upper limits, as in Chapter 6, not shown in Fig. 7.1). The difference in dex is set to the minimal distance between abundance measures with non-overlapping error bars, and to zero for values that are consistent with each other within the error bars. It is also set to zero for non-existing measurements (14 out of a total of 168).

currently inherent in the models. Taking together these two contributions, it seems possible to reconcile a good number of the residuals in Fig. 7.2 with a value near zero.

The third possibility is to attribute the deviations to physical processes ignored so far in the models such as mass-loss, mixing, or accretion. There is, however, no evidence of any clear pattern in the residuals that would help to explore a possible correlation with stellar parameters. While mass-loss effects would disturb equilibrium conditions predominantly in the high metal index range, accretion would be expected to have an effect only at lower metal indices.

In summary, the impression remains that the equilibrium abundances are generally too high. Any suspicion that measurements with homogeneous models may result in systematically lower values is partly invalidated by the results from the EUVE fits. Apart from perhaps a factor of two, the level of iron is well matched by predictions with respect to the UV measurements, and the same agreement, also with a slight trend towards too high equilibrium values, is seen in the EUVE analysis where the spectra are dominated by the iron content of the atmosphere. The few mismatches in the EUV analysis have a tendency to cluster in the intermediate metal index regime. The abundance levels of other elements are relatively unimportant and therefore do not spoil the overall encouraging results from the EUVE analysis. The UV analysis results imply that equilibrium radiative levitation theory still has some problems to reproduce in detail the multi-wavelength spectral evolution of white dwarfs.

There are two results that suggest that a limited supply of elements from the outset may be the key to the problem: The observed nickel abundances appear to be limited by the cosmic nickel abundance. Despite similar reactions to radiative momentum transfer that would result in roughly equal equilibrium abundances for iron and nickel, these cannot be reached in the case of nickel since its cosmic abundance is lower than the predicted abundance level, and lower than that of iron where this restriction does not apply. The same circumstances seem to prevent a realistic description of the less abundant iron group elements that have tentatively been included in test calculations in the equilibrium approach and reach unrealistically high levels. In a less obvious way, this restricting mechanism could also influence the abundances of other elements that in the calculations formally remain below the cosmic abundance limit.

7.3 Perspective

On the observational side, the legacy of HST-STIS was irrevocably completed with the failure of this instrument in August 2004. The set of UV white dwarf spectra available may now only be amended by FUSE, which covers shorter wavelengths, provided it comes back into normal operations from its current safe mode status due

to the failure of another reaction wheel. It can be hoped that a fairly homogeneous and decently calibrated data set will be available from FUSE in a few years' time. Further progress would also be possible with the planned WSO (World Space Observatory) which will take some time to come into existence, if at all.

Another approach is pursued in rocket-based experiments such as J-PEX: In a collaboration with the group who flew with this mission, the high-resolution EUV data of G 191–B2B have been analysed, among other models with the diffusion models from this work. Results will be published in Barstow et al. (2005).

The present successes on a global scale as seen in the EUVE analysis justify a further pursuit of the radiative equilibrium theory approach. Due to remaining puzzles in detailed comparisons, further efforts to improve the existing models are necessary. Those include a strategy for the consideration of *all* elements, the inclusion of fine structure in the atomic data of non-iron-group elements, the implementation of momentum redistribution, and of a more efficient coupling between the computation of the model structure and the chemical stratification.

Ultimately, this method will probably be found to be the correct approach to determine depth-dependent photospheric abundances. What remains to be done is the major step of replacing the present equilibrium approach with the treatment of fully time-dependent diffusion in the non-equilibrium case together with mass-loss for self-consistent NLTE models, where the accumulation and successive removal of reservoirs can be tracked over time. These improvements, necessary in a longer perspective, are beyond the scope of the present thesis.

Bibliography

Abazajian, K., Adelman-McCarthy, J. K., Agüeros, M. A., et al. 2003, AJ, 126, 2081

Acker, A., Marcout, J., Ochsenbein, F., Stenholm, B., & Tylenda, R. 1992, Strasbourg - ESO catalogue of galactic planetary nebulae. Part 1; Part 2 (Garching: European Southern Observatory, 1992)

Bannister, N. P., Barstow, M. A., Holberg, J. B., & Bruhweiler, F. C. 2003, MNRAS, 341, 477

Barnard, A. J., Cooper, J., & Shamey, L. J. 1969, A&A, 1, 28

Barstow, M., Cruddace, R., Kowalski, M., et al. 2005, MNRAS, submitted

Barstow, M. A., Bannister, N. P., Holberg, J. B., et al. 2001a, MNRAS, 325, 1149

Barstow, M. A., Burleigh, M. R., Bannister, N. P., Holberg, J. B., & Hubeny, I. 2001b, in ASP Conf. Ser. 226: $12^{\rm th}$ European Workshop on White Dwarfs, 94

Barstow, M. A., Dobbie, P. D., Holberg, J. B., Hubeny, I., & Lanz, T. 1997, MNRAS, 286, 58

Barstow, M. A., Fleming, T. A., Diamond, C. J., et al. 1993a, MNRAS, 264, 16

Barstow, M. A., Fleming, T. A., Finley, D. S., Koester, D., & Diamond, C. J. 1993b, MNRAS, 260, 631

Barstow, M. A., Good, S. A., Bannister, N. P., et al. 2003a, in NATO ASIB Proc. 105: White Dwarfs, 121

Barstow, M. A., Good, S. A., Burleigh, M. R., et al. 2003b, MNRAS, 344, 562

Barstow, M. A., Good, S. A., Holberg, J. B., et al. 2002, MNRAS, 330, 425

Barstow, M. A., Good, S. A., Holberg, J. B., et al. 2003c, MNRAS, 341, 870

Barstow, M. A., Holberg, J. B., Fleming, T. A., et al. 1994a, MNRAS, 270, 499

Barstow, M. A., Holberg, J. B., Hubeny, I., et al. 2001c, MNRAS, 328, 211

Barstow, M. A., Holberg, J. B., Hubeny, I., et al. 1996, MNRAS, 279, 1120

Barstow, M. A., Holberg, J. B., & Koester, D. 1994b, MNRAS, 268, L35

Barstow, M. A., Holberg, J. B., & Koester, D. 1995, MNRAS, 274, L31

Barstow, M. A., Holberg, J. B., Marsh, M. C., et al. 1994c, MNRAS, 271, 175

Barstow, M. A. & Hubeny, I. 1998, MNRAS, 299, 379

Barstow, M. A., Hubeny, I., & Holberg, J. B. 1998, MNRAS, 299, 520

Barstow, M. A., Hubeny, I., & Holberg, J. B. 1999, MNRAS, 307, 884

Barstow, M. A., Wesemael, F., Fontaine, G., et al. 1992, IAU Circ., 5518, 1

Barstow, M. A., Wesemael, F., Holberg, J. B., et al. 1994d, MNRAS, 267, 647

Benedict, G. F., McArthur, B. E., Franz, O. G., et al. 2000, AJ, 119, 2382

Bergeron, P. & Leggett, S. K. 2002, ApJ, 580, 1070

Bergeron, P., Saffer, R. A., & Liebert, J. 1992, ApJ, 394, 228

Bergeron, P., Wesemael, F., Beauchamp, A.,

et al. 1994, ApJ, 432, 305
Bessell, M. S. 1999, PASP, 111, 1426
Bohlin, R. C. 1996, AJ, 111, 1743
Bohlin, R. C. 2000, AJ, 120, 437
Bohlin, R. C., Colina, L., & Finley, D. S. 1995, AJ, 110, 1316
Bohlin, R. C., Dickinson, M. E., & Calzetti, D. 2001, AJ, 122, 2118
Bowyer, S., Sasseen, T. P., Lampton, M., & Wu, X. 1993, ApJ, 415, 875
Bruhweiler, F., Barstow, M., Holberg, J., & Sahu, M. 1999, Bulletin of the American Astronomical Society, 31, 1419
Bruhweiler, F. C. & Kondo, Y. 1983, ApJ, 269, 657
Budaj, J. & Dworetsky, M. M. 2002, MNRAS, 337, 1340
Chapman, S. & Cowling, T. G. 1970, The mathematical theory of non-uniform gases. An account of the kinetic theory of viscosity, thermal conduction and diffusion in gases (Cambridge: University Press, 1970, 3rd ed.)
Chayer, P., Fontaine, G., & Pelletier, C. 1997, in ASSL Vol. 214: White dwarfs, 253
Chayer, P., Fontaine, G., & Wesemael, F. 1989, in IAU Colloq. 114: White Dwarfs, 253
Chayer, P., Fontaine, G., & Wesemael, F. 1991, in NATO ASIC Proc. 336: White Dwarfs, 249
Chayer, P., Fontaine, G., & Wesemael, F. 1995a, ApJS, 99, 189
Chayer, P., Kruk, J. W., Ake, T. B., et al. 2000, ApJ, 538, L91
Chayer, P., Kruk, J. W., Vennes, S., & Dupuis, J. 2001, in ASP Conf. Ser. 226: 12$^{\rm th}$ European Workshop on White Dwarfs, 90
Chayer, P., LeBlanc, F., Fontaine, G., et al. 1994, ApJ, 436, L161
Chayer, P., Oliveira, C., Dupuis, J., Moos, H. W., & Welsh, B. 2003, in Kluwer Academics NATO Science Series II., Vol. 105, The 13$^{\rm th}$ European Workshop on White Dwarfs, ed. D. de Martino, R. Silvotti, J.-E. Solheim, & R. Kalytis, 127
Chayer, P., Vennes, S., & Dupuis, J. 2005, in ASP Conf. Series: 14$^{\rm th}$ European Workshop on White Dwarfs, ed. D. Koester & S. Möhler, in press
Chayer, P., Vennes, S., Pradhan, A. K., et al. 1995b, ApJ, 454, 429
Chen, B., Schartel, N., Kirsch, M. G. F., et al. 2004, Memorie della Societa Astronomica Italiana, 75, 561
Chu, Y., Guerrero, M. A., Gruendl, R. A., & Webbink, R. F. 2004, AJ, 127, 477
Colina, L. & Bohlin, R. C. 1994, AJ, 108, 1931
Cruddace, R. G., Kowalski, M. P., Yentis, D., et al. 2002, ApJ, 565, L47
Cunto, W. & Mendoza, C. 1992, Revista Mexicana de Astronomia y Astrofisica, vol. 23, 23, 107
Debes, J. H. & Sigurdsson, S. 2002, ApJ, 572, 556
Deetjen, J. L., Dreizler, S., Jordan, S., & Werner, K. 2003, in ASP Conf. Ser. 288: Stellar Atmosphere Modeling, 617
Demers, S., Beland, S., Kibblewhite, E. J., Irwin, M. J., & Nithakorn, D. S. 1986, AJ, 92, 878
Dixon, W. V. D., Dupuis, J., & Hurwitz, M. 2002, PASP, 114, 112
Dreizler, S. 1999, A&A, 352, 632
Dreizler, S. 2002, Sternatmosphären I+II, lecture notes (University of Tübingen), available at http://astro.uni-tuebingen.de/~dreizler/teaching/Sternatmosphaeren.html
Dreizler, S. 2003, in ASP Conf. Ser. 288: Stellar Atmosphere Modeling, 69
Dreizler, S. & Schuh, S. 2001, in ASP Conference Series, Vol. 226, The 12$^{\rm th}$ European Workshop on White Dwarfs, ed. J. L. Provencal, H. L. Shipman, J. MacDonald, & S. Goodchild, 69

Dreizler, S. & Schuh, S. L. 2003, in IAU Symposium 210: Modelling of Stellar Atmospheres, ed. N. E. Piskunov, W. W. Weiss, & D. F. Gray, 33

Dreizler, S. & Werner, K. 1993, A&A, 278, 199

Dreizler, S. & Wolff, B. 1999, A&A, 348, 189

Dupuis, J., Chayer, P., Kruk, J. W., & Vennes, S. 2003, in Kluwer Academics NATO Science Series II., Vol. 105, The 13$^{\rm th}$ European Workshop on White Dwarfs, ed. D. de Martino, R. Silvotti, J.-E. Solheim, & R. Kalytis, 157

Dupuis, J., Chayer, P., Vennes, S., Christian, D. J., & Kruk, J. W. 2000a, ApJ, 537, 977

Dupuis, J., Vennes, S., Bowyer, S., Pradhan, A. K., & Thejll, P. 1995, ApJ, 455, 574

Dupuis, J., Vennes, S., & Chayer, P. 2000b, Bulletin of the American Astronomical Society, 32, 1543

Dupuis, J., Vennes, S., Chayer, P., Hurwitz, M., & Bowyer, S. 1998, ApJ, 500, L45+

Elvis, M., Plummer, D., Schachter, J., & Fabbiano, G. 1992, ApJS, 80, 257

Fan, X. 1999, AJ, 117, 2528

Feautrier, P. 1964, C. R. Acad. Sc. Paris, 258, 3189

Finley, D. S., Basri, G., & Bowyer, S. 1984, Self-consistent recalibration of IUE determination of hot DA white dwarf effective temperatures, Tech. rep.

Finley, D. S., Jelinsky, P., Dupuis, J., & Koester, D. 1993, ApJ, 417, 259

Finley, D. S., Koester, D., & Basri, G. 1997, ApJ, 488, 375

Fontaine, G., Brassard, P., & Bergeron, P. 2001, PASP, 113, 409

Fontaine, G. & Chayer, P. 1997, in The Third Conference on Faint Blue Stars, 169

Fontaine, G. & Michaud, G. 1979, ApJ, 231, 826

Fuhrmeister, B. & Schmitt, J. H. M. M. 2003, A&A, 403, 247

Gonzalez, J.-F., Leblanc, F., Artru, M.-C., & Michaud, G. 1995, A&A, 297, 223

Green, R. F. 1980, ApJ, 238, 685

Green, R. F., Schmidt, M., & Liebert, J. 1986, ApJS, 61, 305

Greenstein, J. L. & Liebert, J. W. 1990, ApJ, 360, 662

Greenstein, J. S., Truran, J. W., & Cameron, A. G. W. 1967, Nat, 213, 871

Griem, H. R. 1974, Spectral line broadening by plasmas (Pure and Applied Physics, New York: Academic Press, 1974)

Gunderson, K., Wilkinson, E., Green, J. C., & Barstow, M. A. 2001, ApJ, 562, 992

Hébrard, G., Allard, N. F., Kielkopf, J. F., et al. 2003, A&A, 405, 1153

Hébrard, G., Lemoine, M., Vidal-Madjar, A., et al. 2002, ApJS, 140, 103

Hagen, H.-J., Groote, D., Engels, D., & Reimers, D. 1995, A&AS, 111, 195

Harris, H. C., Liebert, J., Kleinman, S. J., et al. 2003, AJ, 126, 1023

Hawarden, T. G., Leggett, S. K., Letawsky, M. B., Ballantyne, D. R., & Casali, M. M. 2001, MNRAS, 325, 563

Hearn, D. R., Richardson, J. A., Bradt, H. V. D., et al. 1976, ApJL, 203, L21

Heber, U., Napiwotzki, R., & Reid, I. N. 1997, A&A, 323, 819

Hertzsprung, E. 1911, Publikationen des Astrophysikalischen Observatoriums zu Potsdam, 63

Hill, P. W. & Hill, S. R. 1966, MNRAS, 133, 205

Holberg, J. B., Barstow, M. A., Bruhweiler, F. C., & Collins, J. 1996, AJ, 111, 2361

Holberg, J. B., Barstow, M. A., Bruhweiler, F. C., & Hubeny, I. 2000, Bulletin of the American Astronomical Society, 32, 1543

Holberg, J. B., Barstow, M. A., Bruhweiler, F. C., Hubeny, I., & Green, E. M. 1999a, ApJ, 517, 850

Holberg, J. B., Barstow, M. A., Bruhweiler,

F. C., & Sion, E. M. 1995, ApJ, 453, 313
Holberg, J. B., Barstow, M. A., Buckley, D. A. H., et al. 1993, ApJ, 416, 806
Holberg, J. B., Barstow, M. A., & Green, E. M. 1997a, ApJ, 474, L127+
Holberg, J. B., Barstow, M. A., Hubeny, I., et al. 2002, Bulletin of the American Astronomical Society, 34, 765
Holberg, J. B., Barstow, M. A., Lanz, T., & Hubeny, I. 1997b, ApJ, 484, 871
Holberg, J. B., Barstow, M. A., & Sion, E. M. 1998, ApJS, 119, 207
Holberg, J. B., Basile, J., & Wesemael, F. 1986, ApJ, 306, 629
Holberg, J. B., Bruhweiler, F. C., Barstow, M. A., & Dobbie, P. D. 1999b, ApJ, 517, 841
Holberg, J. B., Hubeny, I., Barstow, M. A., et al. 1994, ApJ, 425, L105
Homeier, D., Koester, D., Hagen, H.-J., et al. 1998, A&A, 338, 563
Hubeny, I. & Lanz, T. 1995, ApJ, 439, 875
Hubeny, I. & Lanz, T. 2000, SYNSPEC - A User's Guide, version 43 edn., NASA/GSFC, Code 681, Greenbelt, MD 20771, (current version is 48)
Hubeny, I. & Lanz, T. 2003, in ASP Conference Series, Vol. 288, Stellar Atmosphere Modeling, ed. I. Hubeny, D. Mihalas, & K. Werner, 51
Hubeny, I., Mihalas, D., & Werner, K., eds. 2003, Stellar Atmosphere Modeling
Hui-Bon-Hoa, A., LeBlanc, F., & Hauschildt, P. H. 2000, ApJL, 535, L43
Hui-Bon-Hoa, A., LeBlanc, F., Hauschildt, P. H., & Baron, E. 2002, A&A, 381, 197
Hummer, D. G. & Mihalas, D. 1988, ApJ, 331, 794
Hurwitz, M., Bowyer, S., Bristol, R., et al. 1998, ApJ, 500, L1+
Jansen, F., Lumb, D., Altieri, B., et al. 2001, A&A, 365, L1
Jordan, S., Koester, D., & Finley, D. 1996, in IAU Colloq. 152: Astrophysics in the Extreme Ultraviolet, 235
Jordan, S., Koester, D., Wulf-Mathies, C., & Brunner, H. 1987, A&A, 185, 253
Jordan, S., Wolff, B., Koester, D., & Napiwotzki, R. 1994, A&A, 290, 834
Kahn, S. M., Wesemael, F., Liebert, J., et al. 1984, ApJ, 278, 255
Kaiser, M. E., Bohlin, R. C., Lindler, D. J., et al. 1998, PASP, 110, 978
Kidder, K. M., Holberg, J. B., & Mason, P. A. 1991, AJ, 101, 579
Kilkenny, D., O'Donoghue, D., Koen, C., Stobie, R. S., & Chen, A. 1997, MNRAS, 287, 867
Kimble, R. A., Davidsen, A. F., Blair, W. P., et al. 1993a, ApJ, 404, 663
Kimble, R. A., Davidsen, A. F., Long, K. S., & Feldman, P. D. 1993b, ApJ, 408, L41
Kippenhahn, R. & Weigert, A. 1990, Stellar Structure and Evolution, 1st edn., ed. I. Appenzeller, M. Harwit, R. Kippenhahn, P. Strittmatter, & V. Trimble, Astronomy and Astrophysics Library (Berlin, Heidelberg, New York: Springer Verlag)
Kleinman, S. J., Harris, H. C., Eisenstein, D. J., et al. 2004, ApJ, 607, 426
Koester, D. 1989, in Lecture Notes in Physics, Vol. 328, IAU Colloq. 114: White Dwarfs, ed. G. Wegner, 206
Koester, D. 2002, A&ARv, 11, 33
Koester, D. & Chanmugam, G. 1990, Reports of Progress in Physics, 53, 837
Koester, D., Dreizler, S., Weidemann, V., & Allard, N. F. 1998, A&A, 338, 612
Koester, D., Napiwotzki, R., Christlieb, N., et al. 2001, A&A, 378, 556
Kruk, J. W. 1998, in IAU Symp. 189: Fundamental Stellar Properties, 67
Kruk, J. W., Brown, T. M., Davidsen, A. F., et al. 1999, ApJS, 122, 299
Kruk, J. W., Howk, J. C., André, M., et al. 2002, ApJS, 140, 19

Kruk, J. W., Kimble, R. A., Buss, R. H., et al. 1997, ApJ, 482, 546
Kunasz, P. B. & Olson, G. L. 1988, Journal of Quantitative Spectroscopy and Radiative Transfer, 39, 1
Kurucz, R. L. 1991, in NATO ASIC Proc. 341: Stellar Atmospheres - Beyond Classical Models, 441
Lamontagne, R., Demers, S., Wesemael, F., Fontaine, G., & Irwin, M. J. 2000, AJ, 119, 241
Lampton, M., Margon, B., Paresce, F., Stern, R., & Bowyer, S. 1976, ApJL, 203, L71
Lanz, T., Barstow, M. A., Hubeny, I., & Holberg, J. B. 1996, ApJ, 473, 1089
Lanz, T. & Hubeny, I. 1995, ApJ, 439, 905
Lehner, N., Gry, C., Sembach, K. R., et al. 2002, ApJS, 140, 81
Lehner, N., Jenkins, E. B., Gry, C., et al. 2003, ApJ, 595, 858
Lemke, M. 1997, A&AS, 122, 285
Lemoine, M., Vidal-Madjar, A., Hébrard, G., et al. 2002, ApJS, 140, 67
Liebert, J., Wesemael, F., Fontaine, G., Hansen, C. J., & Shipman, H. L. 1986, in ASSL Vol. 128: IAU Colloq. 87: Hydrogen Deficient Stars and Related Objects, 387
Lucy, L. B. 1964, in First Havard Smithsonian conference on stellar atmospheres, 93
MacDonald, J. 1992, ApJ, 394, 619
Madej, J. 1998, A&A, 340, 617
Margon, B., Malina, R., Bowyer, S., Cruddace, R., & Lampton, M. 1976, ApJL, 203, L25
Marsh, M. C., Barstow, M. A., Buckley, D. A., et al. 1997a, MNRAS, 286, 369
Marsh, M. C., Barstow, M. A., Buckley, D. A., et al. 1997b, MNRAS, 287, 705
Massa, D. & Fitzpatrick, E. L. 2000, ApJS, 126, 517
Massey, P., Strobel, K., Barnes, J. V., & Anderson, E. 1988, ApJ, 328, 315
McCook, G. P. & Sion, E. M. 1999, ApJS, 121, 1
Mewe, R., Heise, J., Gronenschild, E. H. B. M., et al. 1975, ApJL, 202, L67
Michaud, G. 1970, ApJ, 160, 641
Michaud, G., Vauclair, G., & Vauclair, S. 1983, ApJ, 267, 256
Montmerle, T. & Michaud, G. 1976, ApJS, 31, 489
Morvan, E., Vauclair, G., & Vauclair, S. 1986, A&A, 163, 145
Nagel, T. 2003, Dissertation, Eberhard-Karls-Universität Tübingen
Nagel, T., Dreizler, S., & Werner, K. 2003, in ASP Conf. Ser. 288: Stellar Atmosphere Modeling, 641
Napiwotzki, R. 1999, A&A, 350, 101
Napiwotzki, R., Barstow, M. A., Fleming, T., et al. 1993, A&A, 278, 478
Napiwotzki, R., Green, P. J., & Saffer, R. A. 1999a, ApJ, 517, 399
Napiwotzki, R., Green, P. J., & Saffer, R. A. 1999b, in ASP Conf. Ser. 169: 11th European Workshop on White Dwarfs, 492
Oliveira, C. M., Hébrard, G., Howk, J. C., et al. 2003, ApJ, 587, 235
Olson, G. L. & Kunasz, P. B. 1987, Journal of Quantitative Spectroscopy and Radiative Transfer, 38, 325
Paerels, F. B. S. & Heise, J. 1989, ApJ, 339, 1000
Paquette, C., Pelletier, C., Fontaine, G., & Michaud, G. 1986, ApJS, 61, 177
Petre, R., Shipman, H. L., & Canizares, C. R. 1986, ApJ, 304, 356
Piskunov, N., Weiss, W. W., & Gray, D. F., eds. 2004, Modeling of Stellar Atmospheres
Pounds, K. A., Allan, D. J., Barber, C., et al. 1993, MNRAS, 260, 77
Rauch, T. & Deetjen, J. L. 2003, in ASP Conf. Ser. 288: Stellar Atmosphere Modeling, 103
Redfield, S. & Linsky, J. L. 2004a, ApJ, 602,

776
Redfield, S. & Linsky, J. L. 2004b, ApJ, 613, 1004
Reid, I. N. 1996, AJ, 111, 2000
Reimers, D. & Wisotzki, L. 1997, The Messenger, 88, 14
Rumph, T., Bowyer, S., & Vennes, S. 1994, AJ, 107, 2108
Russell, H. N. 1913, The Observatory, 36, 324
Rutten, R. J. 1997, Radiative Transfer in Stellar Atmospheres, 4th WWW edn., lecture notes (Utrecht University), available at http://www.fys.ruu.nl/~rutten
Sahnow, D. J., Moos, H. W., Ake, T. B., et al. 2000, ApJ, 538, L7
Schatzman, E. 1945, Annales d'Astrophysique, 8, 143
Schatzman, E. 1958, White Dwarfs (North Holland Publishing Company, Amsterdam)
Schöning, T. & Butler, K. 1989a, A&AS, 78, 51
Schöning, T. & Butler, K. 1989b, A&A, 219, 326
Schuh, S. 2000, Diploma thesis, Eberhard-Karls-Universität Tübingen
Schuh, S., Barstow, M. A., & Dreizler, S. 2005, in ASP Conf. Series: 14th European Workshop on White Dwarfs, ed. D. Koester & S. Möhler, in press
Schuh, S., Dreizler, S., & Wolff, B. 2001, in ASP Conference Series, Vol. 226, The 12th European Workshop on White Dwarfs, ed. J. L. Provencal, H. L. Shipman, J. MacDonald, & S. Goodchild, 79
Schuh, S. L. & Dreizler, S. 2003, in ASP Conf. Ser. 288: Stellar Atmosphere Modeling, 633
Schuh, S. L., Dreizler, S., & Deetjen, J. L. 2003, in Kluwer Academics NATO Science Series II., Vol. 105, The 13th European Workshop on White Dwarfs, ed. D. de Martino, R. Silvotti, J.-E. Solheim, & R. Kalytis, 147
Schuh, S. L., Dreizler, S., & Wolff, B. 2002, A&A, 382, 164
Schwartz, R. D., Dawkins, D., Findley, D., & Chen, D. 1995, PASP, 107, 667
Seaton, M. J. 1992, Revista Mexicana de Astronomia y Astrofisica, vol. 23, 23, 180
Seaton, M. J., Yan, Y., Mihalas, D., & Pradhan, A. K. 1994, MNRAS, 266, 805
Seaton, M. J., Zeippen, C. J., Tully, J. A., et al. 1992, Revista Mexicana de Astronomia y Astrofisica, vol. 23, 23, 19
Shipman, H. J. 1994, Nature, 372, 317
Shipman, H. L. 1976, ApJL, 206, L67
Shipman, H. L. & Finley, D. S. 1994, Bulletin of the American Astronomical Society, 26, 870
Shipman, H. L., Provencal, J., Roby, S. W., et al. 1995, AJ, 109, 1220
Silvestri, N. M., Oswalt, T. D., & Hawley, S. L. 2002, AJ, 124, 1118
Smith, E. P., Pica, A. J., Bohlin, R. C., et al. 1996, ApJS, 104, 287
Smith, J. A., Tucker, D. L., Kent, S., et al. 2002, AJ, 123, 2121
Smith, M. A. 2001, PASP, 113, 882
Stobie, R. S., Kilkenny, D., O'Donoghue, D., et al. 1997, MNRAS, 287, 848
Stone, R. P. S. 1996, ApJS, 107, 423
Stoughton, C., Lupton, R. H., Bernardi, M., et al. 2002, AJ, 123, 485
Thomas, H.-C., Beuermann, K., Reinsch, K., et al. 1998, A&A, 335, 467
Trimble, V. & Aschwanden, M. J. 2001, PASP, 113, 1025
Tweedy, R. W. 1995, Nature, 373, 666
Tweedy, R. W. & Kwitter, K. B. 1994, ApJ, 433, L93
Unglaub, K. & Bues, I. 1998, A&A, 338, 75
Unglaub, K. & Bues, I. 2000, A&A, 359, 1042
Unglaub, K. & Bues, I. 2001, A&A, 374, 570
Vauclair, G. 1987, in IAU Colloq. 95: Second Conference on Faint Blue Stars, 341

Vauclair, G. 1989, in IAU Colloq. 114: White Dwarfs, 176

Vauclair, G., Schmidt, H., Koester, D., & Allard, N. 1997, A&A, 325, 1055

Vauclair, G., Vauclair, S., & Greenstein, J. L. 1979, A&A, 80, 79

Vennes, S. 1999, ApJ, 525, 995

Vennes, S., Chayer, P., Fontaine, G., & Wesemael, F. 1989, ApJL, 336, L25

Vennes, S., Chayer, P., Hurwitz, M., & Bowyer, S. 1996a, ApJ, 468, 898

Vennes, S. & Dupuis, J. 2002, in ASP Conf. Ser. 262: The High Energy Universe at Sharp Focus: Chandra Science, 57

Vennes, S., Dupuis, J., Bowyer, S., et al. 1994, ApJ, 421, L35

Vennes, S., Dupuis, J., Rumph, T., et al. 1993, ApJ, 410, L119

Vennes, S., Fontaine, G., & Brassard, P. 1995, A&A, 296, 117

Vennes, S. & Lanz, T. 2001, ApJ, 553, 399

Vennes, S., Polomski, E. F., Lanz, T., et al. 2000, ApJ, 544, 423

Vennes, S., Thejll, P. A., Galvan, R. G., & Dupuis, J. 1997, ApJ, 480, 714

Vennes, S., Thejll, P. A., Wickramasinghe, D. T., & Bessell, M. S. 1996b, ApJ, 467, 782

Vennes, S. & Thorstensen, J. R. 1994, AJ, 108, 1881

Vidal, C. R., Cooper, J., & Smith, E. W. 1973, ApJS, 25, 37

Vidal-Madjar, A., Allard, N. F., Koester, D., et al. 1994, A&A, 287, 175

Welsh, B. Y., Sallmen, S., Sfeir, D., Shelton, R. L., & Lallement, R. 2002, A&A, 394, 691

Werner, K., Deetjen, J. L., Dreizler, S., et al. 2003, in ASP Conf. Ser. 288: Stellar Atmosphere Modeling, 31

Werner, K. & Dreizler, S. 1994, A&A, 286, L31

Werner, K. & Dreizler, S. 1999, in Journal of Computational and Applied Mathematics, Vol. 109, Computational Astrophysics, ed. H. Riffert & K. Werner (Amsterdam: Elsevier Press), 65

Werner, K., Rauch, T., & Dreizler, S. 1998, A Users's Guide to the Tübingen NLTE Model Atmosphere Package, Institut für Astronomie und Astrophysik, Astronomie, Tübingen, available at http://astro.uni-tuebingen.de/~rauch/

Wesemael, F. & et al. 1995, , in preparation

Wilkinson, E., Green, J. C., & Cash, W. 1993, ApJS, 89, 211

Wilms, J., Allen, A., & McCray, R. 2000, ApJ, 542, 914

Wisotzki, L., Christlieb, N., Bade, N., et al. 2000, A&A, 358, 77

Wisotzki, L., Koehler, T., Groote, D., & Reimers, D. 1996, A&AS, 115, 227

Wolff, B. 1999, PhD thesis, Christian-Albrechts-Universität Kiel

Wolff, B., Jordan, S., Bade, N., & Reimers, D. 1995, A&A, 294, 183

Wolff, B., Jordan, S., & Koester, D. 1994, in Astronomische Gesellschaft Abstract Series, 134–134

Wolff, B., Jordan, S., & Koester, D. 1996, A&A, 307, 149

Wolff, B., Koester, D., Dreizler, S., & Haas, S. 1998, A&A, 329, 1045

Wolff, B., Koester, D., & Lallement, R. 1999, A&A, 346, 969

Wolff, B., Kruk, J. W., Koester, D., et al. 2001, A&A, 373, 674

Wood, M. A. 1995, in White Dwarfs, ed. D. Koester & K. Werner, Lecture Notes in Physics 443 (Berlin, Heidelberg: Springer Verlag), 41

Zuckerman, B., Koester, D., Reid, I. N., & Hünsch, M. 2003, ApJ, 596, 477

Zuckerman, B. & Reid, I. N. 1998, ApJ, 505, L143

APPENDIX A

Equilibrium abundances

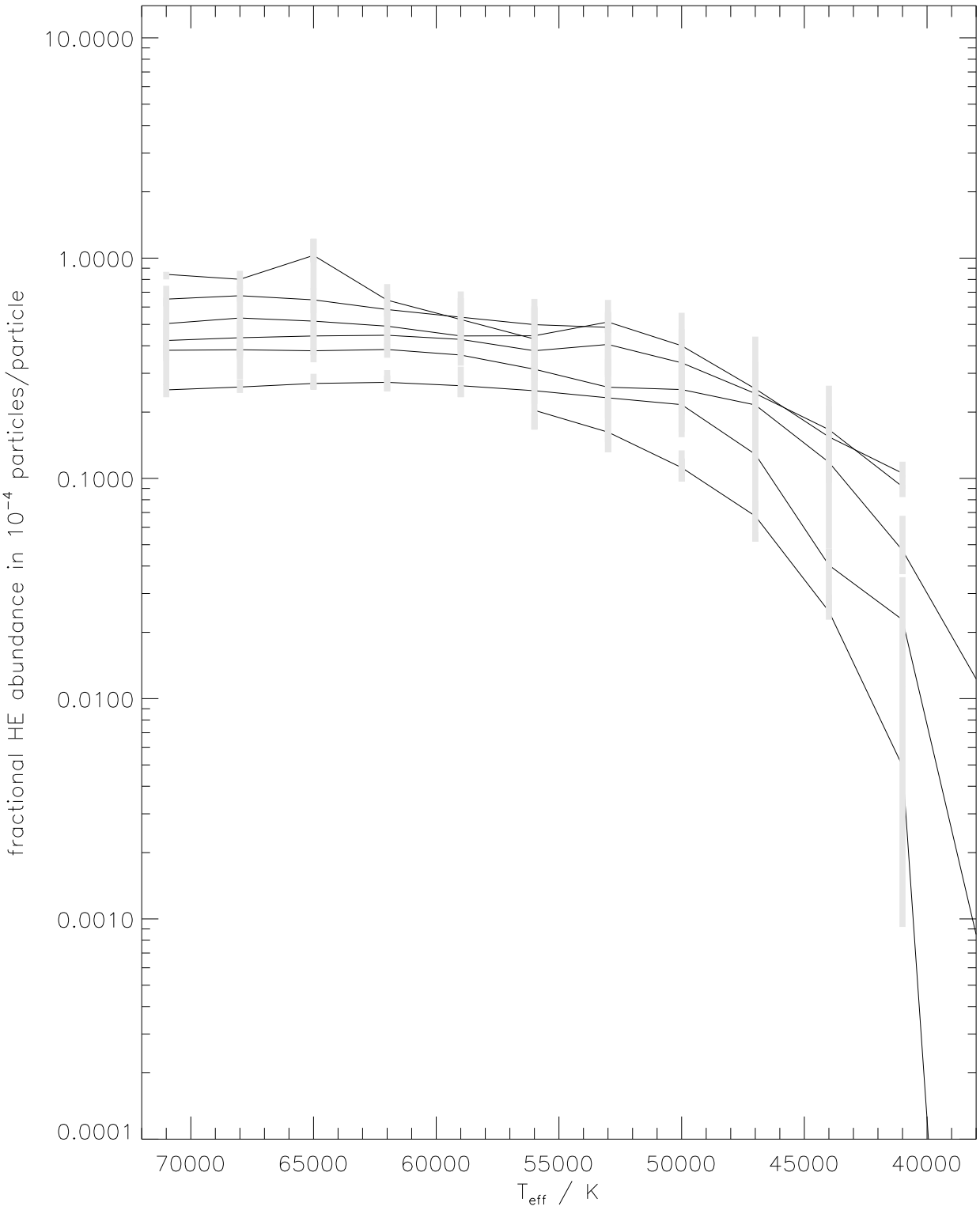

Figure A.1: Helium abundances as a function of effective temperature for different surface gravities.

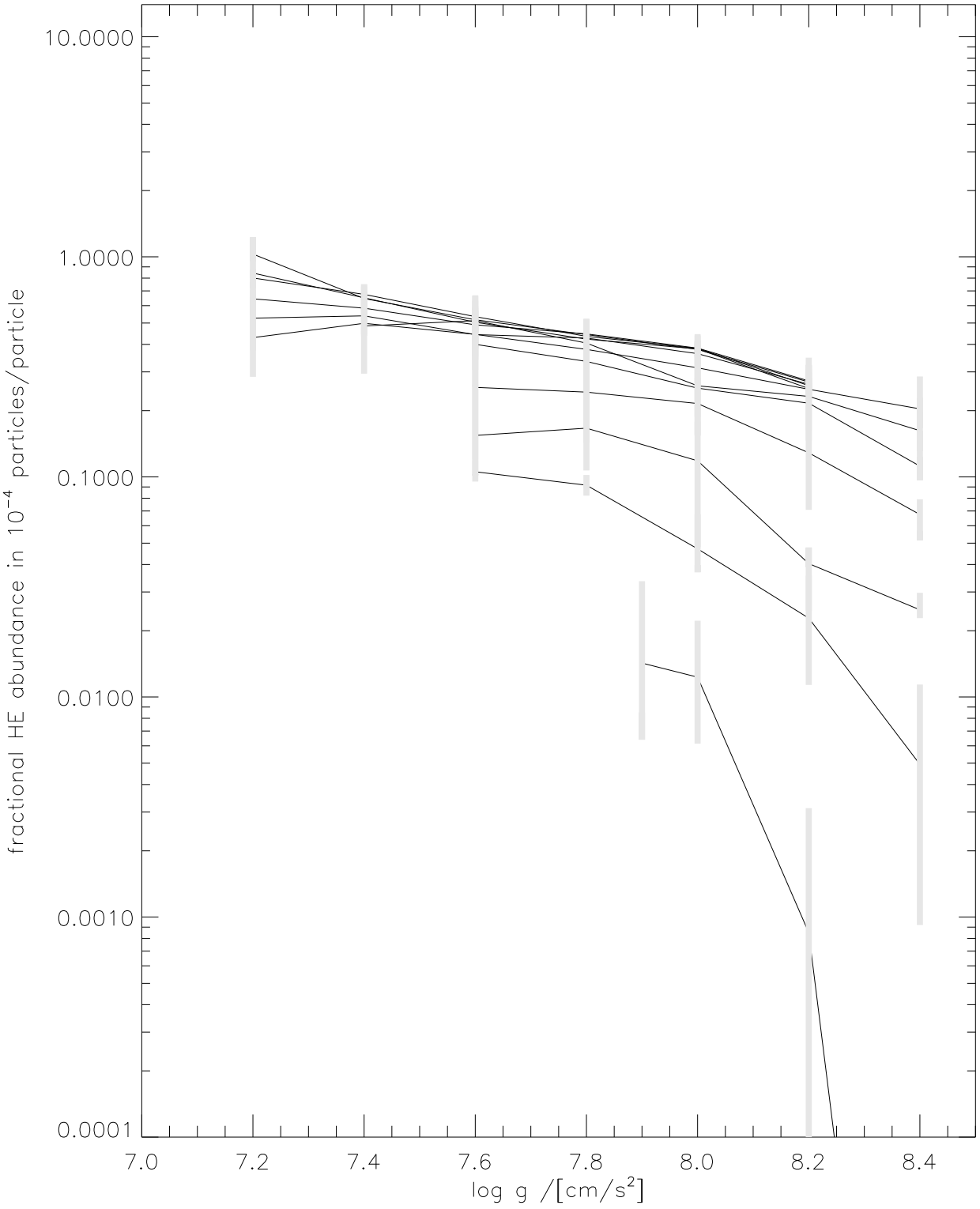

Figure A.2: Helium abundances as a function of surface gravity for different effective temperatures.

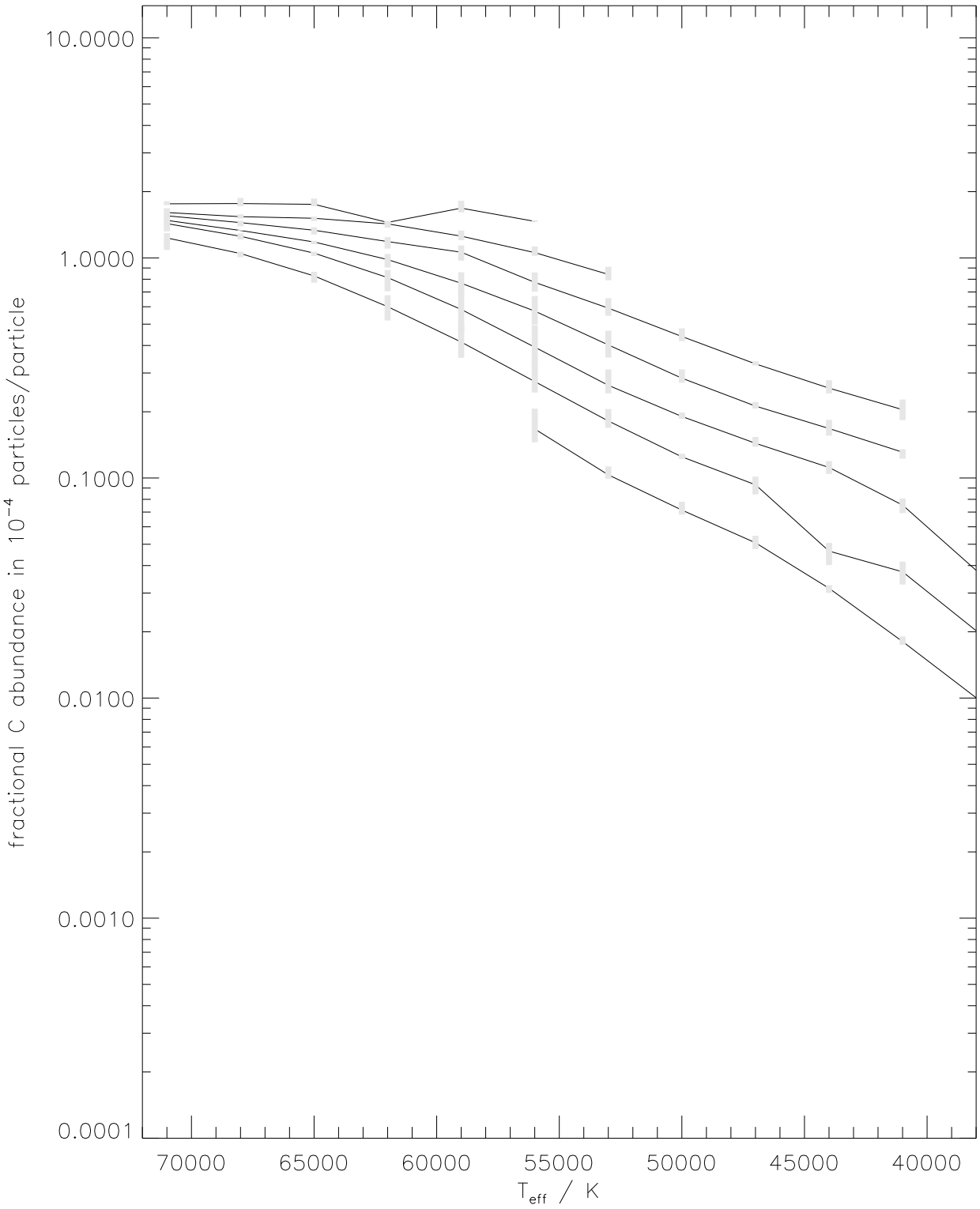

Figure A.3: Carbon abundances as a function of effective temperature for different surface gravities.

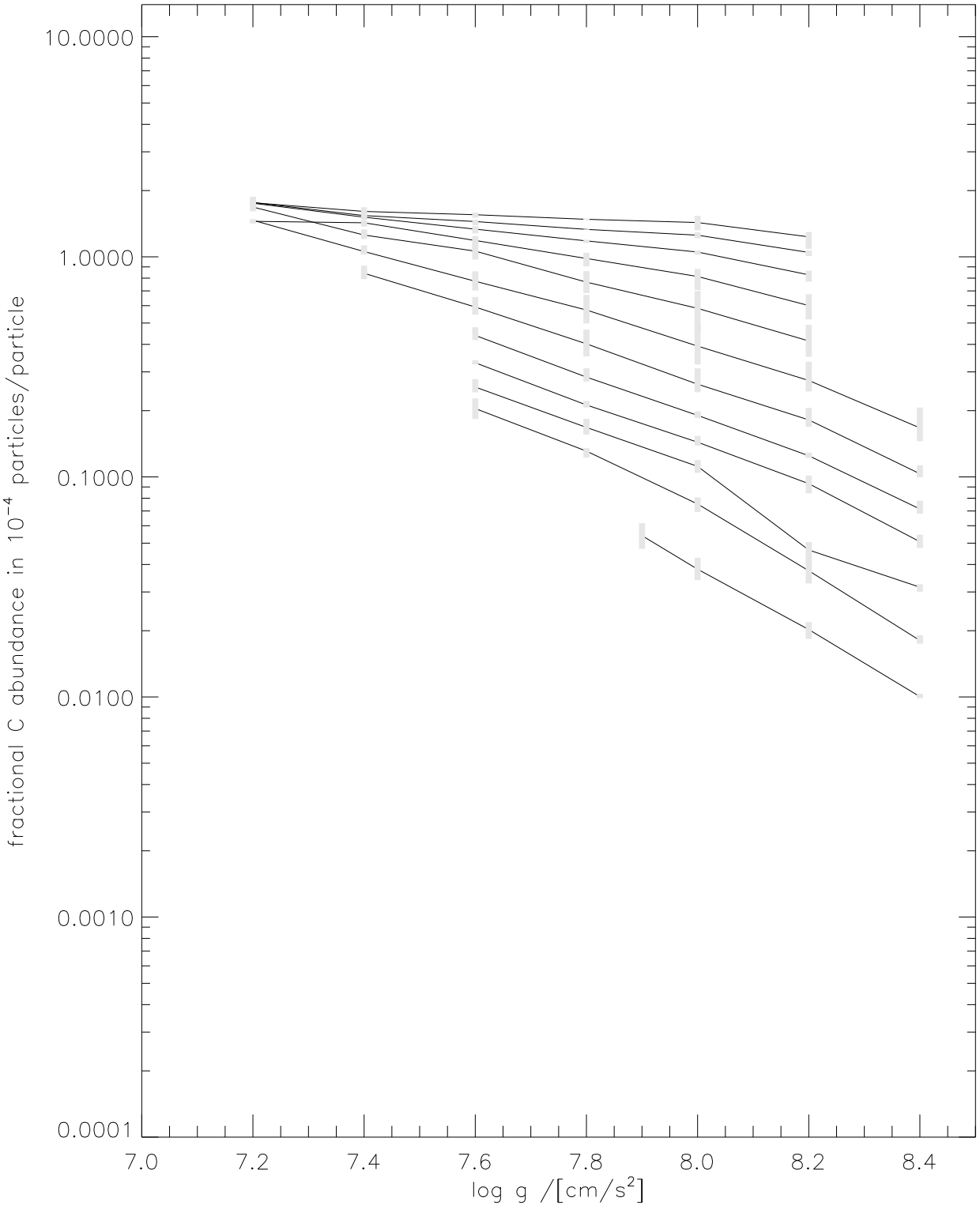

Figure A.4: Carbon abundances as a function of surface gravity for different effective temperatures.

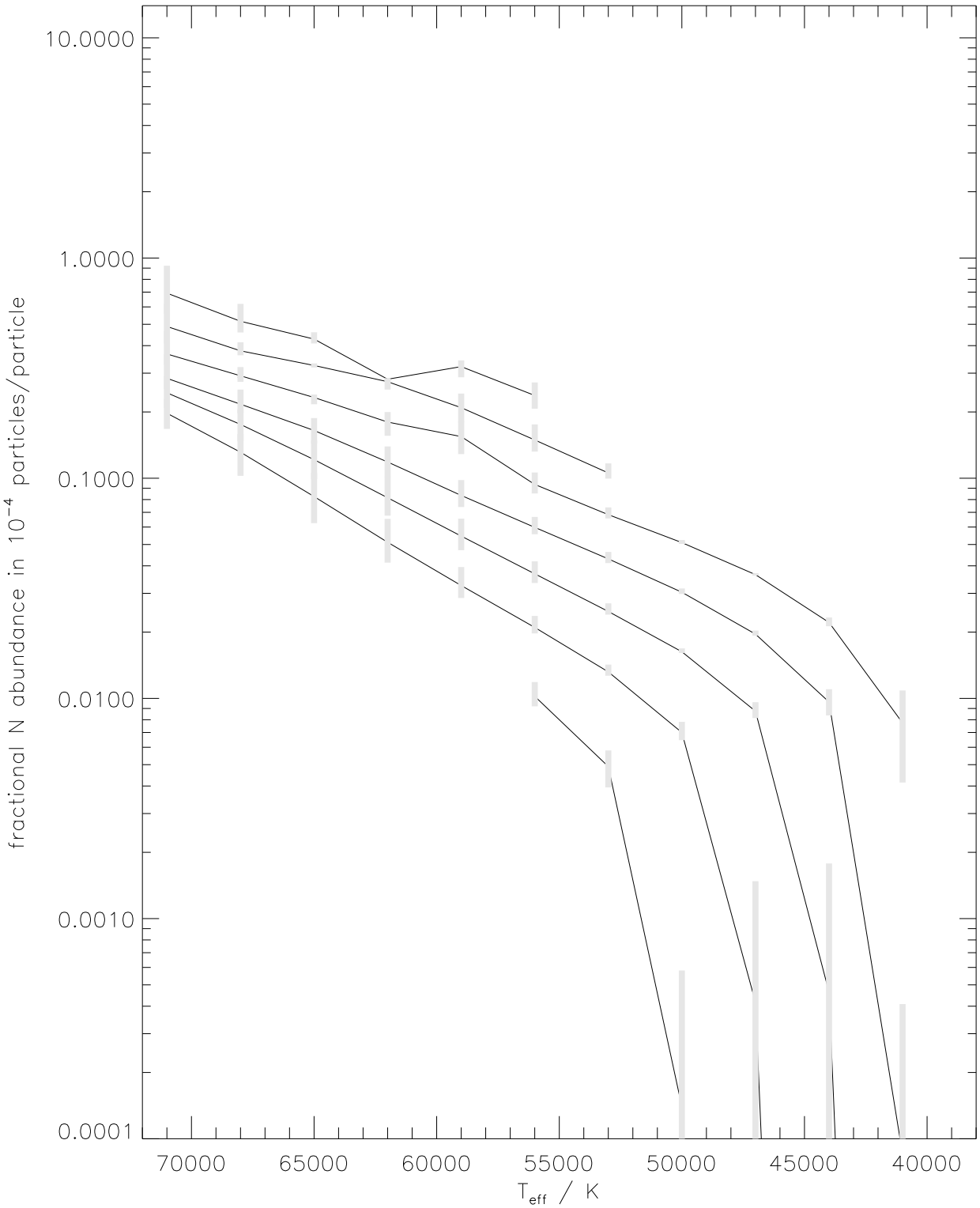

Figure A.5: Nitrogen abundances as a function of effective temperature for different surface gravities.

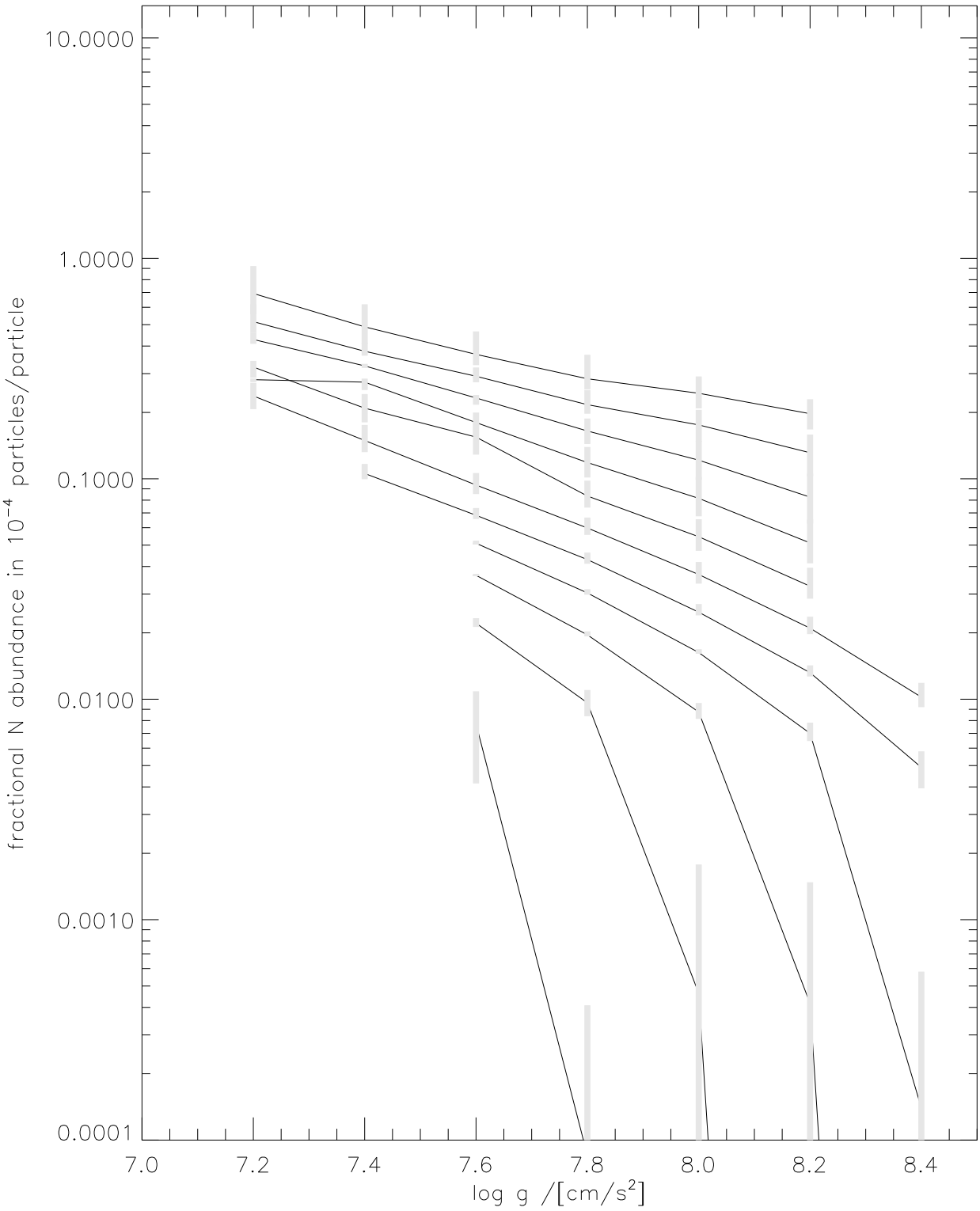

Figure A.6: Nitrogen abundances as a function of surface gravity for different effective temperatures.

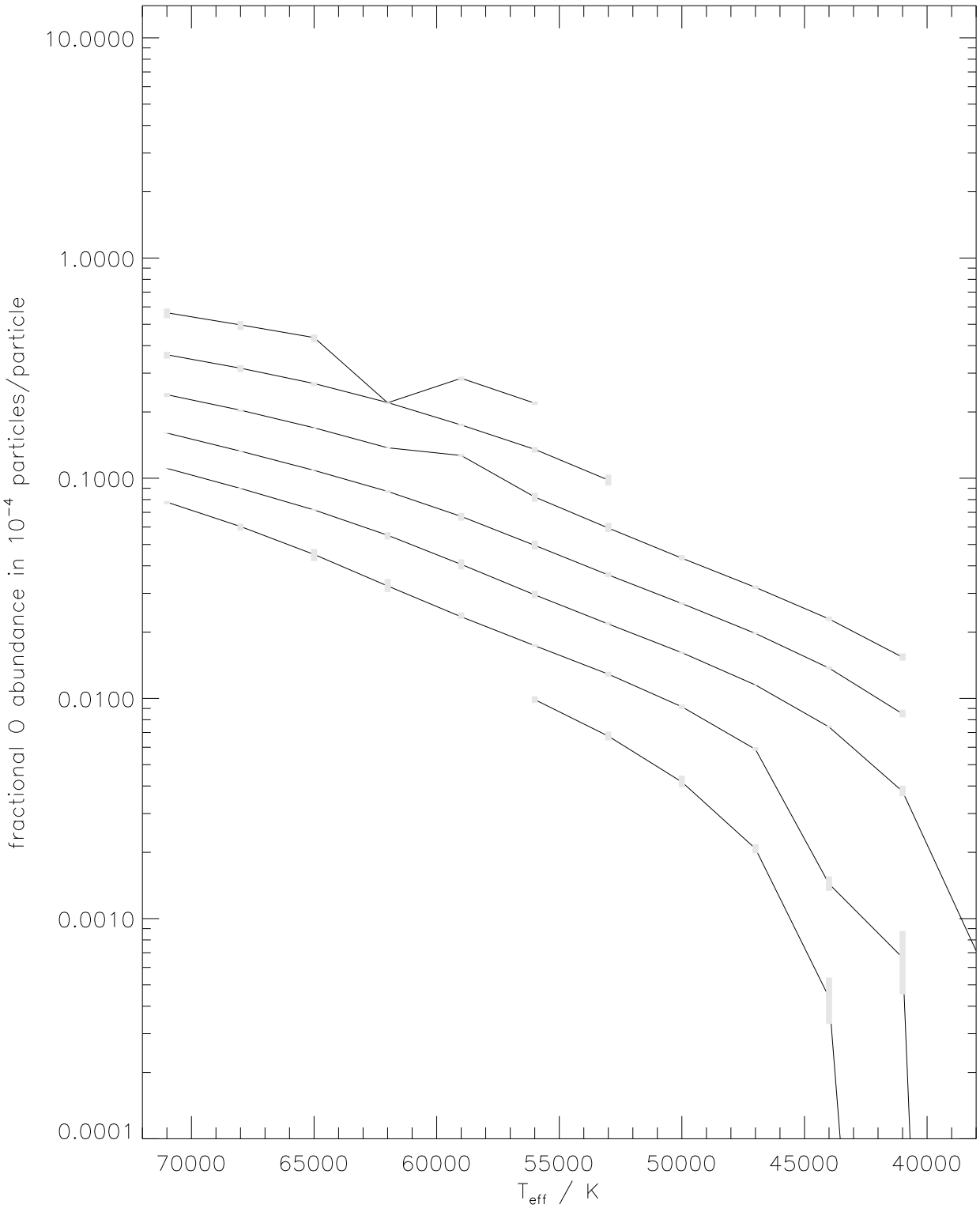

Figure A.7: Oxygen abundances as a function of effective temperature for different surface gravities.

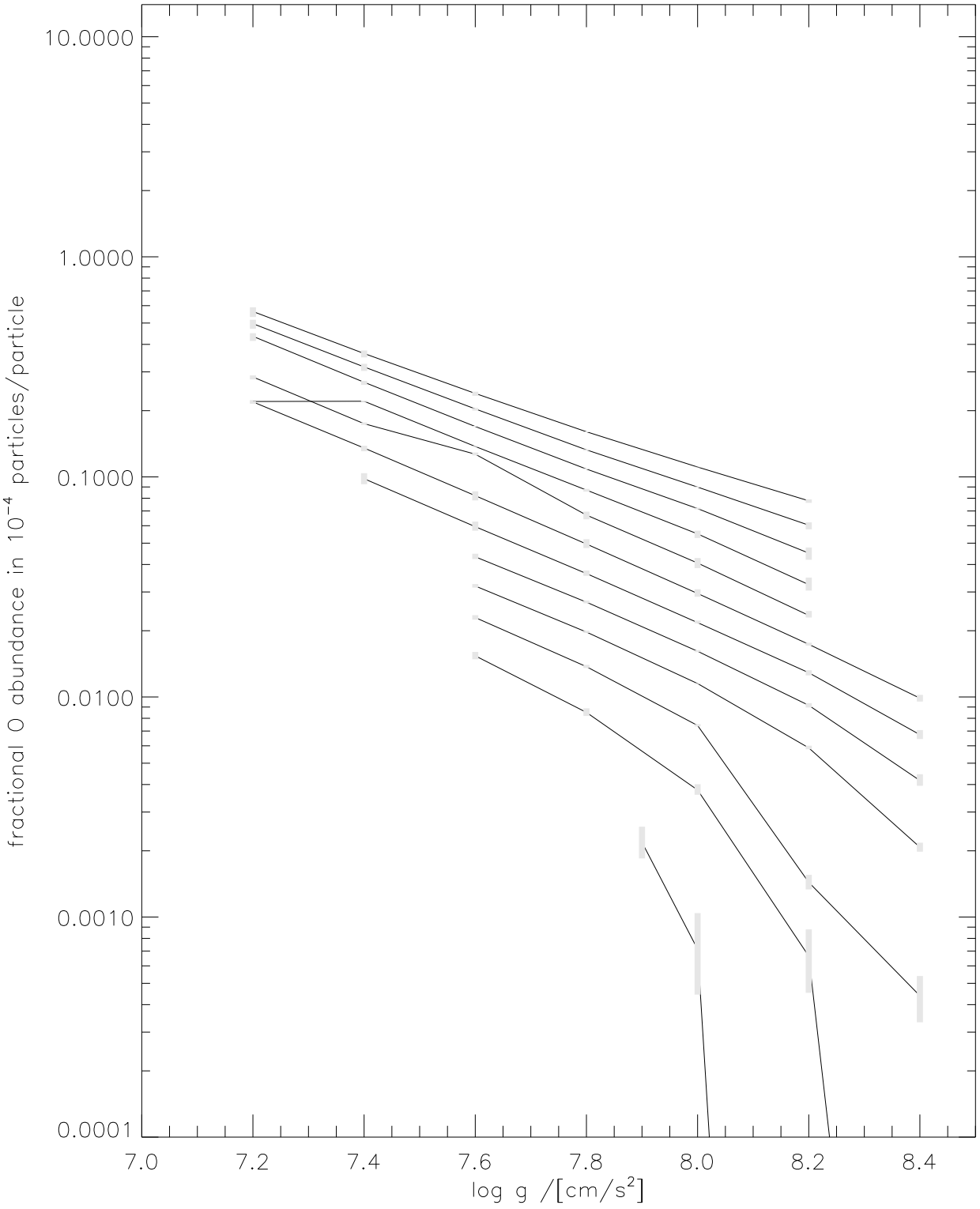

Figure A.8: Oxygen abundances as a function of surface gravity for different effective temperatures.

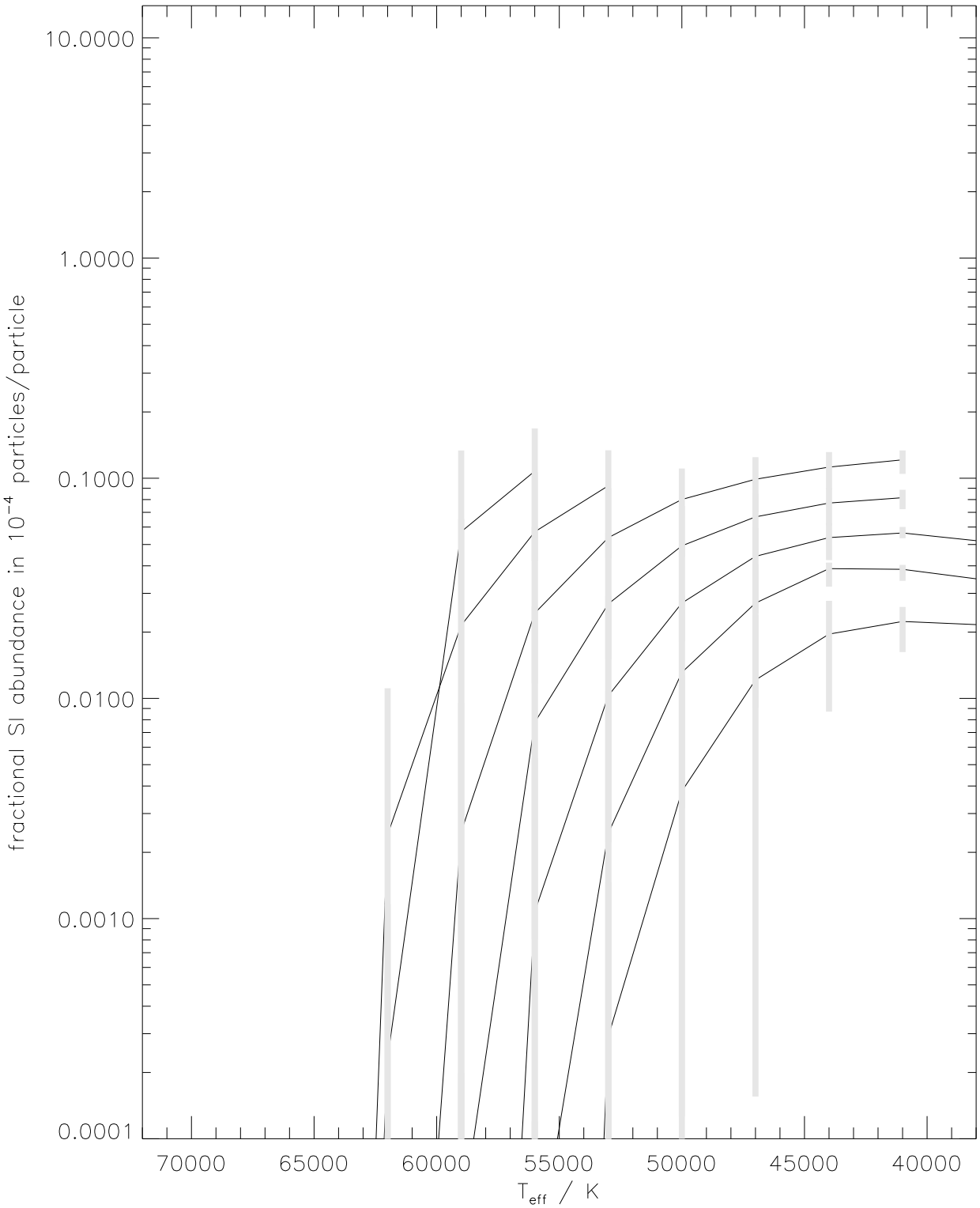

Figure A.9: Silicon abundances as a function of effective temperature for different surface gravities.

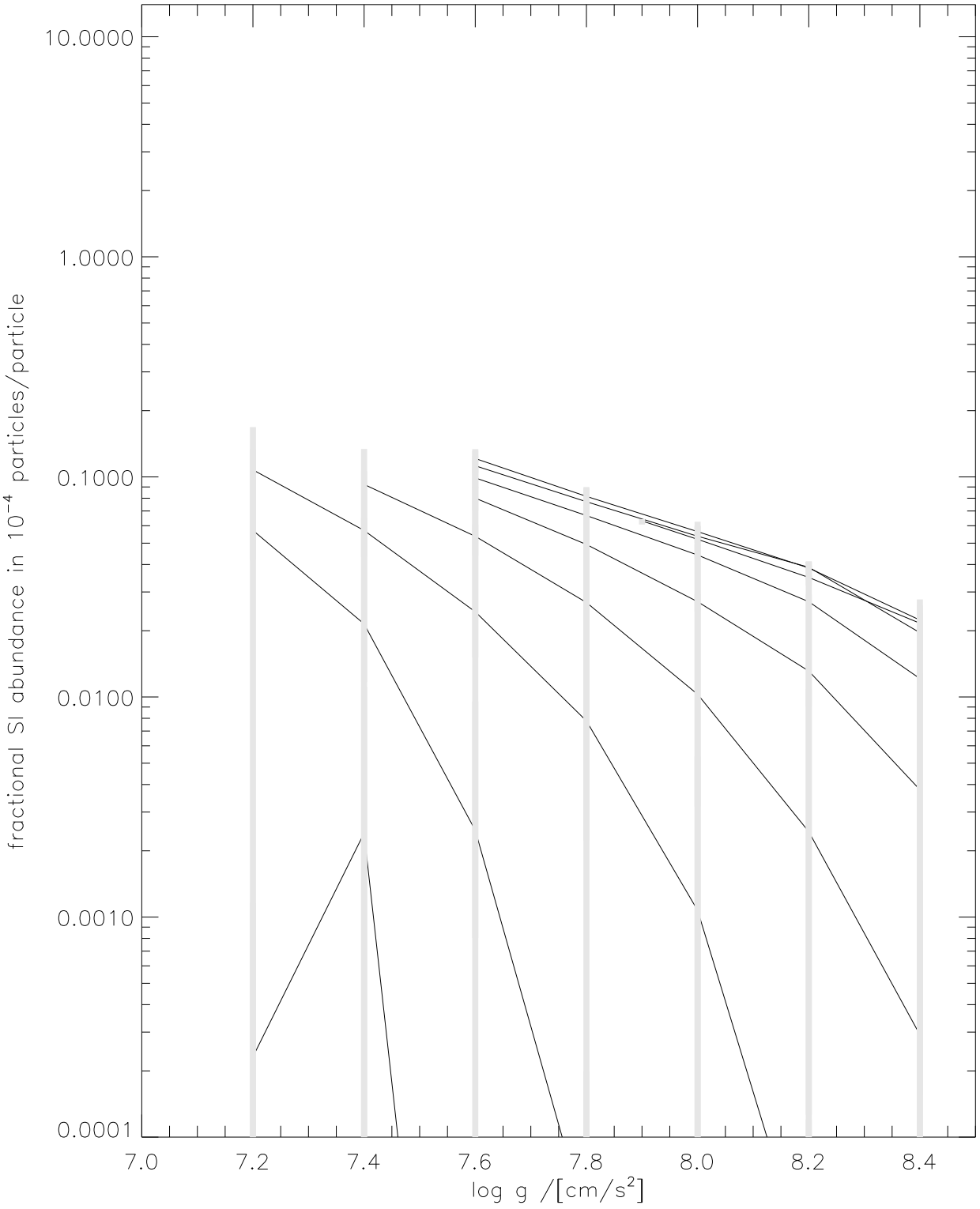

Figure A.10: Silicon abundances as a function of surface gravity for different effective temperatures.

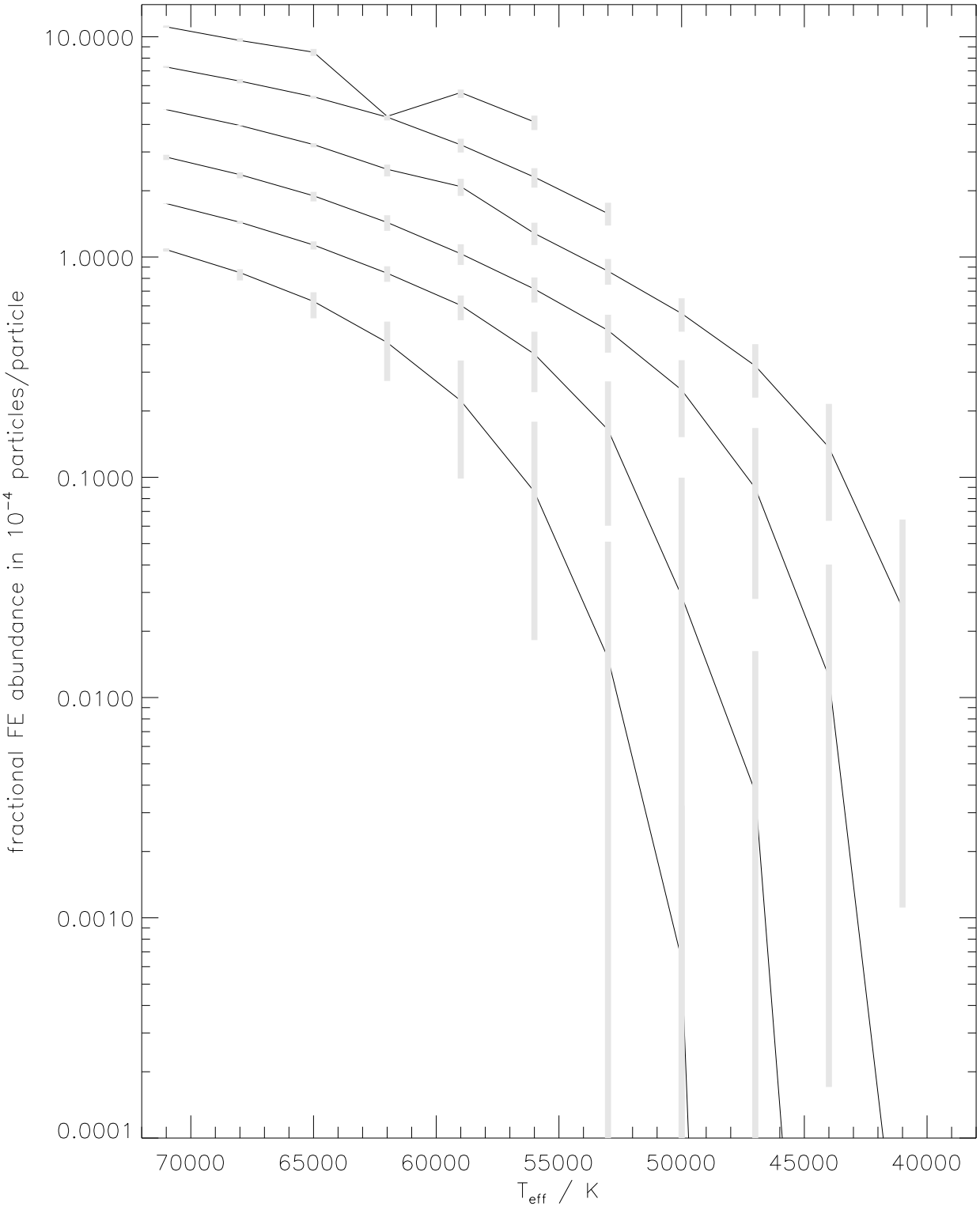

Figure A.11: Iron abundances as a function of effective temperature for different surface gravities.

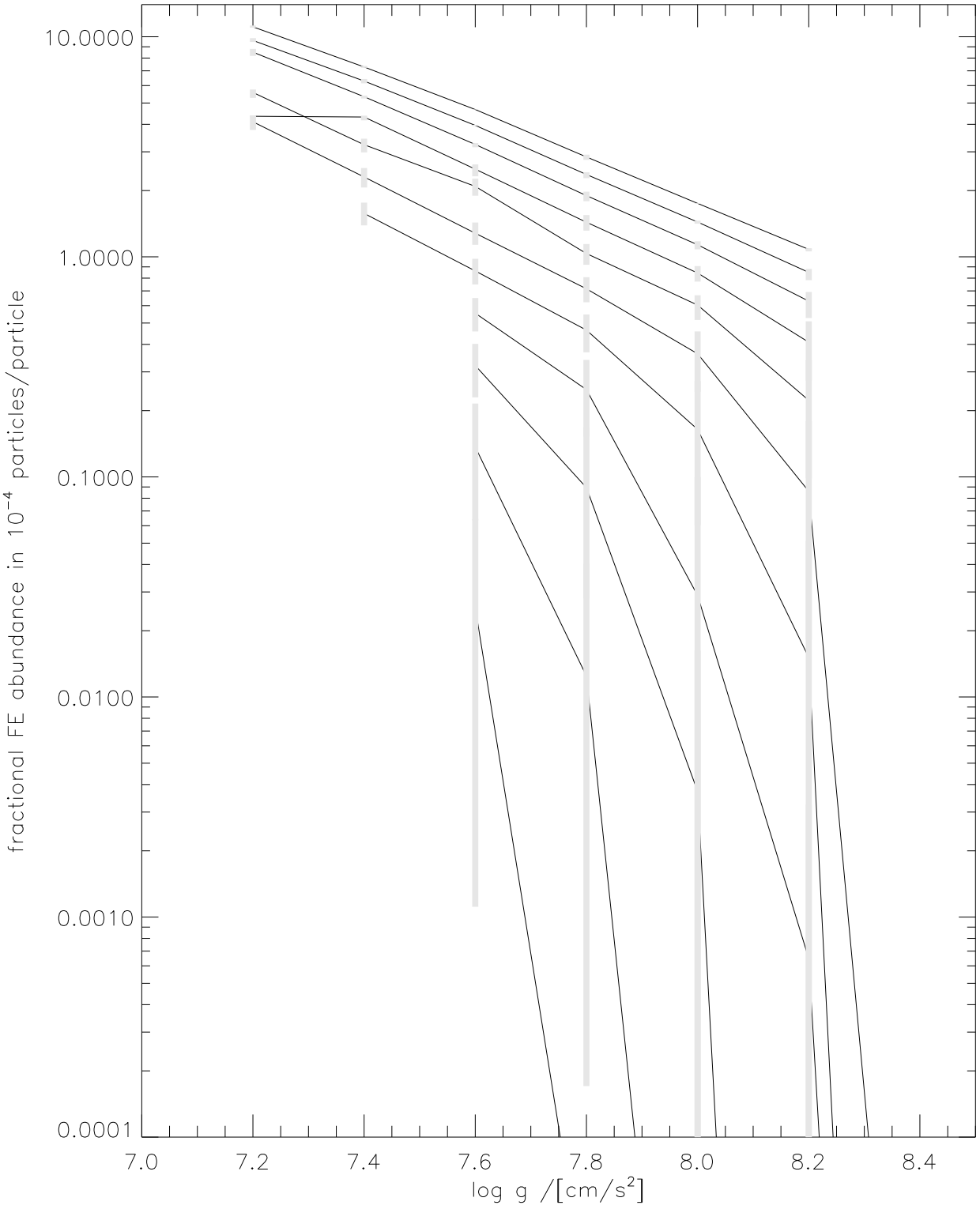

Figure A.12: Iron abundances as a function of surface gravity for different effective temperatures.

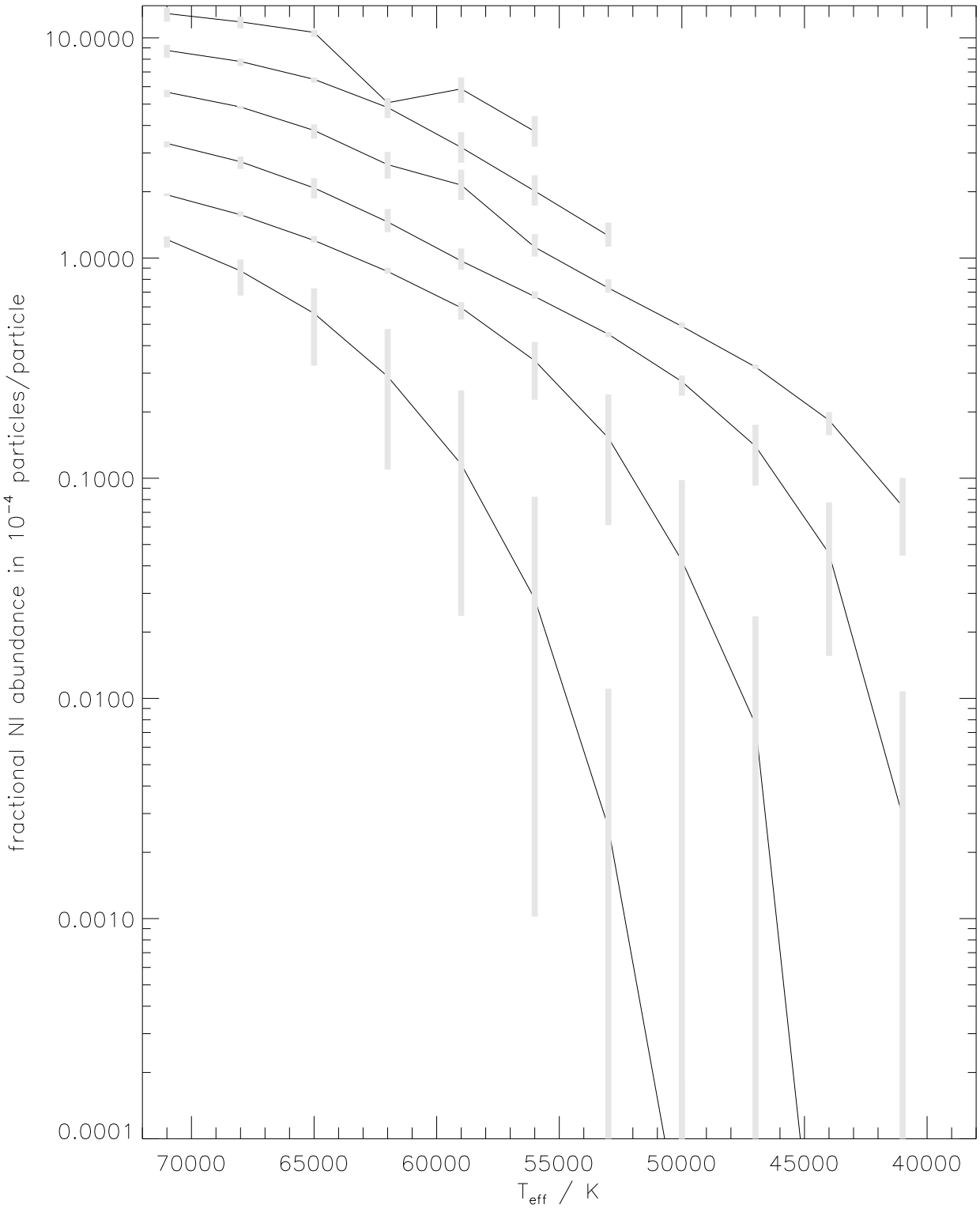

Figure A.13: Nickel abundances as a function of effective temperature for different surface gravities.

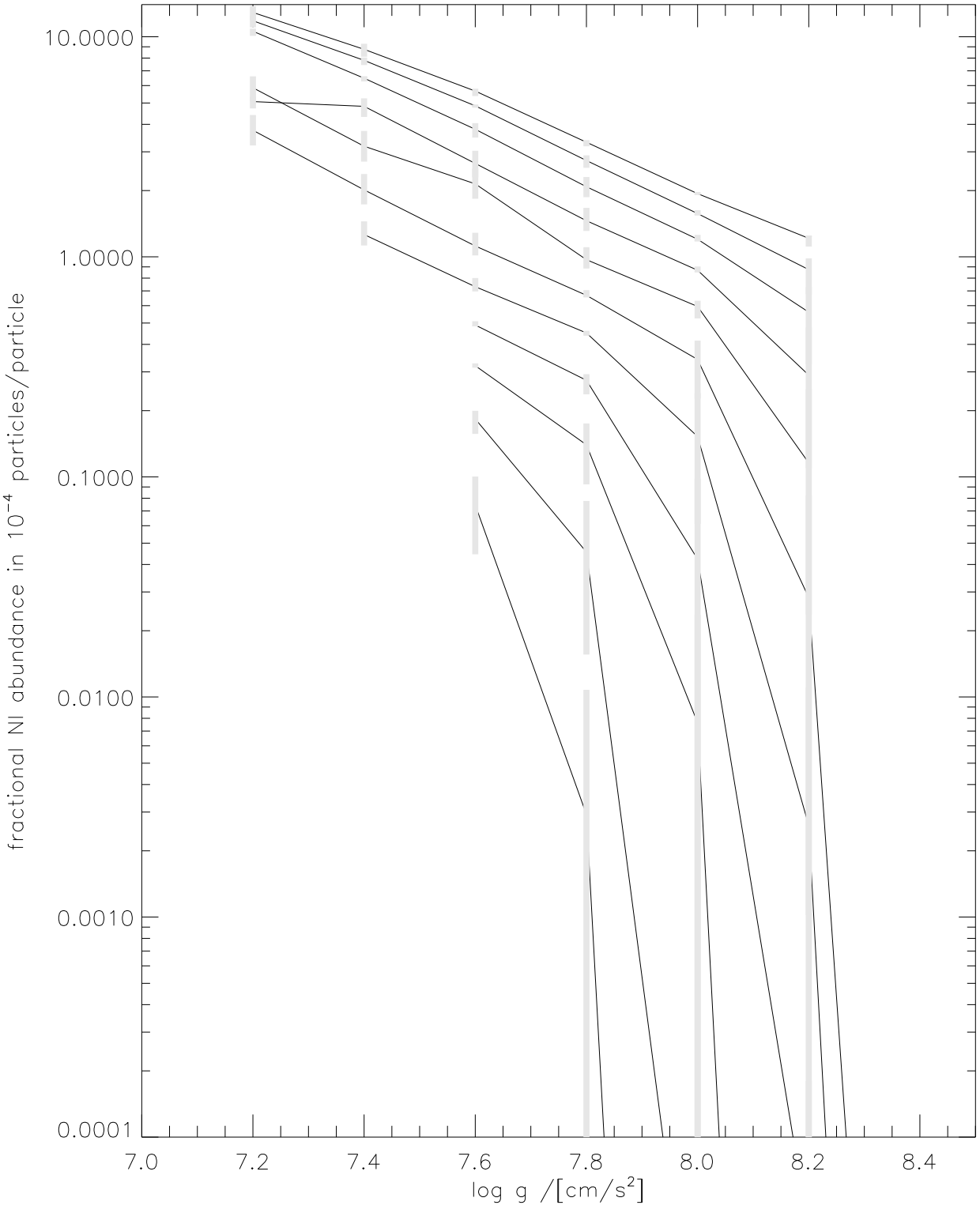

Figure A.14: Nickel abundances as a function of surface gravity for different effective temperatures.

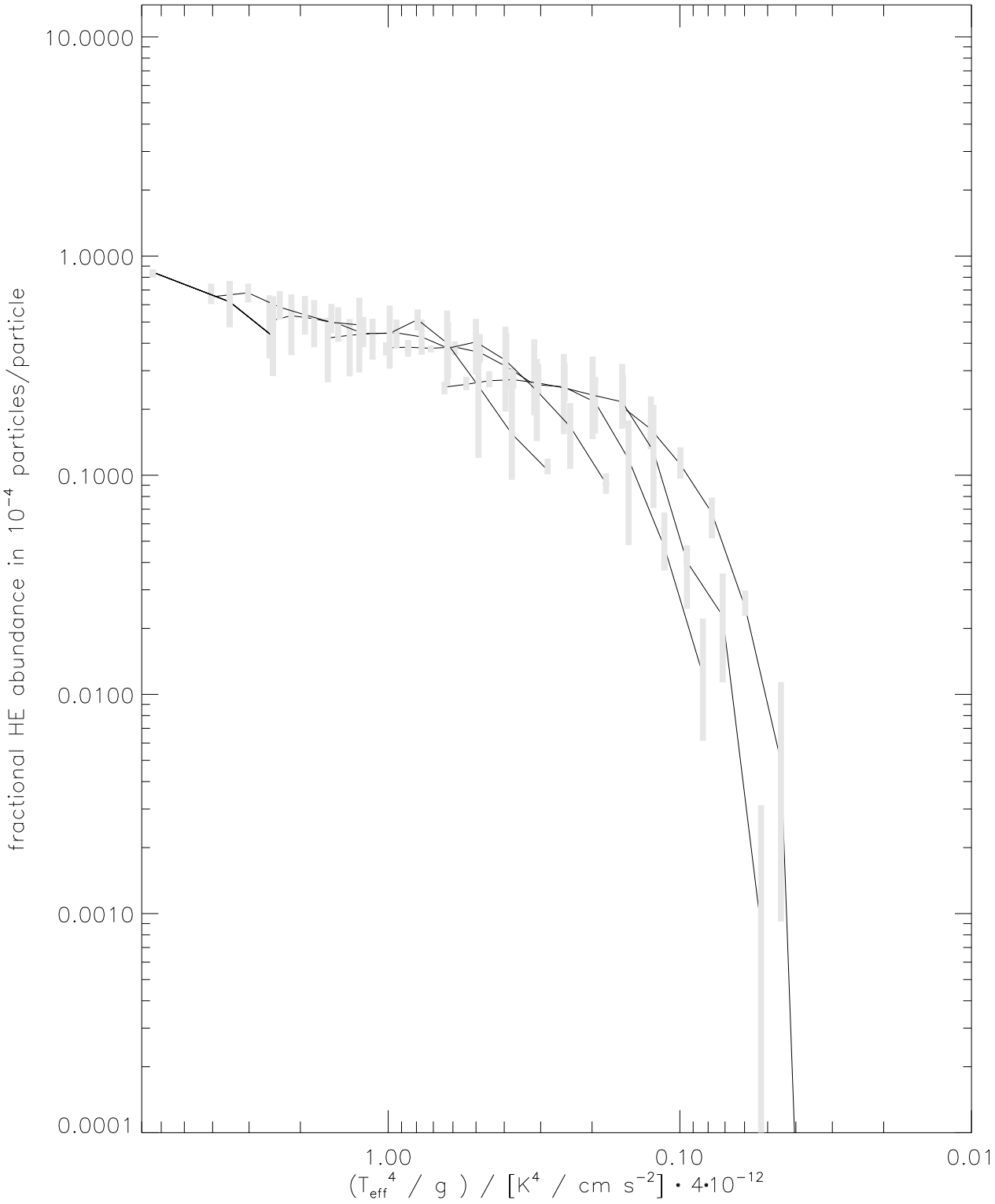

Figure A.15: Helium abundances as a function of the metal index mi.

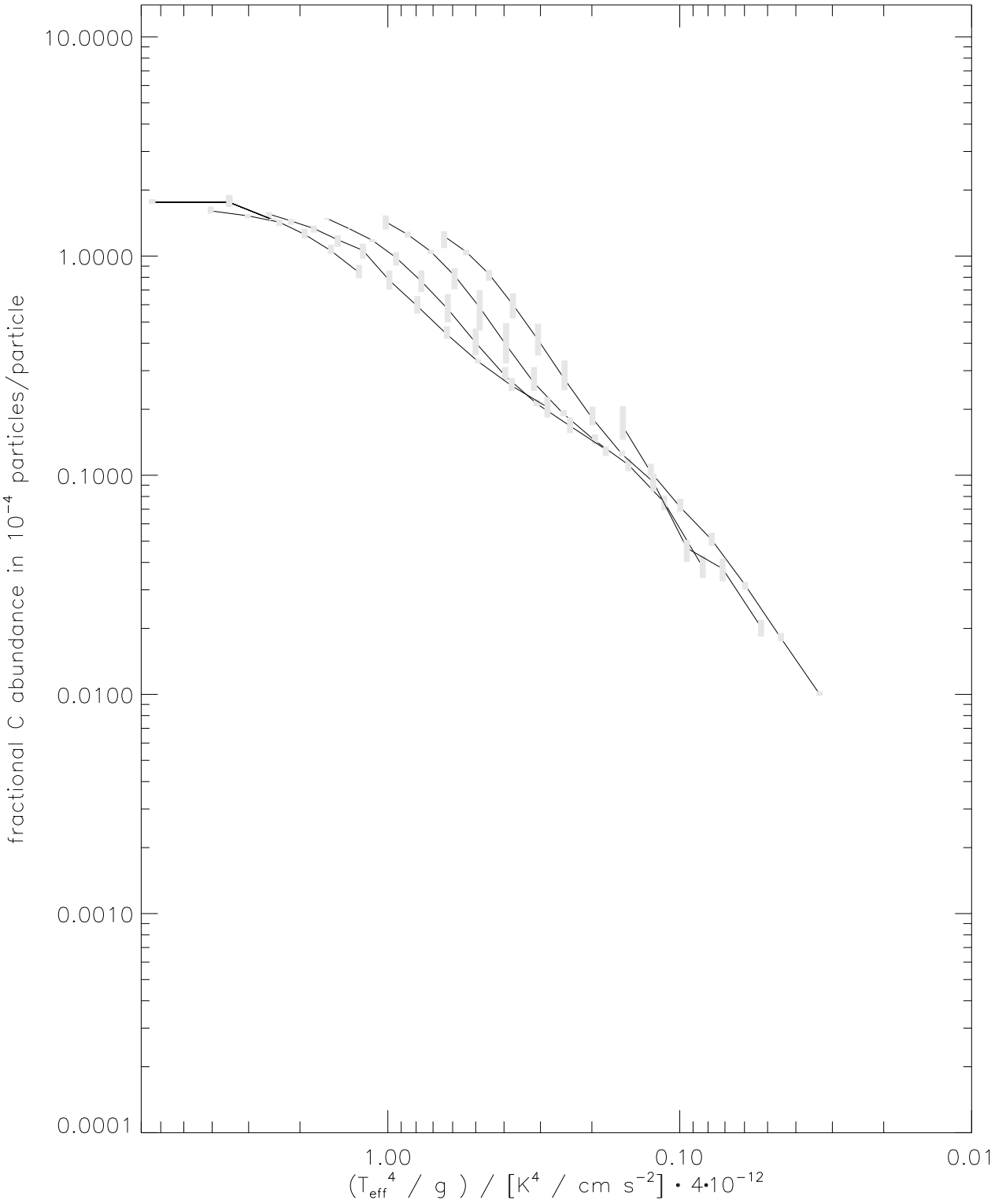

Figure A.16: Carbon abundances as a function of the metal index mi.

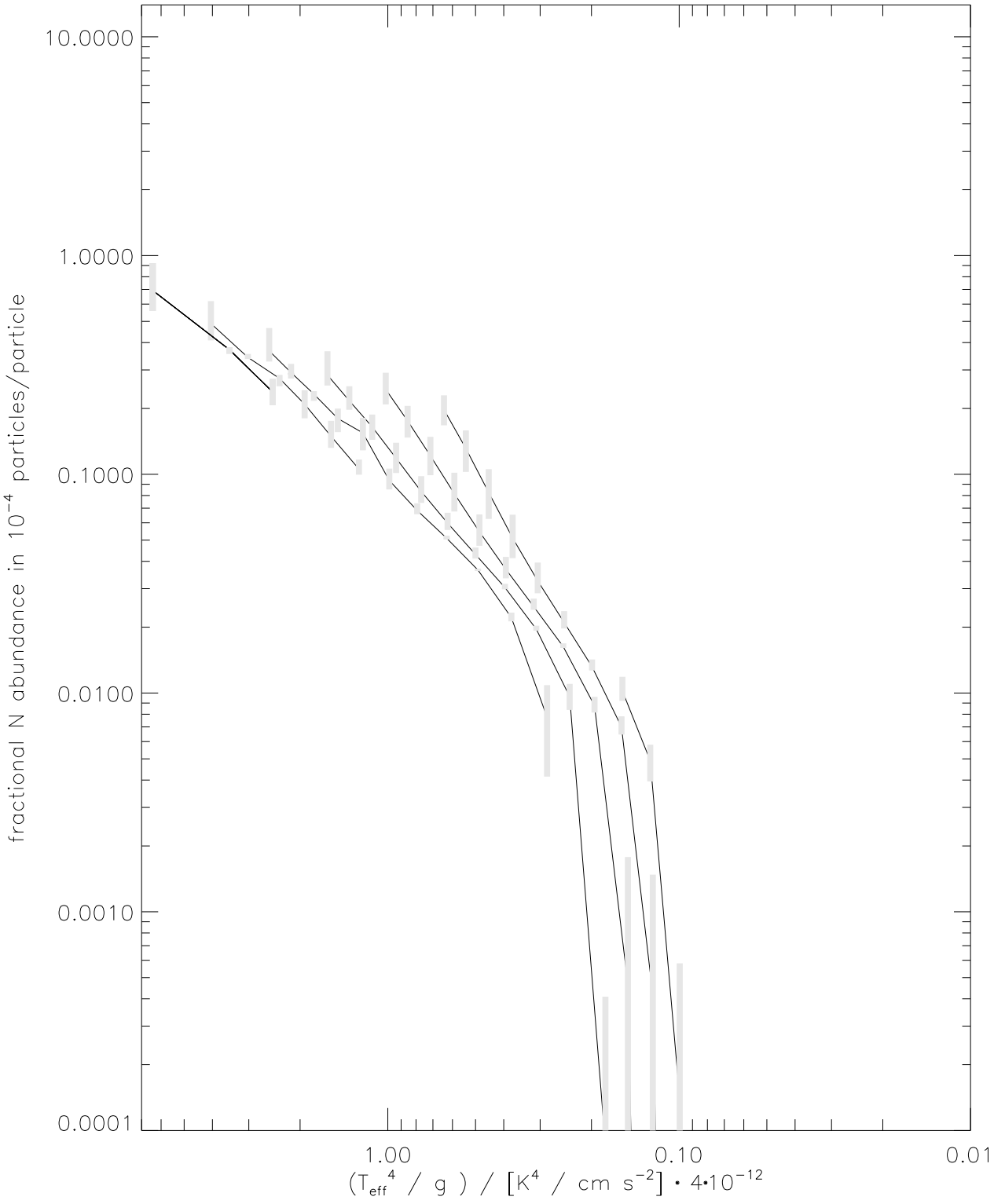

Figure A.17: Nitrogen abundances as a function of the metal index mi.

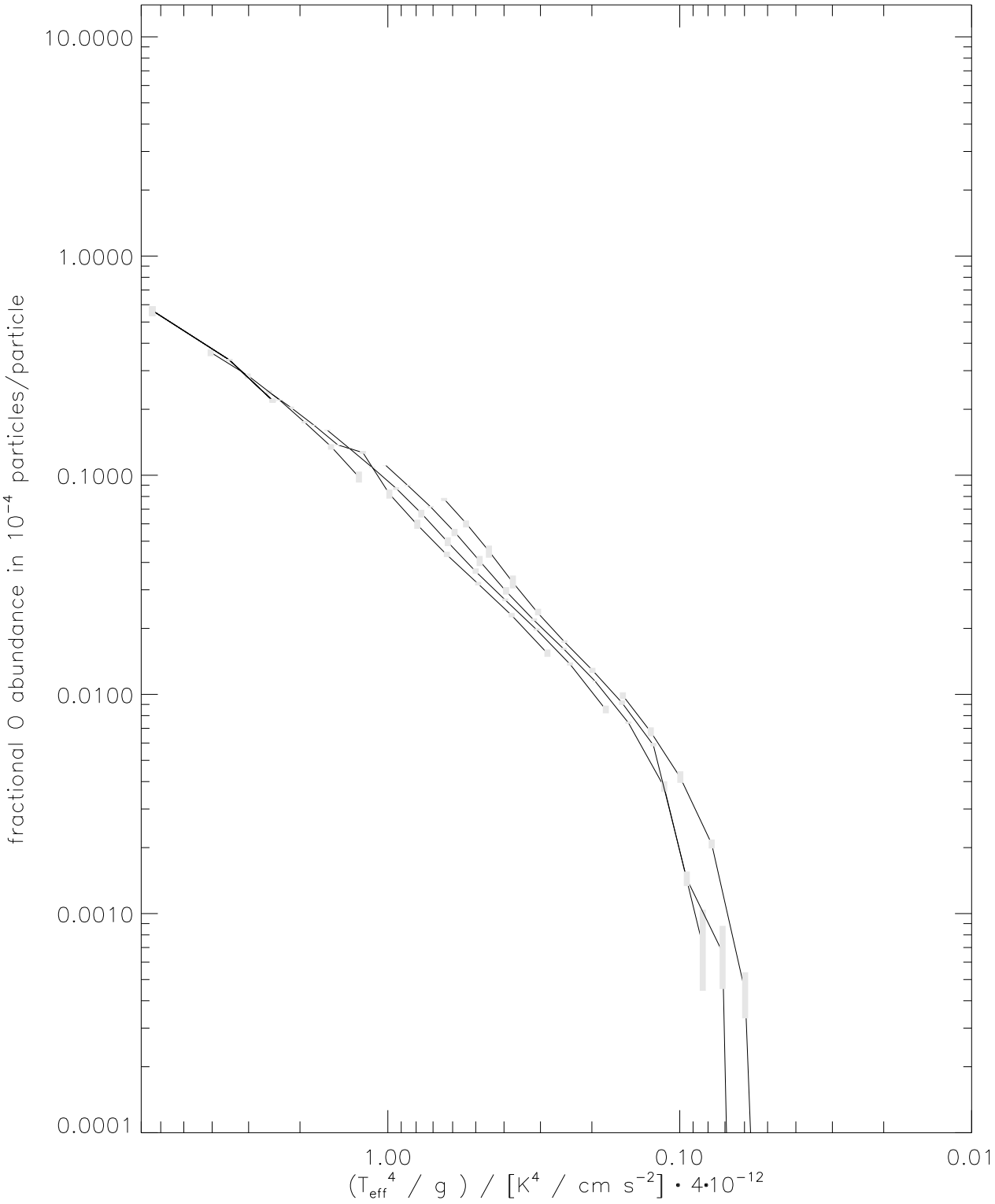

Figure A.18: Oxygen abundances as a function of the metal index mi.

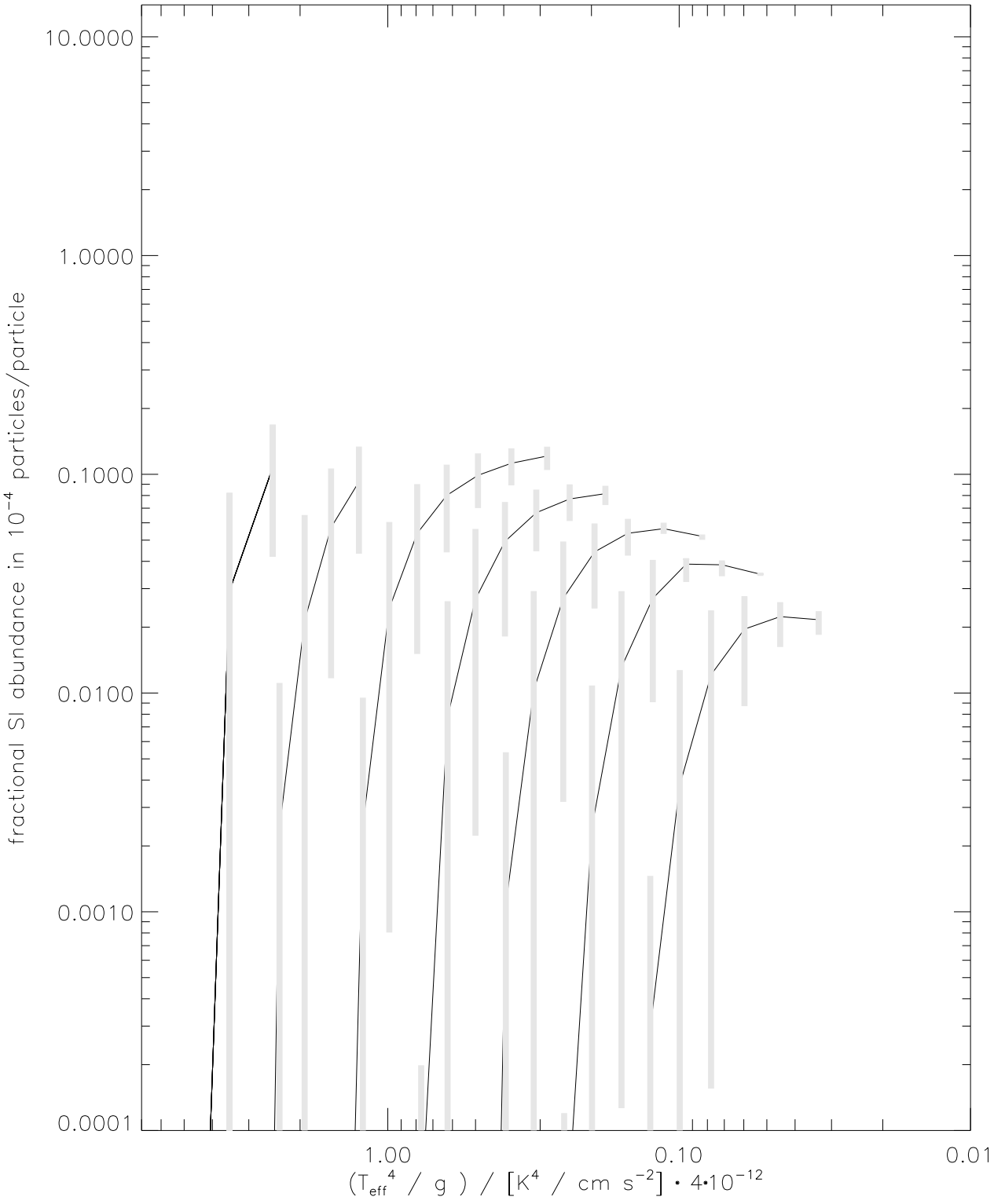

Figure A.19: Silicon abundances as a function of the metal index mi.

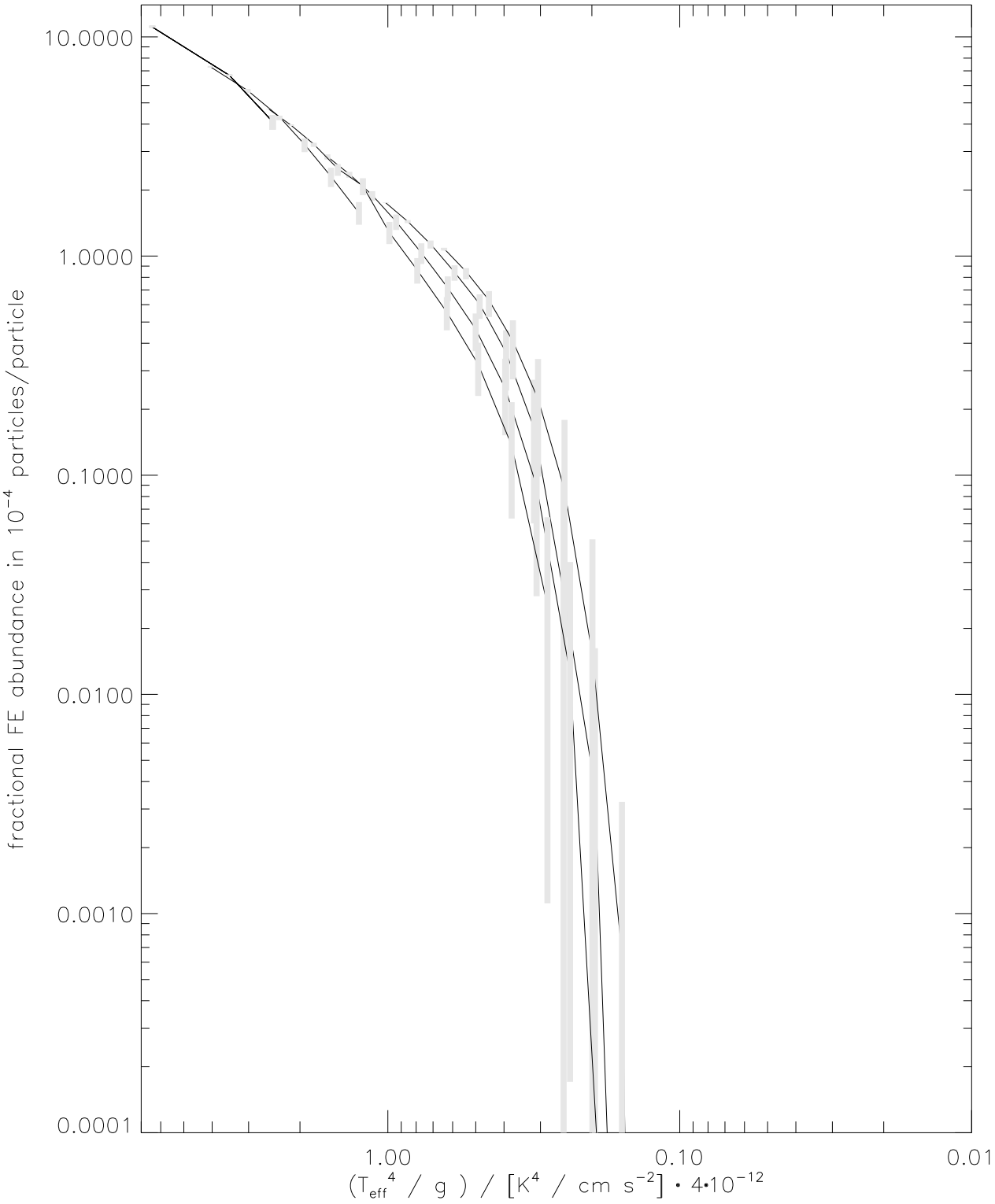

Figure A.20: Iron abundances as a function of the metal index mi.

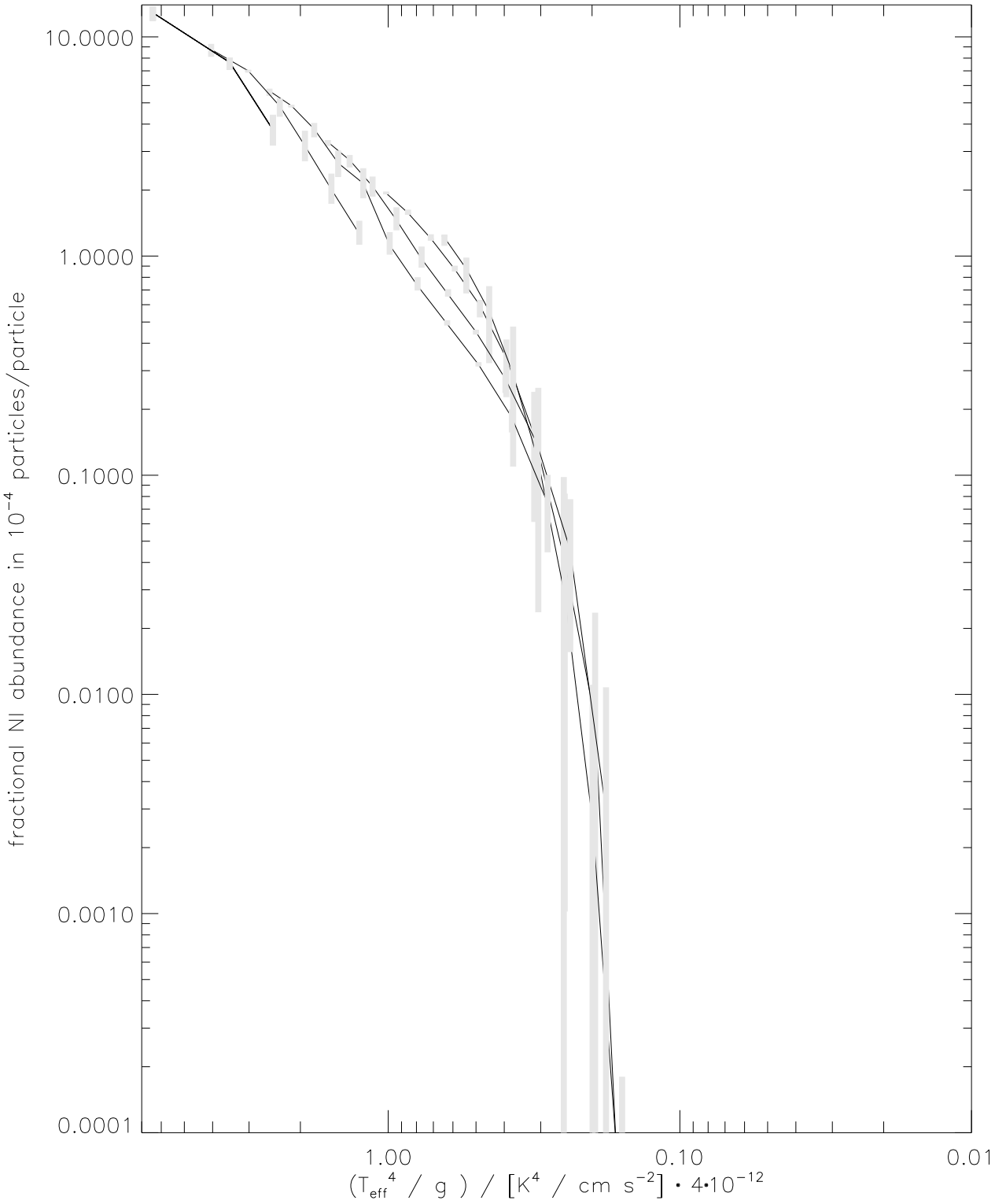

Figure A.21: Nickel abundances as a function of the metal index mi.

Acknowledgements

Klaus Werner's and Stefan Dreizler's advice during the course of this work has been invaluable. It is a great privilege to have such excellent teachers. Without their continued support and steady yet un-intrusive encouragement this thesis might never have been finished. I am particularly grateful for the motivation that radiates from their persons, and for making sure that the funding situation allowed to translate this into what I hope will for some be useful research results. Stefan's trust in me when he decided to continue to foster my career through a position in Göttingen honours me beyond merit.

Burkhard Wolff has laid the grounds for a vital part of this work by providing his reduced EUVE spectra; he and Detlev Koester have additionally provided part of the source code for the handling of the ISM absorption. I also thank Ivan Hubeny and Martin Barstow for fruitful collaborations as well as Pierre Chayer for a stimulating exchange with respect to this work. It is also a pleasure to thank the members of the white dwarf community who have expressed a vivid interest in my subject.

Thorsten Nagel, Klaus Beuermann, and many others have supplied useful comments and discussions. I thank Thorsten, my personal online manual `#tuebingen`, the Tübingen Espressorunde including Jörn Wilms and Katja Pottschmidt, the USW Göttingen "Gang", and many more for technical and moral support.

There are no words to express what role family and friends have played in particular during the last year of finishing this thesis. I deeply thank all those who have expressed their love, friendship and support.

This work was supported by the Deutsche Forschungsgemeinschaft under grants DR 281/13-1 and DR 281/13-2. Travel cost for a research trip to NOAO to visit Ivan Hubeny was funded by the Schuler Stiftung. PPARC, through a University of Leicester travel grant, funded a research visit to work with Martin Barstow and to present this work during a talk. Further presentations were supported through financial contributions by the Astronomische Gesellschaft (Herbsttagungen München 2001 and Berlin 2002), conference fee waivers from the organisers of the European White Dwarf workshop at Kiel (2004) and from the organisers of the Stellar Atmosphere Modelling conference at Tübingen (2002).

Model atmospheres have been calculated on CRAY machines of the Rechenzentrum der Universität Kiel and the IAAT workstation cluster. This research is in parts based on observations made with the EUVE Satellite, has made use of NASA's Astrophysics Data System Bibliographic Services and of the SIMBAD database, operated at CDS, Strasbourg, France.

Lebenslauf

29.01.1975	geboren in Stuttgart, Baden-Württemberg
08.1981–08.1985	Grundschule Bisingen, Baden-Württemberg
08.1985–06.1994	Gymnasium Hechingen, Baden-Württemberg
08.1991–12.1991	Lycée Marguérite de Navarre, Bourges, Frankreich
11.1993	Bundessiegerin im “The Future Astronomers of Europe” Essay Contest des European Southern Observatory
19.06.1994	Abitur
08.1994–07.1996	Eberhard-Karls-Universität Tübingen, Studium der Physik
19.08.1996	Vordiplom
08.1996–08.1997	Queen’s University, Kingston, Ontario, Kanada
09.1997–06.2000	Eberhard-Karls-Universität Tübingen
10.1997–12.1997	Wissenschaftliche Hilfskraft, Fakultät für Physik
04.1998–05.1998	Wissenschaftliche Hilfskraft, Physikalisches Institut
01.1998–07.2003	Dozentin für Physik am Leibniz-Kolleg Tübingen
03.1999–06.2000	Wissenschaftliche Hilfskraft, Institut für Astronomie und Astrophysik (IAA) Tübingen
06.1999–06.2000	Diplomarbeit über “Gleichgewichtshäufigkeiten in heißen Weißen Zwergen” am IAA Tübingen unter der Anleitung von Herrn Prof. Dr. K. Werner
09.06.2000	Diplom
07.2000–06.2003	Wissenschaftliche Angestellte, IAA Tübingen
07.2003–09.2003	Wissenschaftliche Hilfskraft, Universitätssternwarte Göttingen
10.2003–	Wissenschaftliche Angestellte, Universitätssternwarte Göttingen
07.2000–	Anfertigung der Dissertation mit dem Titel “Diffusion processes in stellar atmospheres” an der Eberhard-Karls-Universität Tübingen, Institut für Astronomie und Astrophysik, Abteilung Astronomie, unter Anleitung von Herrn Prof. Dr. K. Werner

Meine akademischen Lehrer waren die Professorinnen, Professoren, Dozentinnen und Dozenten Dres.:
Angewandte Physik: E. Plies; R. Fletcher, A. McLean; *Astronomie und Astrophysik:* H. Mauder, H. Ruder, R. Staubert, K. Werner, S. Dreizler; M.J. Duncan, D.A. Hanes, J. Irwin; *Chemie:* J. Strähle, H. Ebert; *Experimentalphysik:* M. Baumann, H. Clement, F. Gönnenwein, P. Grabmayr, W. Hartmann, R. Hübener, O. Lutz, W. Nakel, G. Staudt, G. Wagner; *Mathematik:* H. Kaul, M. Wolff, H. Fischer, F. Loose; *Theoretische Physik:* A. Fäßler, P. Kramer, H. Müther, N. Schopohl; E. Zaremba, B. Castel.